An Investigation of Matter Enhanced Neutrino Oscillation with the Sudbury Neutrino Observatory

Miles Walter Eldon Smith

A dissertation submitted in partial fulfillment of
the requirements for the degree of

Doctor of Philosophy

University of Washington

2002

Program Authorized to Offer Degree: Physics

University of Washington

Graduate School

This is to certify that I have examined this copy of a doctoral dissertation by

Miles Walter Eldon Smith

and have found that it is complete and satisfactory in all respects,
and that any and all revisions required by the final
examining committee have been made.

Chair of Supervisory Committee:

_____

Steve Elliott

Reading Committee:

_____

Peter Doe

_____

Steve Elliott

_____

Hamish Robertson

Date: _____

University of Washington

Abstract

An Investigation of Matter Enhanced Neutrino Oscillation with the Sudbury Neutrino Observatory

by Miles Walter Eldon Smith

Chair of Supervisory Committee:

Professor Steve Elliott
Department of Physics

Previous experiments have detected fewer electron neutrinos coming from the Sun than are predicted by the Standard Solar Model (SSM). While the Sun makes only ν_e, these can change into other flavors through *neutrino oscillation*, a favored hypothesis for explaining the deficit. The Sudbury Neutrino Observatory (SNO) was designed to measure both the flux of electron neutrinos ϕ_e and the total flux of active neutrinos ϕ_{tot} (where $tot = e + \mu + \tau$). This allows one to separate out the $\mu + \tau$ component by $\phi_{\mu\tau} = \phi_{tot} - \phi_e$. Doing this, SNO measures a flux of non-electron neutrinos $\phi_{\mu\tau} = 3.41 \pm 0.45 (stat.)^{+0.48}_{-0.45} (syst.) \times 10^6 cm^{-2} s^{-1}$, providing evidence of neutrino flavor transformation with 5.3σ significance. By refining the treatment of systematic errors, this improves to 7.4σ. Although this shows that flavor transformation is occurring, it does not identify a specific mechanism such as neutrino oscillation.

Neutrino oscillation can be enhanced by the presence of matter in the Sun and the Earth. This predicts a possible modulation of the flux of electron neutrinos with solar zenith angle, as they transit through varying amounts of matter. However, we do not see a significant difference between the day and night measurements for either

the electron or total neutrino flux. By assuming the total neutrino flux is constant, as predicted by the simplest models, we measure the difference between the day and night electron neutrino flux to be $+7.0 \pm 4.9 \pm 0.9\%$ of the average electron neutrino flux. This result is weak at 1.4σ. By combining this result with that of the Super-Kamiokande experiment, we measure a difference of $6.0 \pm 3.2\%$, or 1.9σ.

By examining a specific oscillation model, we are able to identify allowed regions for the oscillation parameters $\Delta m^2, \tan^2 \theta$. The measured values of $\Delta m^2, \tan^2 \theta$ predict an asymmetry in the day to night flux which is consistent with the measurements above. This specific model also allows for a distortion of the neutrino spectrum. However, this additional observable does little to improve the identification of neutrino oscillation as the cause of flavor transformation in solar neutrinos.

We conclude that, while flavor transformation is definitely occurring for solar neutrinos, we can not specifically identify the mechanism to be matter enhanced neutrino oscillation.

TABLE OF CONTENTS

LIST OF FIGURES

iv

LIST OF TABLES

LIST OF ABBREVIATIONS

8B: Neutrinos from the reaction

$$^8B + e^- \rightarrow {}^8Be^* + e^+ + \nu_e$$

CC: Charged Current

ES: Elastic Scattering

GALLEX: Gallium Experiment

HEP: Neutrinos from the reaction

$$^3He + p \rightarrow {}^4He + e^+ + \nu_e$$

LMA: Large Mixing Angle

NC: Neutral Current

NCD: Neutral Current Detector

PEP: Neutrinos from the reaction

$$p + e^- + p \rightarrow d + \nu_e$$
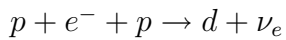
PGT: Pulsed Global Trigger

PMT: Photomultiplier Tube

PP: Neutrinos from the reaction

$$p + p \rightarrow d + e^+ \nu_e$$
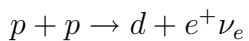
PREM: Preliminary Reference Earth Model

PSUP: PMT Support Structure

SAGE: Russian (formally Soviet) - American Gallium Experiment

SMA: Small Mixing Angle

SNO: Sudbury Neutrino Observatory

SNP: Solar Neutrino Problem

SSM: Standard Solar Model. In this thesis, we will use [2] as our reference model.

SK: Super-Kamiokande

MATHEMATICAL OBJECTS

Event Parameters

E_ν = energy of a neutrino

T_e = kinetic energy of subsequent recoil particle

T_{eff} = measured kinetic energy of an event

R_{fit} = event's measured radial position

$\cos\theta_\odot$ = measured value of the cosine of the opening angle of a recoil electron

$\cos\theta_z$ = cosine of solar zenith angle

$X = \{T_{eff}, R_{fit}^3, \cos\theta_\odot, \cos\theta_z\}$ is the set of measurable quantities.

X_m = value of X for specific event m

$m = 1, N$ runs over the number of events

N = number of events

$u.r = \cos\theta_r$ = direction of event relative to the reconstructed radial position

$\cos\theta_o, \phi_o$ = polar coordinates of reconstructed position

Physics Parameters

η = generic physics parameter

$\boldsymbol{\eta}$ = vector of physics parameters

$\eta[k]$ = kth physics parameter

ϕ_{tot} = total flux of active ^{8}B neutrinos. This, and all other flux parameters, are relative to the SSM, unless otherwise stated

$\phi_e = \nu_e$ flux

$\phi_{\mu\tau}$ = flux of ν_μ and ν_τ

ϕ_{hep} = total flux of active hep neutrinos, *etc.*

$\phi_{tot} = \phi_o + \Delta\phi$ divides ϕ up into unperturbed and perturbed parts

Δm^2 = difference between the square of the masses of two neutrino mass states

$\tan^2 \theta =$ tangent of the mixing angle between two neutrinos

Systematic Parameters

$\alpha =$ generic systematic parameter, such as energy scale uncertainty.

$\alpha(t) =$ time dependent systematic

$\alpha_D =$ average of $\alpha(t)$ for day bin

$\alpha_N =$ average of $\alpha(t)$ for night bin

$\alpha_{av} =$ average of $\alpha(t)$ for total livetime

$\alpha_{dif} = \alpha_N - \alpha_D$

$\boldsymbol{\alpha} =$ vector of systematic parameters. Typically, its components are a combination of α_{av} and α_{dif} systematics.

$\alpha[k] = \mathrm{k}^{th}$ component of a vector of systematic parameters

$\alpha_{cal} =$ nominal value of α, as determined from calibrations

$\alpha_o =$ value of α, around which a perturbative expansion is made. This could be either set to α_{cal} or zero.

Modelling the Number of Events

$\mu = \mu(X|\eta, \alpha) =$ the number density of events. μ may either be continuously distributed over X, or else binned into a histogram. μ also depends continuously on the physics and systematic parameters.

$\mu_o(X|\eta) = \mu(X|\eta, \alpha = \alpha_o)$ is the model when the systematics are set to α_o

$\mu^{cc} = \mu^{cc}(X|\eta) = \mu_o$ evaluated for the CC reaction only

$y_o = \mu_o$ with ϕ_{tot} set to $1 \times$ SSM

$S = S(\eta, \alpha) = \sum_X \mu(X|\eta, \alpha)$

$S_o = S_o(\eta) = \sum_X y_o(X|\eta)$

$\boldsymbol{\beta} = \boldsymbol{\beta}(X|\eta) = \frac{1}{\mu_o(X|\eta)} \frac{\partial \mu(X|\eta,\alpha)}{\partial \boldsymbol{\alpha}^T}\Big|_{\alpha=0}$ is a vector of partial derivatives, describing the 1st order perturbation of the model by a vector of systematics.

Miscellaneous

v = speed of electron

c = speed of light

$\hbar$ = Planks constant/2π

σ = uncertainty on a single parameter. This notation is also used to represent a cross section, although the context should be clear.

$\boldsymbol{\sigma}^2$ = error matrix.

σ_E = width of SNO's electron response function

σ_{NC} = width of neutron peak

N_{hit} = Total number of hit PMTs

N_{total} = Total number of hit PMTs, after some additional cuts to remove poorly calibrated tubes.

N_{prompt} = Number of hit PMTs is the prompt light window

N_{PMT} = Number of PMTs on and collecting data.

τ_{prompt} = width of prompt light window (20 ns)

R_{noise} = Average dark noise rate of PMTs

t, t_N, t_D = total, night, and day livetime

R = event rate for some generic source of events

R_N, R_D = night, day values of R

B = amplitude of some background source, expressed as a total number of events

B_N, B_D = night, day values of B

ACKNOWLEDGMENTS

I would like to thank my advisor Steve Elliott, along with the other faculty and staff of the Electroweak-Interaction Group at the Center for Experimental Nuclear Physics and Astrophysics; Tom Burritt, Peter Doe, Hamish Roberston, Tom Steiger, and John Wilkerson. To these individuals I owe my education in neutrino physics and in experimental technique.

The work presented here was a collaborative effort with the staff, students, and faculty of the Sudbury Neutrino Observatory. I recognize that my thesis would not exist without the contribution of many, although it would be difficult to list them all here. However, I would like to thank a small group, with whom I worked most closely; Mark Chen, Fraser Duncan, Joe Formaggio, Karsten Heeger, Neil McCauley, Scott Oser, and Kathryn Schaffer.

Finally, I would like to thank my parents for their love, support and DNA. To them, I dedicate this thesis.

Chapter 1

INTRODUCTION

1.1   A Little History

In 1933, Pauli postulated neutrinos as a "desperate remedy" for the then problem of the missing energy of beta decay [3]. It was not until 1956 that Reines and Cowen provided direct experimental evidence that the neutrino existed [4], detecting reactor neutrinos *via*

$$\overline{\nu}_e + p \rightarrow n + e^+ \tag{1.1}$$

Subsequently, it has been shown that there are three flavors of neutrino, belonging to the electron, muon [5] and tau [6] families. In addition, cosmological constraints [7], [8] and studies of the width of the Z^o boson [9] have shown that there can be no additional neutrino flavors, if they are to be both less massive than $\frac{1}{2}m_Z$ (where m_Z is the mass of the Z^o) and interact via the weak interaction. The parity non-conservation of weak interactions led to the incorporation of only left handed neutrinos ν_L (and right handed antineutrinos $\overline{\nu}_R$) into the standard model [10].

The neutrino is both chargeless and color neutral, and thus only interacts weakly, passing easily through matter such as the Sun or the Earth. For this reason, solar neutrino experiments are placed deep underground, using the rock to screen out cosmic backgrounds but allowing neutrinos to penetrate.

It was recognized as early as 1939 that the Sun might be a strong source of neutrinos. Bethe suggested that the Sun's energy comes mainly from a chain of

nuclear fusion reactions called the p-p chain [11]. A subset of these reactions yields electron neutrinos, as shown in Fig. 1.1. We shall refer to the different contribution to the neutrino flux as pp, pep, hep, ^{7}Be, and ^{8}B. Except for their energy, there is no way to distinguish between the neutrinos from the various sources. Fig. 1.2 shows the neutrino spectrum for each reaction, as determined by careful nuclear physics calculations. While the shapes of these spectra, to very high accuracy, are independent of the environmental conditions [12], the reaction rates are strongly dependent on both the temperature and pressure in the core of the Sun. Detailed calculations have been made of the expected flux from each reaction, taking into account the thermodynamic equation of state, gravitational and pressure effects, energy transport, opacity, nuclear cross sections, and many finer details. These calculations have culminated in the *Standard Solar Model* (SSM). Actually, there is more than one solar model [2], [13]. In this thesis, we shall use [2] as a reference model.

Solar neutrinos were first detected by Davis *et. al.* [15] *via* the reaction

$$\nu_e + {}^{37}Cl \rightarrow e^- + {}^{37}Ar - 0.814 MeV \tag{1.2}$$
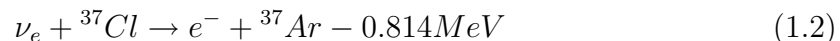
in the Homestake mine. Electron neutrinos interact within a large tank of liquid C_2Cl_4, producing trace amounts of ^{37}Ar. Since Ar is a noble gas, it dissolves into the liquid and can be extracted by purging with helium gas. With an electron capture half life of 35 days, ^{37}Ar is counted to measure the flux of solar neutrino. The measured and SSM calculated fluxes were in disagreement, revealing the *Solar Neutrino Problem.*

Since the Homestake experiment began, five additional experiments have measured a low flux of solar neutrinos. The Gallium experiments SAGE, GALLEX and GNO detect neutrinos *via* the reaction

$$\nu_e + {}^{71}Ga \rightarrow e^- + {}^{71}Ge - 0.233 MeV \tag{1.3}$$

SAGE uses liquid gallium metal as its target, and performs an acid extraction of the ^{71}Ge. GALLEX and GNO use a concentrated $GaCl_3$-HCl solution, with the resulting
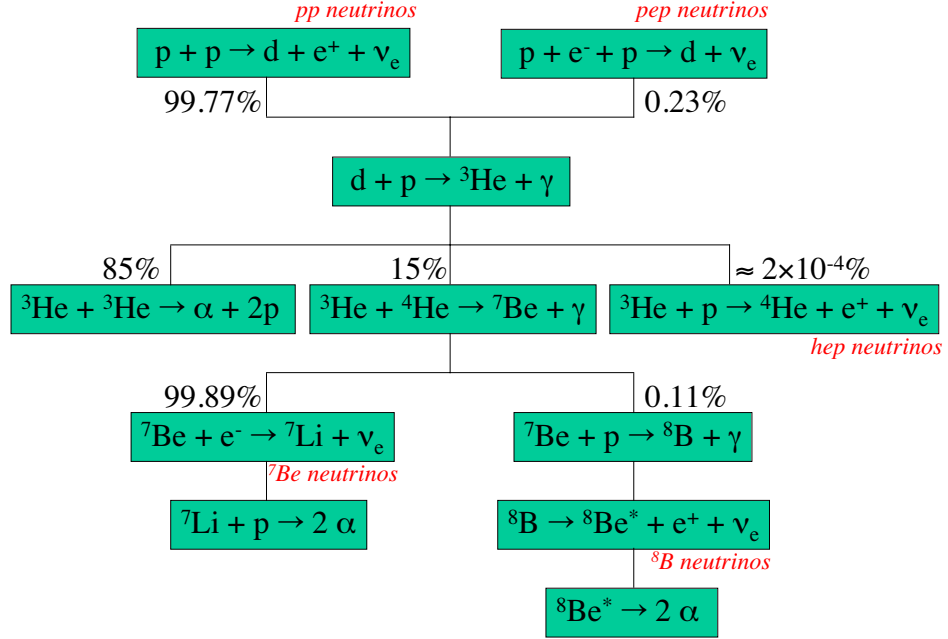
Figure 1.1: The p-p chain. Percentages are given for each branching. For example, 0.11% of the time, ^{7}Be is consumed by proton capture, rather than electron capture. This relative amplitude is calculated by comparing the flux of ^{8}B and ^{7}Be neutrinos, as calculated in [2].

GeCl$_4$ extracted by bubbling nitrogen through the solution. The ^{71}Ge has a half life of 11.4 days and is readily counted to measure the electron neutrino flux. The Gallium and Homestake experiments are examples of *radiochemical* experiments, since they involve the accumulation and chemical extraction of radioactive isotopes.

The H$_2$O experiments Kamiokande and the much larger Super-Kamiokande (SK) detect neutrinos via the elastic scattering of electrons.

$$\nu_x + e^- \rightarrow \nu_x + e^- \tag{1.4}$$

The effective threshold is set between 5 and 8 MeV kinetic, to avoid the Cherenkov light from low energy backgrounds. It is interesting to note that this last reaction is sensitive to *all* active neutrino flavors. However, the dominant contribution is
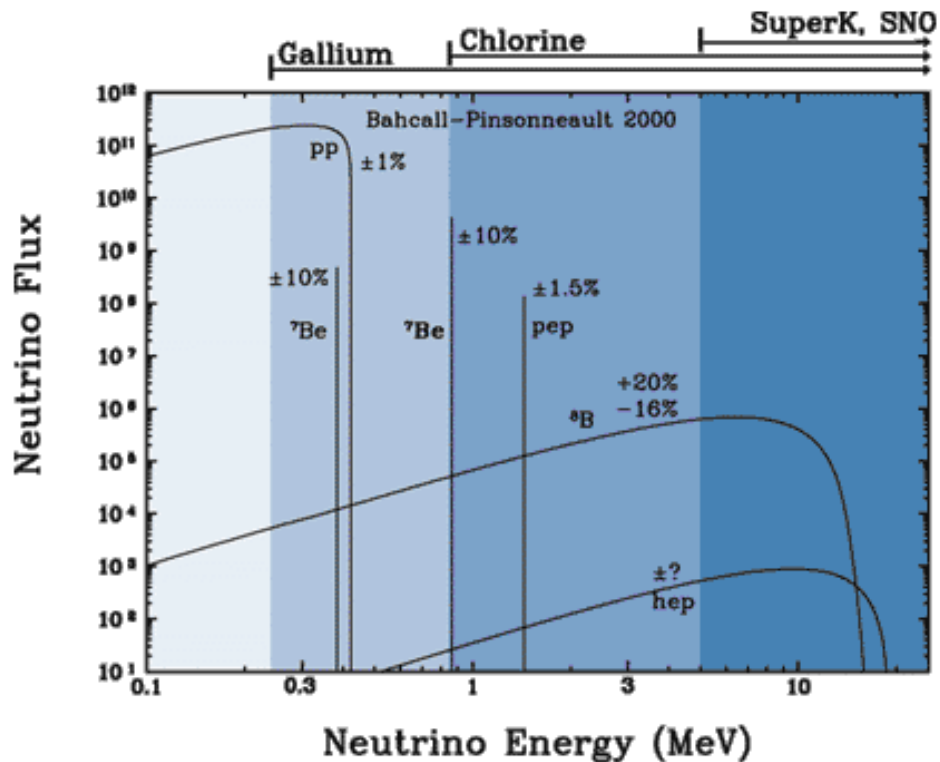
Figure 1.2: Neutrino Spectra from the p-p chain. Only the ^{8}B and hep neutrinos can be observed by SNO. Figure taken from [14].

from the electron neutrino, as the cross section is approximately 6 times higher for interaction with ν_e. Also unique about the water experiments is that they are real-time detectors, measuring information about each event, including the energy and the time of the interaction. Of the neutrino spectra shown in Fig. 1.2, only ^{8}B (and the much less numerous hep) neutrinos exceed the experimental threshold. In contrast, the radiochemical experiments can only measure integrated information, such as the total flux above threshold. However, the threshold is much lower for radiochemical experiments, allowing for the detection of neutrinos from the pp, pep, and ^{7}Be reactions, in addition to ^{8}B and hep.

1.2 The Solar Neutrino Problem

1.2.1 The missing Neutrinos

In this thesis, we shall present neutrino fluxes relative to the SSM of Bahcall, Pin-sonneault, and Basu (BP2000) [2]. Table 1.1 shows the predictions of this model for the flux of various neutrino species, as well as the event rates predicted for each type of experiment. The units used for the Ga and Cl experiments are SNU, or *Solar Neutrino Unit*, where 1 SNU = 10^{-36} *events per target atom per second*. The data from the water Cherenkov experiments is reported as an absolute flux, so is in units of $cm^{-2}s^{-1}$. Results of the Homestake, SAGE, GALLEX, GNO, and SK experiments are taken from [16], [17], [18], [19], and [20] respectively[1]. The important feature for this discussion is the bottom line of the table, where we see that all three sets of ex-perimental data fall significantly short of the predicted event rates. This is the *Solar Neutrino Problem* (SNP), also represented in Fig. 1.4. Either the solar model is in grave error, or the electron neutrinos produced in the core of the Sun are disappearing.

1.2.2 Failure of Astrophysical Solutions

The SSM can be very sensitive to input parameters. The ^{8}B flux, which contributes to the event rate in all experiments, varies as $(T_{core})^{24}$, where T_{core} is the core temperature of the Sun [12]. In contrast, the *pp* rate varies as $(T_{core})^{-1.2}$. The core temperature of the Sun can easily be modified by changing, for example, the chemical abundances or energy transport mechanisms. Exotic particles, such as WIMPs (Weakly Interacting Massive Particles) might carry energy out of the core of the Sun[2]. Such solutions to the SNP are termed *astrophysical*, because they change the environment in the core of the Sun and, ultimately, the flux of neutrinos produced by each of the reactions.

---

[1]We note that the Super-Kamiokande collaboration have since published updated results in [21].

[2]Although WIMPS are a new particle, this is regarded as an astrophysical solution to the SNP because they change the astrophysical environment and equation of state.

Table 1.1: SSM predictions for the flux of pp-chain and CNO-cycle neutrinos, along with the expected event rates for the Ga, Cl, and H2O detectors, taken from [2]. The Ga datum is a combination of the Gallex + GNO [19], and SAGE [17] experimental results. The H_2O datum comes exclusively from the Super-Kamiokande experiment [20] (although see footnote on previous page) and the Cl datum comes exclusively from the Homestake experiment [16]. Uncertainties in the cross section enter into the SSM predictions for the Ga and Cl experiments, while the cross section for elastic scattering (H_2O) is known extremely well. The error on the ratio, calculated in the last line, includes uncertainties from both data and SSM.

		Standard Solar Model Predictions		
Source	SSM Flux	Ga	Cl	H_2O
	$(10^{10} cm^{-2} s^{-1})$	(SNU)	(SNU)	$(\times 10^6 cm^{-2} s^{-1})$
pp	$5.95(1.00^{+0.01}_{-0.01})$	69.7	0.0	0.0
pep	$1.40 \times 10^{-2}(1.00^{+0.015}_{-0.015})$	2.8	0.22	0.0
^7Be	$4.77 \times 10^{-1}(1.00^{+0.10}_{-0.10})$	34.2	1.15	0.0
^8B	$5.05 \times 10^{-4}(1.00^{+0.20}_{-0.16})$	12.1	5.76	5.05
hep	9.3×10^{-7}	0.1	0.04	0.0093
^{13}N	$5.48 \times 10^{-2}(1.00^{+0.21}_{-0.17})$	3.4	0.09	0.0
^{15}O	$4.80 \times 10^{-2}(1.00^{+0.25}_{-0.19})$	5.5	0.33	0.0
^{17}F	$4.80 \times 10^{-2}(1.00^{+0.25}_{-0.19})$	0.1	0.0	0.0
total SSM:		128^{+9}_{-7}	$7.6^{+1.3}_{-1.1}$	$5.05^{+1.01}_{-0.81}$
data:		72.3 ± 4.6	2.56 ± 0.23	2.32 ± 0.08
data/SSM:		**0.56 ± 0.05**	**0.34 ± 0.06**	**0.46 ± 0.08**
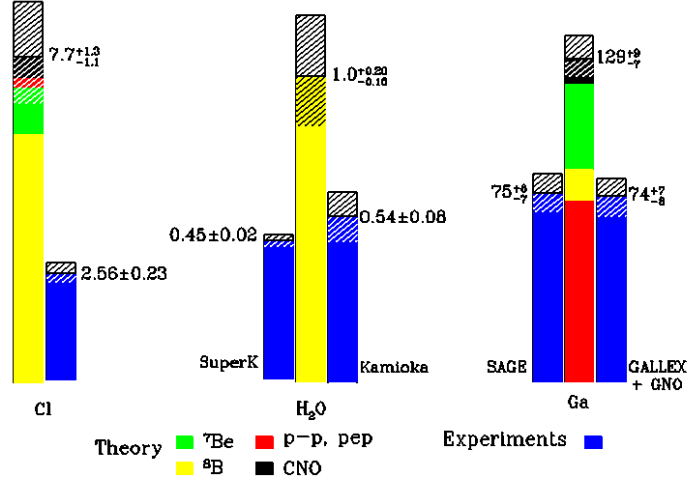
Figure 1.3: Measured neutrino fluxes from the three types of solar neutrino experiments. Figure taken from [14].

A number of model independent analyses have been performed, showing that astrophysical solutions are disfavored [22], [23]. A crude version of this argument is now presented. Other than the pp neutrinos, there are also neutrinos from the CNO cycle. In stars of similar mass to the Sun, this cycle plays only a minor role and we note that these neutrinos contribute only a small amount ($< 7\%$) to any given experiment. We choose to neglect these contributions. We also note that the ratio of the pep and pp fluxes ϕ_{pep}/ϕ_{pp} is largely independent of astrophysical conditions [12], and so we can treat these as a single source. For this analysis we define a vector of fluxes $\boldsymbol{\phi}$, with three components, and a vector of experimental data $\boldsymbol{R}$, also of three components.

$$\boldsymbol{\phi} = \begin{pmatrix} \phi_{pp}/\phi_{pp}^{SSM} \\ \phi_{{}^7Be}/\phi_{{}^7Be}^{SSM} \\ \phi_{{}^8B}/\phi_{{}^8B}^{SSM} \end{pmatrix} \qquad \boldsymbol{R} = \begin{pmatrix} Ga\ rate \\ Cl\ rate \\ H_2O\ rate \end{pmatrix} = \begin{pmatrix} 72.3 \\ 2.56 \\ 2.32 \end{pmatrix} \qquad (1.5)$$

where we have assumed $\phi_{pep}/\phi_{pep}^{SSM} = \phi_{pp}/\phi_{pp}^{SSM}$ and neglected other contributions.
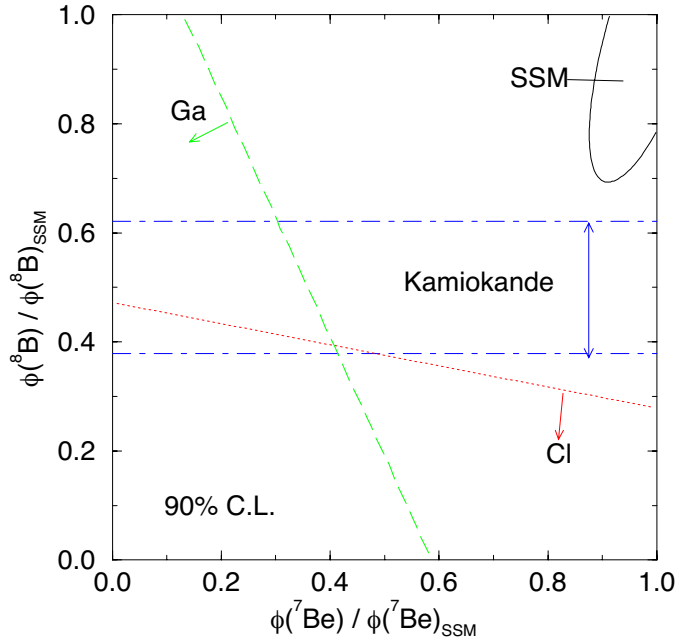
Figure 1.4: Attempted astrophysical solutions to the solar neutrino problem, where the amplitude of each neutrino source is considered unknown but the intrinsic neutrino spectra is well known. Figure taken from [23]

Note that the units of the first two components of $\boldsymbol{R}$ are SNU, and the last component is $\times 10^6 cm^{-2} s^{-1}$. The three experimental errors are assumed to be uncorrelated, so we write an error matrix

$$\boldsymbol{\sigma}_R^2 = \begin{pmatrix} 4.6^2 & 0 & 0 \\ 0 & 0.23^2 & 0 \\ 0 & 0 & 0.08^2 \end{pmatrix} \tag{1.6}$$

We compare the data $\boldsymbol{R}$ to the model $\boldsymbol{S\phi}$, where $\boldsymbol{S}$ is the matrix of cross sections, averaged over the neutrino energy spectra and multiplied by the expected flux,

$$\boldsymbol{S} = \begin{pmatrix} 72.5 & 34.2 & 12.1 \\ 0.22 & 1.15 & 5.76 \\ 0 & 0 & 5.05 \end{pmatrix} \tag{1.7}$$

This corresponds to simply a change of variables (since there are three variables for three data points). The solution is given by

$$\boldsymbol{\phi} = \boldsymbol{S}^{-1}\boldsymbol{R} \qquad \boldsymbol{\sigma}_\phi^{-2} = \boldsymbol{S}^T\boldsymbol{\sigma}_R^{-2}\boldsymbol{S} \qquad (1.8)$$

or, with numerical values

$$\boldsymbol{\phi} = \begin{pmatrix} 1.051 \\ -0.276 \\ 0.459 \end{pmatrix} \pm \begin{pmatrix} 0.131 \\ 0.237 \\ 0.016 \end{pmatrix} \qquad [corr] = \begin{pmatrix} 1.00 & -0.87 & 0.29 \\ -0.87 & 1.00 & -0.37 \\ 0.29 & -0.37 & 1.00 \end{pmatrix} \qquad (1.9)$$

where we have provided the correlation matrix as well. We see that the best fit pp (and pep) flux is $1.13\times$ SSM, while the ^{8}B flux is suppressed to be $0.48\times$ SSM. This could simply be telling us that the ^{8}B reaction is highly sensitive to T_{core}, and some astrophysical process is suppressing that temperature slightly. However, we note that the best fit to the ^{7}Be flux is negative at $\approx 1\sigma$, an unphysical solution. What is alarming about this is that the ^{8}B and ^{7}Be neutrinos come through a common channel ($^3He + {}^4He \to {}^7Be + \gamma$), making it is hard to suppress $\phi_{^7Be}$ completely and not $\phi_{^8B}$. In this way, an astrophysical solution to the solar neutrino problem is disfavored. By adding additional information, such as the relationship between the light and neutrino output of the Sun (known as the *luminosity constraint*), the possibility of an astrophysical solution is even more strongly disfavored.

1.2.3 Particle Physics Solutions

What could be going wrong? Driving the unphysical solution is the fact that there is just no room left for ^{7}Be neutrinos. The Super-Kamiokande experiment (H_2O) tightly constrains $\phi_{^8B}$, which in turn accounts for more than the observed rate in the Homestake experiment (Cl). We have already relaxed the SSM constraint on the individual fluxes and so what else could be incorrect about the model?

A clear way out of this is to assume that the neutrino spectra, seen in Fig. 1.2, are incorrect. If whatever is suppressing the neutrinos removes a larger fraction of

[8]B neutrinos from the Cl experiment than from the H_2O, then $\phi_{7_{Be}} > 0$ will once again be favored. Alternatively, an additional contribution of μ or τ neutrinos can scatter electrons through the neutral current channel, but will not interact in the Cl or Ga experiments. However, there are no astrophysical mechanisms which can alter the intrinsic neutrino spectra, which are determined by well understood weak interaction physics, nor alter the neutrino flavor. The only way to do this is to affect the neutrinos as they propagate through the solar material and to the Earth. Such solutions to the solar neutrino problem are termed *particle physics solutions.*

A number of candidates for a particle physics solution have been proposed. There is the possibility of an anomalous neutrino magnetic moment, interacting with the solar magnetic field to flip the neutrino into an antineutrino. An alternative proposal allows for neutrino decay, and yet another allows for flavor changing neutral currents. The most popular solution is that of *neutrino oscillation*, which allows neutrinos to oscillate from one flavor to another as they propagate. A similar mechanism is already observed in the quark sector between similarly charged quarks.

1.3 Vacuum Oscillation

1.3.1 Neutrino Mass

The standard model of weak interactions does not include a term for neutrino mass. Without right handed neutrinos ν_R, the standard Dirac mass term in the Lagrangian $\frac{M_\nu}{2}(\nu_R^\dagger \nu_L + \nu_L^\dagger \nu_R)$ can not be constructed. Furthermore, there exist only upper limits on direct measurements of the neutrino masses[3]. However, if desired, one can generate mass terms by either adding a right handed component to the model or else constructing Majorana mass terms (which couples the ν_L field to itself). If adding a right handed neutrino, the very natural *see-saw mechanism* breaks the two com-

---

[3]The study of atmospheric neutrinos with Super-Kamiokande has provided evidence for neutrino oscillation and, hence, indirect evidence for neutrino mass.

ponents up into a very heavy *sterile* and light *active* neutrino, both of which are Majorana. For a more detailed description, see [24]. Here it will suffice to assume that neutrinos may have mass and a relativistic dispersion equation $E^2 = p^2 + m^2$.

1.3.2   General Formulation

In general, the weak eigenstates ν_e, ν_μ, ν_τ are not necessarily identical to the mass eigenstates ν_1, ν_2, ν_3, but rather a linear superposition.

$$\begin{pmatrix} \nu_e \\ \nu_\mu \\ \nu_\tau \end{pmatrix} = \begin{pmatrix} U_{e1} & U_{e2} & U_{e3} \\ U_{\mu 1} & U_{\mu 2} & U_{\mu 3} \\ U_{\tau 1} & U_{\tau 2} & U_{\tau 3} \end{pmatrix} \begin{pmatrix} \nu_1 \\ \nu_2 \\ \nu_3 \end{pmatrix} \tag{1.10}$$

The matrix U is the *mixing matrix* or *Pontecorvo-Maki-Nakagawa-Sakata* (PMNS) matrix. A convenient parameterization (for Dirac neutrinos) is given by

$$U = \begin{pmatrix} 1 & 0 & 0 \\ 0 & c_{23} & s_{23} \\ 0 & -s_{23} & c_{23} \end{pmatrix} \begin{pmatrix} c_{13} & 0 & s_{13}e^{-i\delta} \\ 0 & 1 & 0 \\ -s_{13}e^{+i\delta} & 0 & c_{13} \end{pmatrix} \begin{pmatrix} c_{12} & s_{12} & 0 \\ -s_{12} & c_{12} & 0 \\ 0 & 0 & 1 \end{pmatrix} \tag{1.11}$$

where $c_{12} = \cos\theta_{12}$, $s_{23} = \sin\theta_{23}$, etc. Here $\theta_{12}, \theta_{23}, \theta_{13}$ are called the *mixing angles*, while δ is a phase related to CP violation. If the neutrino masses are Majorana, there can be an additional two phases, although these are not important here.

An electron neutrino produced in the core of the Sun, with momentum $\vec{p}$, will propagate as

$$\begin{aligned} |\nu(t) > &= e^{-i\hat{H}t}|\nu_e > \\ &= \sum_j U_{ej} e^{-iE_j t}|\nu_j > \end{aligned} \tag{1.12}$$

where we have taken $c = \hbar = 1$. Under the assumption that $m_j \ll E_j$,

$$\begin{aligned} E_j &= \sqrt{p^2 + m_j^2} \\ &\approx |p| + \frac{m_j^2}{2E} \end{aligned} \tag{1.13}$$

If desired, one could create a wavepacket out of these momentum states, although this will not change the conclusions of this section [25]. After allowing the neutrino to propagate for a time t, we wish to calculate the probability for it still to be an electron neutrino, also known as the *survival probability*.

$$P_{ee} = | < \nu_e | \nu(t) > |^2 = \sum_{jk} |U_{ej}|^2 |U_{ek}|^2 e^{-\frac{i\Delta m_{jk}^2 t}{2E}} \qquad (1.14)$$

where

$$\Delta m_{jk}^2 \equiv m_j^2 - m_k^2 \qquad (1.15)$$

Equation 1.14 becomes unity when $U_{e1} = 1$ and the other two U_{ej} are zero. In this case ν_e is a mass eigenstate. When either U_{e2} or $U_{e3} \neq 0$, the equation can still become unity if $\Delta m_{21}^2 = 0$ (no mass splitting). In the general case, however, $P_{ee} < 1$ and the neutrino is no longer a pure electron neutrino (except when the phase in Eqn. 1.14 is a multiple of 2π). The probability that our neutrino has changed flavor to a ν_μ or ν_τ is given by

$$P_{ee} = 1 - \sum_{jk} |U_{ej}|^2 |U_{ek}|^2 e^{-\frac{i\Delta m_{jk}^2 t}{2E}} \qquad (1.16)$$

This is known as *neutrino oscillation*.

1.3.3 The Two Neutrino Case

The problem simplifies considerably in the case of oscillation between only two neutrinos. In this case, the mixing matrix reduces to a 2×2 matrix

$$U^{(2\nu)} = \begin{pmatrix} \cos\theta & \sin\theta \\ -\sin\theta & \cos\theta \end{pmatrix} \qquad (1.17)$$

where there is now only one mixing angle θ and one mass difference Δm^2. The survival probability simplifies to

$$P_{ee}^{(2\nu)} = 1 - \sin^2 2\theta \sin^2 \left(-\frac{\Delta m^2 t}{2E} \right) \qquad (1.18)$$

Since neutrinos travel at near luminous speeds, one can rewrite the oscillatory term in Eqn. 1.16 as

$$\sin^2\left(\frac{\pi r}{L_V}\right) \qquad L_V = \frac{4\pi E\hbar}{\Delta m^2 c^3} \tag{1.19}$$

where r is the distance travelled from the source and L_V is called the *vacuum oscillation length* (with units of c and $\hbar$ added for completeness). Once the neutrino has travelled an integer multiple of L_V, its survival probability returns to unity and it can only be detected as an electron neutrino.

1.3.4   Constraints from Other Experiments

If neutrinos of a specific energy range are observed to oscillate over a particular length scale, this puts strong constraints on the possible values of Δm^2 for that mode. The Super-Kamiokande experiment has observed oscillation of high energy atmospheric neutrinos, with the $\nu_\mu \to \nu_\tau$ mode being most strongly favored [26]. These energies and the path length of the atmosphere are indicative of a difference in mass-squared of $\approx 1 - 5 \times 10^{-3}$ eV^2. This value is too large to be responsible for solar neutrino oscillations. An oscillation length this short would appear incoherent over Earth-Sun length scales, unable to suppress the solar neutrino flux by more than a factor of 2 (whereas a factor of ≈ 3 is required for some experiments). In addition, the electron neutrino does not appear to participate in atmospheric neutrino oscillation. So there must be another Δm^2 leading to solar neutrino oscillations. By convention[4], we assign

$$\Delta m^2(solar) = \Delta m_{21}^2 > 0$$
$$\Delta m^2(atm.) = \Delta m_{32}^2 \tag{1.20}$$
$$|\Delta m^2(solar)| \ll |\Delta m^2(atm.)|$$

---

[4]This convention has the electron neutrino primarily composed of ν_1 for $\tan^2\theta < 1$ and primarily ν_2 for $\tan^2\theta > 1$ (the *dark side* [27]). An alternate convention is to allow Δm_{21}^2 to be either positive or negative but constrain $\tan^2\theta < 1$. We will not use this alternate convention here.

The sign of Δm_{32}^2 determines if the mass hierarchy is *standard* $(\Delta m_{32}^2 > 0)$ or *inverted* $(\Delta m_{32}^2 < 0)$. The third mass difference is determined by the constraint

$$\Delta m_{31}^2 = \Delta m_{32}^2 + \Delta m_{21}^2 \tag{1.21}$$

By assuming the short oscillation length for the atmospheric mode, the survival probability for solar neutrinos decouples from the parameters θ_{23} and Δm_{23}^2 to give [28]

$$P^{3\nu}(solar) = \cos^4 \theta_{13} \left(P^{2\nu}(\Delta m_{21}^2, \theta_{21}) + \tan^4 \theta_{13} \right) \tag{1.22}$$

An additional constraint comes from the null result of the CHOOZ reactor experiment, looking for disappearance of $\overline{\nu}_e$ [29]. The combined atmospheric and CHOOZ data puts a strong constraint on the mixing between ν_e and the third mass neutrino.

$$\sin^2 \theta_{13} = |U_{e3}|^2 < 1.7 \times 10^{-2} \quad (90\% \; c.l.) \tag{1.23}$$

This limits $\tan^4 \theta_{13} < 3.0 \times 10^{-4}$. To solve the solar neutrino problem, one needs $P(solar) \approx 0.3$. In this way, the $\tan^4 \theta_{13}$ term contributes at most 1 part in 1000 to the solar oscillation model and henceforth shall be neglected.

1.4   The MSW Effect

Neutrino oscillation can be enhanced by the presence of matter, a mechanism known as the MSW effect (named for its discoverers, Mikheyev and Smirnov [30] and Wolfenstein [31]). Here we shall study the problem of 2 neutrino oscillation in matter. Electron neutrinos interact weakly with ordinary matter via both $W^\pm$ and Z^o exchange, while μ and τ neutrinos interact only *via* Z^o exchange. This leads to a difference in the forward scattering cross section for ν_e and $\nu_{\mu\tau}$. The result is that a general neutrino state will propagate in matter as [12]

$$i\frac{d}{dt}|\nu(t)> = (H_o + H_{matter})|\nu(0)>$$
$$H_{matter} = \sqrt{2}G_F n_e|\nu_e><\nu_e| \tag{1.24}$$

where the additional interaction term H_{matter} affects only ν_e [5]. G_F is Fermi's constant and n_e is the electron density profile seen by the neutrino as it propagates. The H_{matter} term leads to an effective mass for the ν_e component, which makes it behave heavier in the denser regions of the Sun. In addition, there is an effective mixing angle θ_M.

$$\tan 2\theta_M = \frac{\sin 2\theta}{\cos 2\theta - L_V/L_e} \qquad L_e = \frac{\sqrt{2}\pi\hbar c}{G_F n_e} \qquad (1.25)$$

We see that a resonance condition occurs when $L_e \to \frac{L_V}{\cos 2\theta}$ or when

$$n_e(resonance) = \frac{\cos 2\theta \Delta m^2}{2\sqrt{2}G_F E} \qquad (1.26)$$

If the resonance condition is achieved at some place in the Sun, there can be almost complete conversion of the electron neutrino into the heavier mass ν_2 [32]. The range of electron densities in the Sun and the energy of the neutrinos allow for MSW oscillations to occur for a mass difference $\Delta m^2 \approx 10^{-8} - 10^{-4}$. Outside of this range neutrino oscillation can still occur, although the matter enhanced conversion is incomplete. With incomplete conversion, the neutrino will not be in a pure mass eigenstate when it leaves the Sun and vacuum oscillation can still occur as it transits the 1 AU from the Sun to the Earth. For a pure vacuum solution, over this length scale, we require $\Delta m^2 \sim \mathcal{O}(10^{-11})\ eV^2$. Figure 1.5 shows an example of the general case, with both matter enhanced and vacuum contributions to neutrino oscillation.

We can also get a feeling for the MSW effect by looking at the survival probability for the 2-neutrino model. Since P_{ee} is energy dependent, we must average over some energy range. We choose here to average over the recoil energy of electrons from the CC reaction $\nu_e + d \to p + p + e^-$. This is one of the primary reactions of the SNO detector, to be discussed in the next chapter, producing recoil electrons with measurable energies above 5 MeV. Lower energy events are not easily distinguished from radioactive backgrounds, so we average over the 5 - 20 MeV range. Above 20

---

[5]While there are other Z^o-exchange interaction terms experienced by all three neutrinos, these terms will cancel in our calculations.
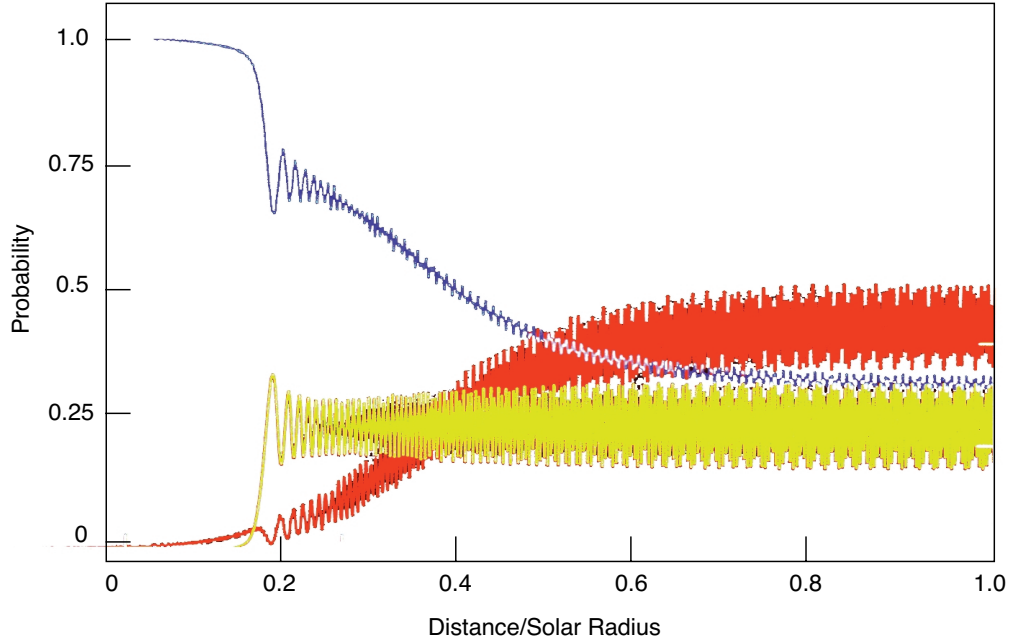
Figure 1.5: Example MSW oscillation between three neutrino flavors, taken from [24]. Although all three flavors ν_e, ν_μ, and ν_τ are shown, this does not necessarily mean that all three mass eigenstates are involved. The oscillation is between the electron neutrino (blue) and a linear superposition of ν_μ and ν_τ (red + yellow).

MeV there are no solar neutrinos. Figure 1.6 shows contours of constant average survival probability. We see that a measurement of the survival probability will strongly constrain the allowed values of the parameters $\Delta m^2, \tan^2 \theta$.

In addition, because the survival probability is energy dependent, we can look for a difference between the high (8 - 20 MeV) and low (5 - 8 MeV) range. This variation is expressed as an asymmetry $2\frac{\phi_{high} - \phi_{low}}{\phi_{high} + \phi_{low}}$ and is plotted in Fig. 1.7. We see that there are some regions of parameter space which have very large energy variations. This will allow for a strong inclusion or exclusion of those regions.
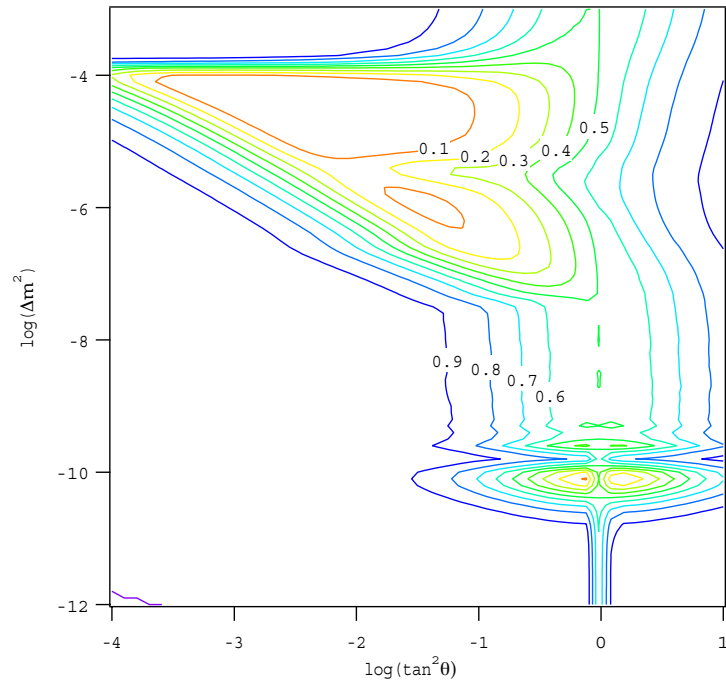
Figure 1.6: Average survival probability for the SNO CC reaction.
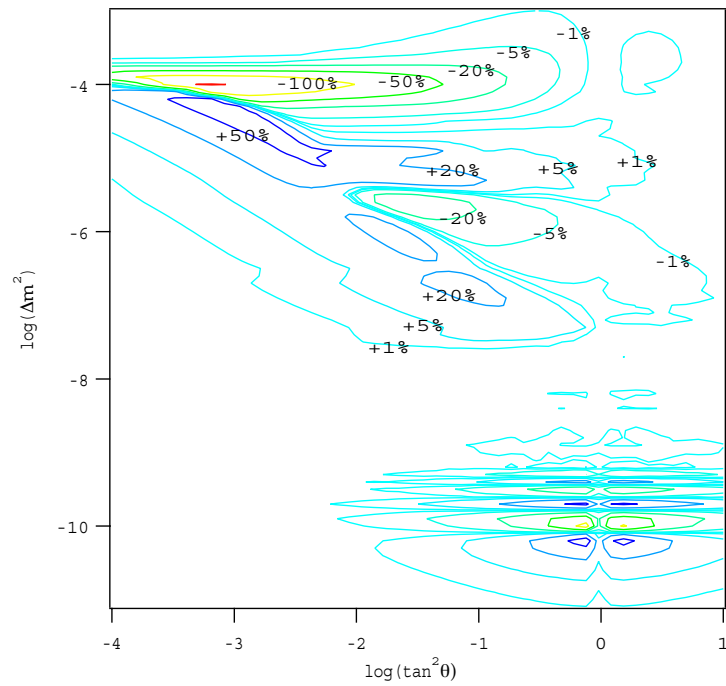
Figure 1.7: Percentage difference between high and low energy part of the CC spectrum

1.5 Earth Regeneration and the Day-Night Asymmetry

Just as solar matter can enhance the oscillation of neutrinos in the Sun, terrestrial matter can effect the oscillation of neutrinos as they pass through the Earth. The path length through the Earth is given by

$$
L \approx
\begin{cases}
0 & \cos \theta_z > 0 \\
2R |\cos \theta_z| & \cos \theta_z < 0
\end{cases}
\tag{1.27}
$$

where R is the radius of the Earth and θ_z is the zenith angle of the Sun. In addition, the electron density along the path has an effect on the matter enhancement (Fig. 1.8 shows the *total* density for the Preliminary Reference Earth Model (PREM) [33]).
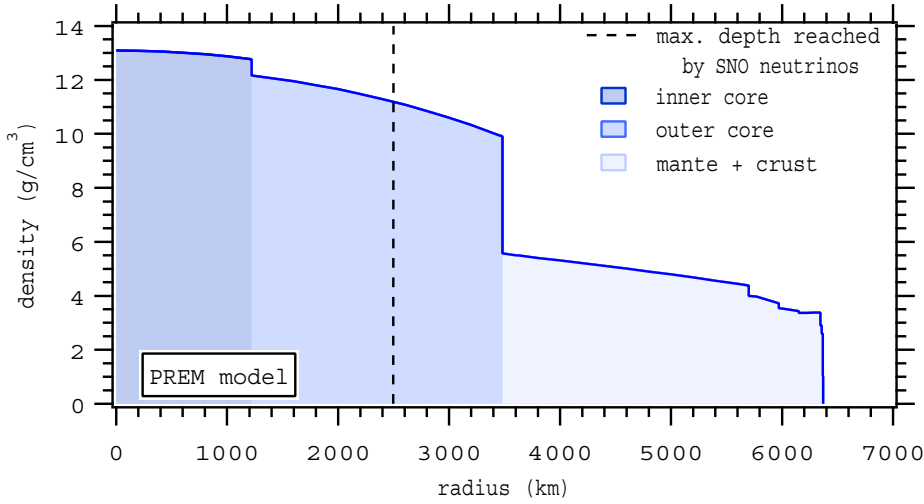
Figure 1.8: Density of the Earth as a function of distance from the center.

If one measures the electron neutrino flux ϕ_e during the day and night separately, then one can form the asymmetry

$$
A_e = 2 \frac{\phi_{Ne} - \phi_{De}}{\phi_{Ne} + \phi_{De}}
\tag{1.28}
$$

where ϕ_{De} is the flux of neutrinos when the Sun is above the horizon (day) and ϕ_{Ne} is the flux when the Sun is below the horizon (night). Figure 4.3 shows the asymmetry

for ν_e as predicted by the 2-neutrino MSW model. Only those regions with significant asymmetry are shown. We see that sign of A_e is positive across essentially all of the MSW plane. For this reason, the Earth matter effect is often termed *regeneration*, with the oscillated neutrinos changing back into ν_e due to transition through the Earth. The positive sign of A_e is rooted in the relationship between solar and Earth matter enhancement, as discussed in [34].
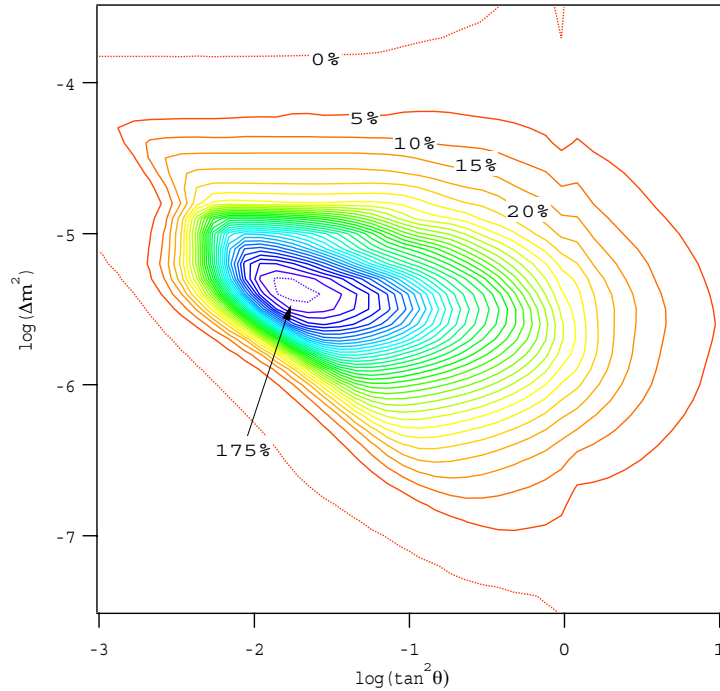
Figure 1.9: Day-night asymmetry for the SNO CC reaction. Note the finer scale for this figure.

1.6   Solar Neutrino MSW Regions Before SNO

By fitting to the solar neutrino data presented in Table 1.1, one can draw confidence level contours in the $\Delta m^2, \tan^2\theta$ plane. Fig. 1.10 shows one such analysis. In this particular analysis, the value of ϕ_{8B} is allowed to float, although the other fluxes are

constrained by the SSM predictions.
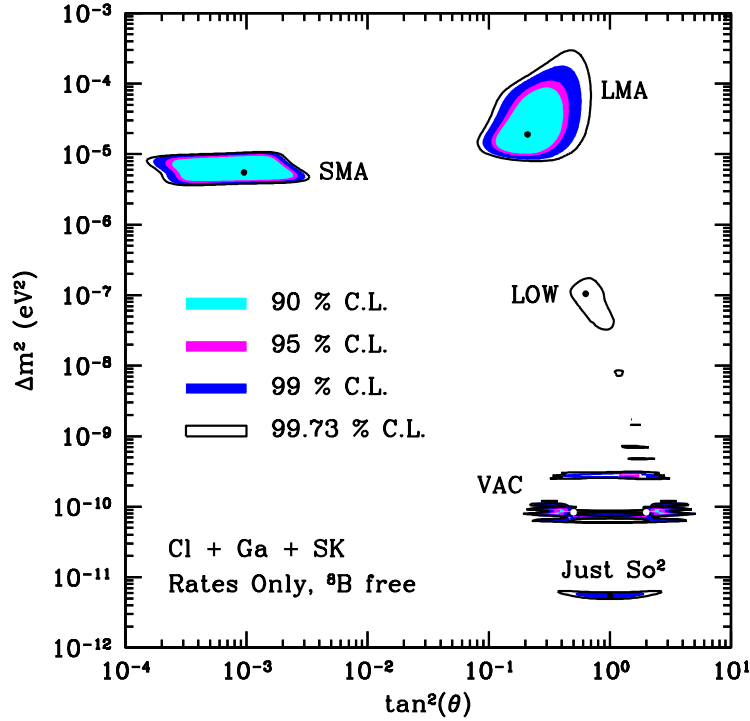
Figure 1.10: A global fit to solar neutrino data, prior to the addition of SNO data. Figure taken from [14].

1.7 Sterile Neutrinos

All previous discussion has assumed that neutrino oscillation occurs only between the three active flavors ν_e, ν_μ, ν_τ. However, it is possible that there are one or more *sterile* neutrinos of similar mass to the active flavors. These neutrinos do not interact via the weak force and are therefore not directly detectable.

Let us characterize the neutrino flux arriving at an experiment by the total flux of active neutrinos ϕ_{tot} and by the subset of these that are electron neutrinos ϕ_e. For oscillation between active neutrinos, the ratio $\frac{\phi_e}{\phi_{tot}}$ is a strong indicator of neutrino oscillation. Indeed, this is a measure of the average survival probability. However,

this indicator can tell nothing about oscillation into a sterile neutrino ν_s, which would produce no signal in the detector. What possible signatures could there be for sterile neutrinos?

A sterile neutrino is often invoked to explain simultaneously the atmospheric and solar neutrino anomalies, along with the positive result of the LSND accelerator experiment [35]. The three length scales in question are very different, making it impossible to satisfy equation 1.21. In [36], Giunti *et. al.* add an additional sterile neutrino to account for oscillations on the length scales of the LSND baseline, with additional mixing angles (θ_{14}, θ_{24}, θ_{34}) and an additional mass difference (*e.g.* Δm_{14}^2). Beginning from the results of [36], we can derive a relationship between the day-night asymmetry for the total flux of active neutrinos A_{tot} and the asymmetry for electron neutrinos A_e

$$A_{tot} = +cos^2\theta_{23}cos^2\theta_{24}\frac{\overline{\phi_e}}{\overline{\phi_{tot}}}A_e \qquad (1.29)$$

We see that the size of A_{tot} is constrained by the size of A_e, $\overline{\phi}_e$ and $\overline{\phi}_{tot}$, where $\overline{\phi}_e$ is the average of the day and night flux of electron neutrinos. The relationship is determined by the mixing between the 2nd, 3rd and 4th neutrinos. We note that the sign of A_{tot} is the same sign as A_e but of smaller amplitude. More generally, for A_{tot} to be of opposite sign to A_e, and yet still accommodate the LSND result, we need at least *two* sterile neutrinos.

Apart from when we explicitly test for $A_{tot} \neq 0$, we will assume that solar neutrino oscillations occur only between active flavors.

Chapter 2

THE SUDBURY NEUTRINO OBSERVATORY: DATA

2.1 Description of SNO

The Sudbury Neutrino Observatory (SNO) is designed to measure not only the flux of electron neutrinos, but also the total active neutrino flux coming from the Sun. This can be achieved because, at the heart of SNO, is 1 kT of ultra pure heavy water (D_2O). There are three ways solar neutrinos can interact of with D_2O.

$$\nu_e + d \rightarrow e^- + p + p \ - 1.44 MeV \qquad CC$$
$$\nu_x + d \rightarrow \nu_x + n + p \ - 2.22 MeV \qquad NC \qquad\qquad (2.1)$$
$$\nu_x + e^- \rightarrow \nu_x + e^- \qquad\qquad\qquad ES$$
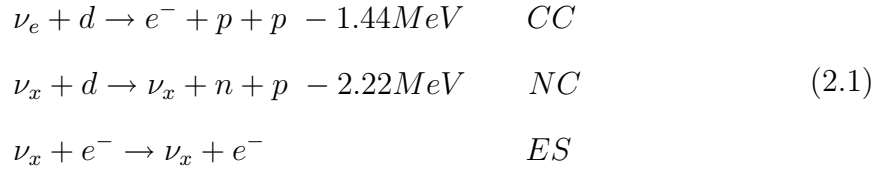
where we see that the charged current (CC) reaction is sensitive only to electron neutrinos and the neutral current (NC) reaction is sensitive to all flavors. The reason for this is that the CC interaction, acting through $W^\pm$ exchange, involves the conversion of a neutral lepton ν_e into its charged partner e^-. There is simply not enough energy in solar neutrinos to convert ν_μ into the heavy μ or ν_τ into τ. On the other hand, the NC reaction, acting through Z^0 exchange, conserves the charge of the lepton and so can proceed for any flavor neutrino. The elastic scattering (ES) reaction acts through both $W^\pm$ and Z^0 exchange for ν_e, but only Z^0 exchange for ν_μ and ν_τ. As a result, if we average over the ES spectrum with a kinetic threshold of 5 MeV, we find that the the cross section for ν_μ and ν_τ scattering is weaker by a factor of $\epsilon = 0.1559$.

The CC interactions occur uniformly throughout the D_2O, but not in the H_2O. Detailed nuclear and electroweak theory is required to calculate the differential cross

section. Apart from the Q-value of 1.44 MeV, most of the neutrino energy is transferred to the electron. With the electron being relativistic, it Cherenkov radiates to produce detectable light. The recoil direction of the electron is defined relative to the direction from the Sun, as shown in Fig. 2.1, with $\cos\theta_\odot$ following the distribution

$$1 - \frac{v}{3c}\cos\theta_\odot \approx 1 - 0.340\cos\theta_\odot \qquad (2.2)$$
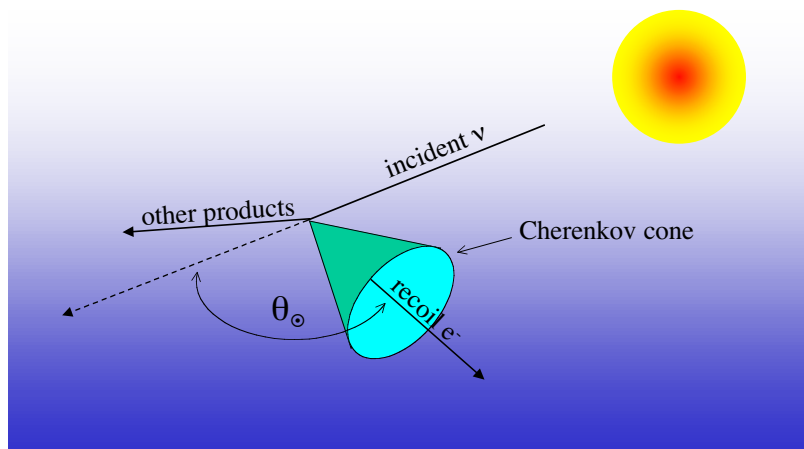
Figure 2.1: Definition of $\cos\theta_\odot$

The ES reaction is much simpler, following from electroweak theory, and can occur in either the D_2O or H_2O. The recoil electron typically carries away only a little of the neutrino energy, although its energy distribution has a long high energy tail. With many fewer events above threshold, the ES reaction provides only a small amount of additional information. It is readily deconvolved from the other reactions, because the $\cos\theta_\odot$ distribution is strongly forward peaked.

The NC interaction also occurs uniformly in the D_2O but not in the H_2O. The free neutron quickly thermalizes and can capture on deuterium to produce a 6.25 MeV γ. This subsequently Compton scatters an electron that Cherenkov radiates. The most probable energy of the scattered electrons is 5.08 MeV kinetic. Because the

neutrons are thermal, there is no directional information and the $\cos\theta_\odot$ distribution is flat. With the finite extent of the D_2O, neutron capture is more likely to occur on deuterium for neutrons produced near the center of the D_2O.

2.1.1 Background Sources

Radioactive backgrounds contribute a large fraction of the event rate for SNO. These events are primarily due to the ^{238}U and ^{232}Th chains (Fig. 2.2), both of which have extremely long-lived isotopes feeding the top of the chain. The U chain can be out of equilibrium because of contamination from the airborne ^{222}Rn, the 3.8 day half life of which allows it to migrate into the detector. The Th chain can be out of equilibrium because of ^{228}Th, which tends to plate out on surfaces. Further down the chain is ^{220}Rn, but it is too short lived to migrate in significant quantities into the detector.

The problematic decays come towards the end of each chain. The $\beta\gamma$ decay of ^{214}Bi (U chain) and ^{208}Tl (Th chain) produce a γ with energy 2.44 and 2.62 MeV respectively and are thus able to photodisintegrate deuterium.

$$\gamma + d \rightarrow n + p \ - 2.22 MeV \tag{2.3}$$

This source of neutrons is indistinguishable from the NC reaction and so is a very important background to understand. Most of these γ's do not produce neutrons, but can instead Compton scatter electrons, giving sufficient Cherenkov light to trigger the detector. This light, together with the light from the associated β's, produces an energy spectrum with a tail which can extend above the experimental threshold for studying neutrinos. By studying the low energy region of this spectrum (< 5 MeV), we can quantify the level of ^{214}Bi and ^{208}Tl, and hence determine both the Cherenkov and neutron backgrounds. As we will be combining many techniques, studying various isotopes in the chains of Fig. 2.2, reference will be made to an *equivalent* quantity of U or Th, assuming that the chain is in equilibrium.
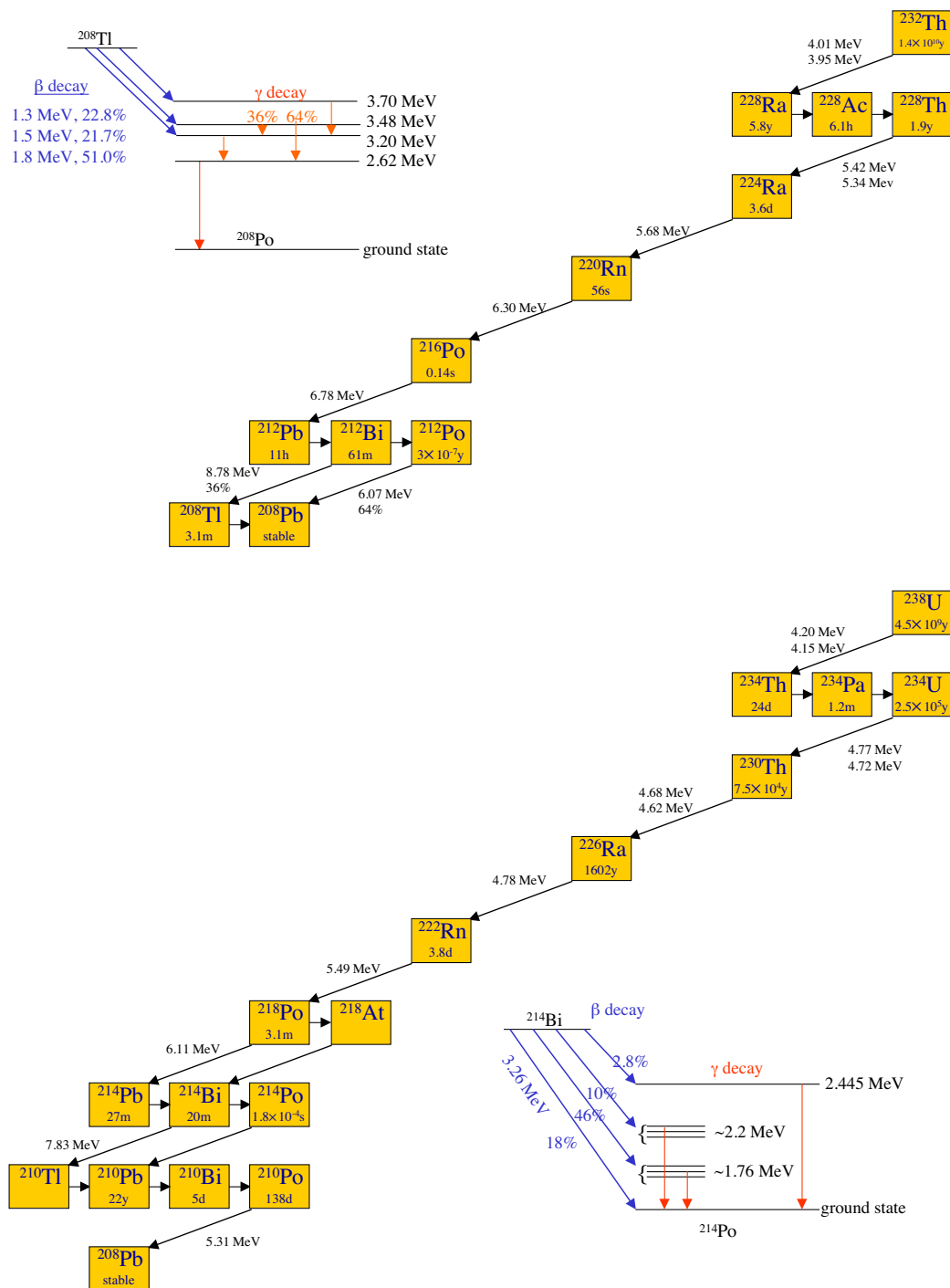
Figure 2.2: ^{232}Th and ^{238}U decay chains. The $\beta\gamma$ decay of ^{208}Tl and ^{214}Bi are shown in detail.

OUTER
H$_2$O

INNER
H$_2$O

D$_2$O

ACRYLIC
VESSEL

PSUP

17.80 M DIA.
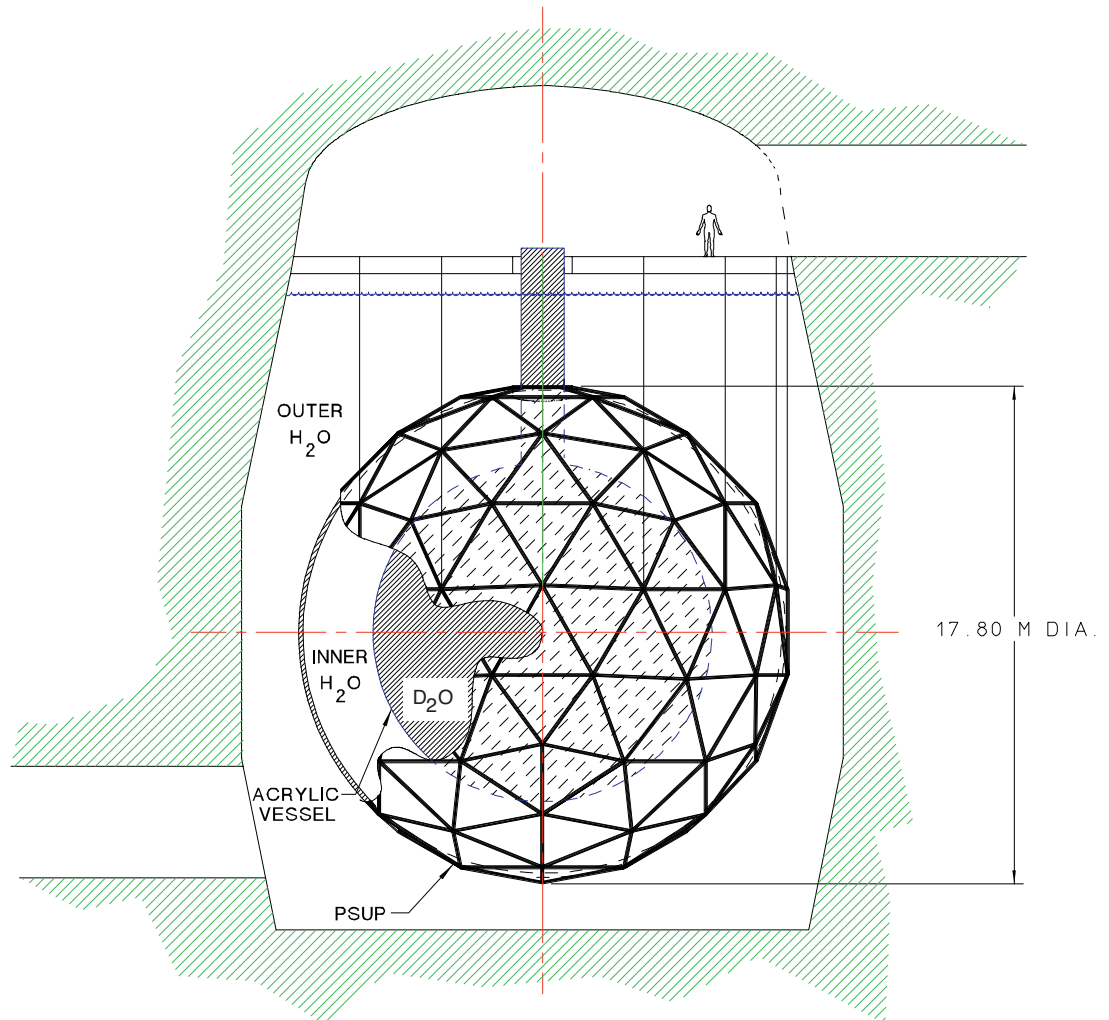
Figure 2.3: Schematic of SNO.

2.1.2   Geometry and Make-up of SNO

This section is largely drawn from [37]. SNO is located at $46^o28'30''$ N, $81^o12'04''$ W, at a depth of 2092 m (6010 m.w.e) in INCO's Creighton mine near Sudbury, Ontario. This depth in norite rock will reduce the flux of cosmic muons by an amount equivalent to 6010 m of water, to about 70 muons passing through the detector per day. The SNO detector is defined by regions shown in Fig. 2.3 and are described as follows.

D$_2$O   The 1000 tonnes of D$_2$O comes from the Ontario Hydro Bruce heavy water plant beside Lake Huron. The isotopic abundances of the heavy water are given in Table 2.1 and are important for understanding the neutron transport properties of the D$_2$O.

Table 2.1: Isotopic abundances of the SNO heavy water

Hydrogen Isotope	Fractional Abundance	Oxygen Isotope	Fractional Abundance
^{2}H	99.9084(23) %	^{17}O	0.0485(5) %
^{3}H	0.097(10) μCi/kg	^{18}O	0.320(3) %
^{1}H	balance	^{16}O	balance

The radioactivity levels of the D$_2$O have to be ultra low, so as to reduce the number of background events. The target levels were set at 3.7×10^{-15} g/g of Th and 4.5×10^{-14} g/g of U. For more details see Section 3.4.

AV   The D$_2$O is contained in a 12-m diameter spherical Acrylic Vessel (AV). The AV is constructed from 122 separate ultraviolet transmitting (UVT) acrylic panels, each approximately 5.6 cm thick, which were bonded together underground in a unique feat of engineering. Access to the interior of the vessel is obtained through a 1.5-m diameter, 6.8-m tall acrylic neck. UVT acrylic was chosen because its light transmis-

sion is similar to the PMT spectral response and it can be cast relatively free from radioactive contaminants.

Inner H$_2$O   Between the AV and PMT array is a buffer of 1700 tonnes of ultra pure light water (H$_2$O). This helps to support the AV and to provide radioactive shielding from the PMT array. The radioactivity requirements of this region are 3.7×10^{-14} g/g of Th and 4.5×10^{-13} g/g of U, an order of magnitude less stringent than the D$_2$O.

PMTs and PSUP   An array of 9438 photomultiplier tubes (PMTs) look inward at the SNO D$_2$O volume. The PMTs, made by Hamamatsu (model R1408), are 20.4 cm in diameter and are each contained in a hexagonal housing, with reflecting concentrator petals increasing the effective photocathode coverage to 54%. The PMT anode is typically between +1700 V to 2100 V. In addition, 91 PMTs face outward to provide muon veto information.

The PMTs are mounted on a PMT-support structure (PSUP). This is a construction of 270 stainless steel struts, assembled underground to make a geodesic sphere 17.80 m in diameter. The PSUP, together with the PMT housing, also provide a 99.99% leak tight barrier between the inner H$_2$O and the less pure outer H$_2$O. In all, the stainless steel of the PSUP and PMT glass provide the largest source of radioactive signal for SNO. Reconstruction of event positions will become critical in reducing this background (see Section 2.2.3)

Outer H$_2$O   Between the rock wall and the PSUP we have a relatively less pure 5700 tonnes of H$_2$O. Water flow is generally maintained to be outward from the inner H$_2$O, so the radiopurity requirements are much less stringent here ($\approx 10^{-12}$ g/g). The rock wall is covered in a Uralon lining that prevents leaking, leaching of material, and diffusion of radon into the water

2.1.3 Data Collection

There are two primary forms of data collection for the SNO detector that are used in this thesis.

• **PMT Electronics and DAQ** The SNO electronics handles data from up to 9529 PMTs. The signal from each PMT is received by one of 19 electronics crates, *via* 32 m of 75 Ω waterproof coaxial cable. Within a crate there are 16 front end cards (FECs), and the signal from each PMT is passed to one of these. Each FEC processes the signal from 32 PMTs, digitizing and temporarily storing the information. The buffer capacity is sufficient to handle a burst of up to 10^6 events (*e.g.* from a supernova).

Each FEC interfaces with the custom SNO backplane, which also interfaces with a trigger card. Basic information is summed by the trigger card, such as the total number of hit PMTs in a given time window. The primary time window used is 100 ns. This allows for the 66 ns direct time-of-flight for light to cross the diameter of the inner H_2O region (reflected light can take even longer to hit a PMT).

Timing is provided by two clocks. A 10 MHz clock, synchronized to a GPS system, provides precision time markers in the data stream, while a 50 MHz quartz oscillator provides the timing between PMT hits. The 50 MHz oscillator is also used to force a trigger every 200 ms, providing a snapshot of the detector and monitoring the PMT noise rate.

The data acquisition (DAQ) also interfaces with the SNO backplane *via* a single VME crate containing a Motorola 68040 computer. For each trigger, the DAQ serves to *build* the individual hits into an *event*. The electronics are monitored by the *SNO Hardware Acquisition and Readout Control* (SHARC), which also serves as a user interface for controlling the running of SNO. In addition, SHARC provides control of the manipulator system used for deploying calibration sources.

• **Water Systems** There are two separate water systems, one for the inner H_2O and one for the D_2O. These serve to both maintain water purity through recirculation

and to collect information about the level of impurities. The D_2O is sampled from six separate locations, through pipes inside the AV. The H_2O is sampled from six positions between the AV and the PSUP. Within each closed loop system, Th, Ra and Pb are collected for counting by microfilters coated with DTiO. Acrylic beads coated with MNO_x also absorb Ra for additional counting. Finally, Rn is extracted by storing six tonnes of liquid in a vacuum degasser, with the Rn atoms subsequently being frozen out in liquid nitrogen for counting. For more details on the data collected by the water systems, see Section 3.4.1

A future configuration of SNO will have [3]He proportional counters installed into the heavy water. These are described in Appendix B.1.

2.1.4   SNO Events

It is instructive to examine some SNO events. Figure 2.4 shows an example of an event from the [16]N calibration source. This source produces γ's of 6.13 MeV, a similar energy to neutron capture on deuterium. Most of the PMT hits are on one side of the detector, showing a pattern characteristic of a Cherenkov ring. In addition, most hits occur in a relatively short time interval (30 ns), corresponding to light that has travelled directly from the source. The later hits are due to reflections off the AV and PMTs, and due to PMT noise. A muon event (Fig. 2.5) shows a much larger number of hits. The positions where the muon crossed the PSUP can be identified by studying the timing and charge distributions. An example of instrumental noise is a *flasher*, where one PMT undergoes high voltage discharge. We see a cluster of early hits due to the discharge, followed by late hits on the far side of the PSUP (Fig. 2.6).
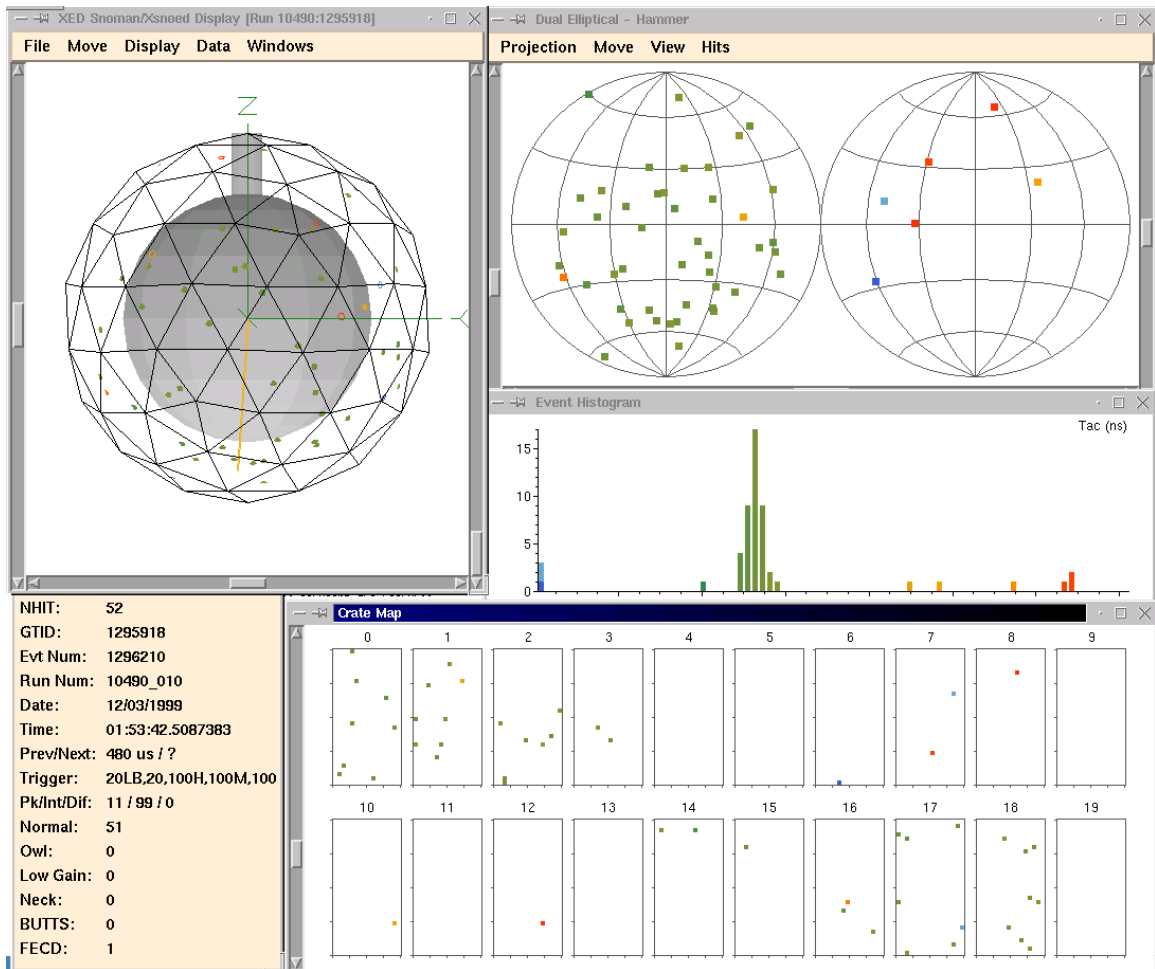
Figure 2.4: Event from the ^{16}N source. Clockwise from top left, we have the 3D hit pattern on the PMT array, its projection onto two hemispheres, the timing distribution of the hits, the map of the hits in electronics space, and some statistics about the event.
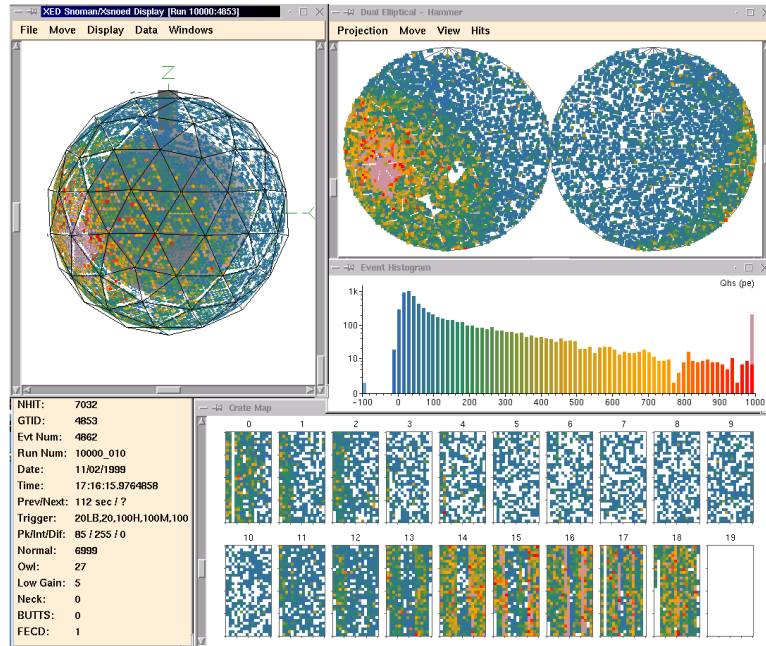
Figure 2.5: Example of a muon event.
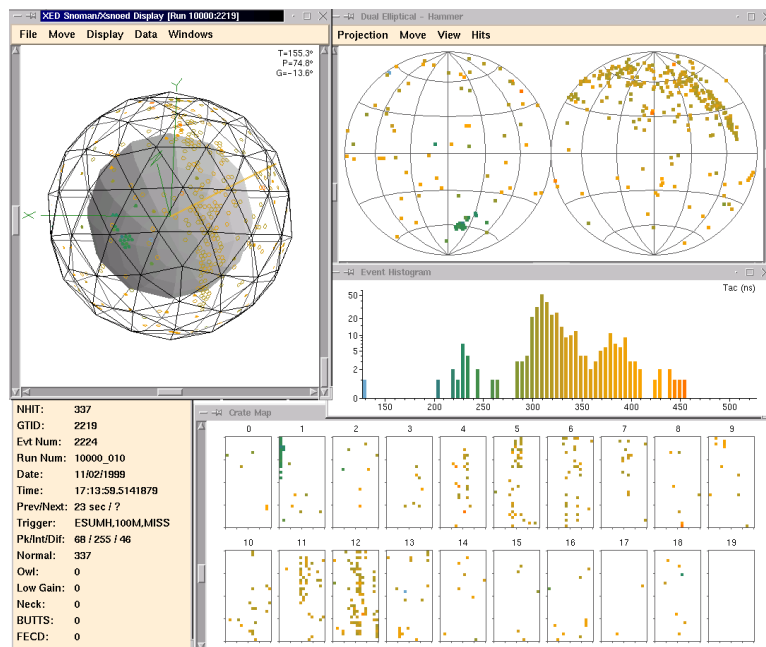
Figure 2.6: Example of instrumental noise (a flasher).

2.2 Data Reduction

2.2.1 Run Selection

The data studied in this thesis were collected during the pure D_2O phase of SNO[1], between November 2, 1999 and May 28, 2001. The data were recorded as a series of runs, with run selection being made on the following criteria.

• Run must be flagged as *neutrino* data. Other run types, including calibrations, maintenance, and source deployment runs, were not included in the neutrino data set.

• All electronics crates online.

• Compensation coils on and stable.

• Run length must be > 30 minutes.

• Runs which overlapped with some unusual condition were discarded (e.g. out of calibration, power failure, GPS inconsistency).

• No activity on the deck directly above the detector.

Selected runs varied in length from 30 minutes to 4 days. There were significant gaps in collection of useable neutrino data, due to calibrations, mine shutdowns, and instrumental problems. The cumulative livetime is shown in Fig. 2.7. The division of livetime into day and night (Fig. 2.8) varies from month to month, both because the detector is not being run continuously and because the length of time the Sun is above the horizon varies with time of year.

2.2.2 First level Cuts

Given the low background radioactivity of SNO, most of the recorded events were caused by *instrumental noise*. This included light created by the electrostatic in-

---

[1]Other phases of SNO are the *salt* and *NCD* phases, discussed in Section 5.2
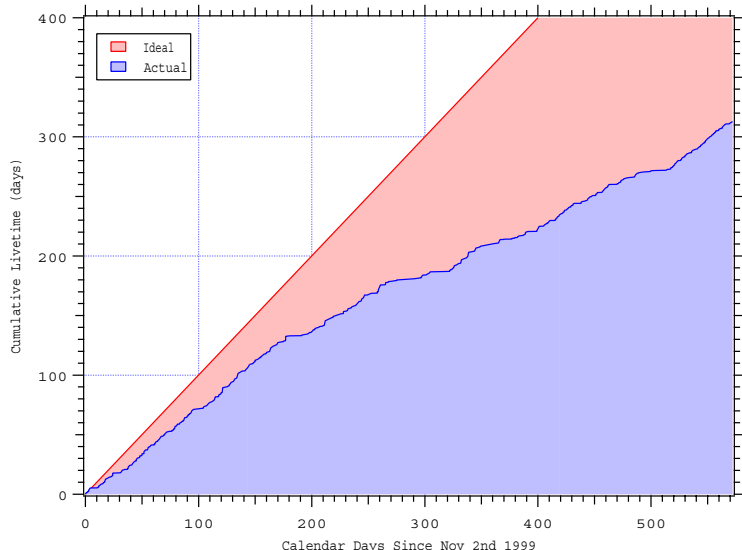
Figure 2.7: Cumulative livetime for the neutrino data set

teractions of dripping water (*neck events*), light emitted from electrical breakdown within the PMTs (*flashers*), and breakdown and pickup within the electronics. Fortunately, each of these event types has a characteristic hit pattern, timing and charge distributions, and often occur in characteristic bursts. This allows for an efficient removal of instrumental noise events. An array of cuts were designed to remove these events from the raw data set and these are extensively discussed in [38]. The instrumental cuts produce the first three steps of data reduction shown in Fig. 2.9. It was found that many of the events were flagged by more than one of the cuts. For example, many flashers occurred in bursts. This allowed us to identify them, not only by the spatial and timing distribution of the hits of each event, but also by the time between events. This kind of redundancy was important in assessing the residual contamination left over after the cuts, as shown in Fig. 2.10. By deploying various sources, one is able to determine what fraction of physics events are lost to these cuts, also known as *sacrifice* (Fig. 2.11)
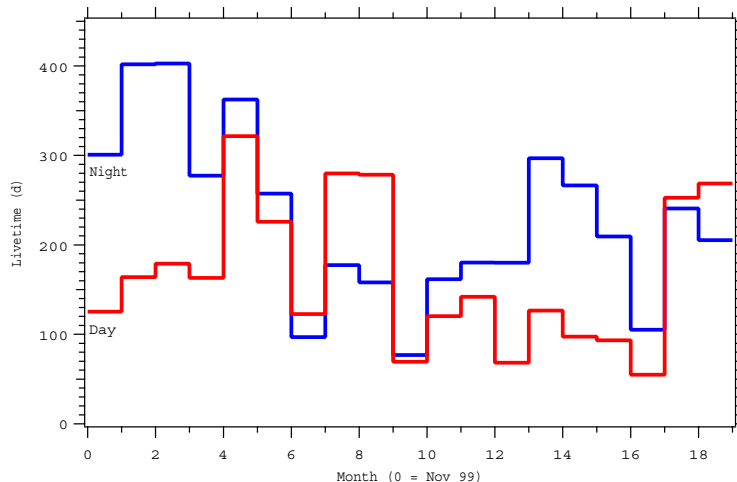
Figure 2.8: Month by month livetime for both day and night.

2.2.3 Reconstruction and High Level Cuts

After the first level of data cleaning was complete, the hit pattern and timing distribution were used to reconstruct the position and direction of the remaining events. A number of different algorithms were developed to do this, with this thesis using the *path fitter*, seeded with the output of the *grid fitter*. These various fitters are described extensively in [39] and will not be discussed further here. It suffices to understand that the position is reconstructed with a width of 10 - 30 cm, depending on the source and Nhit of the event, and that the direction is reconstructed with a width of $\approx 27^o$ (for neutrino data).

For a few of the remaining events, the fitter algorithm simply failed to find a solution and these events were rejected outright. By analyzing Monte Carlo and source data, we can assess the number of accidental failures (*i.e.* physics events that failed to be fit). This was found to be small, indicating that the failed events were probably external backgrounds or missed instrumental noise. Each successfully fitted event was assigned two angular *figures of merit*. Having reconstructed the position and direction of the event, we can create a coordinate system centered on the event,
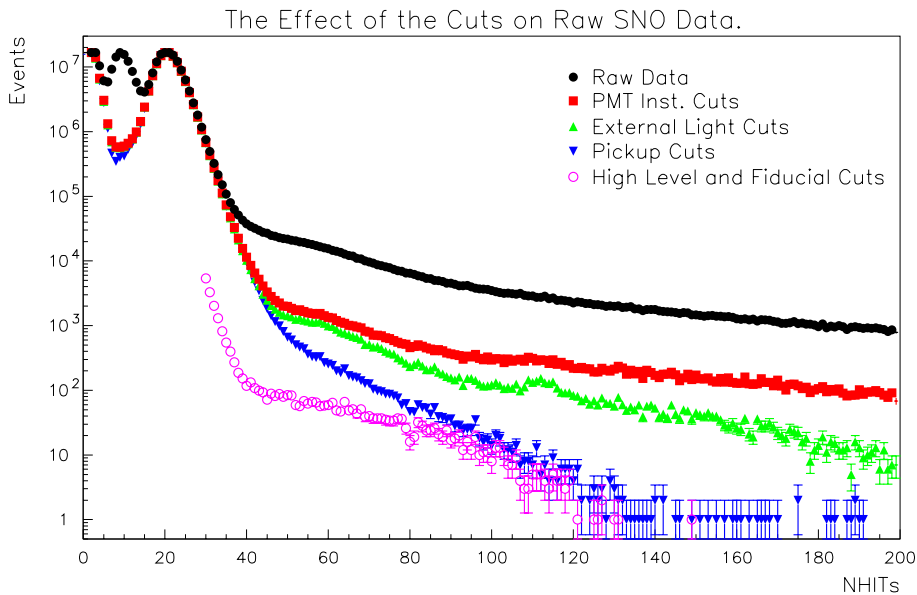
Figure 2.9: The SNO Nhit spectrum for various levels of cuts. The bottom axis is the number of PMTs hit for each event (Nhit). Figure provided by N. McCauley.

with the z axis along the electron track. In this coordinate system, Cherenkov light has characteristic zenith and polar distributions and a Kolmogorov-Smirnov (KS) test of the event can be done against these two distributions. These two tests help reject mis-reconstructed events, typically radioactive background from the light water and PMTs (which have been incorrectly assigned a position inside the AV).

A related measure is an isotropy parameter named Θ_{IJ}, which measures the average opening angle of the rays which connect each hit PMT to the event vertex. A large value of Θ_{IJ} is indicative of isotropic light, generated by certain non-Cherenkov processes. Θ_{IJ} will be discussed more extensively in Section 3.4. In addition, now that the event vertex is known, the time of flight for each photon can be normalized to the line of sight distance. Prompt light is light that appears to have come from the vertex without any additional scattering. Scattering will lead to some late photons, although too much late light is indicative of non-physics sources that can produce

Contamination(%) in each Nhit bin
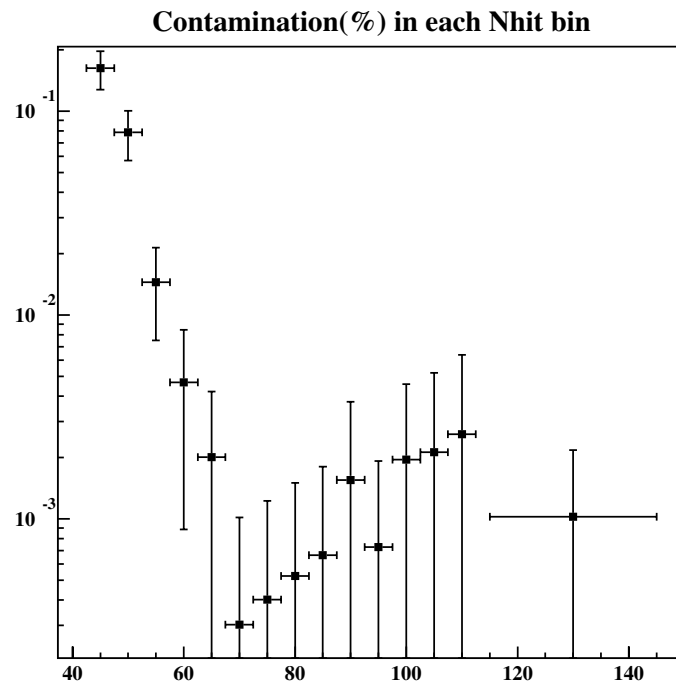
Figure 2.10: Percentage contamination (left axis) remaining after first level cuts, shown as a function of Nhit (bottom axis). Figure provided by Vadim Rusu

light spread over longer time intervals. To this end, we define the *In Time Ratio* (ITR), the fraction of light that is prompt. Figure 2.12 shows a scatter plot of these two measures, where we have overlaid the cleaned data set, a data set from the ^{16}N calibration source, and the instrumental events (already removed by other cuts). We see that Θ_{IJ} and ITR provide a very nice redundancy in removing instrumental noise, as well as catching a handful of events missed by the other cuts.

Finally, a fiducial volume cut is applied, removing all events that do not reconstruct within 550 cm of the center of the AV. This removes a large fraction of the radioactive background events that are mis-reconstructing inside the AV (radius = 600 cm). The collective set of high level cuts provide the last reduction step in Fig. 2.9
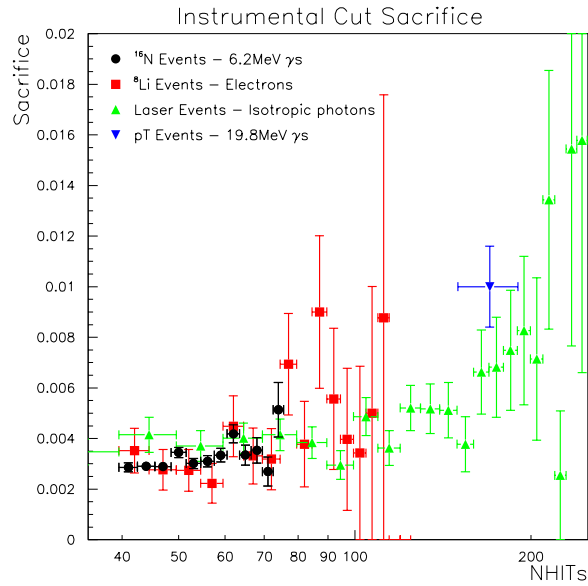
Figure 2.11: Sacrifice from instrumental cuts. Figure provided by Neil McCauley
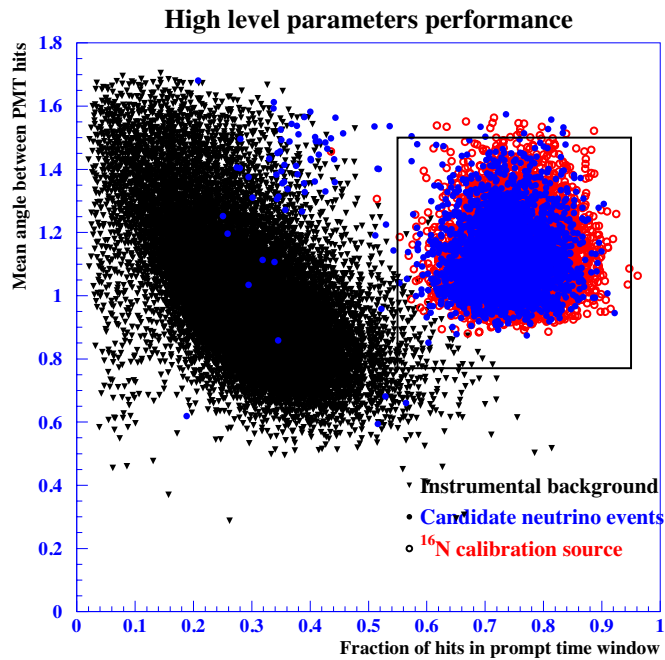
Figure 2.12: The high level cuts Θ_{IJ} and ITR. Closed blue circles are events that passed the first level cuts, while black triangles are the events that failed. Open red circles are events from a calibration source. Figure provided by Vadim Rusu.

2.3   Final Data Set

Reconstruction allows us to assign a position and direction to each event. Although this amounts to six coordinates, we will only be interested in the radial coordinate R_{fit} and the reconstructed direction relative to the incident direction of the neutrino $\cos\theta_\odot$, as defined in Fig. 2.1. We will make a fiducial volume cut, accepting events with $R_{fit} < 550$ cm. Any value of $\cos\theta_\odot$ is acceptable. In addition, we will define an energy measure T_{eff}, which assigns the most probable kinetic energy to each event (see Section 3.2). We take a threshold of $T_{eff} > 5.0$ MeV. Both the fiducial cut and kinetic energy threshold are designed to minimize the contribution from radioactive backgrounds.

The final data set consists of 2928 events, each with individual values for $X = \{T_{eff}, R_{fit}^3, \cos\theta_\odot, \cos\theta_z\}$. To be consistent with our PDFs (see section 3.6), we bin this data into a multidimensional histogram $n(X)$, with n being the number of counts in bin X. There are 17 T_{eff} bins, with the first 16 bins being 0.5 MeV wide from 5 to 13 MeV. The last bin spans from 13 to 20 MeV. There are 30 equally spaced R_{fit}^3 bins and 60 $\cos\theta_\odot$ bins. Finally, we use two bins in zenith angle (day and night).

We will find it simpler to maintain an event-by-event accounting, where we only have to keep track of 2928×4 pieces of information. For each event m, there are four coordinates to describe its position in the histogram $n(X)^2$. We can not present the entire set of 2928×4 data here. Instead we project these onto 1-dimensional histograms, as shown in Fig. 2.13.

Note that there is a significant difference between the number of day and night events. This is almost all due to a difference in livetime, since we have collected more data during the night. To explain this, and to learn if there is some residual difference, we must make a careful accounting of livetime.

---

[2]There is strictly no need to bin the data at all. However, our study of detector response was binned, so we do not have complete information on a finer scale. Furthermore, with the exception of zenith angle, all of the bins are smaller than the resolution of the detector.
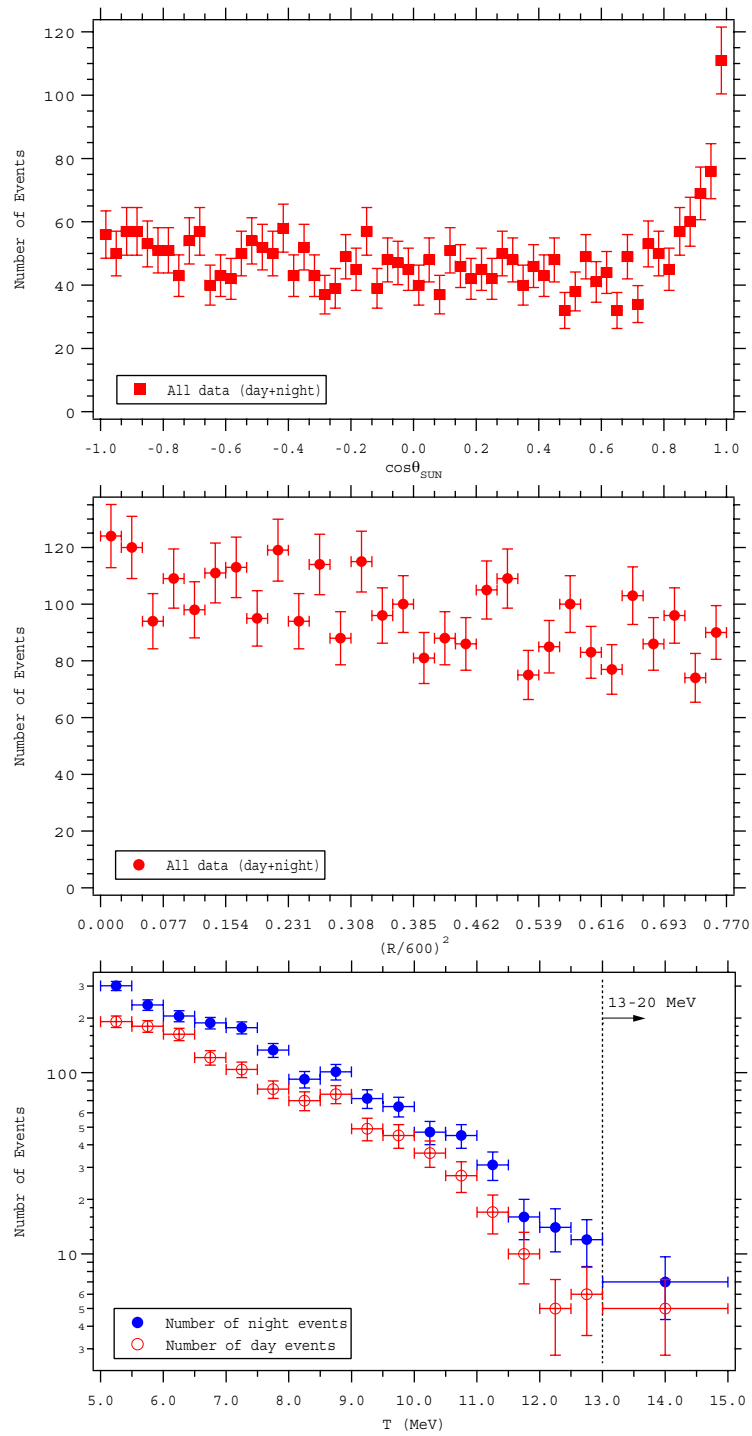
Figure 2.13: Projection of the data onto various axes. The difference between day and night distributions is due primarily to a difference livetime.

2.4   Livetime

A more detailed description of livetime accounting can be found in [38], with only the key points presented here.

2.4.1   Raw Livetime

Events from the SNO electronics stream are assigned two separate trigger times by a 10 MHz and a 50 MHz clock. The 10 MHz clock is synchronized with a Global Positioning Satellite (GPS) receiver and we use this to measure the livetime of each data run, assigning the start time by the first event and the end time by the last event. With > 5 Hz of data, this represents less than a 400 ms error in the livetime accounting of each run. Solar position code also allows us to reconstruct the cosine of the solar zenith angle ($\cos \theta_z$) throughout a run. When the Sun is above the horizon ($\cos \theta_z > 0$), we count the livetime as being *Day* and, when the Sun is below the horizon ($\cos \theta_z < 0$), we count the livetime as being *Night*. The accounting of this raw livetime can be found in Table 2.2.

One can check this measurement by using a second clock. The detector is triggered at 5 Hz with a pulser, synchronized to the 50 MHz clock. These regularly spaced events can be counted as a check of the livetime calculation, with the results shown as solid circles in Fig. 2.15. We see very good agreement between the expected trigger rate and the observed[3]. We take the difference between the two livetime measurements to be a conservative estimate of the error in the raw livetime.

2.4.2   Deadtime

Of the instrumental cuts described in Section 2.2, four remove livetime from the data. As this is similar to the phenomena of *deadtime*, we shall use that term here. The

---

[3]Small differences are attributed to stolen triggers, where other event types overlap with the pulser triggers

four cuts are

- **retrigger cut**   This cut removes the 5 μs of livetime immediately following each event, so to avoid the retriggering of the detector through pickup. In this way, every event is followed by 5 μs of deadtime.

- **muon follower cut**   This removes the 20 s of livetime immediately following a muon event and is designed to cut muon spallation events. Thus, for every muon, we get 20 s of deadtime.

- **burst cut**   This cut is more complicated, as the deadtime is not uniquely defined. Designed to remove short instrumental bursts, the burst cut tags events if at least three occur within 1 ms. However, the deadtime for each burst is not simply 1 ms. Had an additional event occurred shortly after or before the burst, it too would have been cut. In this way, the deadtime τ_d can only have a statistical meaning, with $R \times \tau_d$ giving the expected number of physics events that would have been cut, where R is the rate of physics events. We find that taking τ_d to be the window defined in Fig. 2.14 gives the appropriate statistical definition.

- **Nhit burst cut**   This is similar to the burst cut, except 6 events with Nhit > 40 in 4 seconds will trigger the cut. This is designed to remove instrumental noise occurring in longer bursts. An equivalent definition is made for τ_d, again only having a statistical meaning.

Many of the cuts overlap with each other and our accounting of deadtime allows for this, so to prevent double counting. We can check our deadtime calculation by allowing the above cuts to also remove pulser events. The expected number of events cut and the actual number cut are in close agreement, shown as solid squares in Fig. 2.15.
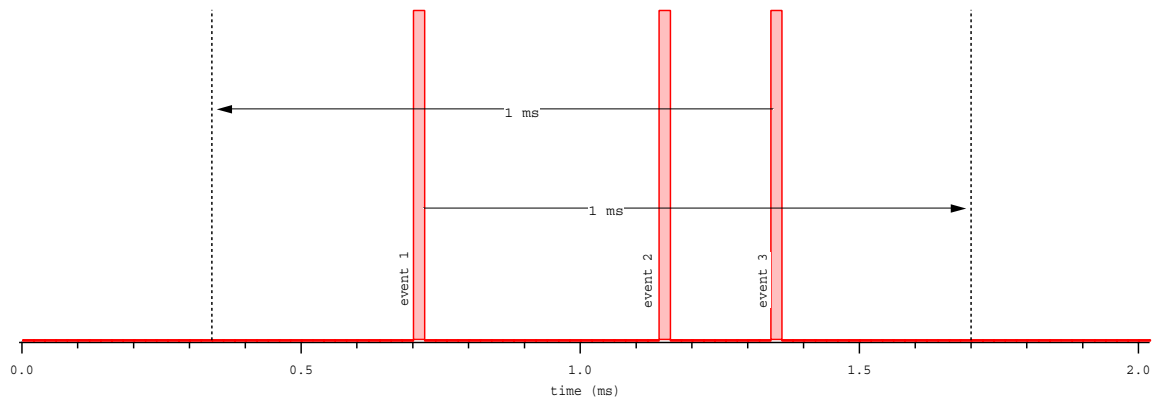
Figure 2.14: Schematic of how the deadtime window is defined for the burst cut. Had an event occurred in this window, it would have been cut, hence the longer than 1 ms deadtime.

2.4.3 Orbital Eccentricity

The number of neutrino events not only scales with the livetime, but also with the inverse square distance to the Sun. We must calculate the time average $< (\frac{1AU}{r})^2 >$ for both the day and night bins. The Earth-orbit equation is given by [40]

$$r^{-1}(t) = \frac{1 + e \cos(\theta(t) - \theta(t_o))}{(1 - e^2) \times 1AU} \tag{2.4}$$

$e = \text{eccentricity} = 0.0167$

$\tau = \text{period} = 364.25 \text{ days}$

$t = \text{Julian day}$

$t_o = \text{Julian day of Perihelion}$

with $\theta(t) \approx \frac{2\pi t}{\tau}$. These averages are computed in Table 2.2[4]

---

[4]It should be noted that the time average of the Earth-Sun distance over one complete year is not exactly 1 AU. In fact, $< r > = 1.00000003$ AU [41]

Table 2.2: Day and night livetime and orbital eccentricity calculations. The error for the final livetime calculation is conservatively estimated to be 0.04% for each zenith bin. For the eccentricity calculations, the error is estimated to be 0.01% in $< (\frac{1AU}{r})^2 >$.

	Day	Night
Raw Livetime	131.4 days	181.6 days
Deadtime correction	68.4 hours	88.6 hours
Corrected Livetime	128.5 days	177.9 days
$< (\frac{1AU}{R})^2 >$	1.0002	1.0117
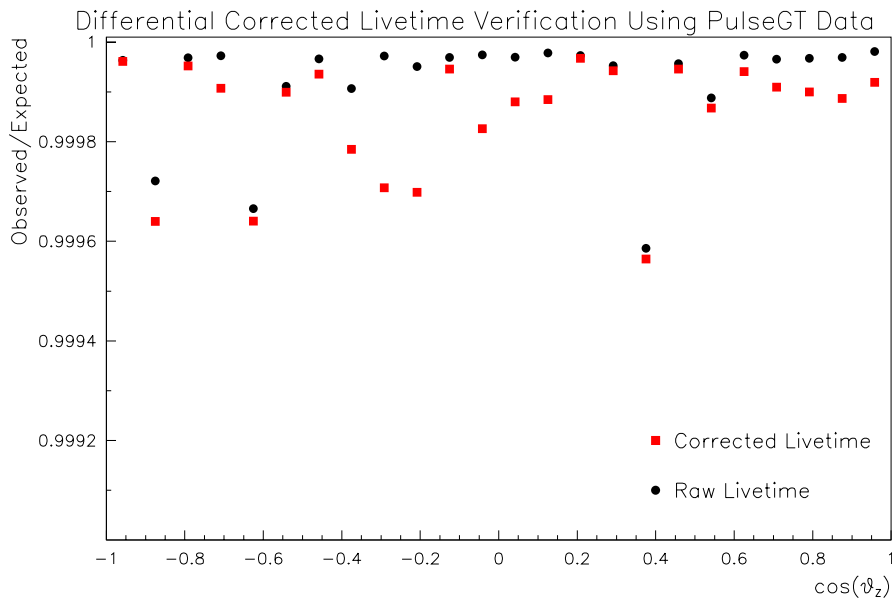
Figure 2.15: Verification of livetime using a pulser, or *Pulsed Global Trigger* (PGT). Figure provided by Neil McCauley.
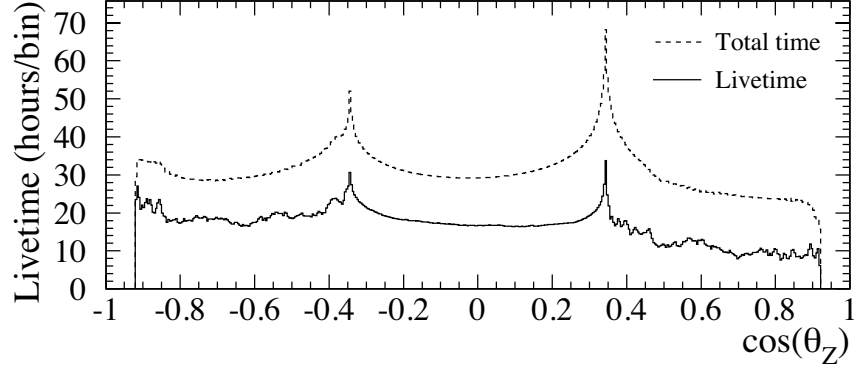
Figure 2.16: Fine binned distribution of livetime over zenith angle $\frac{dt}{d\cos\theta_z}$. The distribution for the actual SNO livetime is compared to the distribution one would have got had SNO been running uninterrupted for the period November 2 1999 to May 28 2001 (total time). Twice a day $\frac{dt}{d\cos\theta_z} \to \infty$, averaging out to give the two peaks. Figure provided by Neil McCauley.

2.4.4   Fine Binned Livetime Distribution

When creating an MSW model for day and night neutrino events, we will need to average the survival probability over the zenith angle.

$$P(E_\nu)_D = \frac{1}{T_D} \int_{day} dt\ P(E_\nu, \cos\theta_z(t)) = \frac{1}{T_D} \int_{\cos\theta_z > 0} d\cos\theta_z\ P(E_\nu, \cos\theta_z) \frac{dt}{d\cos\theta_z}$$

$$P(E_\nu)_N = \frac{1}{T_N} \int_{night} dt\ P(E_\nu, \cos\theta_z(t)) = \frac{1}{T_N} \int_{\cos\theta_z < 0} d\cos\theta_z\ P(E_\nu, \cos\theta_z) \frac{dt}{d\cos\theta_z}$$

$$(2.5)$$

To carry out this integration numerically, the function $\frac{dt}{d\cos\theta_z}$ must be defined over a fine binned distribution, as shown in Fig. 2.16. In this figure we also show the distribution one would have seen had SNO been run continuously with 100% livetime for neutrino data. The two peaks arise from the fact that $\frac{dt}{d\cos\theta_z} \to \infty$ twice a day.

Chapter 3

CALIBRATION, SYSTEMATICS AND BACKGROUNDS

3.1 Optical Calibration and the SNOMAN Monte Carlo

To model the response of the detector to neutrino and background events, we must first calibrate the optical properties of SNO. These properties include the attenuation length of the D_2O, H_2O and acrylic, along with the angular response of the PMTs. The latter is the likelihood of a photon triggering a PMT, tabulated as a function of direction (measured relative to the normal of the PMT). To make these measurements, a *laserball* is used [37]. This is a diffuser ball, located at the end of a fiber-optic cable, through which laser light is fed. Several dye lasers are employed, providing wavelengths in the range 360-700 nm. [37].

The source of photons is localized, so that the direction to each hit PMT is known. This, of course, assumes that the path taken by the photon is direct and has not come from some reflected surface. To ensure that we calibrate with unreflected light, we make a cut on the timing of individual hits. PMTs that were hit at times significantly different from the direct-path time are not used in the calibration. Figure 3.1 shows the distribution of hit times for events from another source (The ^{16}N source, described in Section 3.2).

Physics events are modeled with the SNOMAN Monte Carlo. This Monte Carlo includes a detailed description of the geometry and chemical make up of SNO and its calibration sources. Interaction and propagation of electrons and photons is incorporated though the EGS4 (Electron Gamma Shower) code [42]. Neutron interaction and propagation is handled by the Los Alamos neutron transport code [43].
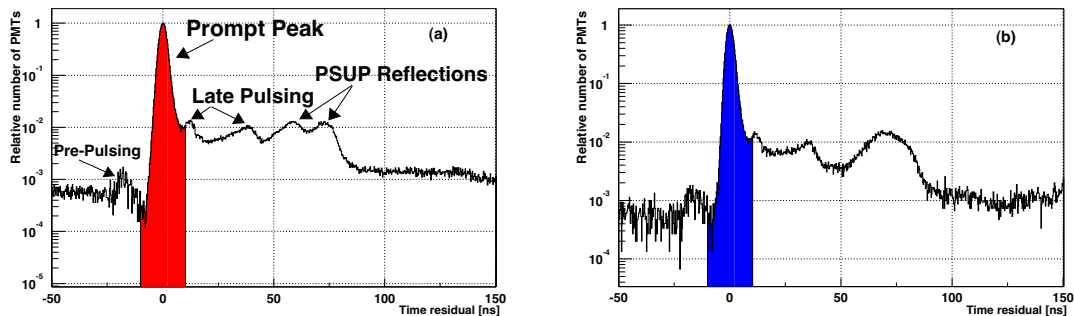
Figure 3.1: Prompt light peak for data and Monte Carlo of the ^{16}N source, placed at the center of the AV. Figure provided by Mark Boulay.

Neutrino interactions are also modeled. The direction to the Sun is varied with time of day, so to simulate the correct zenith angle dependence. The code can also be set to vary the distance to the Sun with time of year, although this feature was not turned on for our simulations and we must include it as a multiplicative correction from Table 2.2. The spectrum of neutrinos is taken from Ortiz *et al.* [44] and the Butler, Chen and Kong (BCK) differential cross sections were used for the CC and NC interactions [45]. The CC and NC cross sections have a single free parameter L_{1A}, which is set to 5.6 fm^3. The flux of ^{8}B and hep neutrinos is set to a reference unit. For this, we use the SSM of the Bahcall, Pinsonneault, and Basu (BP2000) [2].

Ultimately, all neutrino events lead to scattered electrons and their Cherenkov photons. To model these photons correctly, the attenuation of the various regions of SNO must be tuned using the optical calibrations of the previous page.

In addition, detector effects such as PMT noise and trigger efficiency are also included in the Monte Carlo. Calibration sources are also modelled, with careful attention paid to the source geometry, event distribution and rate.

3.2 Energy Response

The discussion of this section is largely drawn from [46]. Now that we have optically calibrated the Monte Carlo, we are almost ready to simulate neutrino data. However the Monte Carlo still has one remaining free parameter. The optical calibrations were unable to determine the overall gain of the detector, expressed as the average gain of the PMTs. The ^{16}N calibration source, described extensively in [47], is used to determine this.

The ^{16}N is produced through (n,p) reactions with oxygen in CO_2. The gas is transported to a decay chamber deployed in SNO, where the ^{16}N β-γ decays. The spectrum of γ energies shown in Fig 3.2. The β particle creates scintillation light in the shielded decay chamber but does not contribute significantly to the light seen by the PMTs. By tagging the events through the β scintillation, we significantly reduce the low energy backgrounds in the ^{16}N data set. The primary channel gives a 6.13 MeV γ, which subsequently Compton scatters, producing Cherenkov light.
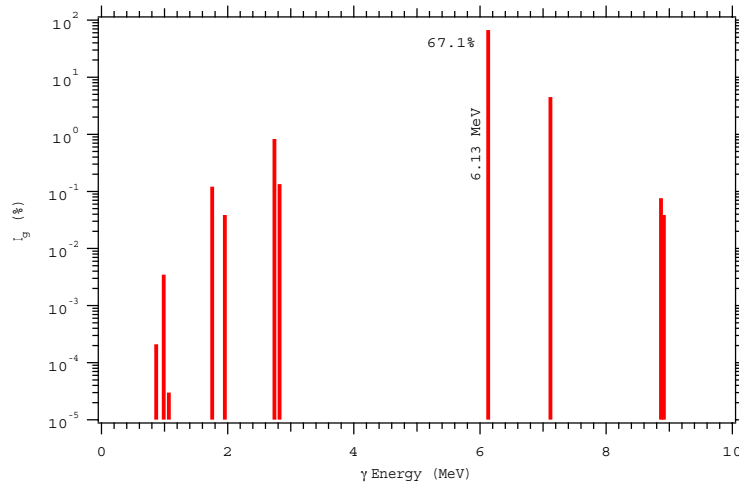
Figure 3.2: Spectrum of γ's produced by the ^{16}N source.

Additional sources, including the pT and ^{8}Li source, allow us to check the cali-

bration at different energies. The pT (proton-tritium) source produces 19.8 MeV γ's *via* $^3He(p, \gamma)^4He$. The ^{8}Li source produces a β spectrum similar to that of the recoil electrons from the CC interaction of ^{8}B neutrinos. The spectra of these three sources is shown in Fig. 3.3 for the total light (Nhit), along with the Monte Carlo for each.
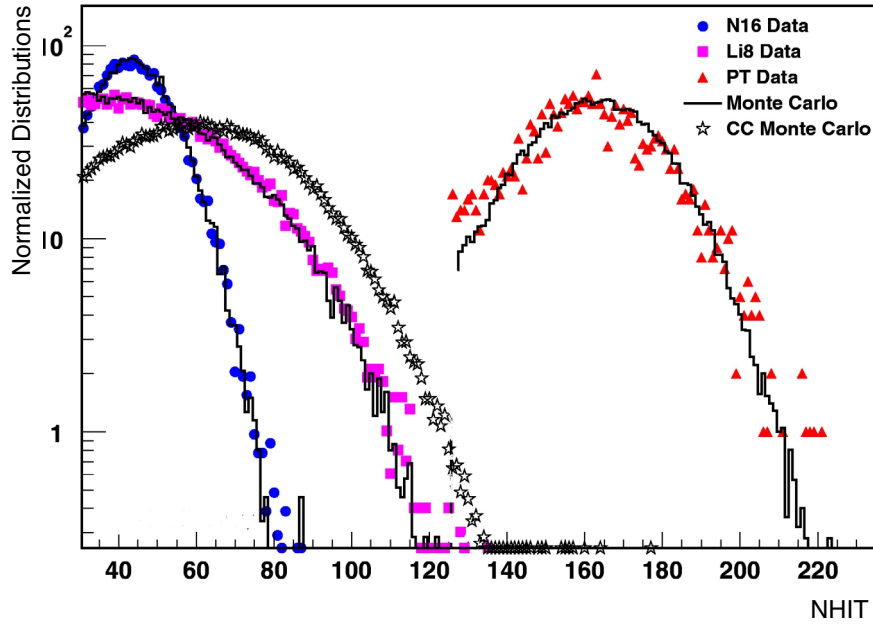
Figure 3.3: Energy calibrations. Figure provided by Andre Hamer.

The primary energy measure used in this thesis will be constructed from the *prompt light* only. After fitting the event position, one can determine the expected arrival time of a photon for each hit PMT. Light that arrives within a 20 ns window around this time is referred to as prompt, the identification of which is shown in Fig. 3.1. We measure the spectrum of N_{prompt}, the number of tubes hit in the prompt window. We can then tune the PMT efficiency in the Monte Carlo, so that the simulations of ^{16}N match the data. The other sources then provide a check of this.

For each event, the number of prompt hits depends on both position and direction of the event, as illustrated in Fig. 3.4. Generated by our calibrated Monte Carlo, $\epsilon_{response}$ quantifies the variation of the detector response relative to the center of the detector (where $\epsilon_{response} \equiv 1$).
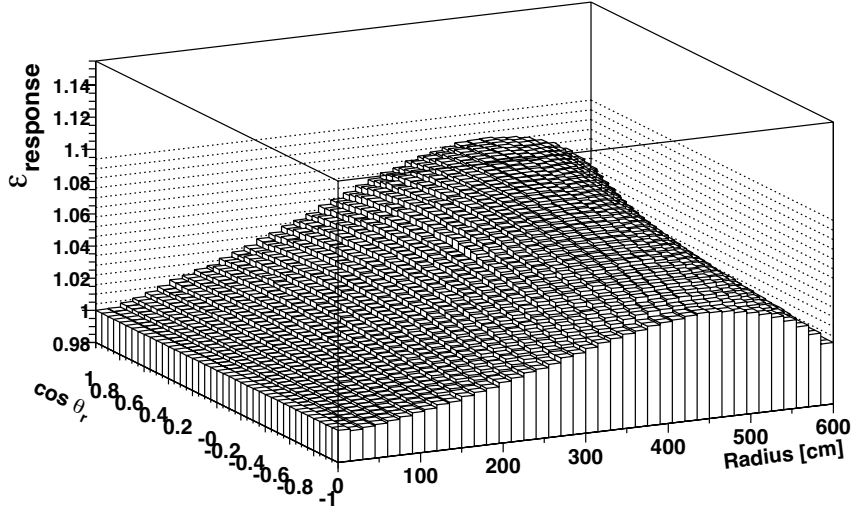
Figure 3.4: Monte Carlo of detector response as a function of radius (relative to the center of SNO) and direction (relative to the radial vector of the event). Shown is the response for 8 MeV electrons. Figure provided by Mark Boulay.

This allows for the definition of a corrected number of hits for each event

$$N_{cor} = \frac{9438}{N_{PMT}}(N_{prompt} - R_{noise}\tau_{prompt}) \times \frac{1}{\epsilon_{response}} \times \frac{1}{\epsilon_{drift}} \qquad (3.1)$$

where

• N_{PMT} is the number of tubes online, working and collecting data. This can vary from run to run, so we normalize it out.

• N_{prompt} is the in-time number of hits

• R_{noise} is the rate of individual PMT triggers that are caused by noise. This is determined by the pulser, which record the background noise hits for SNO.

- τ_{prompt} is the width of the in-time window = 20 ns.

- $\epsilon_{response} = \epsilon_{response}(R_{fit}, \cos\theta_r)$ is the response relative to an equivalent event at the center of the detector.

- $\epsilon_{drift} = \epsilon_{drift}(t)$ will be defined later. It accounts for any possible long-term variation in the energy scale.

Equation 3.1 assumes that the detector is isotropic. This is not quite true, since there will be some PMTs switched off or removed and there are no PMTs in the region of the AV neck. However, Monte Carlo simulations of these features demonstrate that the energy measure N_{cor} is very close to being independent of direction or position. Furthermore, the normalization with respect to the number of tubes online serves to mitigate all significant time dependences in the simulations of N_{cor}. Despite this, a drift was observed in the *measured* centroids of the ^{16}N data, as shown in Fig. 3.5. An empirical function $\epsilon_{drift}(t)$ is fit to this data and associated systematic errors are assigned.

N_{cor} does not vary linearly with the energy of a recoil electron. However, although it is strictly unnecessary for our purposes, one can convert the N_{cor} energy measure into a linear energy measure. This uses Monte Carlo simulations of monoenergetic electrons to create a mapping between kinetic energy T_e and the centroid of the N_{cor} distribution. By inverting this 1-to-1 mapping, we assign to each event a *most probable electron kinetic energy* T_{eff}. This is the energy measure used to study neutrino data.

We must evaluate the systematic uncertainty in the kinetic energy measure T_{eff}. Contributing factors to this are the uncertainty in energy drift, uncertainty in shielding of light by the ^{16}N source and variation between Monte Carlo and ^{16}N data as a function of position (Fig. 3.6). The overall uncertainty is estimated to be 1.21% in the value of T_{eff}.
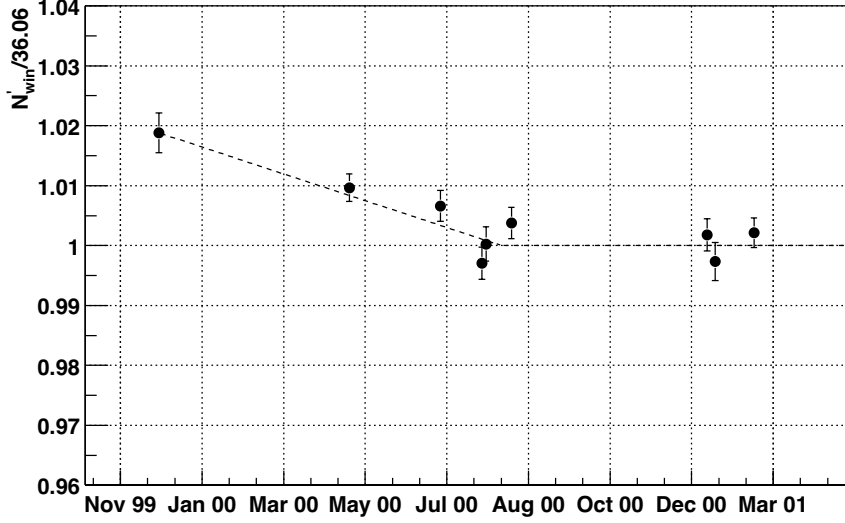
Figure 3.5: Empirical energy drift function. The vertical axis shows N_{cor}, normalized to 36.06 hits. (called $'_{win}$ in this plot). Figure provided by Mark Boulay.

Analytic form of the T_{eff} Distribution

To a very good approximation, one can use a Gaussian distribution to describe the response of SNO to an electron of energy T_e. This is given by[1]

$$\rho(T_{eff}|T_e) = \frac{1}{\sqrt{2\pi\sigma^2(T_e)}}exp\left(-\frac{(T_{eff}-T_e)^2}{2\sigma_E^2}\right)$$

(3.2)

$$\sigma_E^2(T_e) = -0.0684 + 0.331\sqrt{T_e} + 0.0425T_e$$

By design, the energy measure is linear. That is, the centroid of T_{eff} is linear with respect to T_e.

For neutron capture, most events arise from the Compton scattering of an electron by a γ of fixed energy 6.25 MeV (although there can also be a 2.2 MeV γ, occasional

---

[1]A simpler equation gives an almost identical response in the energy range of interest, $\sigma_E^2 = 0.120T_e + 0.0738T_e^2$. However, since any empirical description will do, we shall not depart from the published response function here.
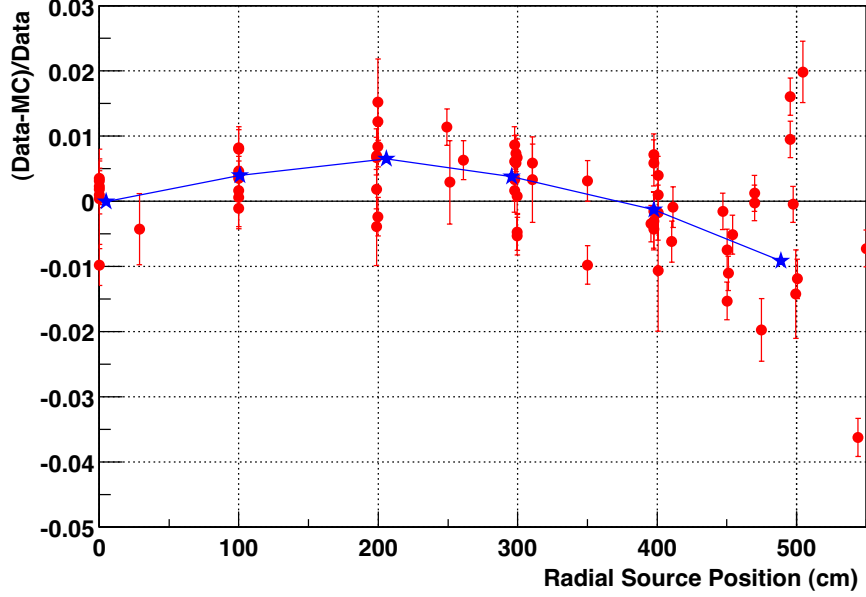
Figure 3.6: Agreement with ^{16}N Monte Carlo as a function of radial position of the source. Much of the spread at high radius is due to the presence of the AV neck at Z = 600 cm. Figure provided by Andre Hamer.

e^+e^- production and some photoemission). The most likely energy of the scattered electron is 5.08 MeV kinetic and, at this energy, $\sigma_E(T_e = 5.08) = 0.89$ MeV. However, because of the additional width of Compton scattering, the total width is

$$\sigma_{NC} = 1.11 \qquad (3.3)$$

In this way, detector resolution contributes about 65% of σ_{NC}^2 and Compton scattering contributes about 35% of σ_{NC}^2.

3.2.1 A Second Energy Measure

For studies of data much below ≈ 5 MeV, the kinetic energy measure T_{eff} defined above is inadequate. The reason for this is that it employs a prompt light cut, which reduces the number of hits for each event and hence increases the statistical width

of the energy measure. For a specific energy T_{eff}, there is a broad distribution of N_{prompt} which will map into it. Software and hardware thresholds can truncate this distribution.

A second energy measure is employed, mainly for use in low energy background studies. This uses only a minimal number of corrections[2]

$$N_{eff} = \frac{9438}{N_{PMT}}(N_{total} - R_{noise}\tau_{total}) \times \frac{1}{\epsilon_{drift}} \tag{3.4}$$

where

- N_{total} is the total number of hit PMTs for the event. This is almost the same as Nhits (discussed earlier), although there may be a few additional tubes removed for calibration reasons.

- τ_{total} is the width of the total light window = 390 ns.

- $\epsilon_{drift} = \epsilon_{drift}(t)$ is the empirical drift function for this energy measure

This energy measure will primarily be used to study the high energy tail of low energy background events. For this reason, we do not map it into a most probable kinetic energy, since that will have no meaning in this context. In addition, there are radial and directional dependences in N_{eff} which would make a most probable energy ambiguous. We have continued to employ the time dependent corrections N_{PMT}, R_{noise}, ϵ_{drift}, so that we might use it to study the stability of SNO. With the software and hardware thresholds used to create the SNO data, we can safely use all events with $N_{eff} > 27.3$ (which is, loosely speaking, equivalent to ≈ 3 MeV).

3.3 Neutron Calibration

This section is largely drawn from [48]. The NC reaction produces neutrons which are uniformly distributed throughout the D_2O. These neutrons quickly thermalize before

---

[2]A warning to SNO collaborators: the term N_{eff} has been used within the collaboration in a number of contexts and one should be careful not to confuse them.

capturing on ^{2}H, ^{1}H, oxygen isotopes, or material in the acrylic. Neutrons which capture on deuterium produce a 6.25 MeV γ, which can compton scatter an electron to produce visible Cherenkov light.

To measure the NC flux, we must calibrate SNO for the transport of these neutrons, calculating the absolute capture efficiency on deuterium, as well as the radial profile for the associated events. Three methods are employed to measure the capture cross section. The primary method places a ^{252}Cf source at various positions in the detector, leading to the results of Table 3.1. The uncertainty arises due to the uncertainty on the source strength, the reconstruction accuracy, and the acceptance of the various cuts used to remove background events.

Table 3.1: Capture efficiency for neutrons on deuterium. ϵ_n is the probability that a neutron will capture and the associated event pass the listed cuts. Radial cuts are made on the *fitted* position.

cuts	ϵ_n
no cuts	$29.9 \pm 1.1\%$
$R_{fit} < 550$ cm	$27.2 \pm 1.0\%$
$R_{fit} < 550$ cm, $T_{eff} > 5.0$ MeV	$14.38 \pm 0.53\%$

Two additional approaches show good agreement. The second approach uses the Monte Carlo, known cross sections and isotopic abundances to calculate the efficiency. The limiting systematics in this approach are the isotopic abundances of ^{1}H and ^{17}O and the capture cross section of neutrons with deuterium. The final approach attempts to circumvent the source strength uncertainty in the primary approach, using the multiplicity of neutrons from ^{252}Cf fission to self-calibrate the source. The mean multiplicity is 3.79 ± 0.006, with standard deviation 1.57 ± 0.02. By measuring the multiplicity distribution of the *observed* events, we can determine the efficiency. Unfortunately, this approach is statistically limited.

The radial profile of neutron capture is shown in Fig. 3.7 for various source positions. The fall off towards 600 cm is due to the capture of neutrons on acrylic and the propagation of 6.25 MeV γ's outside of the AV. The data are compared to the Monte Carlo and the agreement is excellent. No systematic error is associated with the *shape* of this radial profile (only its overall amplitude).
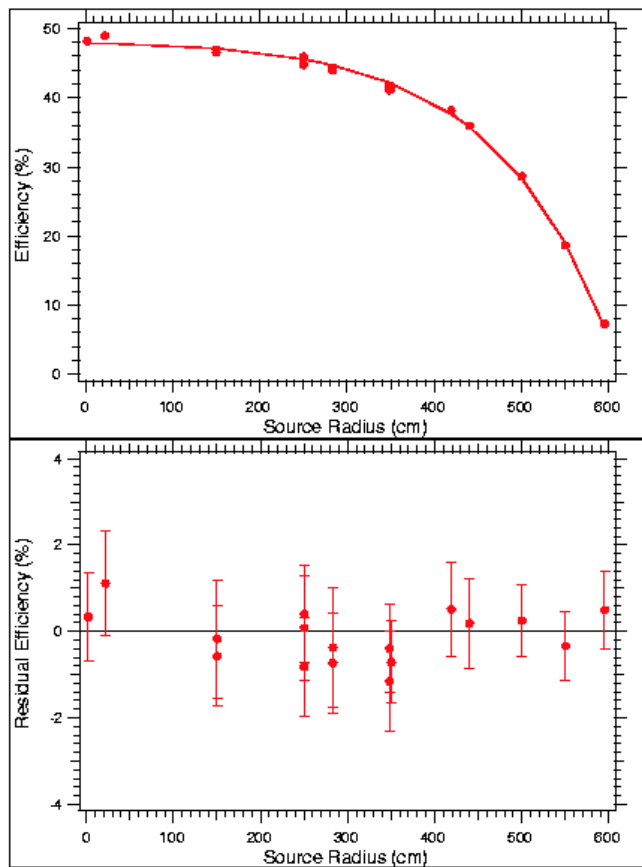
Figure 3.7: Cf source as a function of radius, compared to the model. Figure provided by Mike Dragowsky.

3.4   Backgrounds

This section is largely drawn from [49] and [50]. As discussed in Section 2.1.1, radioactive contamination can lead to two kinds of background events. Radioactive decays that produce a γ above 2.22 MeV can photo-disintegrate deuterium, producing a free neutron which is indistinguishable from an NC event. The same decays can, instead, produce enough Cherenkov light directly from the $\beta\gamma$ decay to trigger the detector, possibly imitating a neutrino event.

There are four regions from where measurable background events can originate: D_2O, AV, H_2O, and $PMTs$. A given region will have its own unique quantity of contamination and we must determine this for each separately. Ultimately, if we know the equivalent U and Th levels for each region and we have a model for the radial and energy distributions for each source, then we have completely described the SNO backgrounds.

3.4.1   Ex-situ Measurements

Periodically, samples are drawn from various regions of the the D_2O and H_2O. The water systems trap Ra isotopes using separately MnO_x beads and HTiO coated membranes. Studying the trapped Ra, we count single α decays and α-β coincidences to measure the equivalent quantity of U and Th.

Due to migration of ^{222}Rn (3.8 day half life), the measurement of ^{226}Ra may not be a good indicator of the lower end of the uranium chain. For this reason, we also run the D_2O and H_2O loops though a degasser, to extract radon. The radon is frozen out and counted to determine the levels of ^{222}Rn. The ^{220}Rn of the Th chain is not counted because of its short half life (56 s).
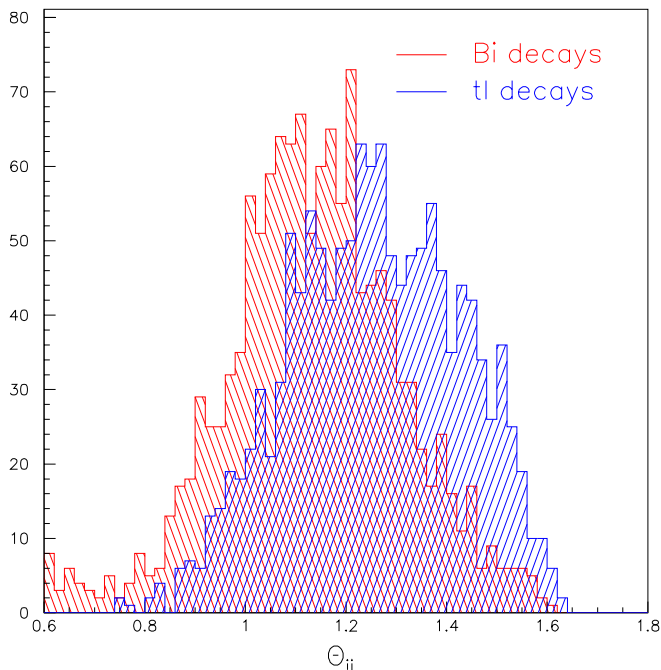
Figure 3.8: Θ_{IJ} for Bi and Tl in the D_2O. Figure provided by Alan Poon.

3.4.2 In-situ Measurements

A completely independent approach is taken, using the PMT data to determine the U and Th contamination. For either D_2O or H_2O, one must be able to separate the ^{214}Bi (U chain) from the ^{208}Tl (Th chain). The Tl decays we see are typically events with multiple β's and γ's, while the Bi decays are typically single electron events. For this reason, the Cherenkov light we see from Tl is typically more isotropic. As a measure of isotropy, we use Θ_{IJ}, which measures the pairwise average opening angle of the rays which connect each prompt hit PMT to the event vertex. The distributions of Θ_{IJ} are shown in Fig. 3.8 for the D_2O region, determined by both calibration data and Monte Carlo. A similar pair of distributions is determined for the H_2O region, where the detector response is somewhat different. One can fit data to Θ_{IJ} distributions in the relatively high statistics window $31 \leq N_{eff} \leq 40$.[3] This leads to correlated

---

[3]This corresponds approximately to 3.4 - 4.4 MeV of kinetic energy, although recall that the N_{eff} energy measure does not uniquely map into a kinetic energy, because it has a different

measurements of the U and Th (equivalent) levels, with a correlation of $\approx$ -0.7.

Figure 3.9 shows a summary of both the *in* and *ex-situ* results for the D_2O volume as a function of date. Errors are both statistical and systematic, with the two approaches having completely independent systematics. We note that the Th levels are consistent with being stable, with relatively good agreement between the two methods. On the other hand, the U measurements show a definite variation, due to the migration of ^{222}Rn into the water, and the agreement between the methods is unimpressive. The *Ex-situ* measurements are not considered to be the best representation of the U chain, given that the ^{222}Rn levels fluctuate more rapidly than the frequency of water extractions. We therefore use the *in-situ* results to provide the final measurement for this chain. On the other hand, both the *in* and *ex-situ* measurements are reliable for the Th chain. Furthermore, they have different systematic errors and are uncorrelated. By combining the measurements for the Th chain, using a weighted average, we break the correlation and reduce the overall error. Table 3.2 shows the results for both regions. Monte Carlo studies translate these measurements into a number of neutrons capturing within $R_{fit} < 550$ cm and with $T_{eff} > 5.0$.

Table 3.2: Photo-disintegration backgrounds from the H_2O and D_2O, integrated over the total livetime of the detector.

region	source	Ex-situ 10^{-15} g/g	In-situ 10^{-15} g/g	combined 10^{-15} g/g	number of neutrons
D_2O	U	$10.1^{+3.4}_{-2.0}$	$17.8^{+3.5}_{-4.3}$	$17.8^{+3.5}_{-4.3}$	$25.9^{+8.2}_{-9.1}$
	Th	$2.15 \pm 0.21^{+0.88}_{-0.92}$	1.63 ± 0.58	1.63 ± 0.58	18.4 ± 6.5
H_2O	U	29 ± 51	755 ± 330	775 ± 330	$5.6^{+4.2}_{-2.9}$
	Th	81^{+27}_{-23}	142 ± 66	91 ± 27	$5.6^{+3.6}_{-2.2}$

interpretation for different regions of the detector.
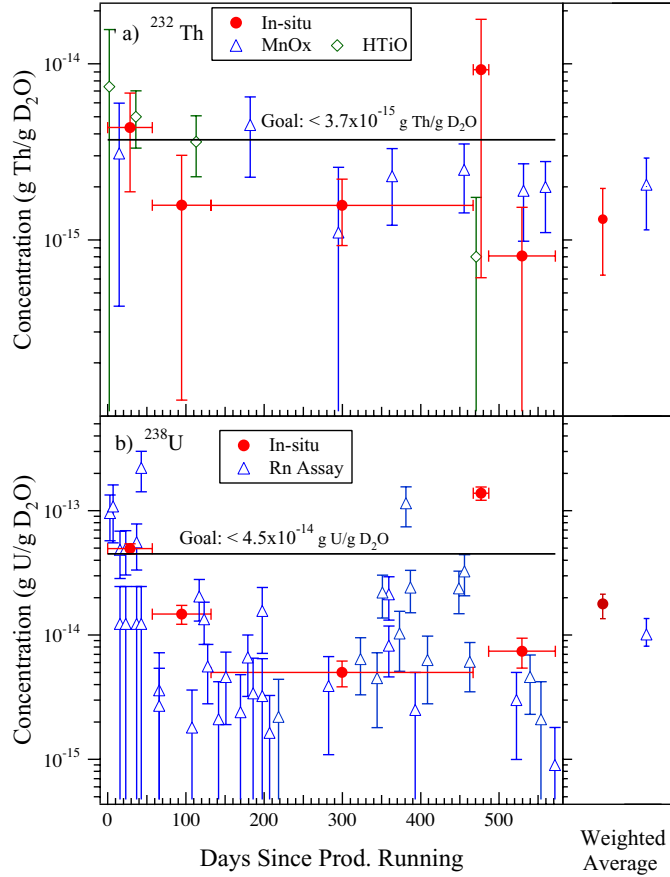
Figure 3.9: *In* and *Ex-situ* measurements for the D_2O. Values are the *equivalent* quantity of Th and U per gram of D_2O, calculated assuming the chains are in equilibrium. Figure provided by Alan Poon and Kevin Lesko.

3.4.3   AV Contamination

Prior to and during construction of SNO, radioassay measurements were made of the U and Th concentrations in the acrylic panels, as well as the bonds between them. This led to the results in Table 3.3. Roughly half of the γ's from the decay of this U and Th will enter the D_2O volume. The cross section for producing photo-disintegration neutrons is well known and, using Monte Carlo, we determine how many of these events misreconstruct with $R_{fit} < 550$ cm and $T_{eff} > 5$ MeV.

Interestingly, there is a localized region of high radioactivity, referred to as the *hot spot*, on the upper hemisphere of the acrylic vessel, as illustrated in the top panel of Fig. 3.10. This is thought to have been introduced during construction and represents a potentially significant background contribution. Analysis of PMT events allows us to calculate the hot spot contamination if we make an assumption that it is decaying via a specific chain. The Th chain produces more neutrons, so we calculate for this worst case scenario. In the end we expand the error to allow for a lower limit of zero. The hot spot is identified by making cuts in the detector polar coordinates $\cos\theta_o$ and ϕ_o, as illustrated in Fig. 3.10, along with a radial cut to select events close to the AV. To evaluate the contamination of this window from sources other than the hot spot, we monitor two background subtraction windows on either side.

Table 3.3: AV backgrounds from bulk, surface and hot spot contributions. The number of neutrons from each source is calculated after radial, energy and other cuts have been applied. The contamination level for the hot spot is listed for the assumption that it is all Th, although the final error range for neutrons covers all possible sources.

source	contamination (total)	estimated number of accepted neutrons
bulk U	$15 \pm 15 \ \mu g$	1.6 ± 1.6
bulk Th	$7.6^{+1.7}_{-1.3} \ \mu g$	$6.2^{+1.4}_{-1.1}$
outer surface U	$0.18 \pm 0.04 \ \mu g$	0.013 ± 0.005
outer surface Th	$0.96 \pm 0.19 \ \mu g$	0.63 ± 0.16
inner surface U	$0.16 \pm 0.04 \ \mu g$	0.024 ± 0.008
inner surface Th	$0.87 \pm 0.17 \ \mu g$	0.88 ± 0.20
hot spot	$10 \pm 1^{+8.5}_{-3.5} \ \mu g$ (Th)	$6.5^{+5.6}_{-6.5}$
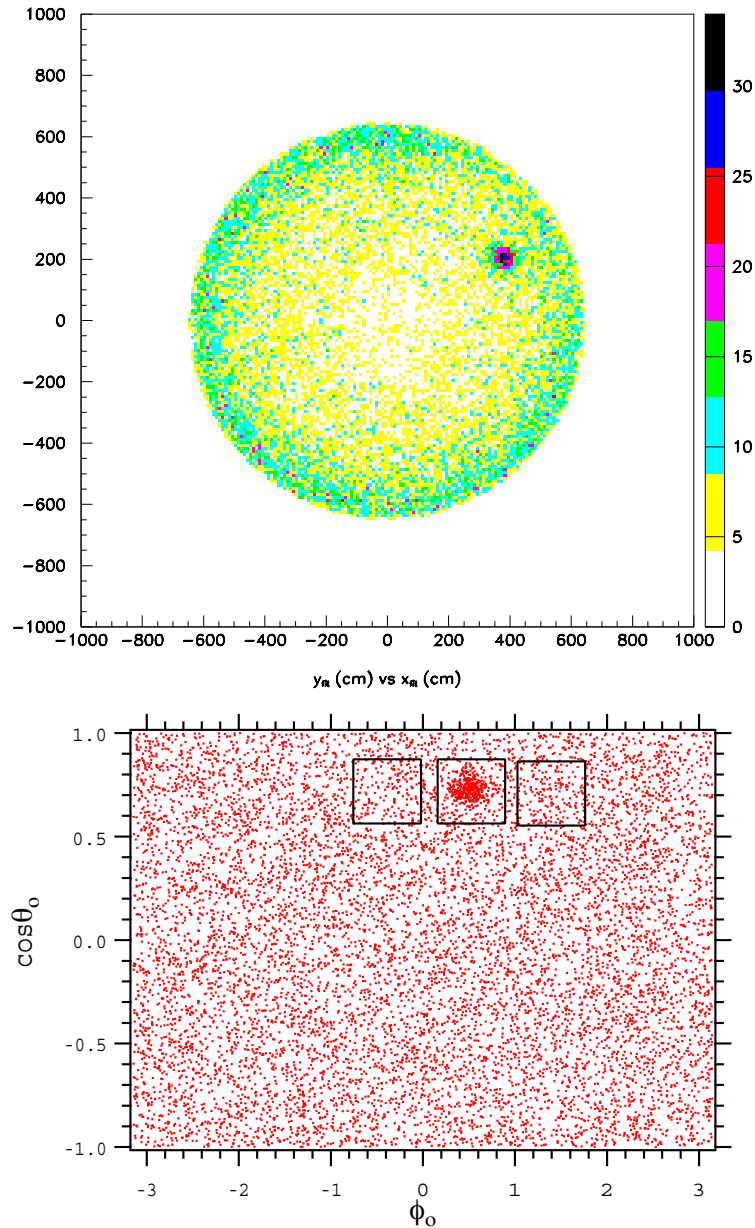
Figure 3.10: The AV hot spot. The top panel shows a projection of SNO data onto the x-y plane, having made a cut to select events close to 600 cm (figure provided by Alan Poon). The lower panel shows a schematic of the monitoring windows used for studying the hot spot, along with the two background subtraction windows. The parameters ϕ_o and $\cos\theta_o$ are the detector polar coordinates.

3.4.4   Cherenkov Tail Backgrounds

In addition to photo-disintegration neutrons, decays of the the U and Th chains can also produce Cherenkov light which can simulate a neutrino event. Using Monte Carlo simulations of low energy ^{214}Bi and ^{208}Tl decays, uniformly distributed in the D$_2$O, PDFs are generated over $X = \{T_{eff}, R^3_{fit}, \cos\theta_\odot\}$. These PDFs compare well to studies with sources and to a period when there was an excess of ^{222}Rn in the D$_2$O. After making cuts $R_{fit} < 550$ cm and $T_{eff} > 5.0$ Mev, we calculate the ratio of accepted Cherenkov events to accepted neutron events in Table 3.4.

Table 3.4: Ratio of detectable $\beta\gamma$ to neutron backgrounds in the D$_2$O.

source	ratio of $\beta\gamma$ to n events	total number of $\beta\gamma$ events
^{214}Bi	$0.670^{+0.460}_{-0.125}$	$17.4^{+12.4}_{-5.3}$
^{208}Tl	$0.162^{+0.092}_{-0.030}$	$3.0^{+2.0}_{-1.3}$

Table 3.5: Result of fitting to the radial PDFs of external backgrounds.

Source	Number of events in ν window
AV	$6.3^{+2.9}_{-6.3}$
H$_2$O	$2.8^{+3.9}_{-2.8}$
PMT	$16.0^{+11}_{-8.0}$

At larger radii, the SNOMAN Monte Carlo is not considered to be well calibrated. We instead use deployed low energy sources in the H$_2$O, near the acrylic vessel and near the PSUP, to determine the PDFs for external sources of events. We also use a period of time when the ^{222}Rn levels were elevated in the H$_2$O. These PDFs are shown
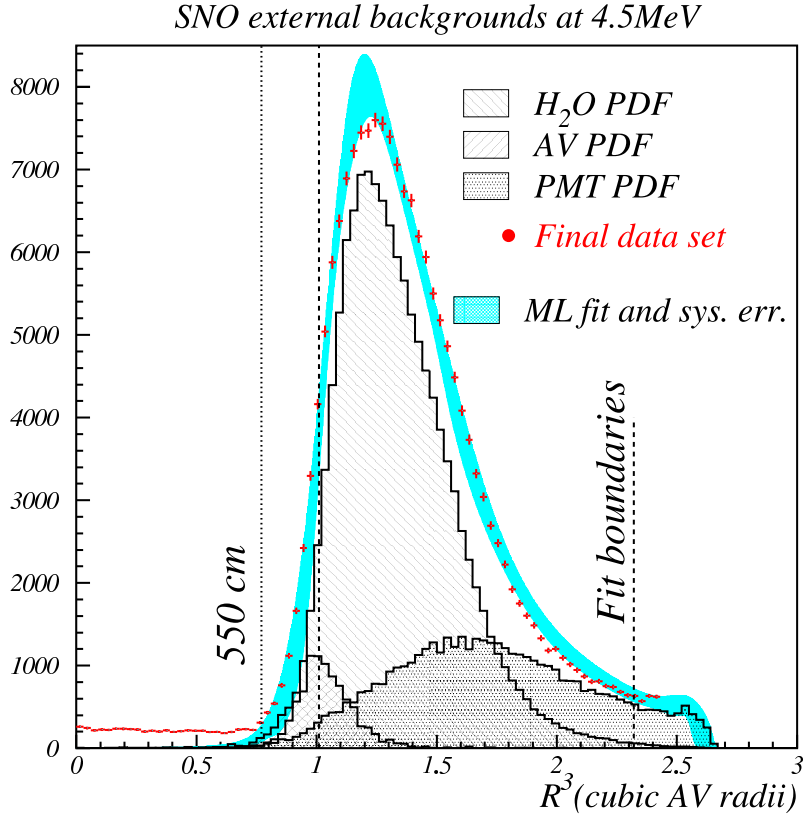
Figure 3.11: External backgrounds as a function of R_{fit}^3. Figure by Vadim Rusu.

in Fig. 3.11 for a kinetic energy > 4.0 MeV (4.5 MeV total). We use this energy cut because there are insufficient statistics to make a fit in the neutrino energy window ($T_{eff} > 5.0$ MeV). This, of course, should be considered a great success for a low background experiment.

By fitting the radial PDFs in the range $1 < (R_{fit}/600)^3 < 2.31$, we extract the amplitude of AV, H_2O, and PMT Cherenkov backgrounds for the lower energy window. We then use the PDFs to extrapolate up into the neutrino energy window, and into the region $R_{fit} < 550$ cm.

3.4.5 Day-night Asymmetry of Backgrounds

We wish to determine if any of the background sources are asymmetric from day to night. We bin all data into a day bin or a night bin, based on the zenith angle of the Sun. The analyses of previous sections have measured the various background sources and we can now repeat that separately for day and night, forming an asymmetry ratio

$$A = 2\frac{B_N - B_D}{B_N + B_D} \tag{3.5}$$

where B_N and B_D are the night and day event rates for a given background source. A large number of the systematic errors cancel in forming this ratio. Since systematics are less of a concern, we can afford to look into a lower energy, higher statistics region, pushing the N_{eff} threshold down to 27.3 (approximately equivalent to 3 MeV). At this energy, the Monte Carlo is less robust, so it is difficult for us to separate out the various components. However, it is still instructive to look at the event rates in various monitoring windows.

We use the windows defined in Fig. 3.10 to measure the asymmetry of the AV hot spot, where we can subtract out the contribution from other sources because the hot spot is localized. To study PMT $\beta\gamma$ events, we look at large fit radii and events moving towards the center. To do this, we define the product $u.r$ of the unit vector in the fitted recoil direction with the unit vector for $\vec{r}_{fit}$. Taking $u.r < -0.7$ selects inward going events, primarily $\beta\gamma$ decays at the PMTs. Finally, we use the same windows defined for the *in-situ* D_2O and H_2O analyses, although now the threshold is significantly lower (and the statistics much larger). The day-night asymmetries of these various windows are shown in Table 3.6. We can conclude a number of things from this table.

1. The hot spot has essentially no asymmetry

2. PMT $\beta\gamma$'s have essentially no asymmetry

3. There is a mild asymmetry in the H_2O and a significant asymmetry in the D_2O.

Table 3.6: Definition of various monitoring windows. All windows have additional instrumental cuts, high level cuts, and muon followers removed. The N_{eff} threshold is chosen to avoid software threshold effects, with a window $27.3 < N_{eff} < 40$.

Window	CUTS			Asymmetry
Name	Radial	Direction	Polar	
1. Hot Spot	550<R<650	–	$0.25 < \phi_o < 0.75$	$-1.4 \pm 3.2\%$
	(Bkgnd. : $-0.4 < \phi_o < 0.2$ and $0.8 < \phi_o < 1.4$)			
2. PMT $\beta\gamma$	755<R<815	u.r<-0.7	–	$0.46 \pm 0.38\%$
2a. PMT $\beta\gamma$	R>815	u.r<-0.7	–	$1.62 \pm 0.18\%$
3. H_2O	650<R<680	u.r>0	–	$6.94 \pm 0.72\%$
4. D_2O	R<450	u.r>0	–	$30.5 \pm 4.2\%$

One should be careful to note that a large asymmetry in a particular background source does not necessarily imply a large total asymmetry, since the backgrounds are only a small fraction of the total number of events.

A day-night asymmetry in the hot spot rate would be indicative of either an intrinsic asymmetry in the source or some effect like drifting energy scale causing a variation in acceptance from day to night. The fact that we don't see a day-night asymmetry tells us that these effects are either not present or they are cancelling. Either way, we are only interested in the total asymmetry of the event rate, which is small. Bulk AV contamination is not expected to have any intrinsic variation, so we conclude that the asymmetry of all AV sources is negligible.

We note that the analysis of PMT events is relatively stable to the choice of radial cuts, as demonstrated in Fig. 3.12. First, we see that Window 2 is intentionally situated in a region where the slope with respect to radius is shallow. This prevents a small perturbation in reconstruction aliasing into an asymmetry in the PMT $\beta\gamma$ event rate. By moving the window out in radius, we get more statistics. The result

is now inconsistent with zero, although still small. Possibly this is due to variable contamination of the outer H_2O with radon, with γ's passing through the PSUP to be detected. Despite this, we conclude that the asymmetry in PMT $\beta\gamma$'s is essentially negligible.
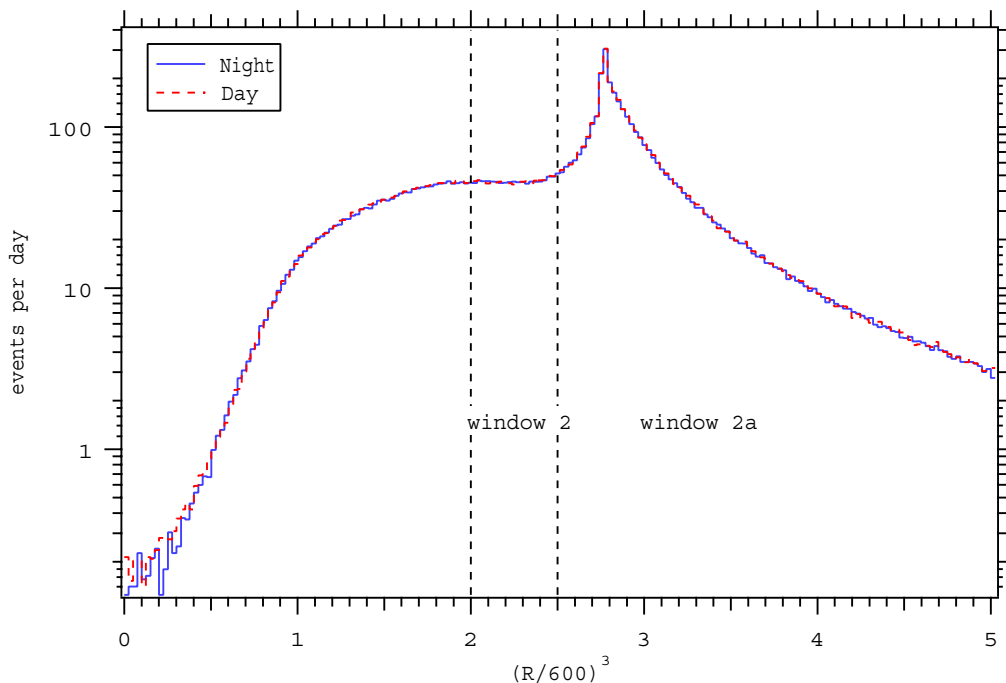
Figure 3.12: The day and night PMT $\beta\gamma$ rate as a function of fiducial volume.

It is believed that ^{222}Rn from the U chain is responsible for the asymmetries we see in the H_2O and D_2O regions. Since the chain is expected to be in equilibrium below ^{222}Rn, this allows us to infer an asymmetry for both $\beta\gamma$ and neutron backgrounds.

In Section 3.6 we will construct a model of the SNO data. To do this, we will need to know how the number of background events divides between day and night. The fraction of events for the night and day is

$$\frac{B_N}{B} = \frac{(1 + A/2)t_N}{t + (t_N - t_D)A/2} \qquad \frac{B_D}{B} = \frac{(1 - A/2)t_D}{t + (t_N - t_D)A/2} \qquad (3.6)$$

where t_D, t_N and t are the day, night, and total livetimes.

3.5   Instrumental Parameters

Of course, the model we create of the detector response is not known with 100% accuracy. We describe the perturbation from this model by instrumental parameters α, such as energy scale, position resolution, *etc.* Many systematics are time dependent, so that we must write $\alpha = \alpha(t)$. The discussion of this time variability will not be exact but, since the time dependence of the systematics will be seen to be small, an exact treatment is unnecessary. Since we are considering data in two zenith angle bins (D and N), we define two time averages

$$\alpha_N = \frac{1}{t_N} \int_N dt \; \alpha(t)$$
$$\alpha_D = \frac{1}{t_D} \int_D dt \; \alpha(t)$$

(3.7)

where t_N and t_D are the night and day livetimes. We can change basis to

$$\alpha_{av} = \frac{t_N \alpha_N + t_D \alpha_D}{t_N + t_D}$$
$$\alpha_{dif} = \alpha_N - \alpha_D$$

(3.8)

The reason we write our equations this way is that α_{av} and α_{dif} are measured by independent techniques and are hence largely uncorrelated. In Section 4.2 we will derive time-averaged fluxes for the electron and non-electron neutrino components (ϕ_e and $\phi_{\mu\tau}$). These measured fluxes will depend only on the time averaged systematics α_{av}. In Section 4.3, we will derive asymmetry parameters, e.g. $A_e = 2\frac{\phi_{eN} - \phi_{eD}}{\phi_{eN} + \phi_{eD}}$. These asymmetries will depend only on the differential systematics α_{dif}.

3.5.1   Energy Scale

As discussed in Section 3.2, we have created a mapping from measurable quantities such as N_{prompt} into a linear energy scale T_{eff}. For energies of interest, the T_{eff} distribution is gaussian, centered at T_e (the actual e^- recoil energy). We might assume that this energy mapping is in error, so the centroid of the distribution is

really at

$$T_{eff} = (1 + \alpha)T_e \tag{3.9}$$

In Section 3.2, we discussed the time average value $\alpha_{av} = \pm 1.21\%$. We now wish to discuss its time dependences.

Consider a spectrum of any kind of event, distributed over some generic energy measure E. At any given time, the actual energy scale might be different to the intrinsic energy scale of a stable detector.

$$\tilde{E} = (1 + \alpha(t)) \times E \tag{3.10}$$

This leads to a shift in the rate of events R above threshold E_{th}

$$R(\alpha(t)) = R_o + \gamma R_o \alpha(t) + \mathcal{O}(\alpha^2) \tag{3.11}$$

where $R_o = R(\alpha = 0)$ and

$$\gamma = \frac{1}{R}\frac{dR}{d\alpha}\bigg|_{\alpha=0} = \frac{E_{th}}{R}\left(\frac{dR}{dE}\right)_{E=E_{th}} \tag{3.12}$$

where we have recognized that near threshold $d\alpha = \frac{dE}{E_{th}}$.

Now let us write α in terms of two components, a long term energy drift α_L and a term that varies with time of day α_S

$$\alpha(t) = \alpha_L(t) + \alpha_S(t)$$

We note that if α_S has no systematic difference from day to night, but it fluctuates randomly, then these fluctuations will tend to average out over time. For example, if α_S is typically different between day to night by $\pm 0.5\%$, but in a random way, then this will average out to a 0.03% difference over the livetime of SNO (which is not one complete year). It turns out that the average $< \alpha(t) >$ is the important quantity. One can see this by noting that any observable such as $A_x(\alpha)$ can be expanded linearly in α (which is small) and then averaged over time.

Long-term Energy Drift (α_L)

As already discussed in Section 3.2, a slow drift was observed in the energy scale of the SNO detector, as measured with the ^{16}N calibrations and shown in Fig. 3.5. The cause of this drift, and its actual functional form, are unknown. An empirical "best fit" model has been identified.

$$
\epsilon_{drift} = \begin{cases} 1.00506 \times (1.58719 - 6.28308 \times 10^{-5} \times t_{JDY}) & t_{JDY} < 9356 \\ 1.00506 \times (0.999345 - 9.12406 \times 10^{-6} \times (t_{JDY} - 9356)) & t_{JDY} \geq 9356 \end{cases}
$$

$$(3.13)$$

where t_{JDY} is the Julian day. This model is used to correct the assigned energy (T_{eff}) for each event. The question now is, *how wrong could this drift formula be?* An error in the correction factor can lead to an artificial asymmetry in a day-night analysis. The reason for this is that the relative size of day and night livetime varies with season, so that a slowly varying PMT efficiency can alias into an artificial day-night asymmetry.

A number of worst case models were identified (Fig. 3.13), although only the most extreme are presented here [51]. Here we chose to maximize the difference between summer and winter energy scales, with the model pushed to the extreme allowed value for those time periods. Choosing the extreme models gives the most conservative estimate of the associated systematic error. Indeed, this is thought to give an overestimate of the uncertainty.

As discussed above, a time-averaged systematic is sufficient to describe the perturbation of the energy response function.

$$
\alpha_{diff} = \int_N dt \, [\epsilon(t) - \epsilon_o(t)] - \int_D dt \, [\epsilon(t) - \epsilon_o(t)]
$$

$$(3.14)$$

where $\epsilon_o(t)$ is the best fit model to the drift. The results of this integration are found in Table 3.7. When studying systematics as perturbative parameters, it is sufficient to allow the day and night energy scale to be different by $\pm 0.14\%$
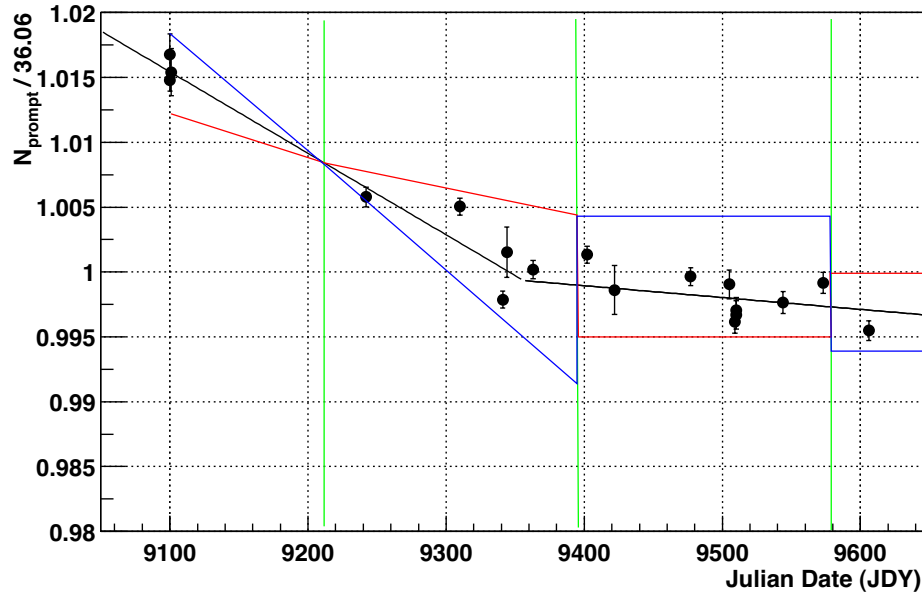
Figure 3.13: Worst case energy drift models.

Table 3.7: Difference between the night and day time-averaged energy scales due to long term drift in the detector gain. The perturbation is measured relative to the best fit model.

model	α_{dif} (%)
normal drift model	0 (by construction)
no drift model used	- 0.11 %
+ extreme drift model (blue)	+0.14 %
- extreme model (red)	-0.13 %

Diurnal Variation (α_S)

In addition to the long term energy drift, we have to consider the possibility of a diurnal variation in energy scale. Over the time scale of a day, the optical properties of the H_2O and D_2O are not expected to change, nor do we expect changes in the concentrator reflectivity or in the AV optics. However, one might anticipate diurnal variations in the PMT response. For example, the PMT voltage may drift, the compensation coils might be incorrectly set, or there could be errors in our tube accounting.

To test for such variables we need a source of light which, for any given calendar day, is constant from day to night. This source should illuminate all PMTs approximately uniformly but otherwise can be located anywhere within the PSUP. It also should be continuously present and, for this reason, deployed sources are not useful. Fortunately, we have multiple "sources" which satisfy these criteria, including the AV hot spot and PMT $\beta\gamma$'s. The monitoring of these was described in Section 3.4. We can use the N_{eff} energy measure to test for diurnal variations, because we don't care about a misunderstanding of the optics (which can't change on the time scale of a day). This allows for a lower effective threshold and hence more statistics.

We consider a source of events with rate R, assumed to be stable. If the average day and night energy scales (α_D and α_N) are different, then this will induce an artificial asymmetry in the event rate

$$A = \gamma \times \alpha_{dif} \tag{3.15}$$

where A is defined in terms of the night event rate (R_N) and day event rate (R_D).

$$A = 2\frac{R_N - R_D}{R_N + R_D}$$

One can approximate γ by binning the data and using the discrete approximation $\gamma = \frac{E_{th}}{R}\frac{\Delta R}{\Delta E}$ in the threshold bin. γ and A are measured in a number of monitoring windows, defined in Table 3.6 using the N_{eff} energy measure.

These monitoring windows can only be used to check for energy scale variation if their event rates are intrinsically stable. This is rarely the case as can be seen in Fig. 3.14. The H_2O and D_2O windows show large variations due to the changing background contamination in the detector. The Hot Spot and PMT $\beta\gamma$ windows show a slow decrease in event rate. This is suspected to be due to an unaccounted energy drift, but could be an indication of decaying activity. We would like to limit/measure
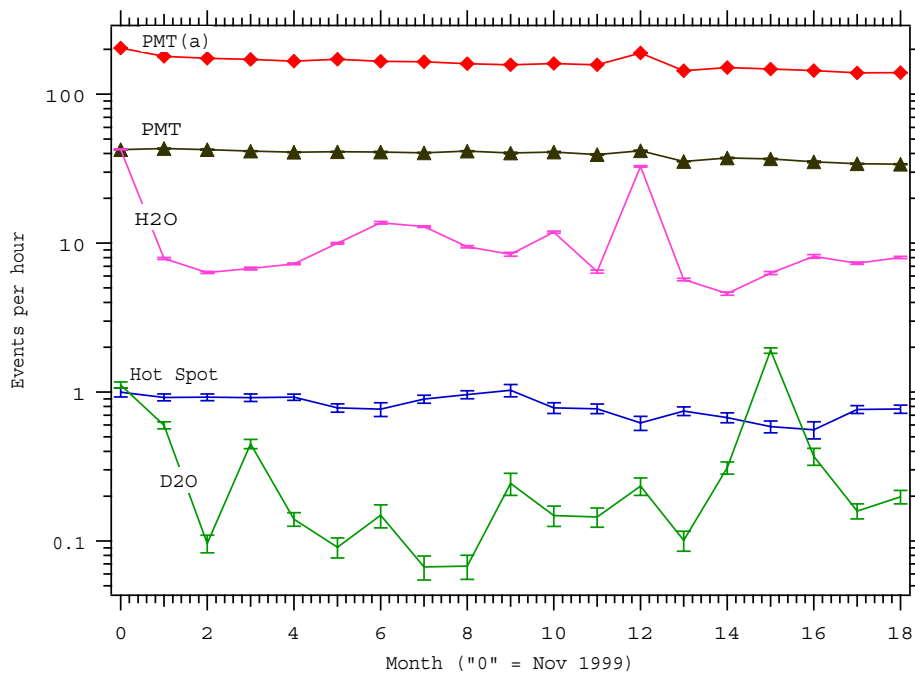
Figure 3.14: The month-to-month variation of each monitoring window.

the difference in the day and night average energy scale using the asymmetry of hot spot or PMT $\beta\gamma$'s. This would include a component from the energy scale drift, aliasing into a day-night asymmetry. However, we can't be completely sure that the intrinsic event rates in these windows are not also changing slowly, aliasing into a day-night asymmetry. For example, an event rate that was high in December, but low in June, could produce an asymmetry simply because there is more night livetime in December. To get around this problem, we can form a different day-night asymmetry

A^*. We measure the day-night asymmetry over short time intervals and then combine the results statistically. This can be done using

$$A^* = 2\frac{\sum_k w_k(R_{Nk} - R_{Dk})}{\sum_k w_k(R_{Nk} + R_{Dk})} \tag{3.16}$$

k labels bins of similar Julian time, where the night and day event rates are measured separately in each bin. w_k is used to give higher statistics bins more weighting. It can be shown[4] that we get the best statistical measure by taking

$$w_k = \left(\frac{1}{t_{Nk}} + \frac{1}{t_{Dk}}\right)^{-1} \tag{3.17}$$

A^* tests for an asymmetry that occurs on a time scale *shorter* than the duration of the individual k-bins. In this way, if there is a long term drift in energy scale or if the intrinsic rate is changing slowly, it will not alias into a day-night asymmetry and we are only sensitive to short term energy scale changes. The duration of each k-bin is a tunable parameter in this analysis, although we find that we are insensitive to it. The data are binned into bins of approximately 5 calendar days each. Typically, the livetime in each of these bins is around 3 days. Variations on a time scale shorter than this will not be normalized out by the formation of A^*.

The most stable and highest statistics window is the PMT $\beta\gamma$ window. It also has the most steeply falling spectrum, hence providing the most sensitive test of energy scale variations. One sees that the result is consistent with almost no asymmetry and the 1σ limit on $A^* \times 100\%$ is $\approx 0.4\%$. This translates into a limit on $\alpha_{dif} = \alpha_N - \alpha_D$

$$\alpha_{dif} < 0.015\% \quad 1\sigma\ limit$$

---

[4]This is seen most easily by noting that the statistical error is given by $\sigma_N = \frac{\sqrt{R_N \times t_N}}{t_N}$ and $\sigma_D = \frac{\sqrt{R_D \times t_D}}{t_D}$. If we assume that $R_N \approx R_D \approx R$, then the statistical weight of each bin is given by

$$w_k \sim (\sigma_{Nk}^2 + \sigma_{Dk}^2)^{-1} \sim \left(\frac{1}{t_{Nk}} + \frac{1}{t_{Dk}}\right)^{-1}$$

Table 3.8: The day-night asymmetry of event rate in various monitoring windows. Errors are statistical only.

window	γ	$A(\%)$	A^* (%)
Hot Spot	10.3 ± 2.4	$-1.4 \pm 3.2\%$	$0.2 \pm 3.3\%$
PMT $\beta\gamma$	26.1 ± 0.2	0.46 ± 0.38	$-0.08 \pm 0.39\%$
PMT $\beta\gamma$ (a)	24.1 ± 0.1	1.62 ± 0.18	$-0.04 \pm 0.19\%$
H_2O In-situ	13.0 ± 0.2	$6.94 \pm 0.72\%$	$-0.71 \pm 0.75\%$
D_2O In-situ	11.7 ± 1.1	$30.5 \pm 4.2\%$	$-2.0 \pm 4.4\%$

Henceforth, we will ignore possible *diurnal* variations in energy scale.

In Fig. 3.14, we note that there is an apparent correlation between PMT $\beta\gamma$ rates in Window 2 and with H_2O decays in Window 3, as seen in the radon spike of November 2000. However, we see no correlation between rates for the larger radon spike of November 1999. We might conclude that the November 2000 correlation is coincidental. Alternatively, perhaps the November 1999 spike is due to an excess in radon in the outer H_2O region only, explaining the lack of correlation between Windows 2 and 3. Either way, the contamination from Window 2 is small and we have shown that the procedure of forming A^* mitigates the asymmetries of H_2O backgrounds. For this reason, the analysis presented here is independent of a possible contamination of the PMT monitoring window.

3.5.2   Energy Resolution

A discrepancy was noticed between the width of the modelled and actual ^{16}N energy resolution. The Monte Carlo generates a width that is less than the data.

$$\frac{\sigma(data) - \sigma(MC)}{\sigma(data)} \approx 0.045 \tag{3.18}$$

It is not clear which resolution we should use to describe SNO. Due to the complications of modelling source geometry, the Monte Carlo could be incorrect for describing ^{16}N yet still be correct for modelling neutrino interactions. We take the Monte Carlo width as the official model for neutrinos, but assign an error

$$\frac{\delta\sigma}{\sigma} = 0.045 + 0.00401 \times (T_e - 4.98) \tag{3.19}$$

We also wish to know if there is any *variation* in the resolution with time. Studies with the ^{16}N source rule out any significant long term behavior. The N_{eff} energy measure, along with PMT $\beta\gamma$'s can also be used to put a limit on the *diurnal* variations in resolution. To study the effects of a shift in resolution, the energy (N_{eff}) of each PMT $\beta\gamma$ event was perturbed, using a Gaussian smearing function of standard deviation $\delta \times \sqrt{N_{eff}}$ and then recounted above threshold.

We have limited the PMT $\beta\gamma$ diurnal asymmetry to be approximately $< 0.4\%$ and, from Fig. 3.15 we see that, to get a 0.4% variation in counts above threshold, we must perturb the resolution with $\delta^2 = 1 \times 10^{-3}$. We know from ^{16}N studies that, for a total light energy measure, $\sigma^2 \approx 2 \times N_{hits}$, giving

$$\alpha_{dif} = \frac{\sigma_N^2 - \sigma_D^2}{\sigma^2} < 5 \times 10^{-4} \quad (0.05\%)$$

This may not be exactly correct for a prompt light energy measure, but it should be the same order of magnitude. We will see that a variation in resolution this small has essentially no effect on the final analysis of SNO data. Less stringent limits can be placed using the hot spot (1.7%) or with D$_2$O Cherenkov backgrounds (0.3%).

3.5.3 Energy Non-linearity

By comparing source data and Monte Carlo at different energy scales, we can get an idea if our mapping $T_e \rightarrow T_{eff}$ is indeed linear. The PT source (see Section 3.2) produces γ's at 19.1 MeV. This second calibration point showed extremely good agreement between data and Monte Carlo, despite the fact that the Monte Carlo had
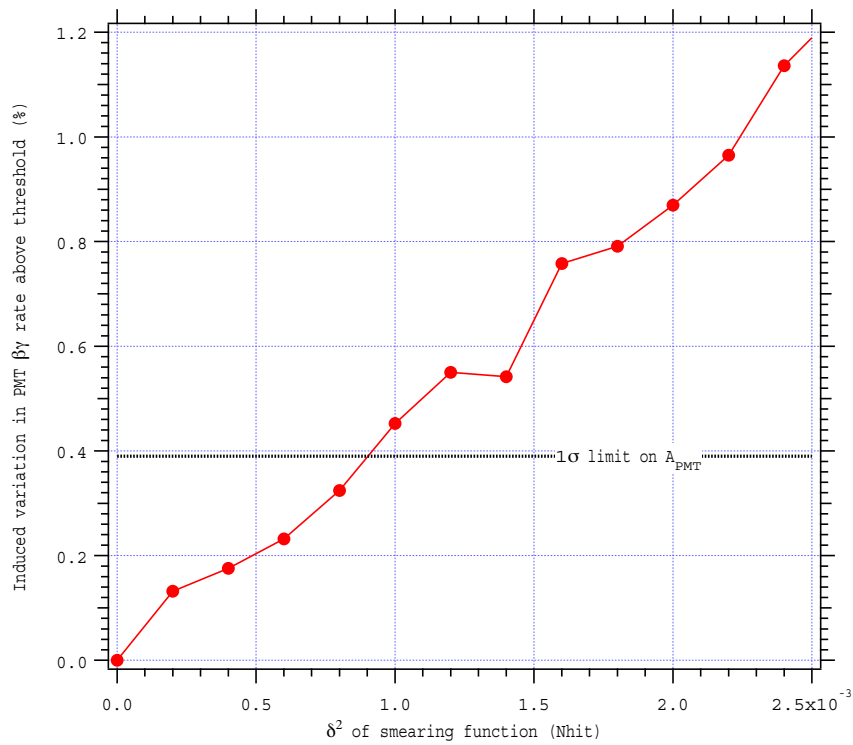
Figure 3.15: Variation in the event rate above threshold for PMT $\beta\gamma$'s as a function of energy resolution. We see that, for a 1×10^{-3} Nhit change in resolution, we get an approximately +0.4% change in the counts above threshold.

been tuned using the ^{16}N source. With the centroid of the response function being at $T_{eff} = T_e$, we describe a deviation from this by

$$\Delta T_{eff} = \alpha \times 1.40(T_e - 4.98) \tag{3.20}$$

where $\alpha = \pm 0.0023$, as limited by the PT source.

3.5.4 Vertex Accuracy

Placement of the ^{16}N source at various locations in the detector allows us to determine if the reconstruction algorithm is correctly assigning the vertex of each event. A set of these comparisons is shown in Fig. 3.6. The ^{8}Li source provides an additional handle on this systematic, particularly because ^{8}Li is a point source of β's, while ^{16}N

is a distributed source of Compton scattered electrons. These studies tell us that the reconstruction of the radial coordinate is accurate to within $\alpha_{av} = \pm 1\%$. In this way, a fiducial cut of 550 cm may actually be equivalent to 555.5 cm or 544.5 cm, for a $+1\%$ or -1% rescaling of vertex reconstruction. The uncertainty is a little larger towards the AV neck, where there are no PMTs. However, the fiducial volume in this region is not particularly significant.

We also wish to determine if the vertex accuracy is changing from day to night. Using the same monitoring windows shown in Fig. 3.10, we plot the hot spot event rate as a function of position (Fig. 3.16). The hot spot can not be used as an absolute measure of fitter accuracy and reconstruction, since it occurs in a region (the AV) where the optics are unusual. However, the stability of its reconstruction provides an excellent measure of α_{dif}, the systematic difference between day and night. The summary of these results are found in Table 3.9. We conclude that the radial reconstruction is stable from day to night, with $\alpha_{dif} = \pm 0.20\%$.

Table 3.9: Day-night differences in reconstruction, as measured using the AV hot spot.

datum	day	night	difference α_{dif} = night - day
centroid R (cm)	603.99 ± 0.88	603.37 ± 0.81	-0.62 ± 1.20 cm $(0.10 \pm 0.20\%)$
width σ_R (cm)	24.32 ± 0.83	24.76 ± 0.76	0.44 ± 1.13 cm

3.5.5 Vertex Resolution

By making additional comparisons between Monte Carlo and the deployed sources, we can measure the resolution in the radial coordinate. Typically, we find that the
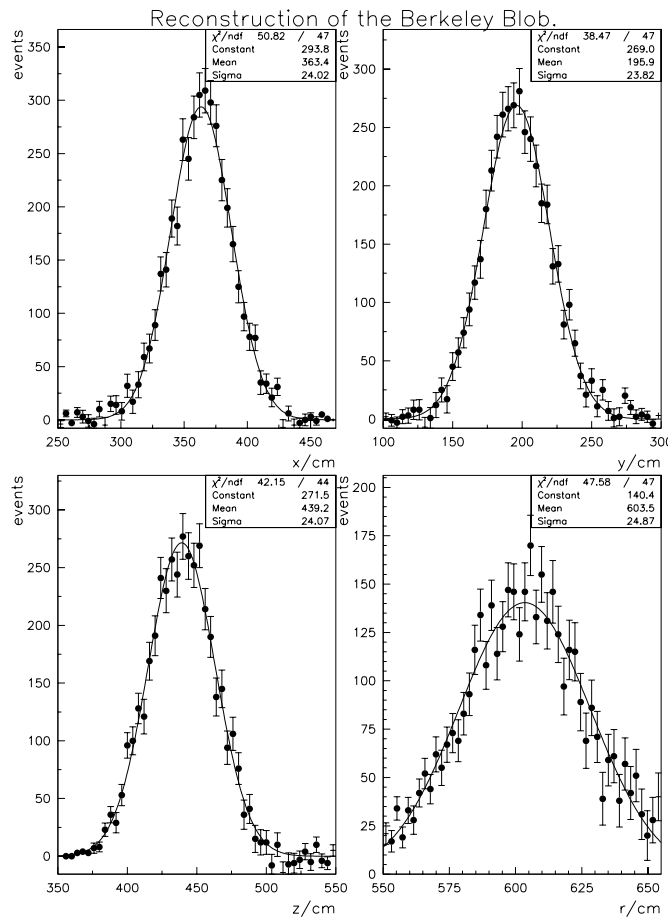
Figure 3.16: Reconstruction properties of the AV hot spot (a.k.a. the *Berkely Blob*, named for the institution which first identified it). Figure provided by Neil McCauley.

resolution is 18 ± 2 cm, with the error being largely due to differences between Monte Carlo and data. The uncertainty is a little larger towards the AV neck, where there are no PMTs. However, the fiducial volume in this region is not particularly significant. We therefore take the time-averaged systematic to be $\alpha_{av} = \pm 2$ cm. As seen in Table 3.9, the AV hot spot limits the variation of the vertex resolution to be $\alpha_{dif} = \pm 1.13$ cm. Vertex resolution will be seen to have almost no effect on the final analysis. The reason for this is that an error in resolution will move some events inside and some

outside of the fiducial volume. For a signal with a flat gradient across the fiducial boundary (CC and ES), the effect washes out to zero. For the NC reaction, there is a small residual effect, amounting to $\approx 0.1\%$ in the acceptance of neutrons.

3.5.6 Neutron Efficiency

Neutron efficiency was discussed in Section 3.3. We saw there that the efficiency for neutron captures that produce a measurable signal is $14.38 \pm 0.53\%$ (with $T_{eff} > 5.0\ MeV$ and $R_{fit} < 550\ cm$). The uncertainty can also be expressed as a relative value

$$\alpha_{av} = \frac{0.53\%}{0.1438} = 3.7\% \tag{3.21}$$

It is this relative value that we will use to parametrize our model for neutron capture.

The total neutron capture efficiency does not vary because the isotopic abundance of the heavy water is constant. The acceptance of the radial and energy cuts can vary, although these effects are already described by other parameters and need not to be considered here.

3.5.7 Acceptance

We have seen in Fig. 2.11 that, over most of the energy range of solar neutrino interactions, the physics events lost to instrumental cuts is small and well understood. The high level cuts of Section 2.2.3 remove a larger fraction of physics events. For γ events (NC), the ^{16}N source helps us measure this loss at $\approx 2.3^{+0.4}_{-0.2}\%$. For electron events (CC and ES) this is measured with the ^{8}Li source to be $\approx 1.4^{+0.4}_{-0.2}\%$. The model we create for SNO will include these as correction factors.

The stability of these cuts is shown in Fig. 3.17. As a conservative estimate of how the acceptance might vary from day to night, we could take the spread of this plot and set $\alpha_{dif} = 0 \pm 0.3\%$. This is what we will use when calculating the day-night asymmetry in Section 4.3. However, it should be noted that this is an extreme

overestimate. We have seen very good diurnal stability in the detector and have no reason to believe that the acceptance is changing over the time scale of a day. If this is the case, then we need only consider the possibility of long-timescale variation. With the very mild variation observed in the ^{16}N runs, any plausible long-timescale change in acceptance would average out to be negligible. Either way, α_{dif} has essentially no effect on the final MSW contours of Section 4.4 and, for that analysis, we take $\alpha_{dif} = 0$.
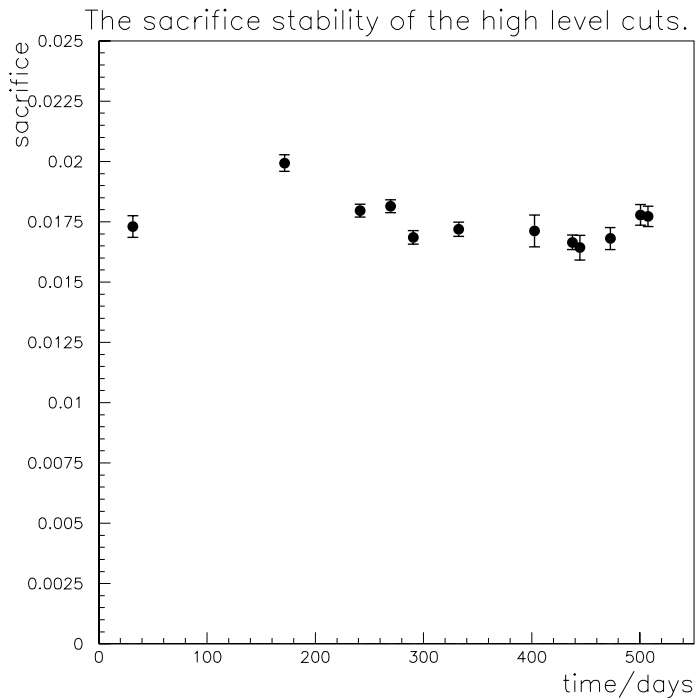
Figure 3.17: The stability of the high level cuts from ^{16}N runs.

3.5.8 Monte Carlo Statistics

Naturally, the Monte Carlo is generated with finite statistics. In Sections 4.2 and 4.3, we will use these simulations to extract fluxes ϕ, relative to the SSM. The uncertainty

in the calculation of ϕ has a component due to the finite statistics.

$$\frac{\sigma_\phi}{\phi} = \frac{1}{\sqrt{N_{MC}}} \tag{3.22}$$

where N_{MC} is the number of events in the Monte Carlo simulation. We typically run our Monte Carlos with a ^{8}B flux of 50× SSM. This leads to an error in the total number of expected events which is 0.19% (for CC interactions), 0.59% (ES interactions) and 0.59% (NC interactions). These errors are small and are neglected in the analysis of Section 4.2, being dwarfed many larger systematics. However, when calculating day-night asymmetries (Section 4.3), the larger systematics cancel and finite Monte Carlo statistics becomes the largest contribution to the error budget.

3.5.9 Directional Systematics

There is a final class of systematics. If the detector has a different response for electrons moving in different directions, this may introduce some systematic error into the analysis. For example, during the night almost all ES electrons move upward, while during the day they move downward. Due to the lack of PMTs around the neck area or PMTs being switched off, there may be a different response during the day and night. If this is incorrectly modelled, we might calculate an artificial day-night asymmetry. Similarly, the CC reaction produces directional information and so is also sensitive to directional systematics. However, the NC reaction carries no direction information, so in unaffected by such effects. Monte Carlo simulations include all of the geometric effects due to missing and inactive PMTs, and integrate the detector response over the livetime, taking into account the variation in incident neutrino direction. These simulations show no significant asymmetry in the acceptance of CC or ES events from day to night, although this claim is limited by Monte Carlo statistics. For this reason, we choose to neglect this kind of systematic in the analysis.

3.6 Summary of Systematics and Creating a Model for SNO

In this section we will construct a model of SNO events and summarize the systematics. First, let us define three variables types.

- $X = \{T_{eff}, R_{fit}^3, \cos\theta_\odot\}$ is a set of measurable quantities.

- η represents a physics parameter. We will consider a number of different physics models, each described by a different set of physical parameters $\boldsymbol{\eta}$.

- α represents a systematic parameter, either *background amplitude* or *instrumental parameter*. Collectively we describe the set of systematics by a vector $\boldsymbol{\alpha}$.

3.6.1 Probability Density Functions (PDFs)

For each reaction (CC, ES, NC), one defines the PDF over X

$$\rho^{cc}(X|\eta, \alpha) \tag{3.23}$$

with ρ^{es} and ρ^{nc} for the other reactions. In this thesis we will treat ρ as a binned histogram over X, with X labelling the bins. The normalization condition is

$$\sum_X \rho^{cc}(X|\eta, \alpha) = 1 \tag{3.24}$$

(with $\sum \to \int dX$ in the continuous case). In addition, ρ^{cc} depends continuously on both physics parameters η and instrumental parameters α. It is a conditional probability, read as $\rho^{cc}(X|\eta, \alpha)$ *is the probability of getting X, given η and α.*

To a good approximation, we can write the 3-dimensional PDF ρ^{cc} as a product of three 1-dimensional PDFs, f, h, and g.

$$\rho^{cc}(T_{eff}, R_{fit}^3, \cos\theta_\odot) = f^{cc}(T_{eff}) \times g^{cc}(R_{fit}^3) \times h^{cc}(\cos\theta_\odot) \tag{3.25}$$

We can do this because the energy measure T_{eff} has been defined to be independent of position and direction. Otherwise, f would depend strongly on the other variables.[5]

---

[5]There is a weak dependence in g and h on the energy and this has been neglected. A more sophisticated treatment would write these as conditional PDFs $g(R^3|T)$ and $h(\cos\theta_\odot|T)$.
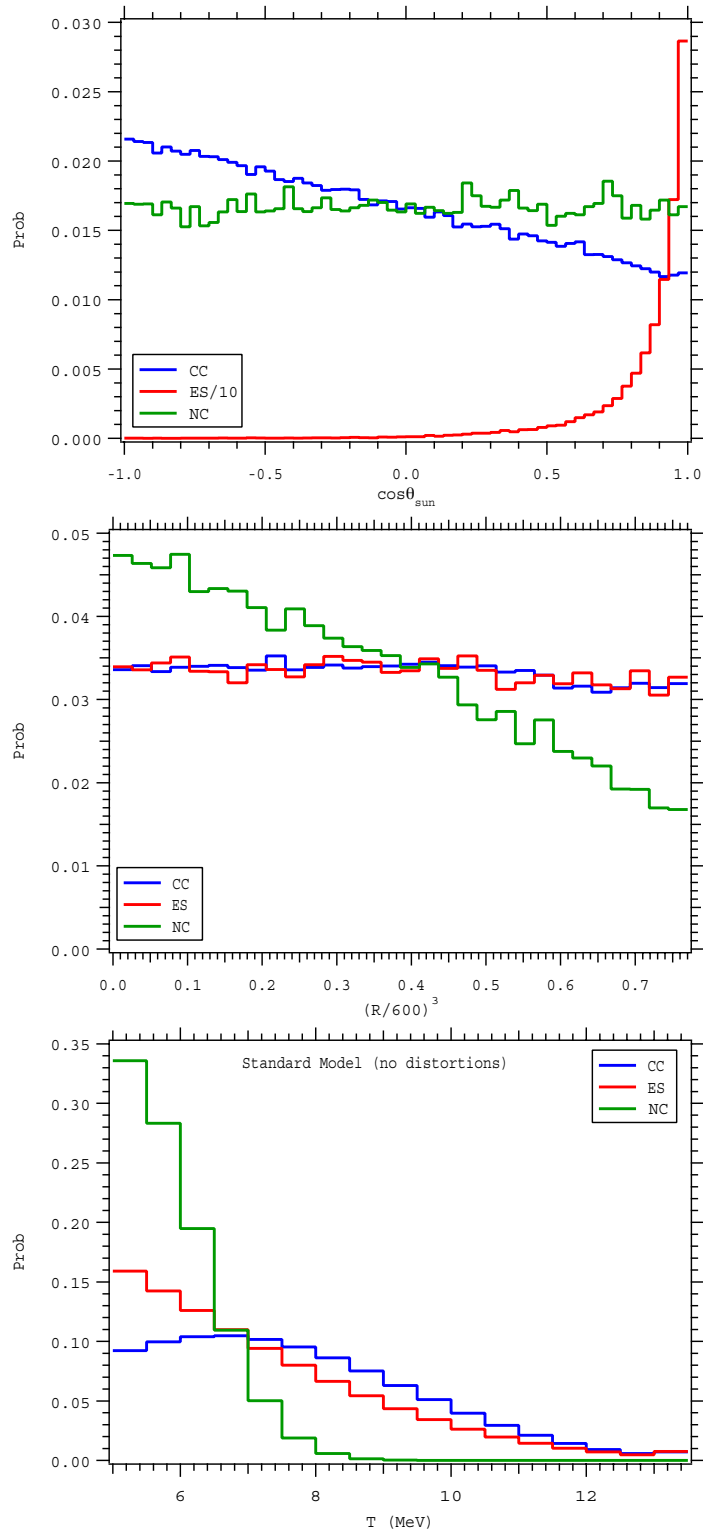
Figure 3.18: The CC, ES, and NC PDFs for ^{8}B neutrinos, projected onto the $\cos\theta_\odot$, R_{fit}^3, and T_{eff} axes. To generate this figure, the instrumental parameters describing the detector response were set to their best-fit calibration values.

Monte Carlo PDFs

The SNOMAN Monte Carlo assumes an undistorted SSM spectrum of ^{8}B neutrinos, as well as a specific set of instrumental parameters. The instrumental parameters are tuned so to give our best model of detector response. We shall refer to this setting of the instrumental parameters as the *calibration values*, or α_{cal}. The radial and $\cos\theta_\odot$ PDFs derived from Monte Carlo are shown in Fig 3.18. Because the Monte Carlo has finite statistics, we see some noise in the distributions. We use 30 bins of equal width in R_{fit}^3, from $R_{fit} = 0$ to $R_{fit} = 550$ cm. For the $\cos\theta_\odot$ distribution, we use 60 bins of equal width from -1 to +1. We can also generate energy PDFs using the Monte Carlo, although these will only be useful for physics models which assume that the neutrino spectrum is undistorted from its standard shape. We use sixteen 0.5 MeV-wide bins from 5 to 13 MeV, with a seventeenth bin being 13 - 20 MeV.

Analytic PDFs

The radial and $\cos\theta_\odot$ PDFs are independent of physics parameters. However, the energy distribution will be different for different values of $\Delta m^2, \tan^2\theta$ and, for some analyses, we will need to take this into account. For the more general case, we construct a semi-analytic model which, up to a normalization, is defined by

$$f^{cc}(T_{eff}, \cos\theta_z) \sim \frac{dt}{d\cos\theta_z} \int dE_\nu P_{ee}(E_\nu, \cos\theta_z)\lambda(E_\nu) \int dT_e \frac{d\sigma^{cc}(E_\nu, T_e)}{dT_e}\rho_e(T_{eff}, T_e)$$
(3.26)

- $\lambda(E_\nu)$ is the neutrino energy spectrum for neutrinos created in the core of the Sun.

- $P_{ee}(E_\nu, \cos\theta_z)$ is the survival probability for the given value of $\Delta m^2, \tan^2\theta$. It is dependent on the neutrino energy and on the solar zenith angle. Typically, we will also average over zenith angle (e.g. to create day and night averages).

- $\frac{d\sigma^{cc}(E_\nu, T_e)}{dT_e}$ is the differential cross section.

- $\rho_e(T_{eff}, T_e)$ is the SNO energy response function, the probability that an electron of energy T_e will be measured as having an energy T_{eff}.

There is a similar model for the ES reaction. To create *binned* PDFs, we integrate T_{eff} over each of the 17 energy bins and $\cos\theta_z$ over the 2 zenith bins. In what follows, we shall compress the notation and use the single symbol T_{eff} to represent all 34 energy-zenith bins. To perform an MSW analysis, we will need these analytic energy PDFs. However, for other analyses (which assume no spectral distortions), we can use either analytic or Monte Carlo PDFs with little affect on the results. When we set $P_{ee} = 1$, we recover the conditions under which the Monte Carlo was derived, shown in the bottom panel of Fig. 3.18.

3.6.2 Expected Number of Events

For each reaction, we have a model for the *expected number of events* that pass the cuts. These are not distributed over X, but may still depend on physics and instrumental parameters. For example, if we change the energy scale of the model, there will be greater or fewer events above threshold.

Assuming a SSM of ^{8}B neutrinos, we can use the SNOMAN Monte Carlo to generate the expected number of events for each reaction. They can also be modelled by knowing the normalization in equation 3.26, given by $\phi_{^8B} \times V \times n_d$, the product of the flux, the livetime, the volume, and the number density of targets (deuterium for the CC reaction). There are also small correction factors to account for the orbital eccentricity of the Earth and for cut acceptance. The expected number of events for the SSM and for a particular oscillation scenario are shown in Table 3.10.

Regardless of whether we simulate only the SSM or allow for MSW effects, the expected number of events will be different from day to night. In both cases, the livetime is different for day and night and the expected number of events increases linearly with the livetime. In the full MSW model, there can also be some non-trivial dependence on zenith angle. However, the distribution of events between day and night is handled by the 34-bin energy-zenith PDF. We report only the *total* number of expected events here.

Table 3.10: Expected number of total (day + night) events for both the ^{8}B and hep neutrinos, interacting via the CC, ES, or NC reaction, with all cuts applied. For the SSM case, Monte Carlo and analytic simulations differ by $\approx 0.1\%$. The *oscillated* example is generated using the analytic approach and is shown for the point in MSW space $\Delta m^2 = 10^{-4.3}$, $\tan^2 \theta = 10^{-0.43}$.

	SSM (MC)		SSM (analytic)		oscillated example	
	^{8}B	hep	^{8}B	hep	^{8}B	*hep*
CC	5632.1 ± 10.7	not calculated	5646.6	32.5	1698.3	11.5
ES	557.2 ± 3.3	not calculated	557.8	2.3	227.4	1.1
NC	567.4 ± 3.3	not calculated	563.9	2.8	563.9	2.8

3.6.3 Combining Objects into a Model

In addition to the signal from the CC, ES and NC interactions, there will also be a number of background sources. We will label the number of events from each background as B^1, B^2, ..., one for each background source. There will also be a PDF for each source (ρ^1, ρ^2, ...) distributed over $X = \{T_{eff}, R_{fit}^3, \cos \theta_\odot\}$.

We recognize that the number of CC, ES, NC events, discussed in Section 3.6.2, have been derived assuming a specific flux of ^{8}B neutrinos ($5.05 \times 10^6 cm^{-2} s^{-1}$). It is unlikely that the Sun is producing exactly this number of neutrinos, since there are significant uncertainties in the solar model. To account for this, we introduce the parameter ϕ_{tot}, which measure the size of the actual flux, relative to the SSM flux. When $\phi_{tot} = 1$, the Sun is making $5.05 \times 10^6 cm^{-2} s^{-1}$ of ^{8}B neutrinos. When $\phi_{tot} = 2$, the Sun is making twice that number.

We combine the various components of the model into a *number density of events*,

$$\mu(X|\eta, \alpha) = \phi_{tot} \times (S^{cc}\rho^{cc} + S^{es}\rho^{es} + S^{nc}\rho^{nc})$$
$$+ B^1\rho^1 + B^2\rho^2 + ... \quad (3.27)$$

where $\mu(X|\eta, \alpha)$ is the number of events in bin X, given the parameters η and α. In

this thesis, we will treat *hep* neutrinos as a type of background. For all other background sources, the expected number of events and PDF shape will be independent of the physics parameters η. By setting the backgrounds to zero and the instrumental parameters to their best-fit calibration values, we generate the *ideal* model of SNO.

$$\mu_o(X|\eta) = \mu(X|\eta, \alpha = \alpha_o) \qquad \alpha_o = \begin{cases} 0 & background\ amplitudes \\ \alpha_{cal} & instrumental\ parameters \end{cases} \qquad (3.28)$$

This ideal model will be useful in the next chapter. We will use it to perform extraction of physics parameters, incorporating systematics $\boldsymbol{\alpha}$ as a perturbation around it.

3.6.4   Summary of Systematics

We wish to reduce the information about backgrounds somewhat. Since there are a large number of sources, it is relatively safe for us to *symmetrize* the errors. That is, for asymmetric errors σ_+ and σ_-, we define $\sigma = \frac{|\sigma_+|+|\sigma_-|}{2}$ to be the width of an equivalent (symmetric) gaussian. The central limit theorem ensures that this procedure leads to a correct analysis in the limit of a large number of sources of error.

We also realize that a number of background sources can have very similar PDF tails extending into the neutrino window. In this case, we choose to group them together as a single source. For example, U and Th neutrons look identical, while H_2O and AV Cherenkov tails are similar enough the we can approximate them as having a common PDF tail.

By regrouping the backgrounds like this, we reduce the number of parameters needed to describe them. The downside is that we introduce correlations between previously uncorrelated measurements. For the analyses presented in future sections, we shall neglect these correlations. It is understood that a more refined analysis will improve upon this (see Section 5.1).

Table 3.11: Summary of the amplitude and asymmetry of backgrounds. The uncertainties have been symmetrized for summary purposes and later use in the MSW analysis of Section 4.4. The internal neutrons are a combination of photo-disintegration and more exotic sources (atmospheric neutrinos, fission, $^2H(\alpha, \alpha)pn$, and $^{17}O(\alpha n)$ reactions).

background	Amplitude	Asymmetry
internal neutrons	51.7 $\pm$9	31 $\pm$ 4%
external neutrons	27 $\pm$8	6.9 $\pm$ 0.7%
D2O β-γ	20.4 $\pm$9	31 $\pm$ 4%
H2O+	9.1 $\pm$6	6.9 $\pm$ 0.7%
AV β-γ	(combined)	≈ 0
PMT β-γ	16 $\pm$10	≈ 0

Table 3.12: Systematic errors for instrumental parameters. Note that the differential sacrifice is treated as negligible for the MSW analysis of Section 4.4.

instrumental parameter	α_{av}	α_{dif}
energy non-linearity	$\pm$ 0.23%	neg.
energy scale	$\pm$ 1.21%	$\pm$ 0.14%
radial shift	$\pm$ 1%	$\pm$ 0.20%
radial resolution	$\pm$ 2.0 cm	$\pm$ 1.13 cm
energy resolution	$\pm$ 4.5%	$\pm$ 0.05%
sacrifice	$\pm$ 0.30%	$\pm$ 0.3%
neutron capture	$\pm$ 3.68%	neg.

<div style="text-align: center">

Chapter 4

INTERPRETATION

</div>

In this chapter the data are compared to various models. The simplest of these models is the so called *null hypothesis*, which assumes that there are no particle physics processes that change the nature of the electron neutrinos after their production in the Sun. The simplest extension to this model is to allow the neutrinos to change flavor, but in a way that does not depend on energy or zenith angle. This allows for the construction of a model, linear in the physics parameters, which will prove useful in making a null-hypothesis test. We then allow our model to have a neutrino flux which can be different from day to night, thus measuring the day-night asymmetry. Finally, we consider a detailed MSW model which includes flavor change, day-night asymmetry, and spectral distortions. This information will be encoded through the non-linear MSW parameters $\Delta m^2, \tan^2 \theta$.

4.1 General Formalism

We now define the log-likelihood function for the combined set of physics parameters, *e.g.* $\eta = \{\Delta m^2, \tan^2 \theta...\}$ and systematics $\alpha = \{$Energy-scale, AV background,...$\}$. The complete set of information about these parameters is contained in both neutrino data and in the calibration data. Here the term *calibration data* refers to data collected outside of the neutrino window and with non-neutrino runs. For each value of the parameters $\{\eta, \alpha\}$, one can calculate the probability of observing our two data sets

$$P_\nu = Prob(\nu \ data | \eta, \alpha) \qquad and \qquad P_{cal} = Prob(cal \ data | \alpha) \qquad (4.1)$$

where these are read as conditional statements; the probability of generating a data set, given the parameters η and α. However, we note that the calibration data set does not depend on η. Because the two data sets are distinct, the joint probability function is defined as the product of the two functions. To learn about our parameters, we can either study this or equivalently the log-likelihood function $\mathcal{L}$[1].

$$\mathcal{L} = -2ln P_{total}, \qquad P_{total} = P_\nu P_{cal} \tag{4.2}$$

To construct the neutrino part of $\mathcal{L}$, one must first have a model for the number density of events μ, discussed extensively in Section 3.6. μ is distributed over the measurable quantities $X = \{T, R^3, \cos\theta_\odot, ...\}$ and also depends continuously on both physics parameters and systematics.

$$\mu = \mu(X|\eta, \alpha) \tag{4.3}$$

It can be read as a conditional statement, with $\mu(X|\eta, \alpha)$ being the *expected number of events in bin X, given the values of α and η*. We define the total expected yield

$$S(\eta, \alpha) = \sum_X \mu(X|\eta, \alpha) \tag{4.4}$$

The normalization is such that $S(\eta, \alpha)$ is the total number of expected events for the particular choice of physics parameters and systematics.

The neutrino part of the likelihood function is then given by the Poisson equation

$$P_\nu(\eta, \alpha) = \prod_X \frac{e^{-\mu(X)}\mu(X)^{n(X)}}{n(X)!} \tag{4.5}$$

where $n(X)$ is the distribution of measured events into the bins X. This turns out not to be the most efficient way of calculating the log-likelihood function, since most of the 61200 bins do not contain events (*i.e.* $n(X) = 0$ for those bins). Taking the

---

[1]This is not the standard definition of the log-likelihood function. The factor of -2 is used here for convenience, so that in the Gaussian limit $\mathcal{L} \to \chi^2$

logarithm, we find, up to an additive constant,

$$-2lnP_\nu = 2\sum_X \mu(X|\eta,\alpha) - 2\sum_X n(x)ln\ \mu(X|\eta,\alpha)\quad +\quad const.$$

$$= 2S(\eta,\alpha) - 2\sum_{m=1}^{N} ln\ \mu(X_m|\eta,\alpha)\quad +\quad const.$$

$$(4.6)$$

Here we have switched to a summation over individual *events*, with the index m labelling each event. There are a total of only N = 2928 events, and so we have greatly reduced the computational effort. Each event is expressed by a specific assignment to X, i.e. $X_m = \{T_m, R_m^3, ...\}$ and, for each event, we calculate the value of the number density model $\mu(X_m|\eta,\alpha)$.

Calibration data is studied to measure the values of instrumental parameters and backgrounds. Collectively, we refer to these measurements as $\boldsymbol{\alpha}_{cal}$, with error matrix $\boldsymbol{\sigma}_\alpha^2$. If our uncertainties are non-zero, the true values of the parameters $\boldsymbol{\alpha}$ may deviate from best-fit calibration values. In the case that the deviations from best fit are Gaussian distributed, we write

$$-2lnP_{cal}(\alpha) = (\boldsymbol{\alpha} - \boldsymbol{\alpha}_{cal})^T\boldsymbol{\sigma}_\alpha^{-2}(\boldsymbol{\alpha} - \boldsymbol{\alpha}_{cal})\quad +\quad const.\qquad(4.7)$$

The values of $\boldsymbol{\alpha}_{cal}$ and the diagonals of $\boldsymbol{\sigma}_\alpha^2$ are given in Tables 3.11 and 3.12. The constant in Eqn. 4.7 includes $ln(2\pi)$ terms, but these are unimportant here. Although we have assumed a Gaussian, the form of $P_{cal}(\alpha)$ can be completely general. A simple generalization would be to allow for asymmetric errors by using a skewed function instead of a Gaussian.

The total log-likelihood function is therefore, to within a constant

$$\mathcal{L} = 2S(\eta,\alpha) - 2\sum_{m=1}^{N} ln\ \mu(X_m|\eta,\alpha)$$

$$+ (\boldsymbol{\alpha} - \boldsymbol{\alpha}_{cal})^T\boldsymbol{\sigma}_\alpha^{-2}(\boldsymbol{\alpha} - \boldsymbol{\alpha}_{cal})$$

$$(4.8)$$

If desired, one could add terms to the likelihood function which include information from other experiments and/or solar models. This is done in Section 4.7.

4.1.1   Physics Models

We now consider the physics parameters η, which are specific to the physics model we are studying. Recall from Section 3.6 that the idealized model is given by $\mu_o(X|\eta)$, which is the same thing as μ, but with backgrounds set to zero and the instrumental parameters set to their best fit calibration values ($\alpha = \alpha_{cal}$). For this discussion, it will suffice to talk about μ_o. The reader should recall that it is constructed out of the PDFs $\rho(X|\eta)$ and expected number events $S(\eta)$ for each reaction.

$$\mu_o(X|\eta) = \phi_{tot} \times (S^{cc}\rho^{cc} + S^{es}\rho^{es} + S^{nc}\rho^{nc}) \tag{4.9}$$

where ϕ_{tot} is the flux of ^{8}B neutrinos, relative to the SSM. (Note that hep neutrinos are treated as a background.) We will be studying the following models, listed in order of increasing complexity.

- **Model 1. The Standard Model of Particles and Fields**

  The simplest model assumes that there are no particle physics processes that change the nature of the electron neutrinos after their production in the Sun. In this case, there is only a single physics parameter ϕ_{tot} (which is free to float). For the neutrino part of the model, we have

  $$\mu_o(X) = \phi_{tot} \times \{S^{cc}_{ssm}\rho^{cc}(X|ssm) + S^{es}_{ssm}\rho^{es}(X|ssm) + S^{nc}_{ssm}\rho^{nc}(X|ssm)\}$$
  $$\tag{4.10}$$

  where we have used the notation *ssm* to indicate that the physics parameters are fixed to describe the standard solar model. However, Model 1 is not quite the same as the Standard Solar Model, which also constrains the relative flux ϕ_{tot} by astrophysical arguments.

- **Model 2a. The Linear Flavor Change Model**

  The simplest extension of the above model is one that allows the flux of solar neutrinos to have two components $\phi_{tot} = \phi_e + \phi_{\mu\tau}$. Since SNO can not distinguish

between μ and τ neutrinos, we have defined $\phi_{\mu\tau} \equiv \phi_\mu + \phi_\tau$. The motivation for this model comes from neutrino oscillation, where the oscillation is described by the survival probability P_{ee}. If we assume that P_{ee} is independent of energy or zenith angle (which is a good approximation for many regions of MSW space) then we can construct our model as

$$
\begin{aligned}
\mu_o = \phi_{tot} \times \{ & P_{ee}S^{cc}_{ssm}\rho^{cc}(X|ssm) \\
& + (P_{ee} + \epsilon(1 - P_{ee}))S^{es}_{ssm}\rho^{es}(X|ssm) \\
& + S^{nc}_{ssm}\rho^{nc}(X|ssm) \}
\end{aligned}
\tag{4.11}
$$

where $\epsilon = 0.1559$ is the ratio of the ES cross section for $\nu_{\mu\tau}$ to the ES cross section for ν_e (averaged over T_{eff} with a threshold of 5.0 MeV). One can further simplify this model by changing to the linear parameters

$$
\phi_e = \phi_{tot} \times P_{ee} \qquad \phi_{\mu\tau} = \phi_{tot} \times (1 - P_{ee})
\tag{4.12}
$$

giving

$$
\begin{aligned}
\mu_o = \phi_e & \left\{ S^{cc}_{ssm}\rho^{cc}(X|ssm) + S^{es}_{ssm}\rho^{es}(X|ssm) + S^{nc}_{ssm}\rho^{nc}(X|ssm) \right\} \\
& + \phi_{\mu\tau} \left\{ \epsilon S^{es}_{ssm}\rho^{es}(X|ssm) + S^{nc}_{ssm}\rho^{nc}(X|ssm) \right\}
\end{aligned}
\tag{4.13}
$$

Our model now has one additional degree of freedom, with Model 1 being described in the limit $\phi_e \to \phi_{tot}$, $\phi_{\mu\tau} \to 0$. This allows for a null hypothesis test. If $\phi_{\mu\tau}$ is significantly different from zero, then the standard model of particles and fields is considered insufficient to describe the creation and propagation of solar neutrino. Somehow there is a conversion of electron neutrinos into μ or τ neutrinos.

- **Model 2b. Constrained Linear Day-Night Model**

  A simple modification to Model 2a is one where the ν_e flux is allowed to be different from day to night. We continue to assume that there are no observable spectral distortions for either day or night and simply extract separate flux

amplitudes for day and night. For convenience, we use the parameters ϕ_e and ϕ_{tot}. (This is simply a linear transformation of the pair $\phi_e, \phi_{\mu\tau}$.) During the day we require two free parameters ϕ_{eD}, ϕ_{tot}, and during the night ϕ_{eN}, ϕ_{tot}. The parameter ϕ_{tot} is common to both zenith bins. The motivation for this model is that there are large regions of MSW space which predict a significant day-night asymmetry without significant spectral distortions. For oscillation to active neutrinos, there can be no asymmetry in the total flux, so we have fixed ϕ_{tot} to be the same for day and night. We will define the asymmetry parameter

$$A_e = 2\frac{\phi_{eN} - \phi_{eD}}{\phi_{eN} + \phi_{eD}} \tag{4.14}$$

Measuring $A_e \neq 0$ would therefore be an indicator for MSW physics beyond that of simple flavor change.

- **Model 2c. Unconstrained Linear Day-Night Model**

  More general still, we might have a sterile neutrino component. In this case, the active neutrino flux need not be the same from day to night. This requires yet another free parameter, bringing the total to $\{\phi_{eD}, \phi_{eN}, \phi_{totD}, \phi_{totN}\}$. If desired, we could derive the results of Model 2b by adding a constraint $\phi_{totD} = \phi_{totN}$ to the results of Model 2c. By adding yet another constraint, $\phi_{eD} = \phi_{eN}$, we would re-derive the results of Model 2a.

- **Model 3. Two Active Neutrino MSW Model**

  Until now, we have assumed that there are no measurable spectral distortions. Relaxing this constraint, we consider the MSW oscillation model between two active neutrinos. In this case, there are 3 physics parameters $(\phi_{tot}, \Delta m^2, \tan^2\theta)$. We no longer approximate the survival probability as energy independent. The flux suppression previously described by $\phi_e \neq \phi_{tot}$ is now encoded in the model

Table 4.1: Various models considered for the likelihood analysis.

Model	parameters	assumptions
1	ϕ_{tot}	no particle physics affecting neutrinos
2a	ϕ_e, ϕ_μ	no spectral or zenith distortions
2b	$\phi_{eD}, \phi_{eN}, \phi_{totD}(=\phi_{totN})$	no spectral distortions, active only neutrinos
2c	$\phi_{eD}, \phi_{eN}, \phi_{\mu D}, \phi_{\mu N}$	no spectral distortions
3	$\phi_{tot}, \Delta m^2, \tan^2\theta$	active only neutrinos

via the survival probability $P_{ee}(\Delta m^2, \tan^2\theta)$.

$$\mu_o(X|\phi_{tot}, \Delta m^2, \tan^2\theta) = \phi_{tot} \times \{S^{cc}(\Delta m^2, \tan^2\theta)\rho^{cc}(X|\Delta m^2, \tan^2\theta)$$
$$+ S^{es}(\Delta m^2, \tan^2\theta)\rho^{es}(X|\Delta m^2, \tan^2\theta) \quad (4.15)$$
$$+ S^{nc}_{ssm}\rho^{nc}(X|ssm)\}$$

The model of the NC reaction is unchanged because the thermal neutrons carry no information about the neutrino spectrum and $A_{tot} = 0$ for this model. However, this model does have large regions of parameter space which predict a day-night dependence in the ν_e flux. The complication of this model comes from the fact that the parameters $\Delta m^2, \tan^2\theta$ are non-linear. These complications will be dealt with in Section 4.4.

We will use different techniques to extract the parameters for the various models. These techniques are explained in Appendix 1. To understand the uncertainty on the extracted parameters, the model is expanded to describe the systematics $\boldsymbol{\alpha}$. These parameters describe how the model deviates from its ideal form μ_o, due to a change in an instrumental parameter or the addition of a background. The details of this are discussed in Section 3.6 and Appendix A.1.

4.2 A Preliminary Null Hypothesis Test (Model 2a)

This section is largely drawn from [52]. Model 2a has two physics parameters ϕ_e and $\phi_{\mu\tau}$, which are extracted according to the techniques of Appendix A.2. We begin by fixing all of the systematic parameters (including background amplitudes) to their calibrated values α_{cal} and minimizing $\mathcal{L}$ with respect to ϕ_e and $\phi_{\mu\tau}$. This gives us the best fit values, with the second derivatives of $\mathcal{L}$ providing a statistical error matrix for the pair of parameters. The parameters ϕ_e and $\phi_{\mu\tau}$ are defined relative to the SSM. Here we multiply them by 5.05×10^6 to convert them to flux units.

$$\begin{pmatrix} \phi_e \\ \phi_{\mu\tau} \end{pmatrix}_{best\ fit} = \begin{pmatrix} 1.76 \\ 3.41 \end{pmatrix} \times 10^6 cm^{-2}s^{-1} \qquad \boldsymbol{\sigma}_\phi^2(stat) = \begin{pmatrix} 0.00292 & -0.01662 \\ -0.01662 & 0.20612 \end{pmatrix}$$

(4.16)

From this matrix, the square-root of the diagonals gives us the single parameter statistical variances σ_e and $\sigma_{\mu\tau}$, while $\frac{\boldsymbol{\sigma}_{e,\mu\tau}^2}{\sigma_e \sigma_{\mu\tau}} = -0.678$ gives the statistical correlation.

We wish to use the calibration data to determine how the results vary with the systematics. One by one, we perturb each systematic parameter $\alpha[k]$ by an amount $\pm\sigma_\alpha[k]$. This allows us to repeat the extraction of ϕ_e and $\phi_{\mu\tau}$. The amount by which these physics parameters are shifted defines the systematic uncertainty on them. These perturbations are shown in Table 4.2 and are combined to give the total systematic error. The final results are

$$\phi_e = 1.76 \pm 0.05(stat.)^{+0.09}_{-0.09}(syst.) \times 10^6 cm^{-2}s^{-1}$$

$$\phi_{\mu\tau} = 3.41 \pm 0.45(stat.)^{+0.48}_{-0.45}(syst.) \times 10^6 cm^{-2}s^{-1}$$

(4.17)

These results are represented graphically in Fig. 4.2 as an ellipse in the $\phi_e, \phi_{\mu\tau}$ plane.

By combining the statistical and systematic errors in quadrature, we see that

$$\frac{\phi_{\mu\tau}}{\sqrt{\sigma_{\mu\tau}^2(stat.) + \sigma_{\mu\tau}^2(syst.)}} = 5.3$$

(4.18)

We therefore reject the null hypothesis (Model 1) with a significance of 5.3σ. This is the result reported in [52].

Table 4.2: The effect of time averaged systematics on the flux extraction. The perturbations are relative to the SSM, so one must multiply by 5.05×10^6 to get absolute flux units. The cross section uncertainty, discussed in [52], is largely correlated between ϕ_e and ϕ_{tot} and so does not contribute to the significance of Equation 4.18.

instrumental parameter	α_{av}	$\delta\phi_e$	$\delta\phi_{\mu\tau}$
energy non-linearity	$\pm$ 0.23%	$\mp$ 0.0012	$\pm$ 0.0132
energy scale	$\pm$ 1.21%	-0.0152,+0.0154	+0.0683,-0.0725
radial shift	$\pm$ 1%	-0.0098,+0.0096	-0.0089,+0.0147
radial resolution	$\pm$ 2.0 cm	-0.0000,+0.0000	-0.0056,+0.0056
energy resolution	$^{+4.5}_{-0.0}$%	+0.0000,-0.0012	-0.0000,+0.0286
cut acceptance	$^{+0.4}_{-0.2}$%	+0.0013,-0.0007	+0.0029,-0.0017
neutron capture	$\pm$ 3.68 %	-0.0000,+0.0000	-0.0408,+0.0425
internal neutrons	44 $^{+8}_{-9}$ events	+0.0001,-0.0001	-0.0145,+0.0159
external neutrons	27 $^{+8}_{-8}$ events	-0.0000,+0.0001	-0.0112+0.0106
D2O β-γ	20 $^{+13}_{-6}$ events	+0.0010,-0.0004	-0.0264,+0.0118
H2O+AV β-γ	9 $^{+5}_{-7}$ events	+0.0001,-0.0000	-0.0036,+0.0090
PMT β-γ	16 $^{+11}_{-8}$ events	+0.0006,-0.0006	-0.0213,+0.0158
Total Experimental		$^{+0.092}_{-0.092}$	$^{+0.442}_{-0.437}$
Cross Section	L_{1A}	$\pm$ 1.8%	$\pm$ 1.4%

4.2.1   A Look Ahead

Equation 4.18 assumes that the parameter $\phi_{\mu\tau}$ is Gaussian distributed, and this may be slightly incorrect. A more general null-hypothesis test is the likelihood-ratio test, described in Section 4.5. In that section we will also add additional information, allowing the neutrino data to further constrain the size of our systematic errors. This will be seen to significantly improve the result shown here.
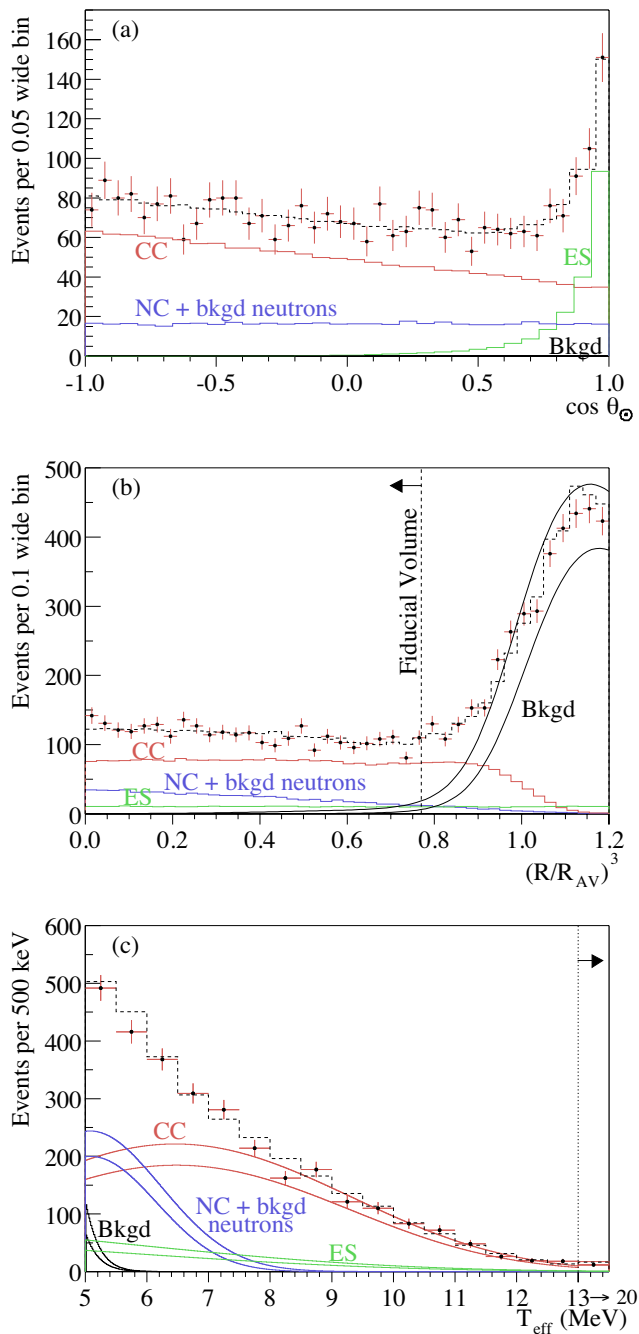
Figure 4.1: Contributions to the fit to SNO data from CC, ES, and NC signals, as well as backgrounds. While the fit was made to a 3-dimensional distribution, we have shown the projection onto three separate axes. For each signal, the PDF shapes are those of the SSM. The error range for each signal is therefore due only to uncertainties in the amplitudes (ϕ_e and $\phi_{\mu\tau}$ and backgrounds). Figures created by Mark Boulay, Aksel Hallin, Scott Oser, and Vadim Rusu.
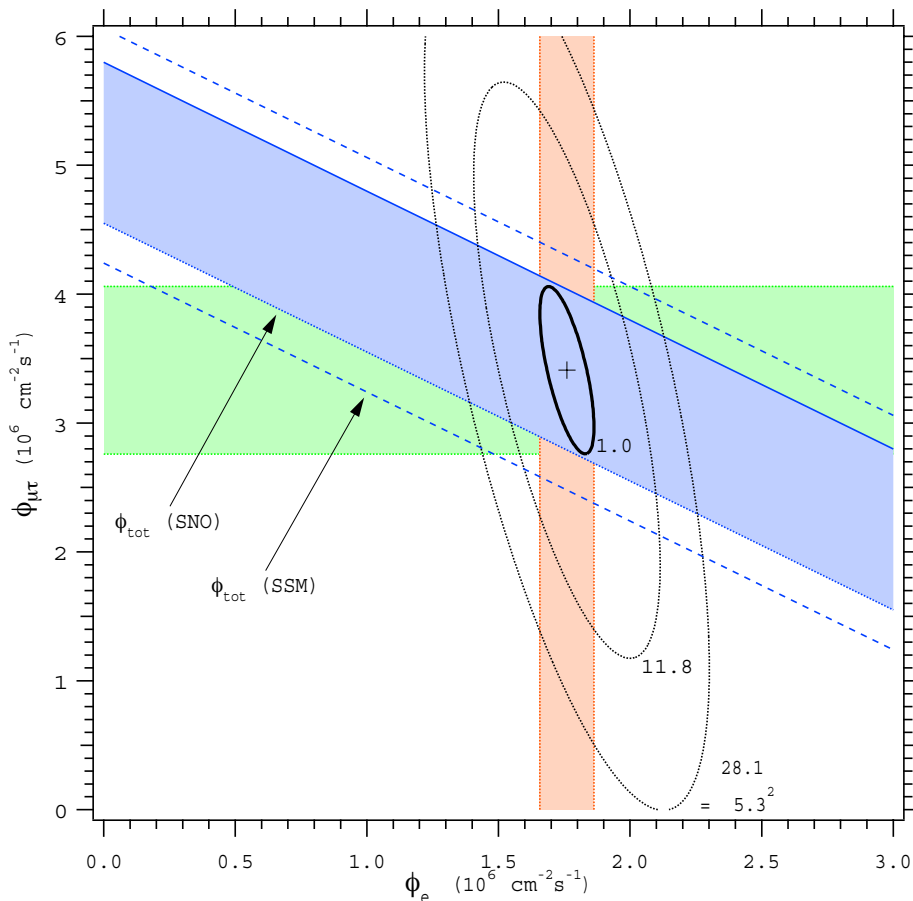
Figure 4.2: Graphical representation of extracted fluxes. The ellipses show lines of constant $\Delta\mathcal{L}$ from the best fit solution. The $\Delta\mathcal{L} = 1$ ellipse is appropriate for defining the 1σ error on any one parameter ϕ_e **or** $\phi_{\mu\tau}$ (recall that $\mathcal{L}$ is defined to be the same thing as χ^2 in the Gaussian limit). These error ranges are also shown as bands (red for ϕ_e and green for $\phi_{\mu\tau}$). The blue band shows the 1σ error on $\phi_{tot} = \phi_e + \phi_{\mu\tau}$. The $\Delta\mathcal{L} = 11.8$ contour encloses the 99.73% allowed region for the **pair** of parameters $(\phi_e, \phi_{\mu\tau})$. The $\Delta\mathcal{L} = 28.1$ contour just touches the axis $\phi_{\mu\tau} = 0$. This tells us to what extent the null hypothesis (Model 1) is allowed. Because the alternate hypothesis has one additional degree of freedom $\phi_{\mu\tau}$, $\Delta\mathcal{L} = 28.1$ is equivalent to a 5.3σ rejection of Model 1.

Note: This figure was constructed only approximately. The 1σ errors and covariance were derived for the two physics parameters. The likelihood function was then approximated to be a 2-dimensional Gaussian, defined by the measured errors and covariance. This Gaussian likelihood was than used to generate the contours.

This is a variant of a figure created by Andrew Hime.

4.3   Measuring the Day-Night Asymmetry (Models 2b and 2c)

4.3.1 $\mathcal{A}_{active}$ floating (Model 2c)

We now repeat the flux extraction for the 4 parameter linear model (with parameters $\phi_{eD}, \phi_{eN}, \phi_{totD}, \phi_{totN}$). Once this extraction has been performed, we can choose to change basis to

$$\phi_e = \frac{t_N \phi_{eN} + t_D \phi_{eD}}{t_N + t_D} \qquad \phi_{\mu\tau} = \frac{t_N(\phi_{totN} - \phi_{eN}) + t_D(\phi_{totD} - \phi_{eD})}{t_N + t_D}$$

(4.19)

$$A_e = 2\frac{\phi_{eN} - \phi_{eD}}{\phi_{eN} + \phi_{eD}} \qquad A_{tot} = 2\frac{\phi_{totN} - \phi_{totD}}{\phi_{totN} + \phi_{totD}}$$

Strictly speaking, the last two variables are no longer Gaussian distributed, since they are a non-linear function of Gaussian distributed variables. However, in practice, their non-Gaussian behavior is negligible. Since we have already studied the first two variables, we will focus our attention on the latter two. These are the asymmetry parameters. If A_e is significantly different from zero, we will conclude that there is some matter enhanced oscillation occurring in the Earth. If A_{tot} is significantly different from zero, we will conclude that the matter enhanced oscillation in the Earth involves a sterile component.

The systematics propagate as shown in Table 4.4 and the resulting asymmetries are

$$A_e = 12.8 \pm 6.2(stat.) \pm 0.9(syst.)\%$$
$$A_{tot} = -24.2 \pm 16.1(stat.)^{+2.2}_{-2.6}(syst.)\%$$
$$correlation = -0.602$$

(4.20)

These results are represented graphically in the left hand panel of Fig. 4.3. By studying the χ^2 distribution for $\nu = 2$ degrees of freedom (Appendix A.5, we note that the pair of day night asymmetries are different from (0,0) at the 88.8% confidence level (1.59σ). The single parameter A_{tot}, independent of A_e, is different from zero

at the 86.6% confidence level (1.50σ). These probabilities are considered not to be statistically significant.

4.3.2 $\mathcal{A}_{active}$ fixed (Model 2b)

The day-night results of the previous section are statistically weak. In particular, we see no evidence for an asymmetry in the total flux of active neutrinos. In addition, theoretical models for the oscillation of electron neutrinos into other active flavors predict $A_{tot} = 0$. It is therefore reasonable to constrain our experimental results to give $A_{tot} = 0$. This generates a new model, with only three parameters ($\phi_{eD}, \phi_{eN}, \phi_{tot}$). We can either perform the signal extraction with just these parameters, or else take the four measurements from the previous section and constrain them. Either way, we get the same result.

$$A_e = 7.0 \pm 4.9(stat.) \pm 0.9(syst.)\% \tag{4.21}$$

Table 4.3: Various questions one can ask about the day night asymmetry.

Question	d.o.f.	$\Delta\mathcal{L}$	confidence level	significance
Is there an asymmetry of any kind?	2	4.37	88.8%	1.59σ
Is there an asymmetry in the total neutrino flux?	1	2.26	86.6%	1.50σ
Do we see an asymmetry for ν_e (with A_{tot} constrained to zero) ?	1	2.00	84.3%	1.41σ

Table 4.4: Summary of how differential systematics affect the day-night asymmetries. A_e and A_{tot} are typically expressed as percentages themselves, so that δA_e and δA_{tot} are also percentages. A number of systematics are evaluated differently than those of [53]. In particular, the diurnal energy scale and resolution are much more strongly constrained here. In addition, the uncertainty due to finite Monte Carlo statistics is introduced here for the first time. The number of D_2O backgrounds events is important because it is the largest contaminating asymmetry, which is incorrectly subtracted if we have incorrectly estimated the number of events.

Systematic	α_{dif}	δA_e (%)	δA_{tot} (%)
diff. energy scale (long term)	$\pm 0.14\%$	-0.34, +0.36	+0.12, -0.40
diff. energy scale (diurnal)	$\pm 0.015\%$	-0.06, +0.06	+0.07, -0.02
diff. vertex shift	$\pm 0.20\%$	-0.44, +0.50	-0.72, +0.55
diff. vertex resolution	± 1.13 cm	-0.15, +0.15	+0.47, -0.30
diff. energy resolution	$\pm 0.05\%$	-0.00, +0.00	+0.00, -0.00
diff. sacrifice	$\pm 0.30\%$	+0.30, -0.30	+0.30, -0.30
asymmetry of D_2O backgrounds	$31\pm4\%$	+0.04, -0.04	-0.65, +0.67
asymmetry of H_2O backgrounds	$6.9\pm0.7\%$	+0.07, -0.03	-1.49, +0.63
no. of D_2O backgrounds events	72.1 +12.7	-0.01, +0.02	-0.41, +0.40
finite MC statistics	$\sqrt{N_{MC}}$	± 0.55	± 1.78
Total		**+ 0.89, - 0.85**	**+2.19,-2.61**
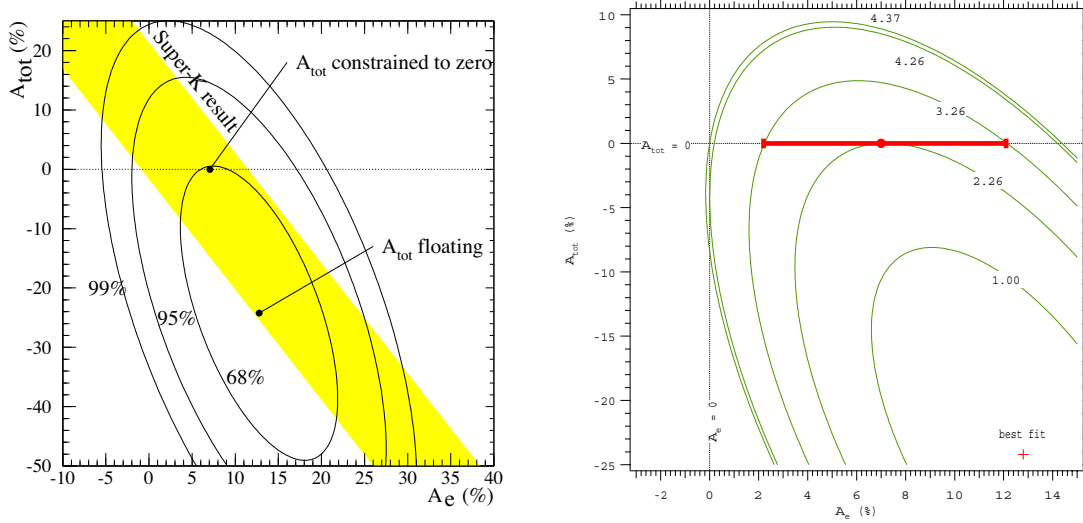
Figure 4.3: Graphical representation of extracted asymmetries. The left hand panel, provided by Scott Oser, shows joint confidence ellipses for the **pair** of extracted parameters A_e, A_{tot}. These contours are not appropriate for interpreting the uncertainty on any single parameter. We also show the 68% confidence region provided by the SK experiment (yellow band). Because the ES signal of SK is not separated into charged and neutral current components, it can only constrain the allowed region in one direction.

The right hand panel shows some specific contours. The $\Delta\mathcal{L} = 1$ contour is that appropriate for determining the variances of the individual parameters. (Recall that $\mathcal{L} \to \chi^2$ in the Gaussian limit.) On the other hand, the $\Delta\mathcal{L} = 4.37$ contour just intersects the point (0,0). This tells us that the pair of parameters are different from zero at the 88.8% confidence level (1.59σ)

The $\Delta\mathcal{L} = 2.26$ contour just touches the $A_{tot} = 0$ axis. Since Model 2c has one fewer parameters than Model 2b, $\Delta\mathcal{L} = 2.26$ is equivalent to a confidence level of 86.6% (1.50σ) for rejecting the hypothesis that $A_{tot} = 0$. This is a weak result and, given that many theoretical models do not allow an asymmetry in the total active flux, we constrain A_{tot} to zero. By increasing $\mathcal{L}$ by an additional $+1$, we find the single parameter variance for A_e with A_{tot} constrained to be zero (red bar). By instead increasing $\mathcal{L}$ by $+2$ (to 4.26), we just touch the $A_e = 0$ axis. This tells us that (with A_{tot} constrained to zero) we have seen evidence for a non-zero A_e at the $\sqrt{2.00} = 1.41\sigma$ level.

4.3.3   Combining with SK Day-Night results

The Super-Kamiokande experiment has measured the day-night asymmetry with the ES reaction. Assuming that there is no NC asymmetry, their measurement is diluted by the NC component of the ES reaction. One can use the SNO data to remove this dilution. Using the SNO-only measurement of ϕ_{total} from Section 4.3.2, we can combine with the SK ES measurements to get (see Appendix A.3)

$$A_e^{SK} = A_{ES}^{SK} \left(1 - \frac{2\epsilon \; \phi_{total}^{SNO}}{\phi_{ES,D}^{SK} + \phi_{ES,N}^{SK}} \right)^{-1} \tag{4.22}$$

From Section 4.2, we have $\phi_{total}^{SNO} = 5.17 \pm 0.42(stat.) \times 10^6$ and, from SK[2] we have $\phi_{ES,N}^{SK} = 2.36 \pm 0.04(stat.) \pm_{-0.07}^{+0.08}(sys.)$ and $\phi_{ES,N}^{SK} = 2.28 \pm 0.04(stat.) \pm_{-0.07}^{+0.08}(sys.)$. Thus we get

$$A_e^{SK} = 5.3 \pm 3.7_{-1.7}^{+2.0}\% \tag{4.23}$$

Slightly different results are obtained for different choices of ϕ_{total}^{SNO}. Here we have used the measurement with $A_{total} = 0$, so we can make a comparison to the final SNO asymmetry. This result corresponds to the intersection of the yellow band in Figure 4.3 with the $A_{tot} = 0$ axis.

The two results A_e^{SK} and A_e^{SNO} are uncorrelated. This is because the parameters $\phi_{e,N}^{SNO}$ and $\phi_{e,D}^{SNO}$ were not involved in the derivation of Equation 4.22. We can therefore combine them in quadrature.

$$A_e^{SK+SNO} = 6.0\% \pm 3.2\% \tag{4.24}$$

This is 1.9σ different from zero (94% confidence level). This is suggestive, but still no smoking gun, for a day-night asymmetry for electron neutrinos.

---

[2]For the SK ES systematic errors, we choose to use a correlation $\rho(\phi_{D,ES}^{SK}, \phi_{N,ES}^{SK}) = +0.93$. This correlation reproduces the systematic errors for A_{ES}^{SK}. The statistical errors are uncorrelated between day and night bins.

4.4 MSW Contour Analysis (Model 3)

We now examine the non-linear Model 3, with the intention of drawing contours in the MSW plane. There are three physics parameters $\boldsymbol{\eta} = \{\phi_{tot}, \Delta m^2, \tan^2\theta\}$ and a set of systematics $\boldsymbol{\alpha}$, including both instrumental parameters and background amplitudes. The treatment of systematics, used in Sections 4.2 and 4.3, will become difficult to implement here. In that section we calculated flux values such as ϕ_e and $\phi_{\mu\tau}$. We then perturbed the analysis by a discrete amount $\Delta\alpha = \sigma_\alpha$ for each systematic, to derive a discrete perturbation $(\delta\phi_e, \delta\phi_{\mu\tau})$. If we were to repeat that procedure here, we would generate a large number of alternate MSW contours, with no method of combining them. Instead we must treat each systematic α as a continuous parameter and so must consider the full log-likelihood function $\mathcal{L}(\eta, \alpha)$. Our problem now comes down to the following.

We pick a confidence level, say 99%. For each MSW point $\Delta m^2, \tan^2\theta$, we ask if there is any value of ϕ_{tot} and the systematics α which would cause this point to be allowed with 99% confidence. If so, we include this point within the 99% contour.

The practical implementation of this is that we must *minimize $\mathcal{L}(\eta, \alpha)$* with respect to α and ϕ_{tot}. The approach used for performing this minimization is given in Appendices A.1 and A.4, with only a brief outline given below. Because we are using the full log-likelihood function, we are allowing the neutrino data to further constrain the possible values of the systematics parameters. For example, the measurement of the end point of the ^{8}B neutrino spectrum provides a strong constraint on this size of the energy scale uncertainty. This approach of *fitting for systematics* has been used in high energy physics, cosmology, and economics. The application of this approach to MSW analysis was introduced in [54], although it appears that we independently stumbled across it[3].

---

[3]The idea of using the ^{8}B end point to fit for the energy scale was proposed by Hamish Robertson and Karsten Heeger. This was later expanded to include all systematics by Joe Formaggio, Scott Oser and Miles Smith.

To a very good approximation, because $\boldsymbol{\alpha}$ is small, we can expand the model as a linear function of the systematics. This provides a continuous parametrization of $\mathcal{L}$ with respect to α.

$$\mu(X|\eta, \alpha) = \mu_o \times \left[1 + \boldsymbol{\beta}^T(\boldsymbol{\alpha} - \boldsymbol{\alpha_o})\right] \tag{4.25}$$

where $\mu_o(X|\eta)$ is independent of α and

$$\boldsymbol{\beta}(X|\eta) = \frac{1}{\mu_o} \left.\frac{\partial \mu}{\partial \boldsymbol{\alpha}^T}\right|_{\boldsymbol{\alpha}=\boldsymbol{\alpha_o}} \tag{4.26}$$

For instrumental parameters, we set $\alpha_o = \alpha_{cal}$, so that μ_o (the model we expand around) includes our best estimate of the detector response. However, for background amplitudes, we set $\alpha_o = 0$, so that μ_o also describes a detector with zero backgrounds.

The next step is, for each point of the MSW plane, to minimize $\mathcal{L}$ with respect to ϕ_{tot} and the systematics $\boldsymbol{\alpha}$. To facilitate this, we split ϕ_{tot} up into two parts $\phi_{tot} = \phi_o + \Delta\phi$, where ϕ_o is the flux that one would infer if the model μ_o were correct. We retain ϕ_o as one of the physics parameters $\boldsymbol{\eta}$. However, we define a new parameter $\alpha[0] = \frac{\Delta\phi}{\phi_o}$ and add this to the list of perturbative parameters in Equation 4.25[4]. The log-likelihood function now naturally breaks into two parts.

$$\mathcal{L}(\eta, \alpha) = \mathcal{L}_o(\eta) + \mathcal{L}'(\eta, \alpha) \tag{4.27}$$

There are no systematics or backgrounds contributing to the definition of $\mathcal{L}_o$ and it is minimized by ϕ_o (which has an analytic solution). This intermediate solution, is shown in Fig. 4.4. The remaining term $\mathcal{L}'$ is expanded to 2nd order[5] in $\boldsymbol{\alpha}$. We minimize with respect to $\boldsymbol{\alpha}$, including the newly defined $\alpha[0] = \frac{\Delta\phi}{\phi_o}$. The minimized solutions of $\mathcal{L}_o$ and $\mathcal{L}'$, added together, provide the definition of the final MSW contours. This is shown in Fig. 4.5.

---

[4]The hep flux, although not strictly a background, is also treated as a perturbative parameter.

[5]A 2nd order expansion is necessary for stability, even though α is small
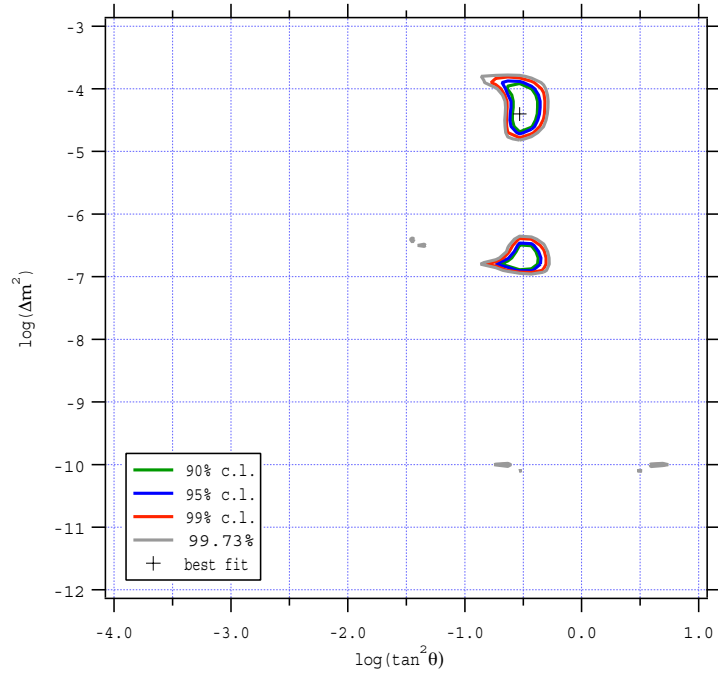
Figure 4.4: Contours for $\mathcal{L}_o$, with nominal values of the instrumental parameters and backgrounds set to zero. This is not the final solution to the problem of drawing MSW contours, only an intermediate step. See figure 4.5 for the final set of contours.
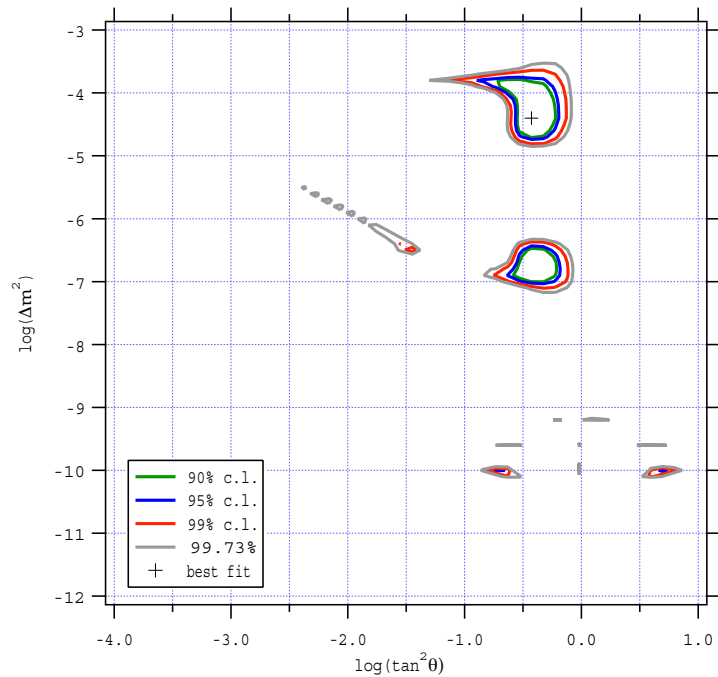
Figure 4.5: Contours for $\mathcal{L} = \mathcal{L}_o + \mathcal{L}'$, with systematics and backgrounds incorporated and allowed to float.

In addition to defining MSW contours, we have used the neutrino data to further constrain the values of the systematics parameters. The results of this are shown in Table 4.5. We initially assumed that the systematic parameters were uncorrelated (an approximation that is discussed in Section 5.1). The process of allowing neutrino data to further constrain the parameters induces some correlations, although these are not shown in the table. (We would need to show a 15×15 matrix.) The actual size of the uncertainties has also changed. For example, we see that the error range for the energy scale is reduced from 1.21% to 0.79%. If we kept adding neutrino data, we would continue to constrain this parameter, limited only by statistics. On the other hand, the uncertainty on the sacrifice is unchanged by the addition of more data (because, in this case, the sacrifice is completely correlated to the flux ϕ_{tot}).

4.4.1 Check of Approximations

A natural question to ask is whether we have over-approximated by making an expansion in α. This was done to make the problem analytic, with the large number of parameters making a numerical solution unattractive. However, a full numerical solution is relatively fast if we restrict ourselves to one or two systematics, while keeping the others fixed at zero. This was done for each systematic separately and compared to the corresponding approximate analysis. Essentially no changes were observed between the approximate and full treatment. The only thing that was not checked was the linearization of the instrumental parameters. However, the linear and full versions of the model were compared directly and seen to be essentially identical.

Theoretical Systematics

We have omitted the theoretical systematics for the intrinsic neutrino spectrum, cross sections, and earth-density model. The implications of this are discussed in Section 5.1 and in Appendix A.7.

Table 4.5: Systematics, before and after fitting. We have only shown fitted values for $\Delta m^2 = 10^{-4.3}$, $\tan^2 \theta = 10^{-0.43}$. The difference between the errors in the two columns is a measure of how much information we gain by allowing the neutrino data to serve as an additional constraint on the size of systematics. For this MSW point, the solution of $\mathcal{L}_o$ gives $\phi_o = 5.94 \times 10^6$, although remember that this is calculated by ignoring backgrounds and systematics. The final calculation is given by $\phi = \phi_o \times (1 + \alpha[0]) = 5.55 \pm 0.20 \times 10^6$. Theoretical systematics have not been considered at this stage (see Section 5.1 for a discussion).

parameter $\alpha[k]$	initial value assigned to χ^2_{cal}	fitted value (shown here for best fit $\Delta m^2, \tan^2 \theta$)
0. $\alpha[0] = \frac{\Delta\phi}{\phi_o}$	$0 \pm \infty$	-0.0651 ± 0.0334
1. energy non-linearity	0 ± 0.0023	-0.0001 ± 0.0023
2. energy-scale	0 ± 0.0121	0.0056 ± 0.0079
3. radial-shift	0 ± 0.0100	-0.0033 ± 0.0084
4. radial-resolution	0 ± 2.0 cm	0.99 ± 1.59 cm
5. energy-resolution	0 ± 0.0450	-0.0214 ± 0.0300
6. diff. energy-scale	0 ± 0.0014	$3 \times 10^{-5} \pm 0.0014$
7. diff. radial-shift	0 ± 0.0020	0.0003 ± 0.0020
8. sacrifice	0 ± 0.0030	0.0000 ± 0.0030
9. neutron-capture	0 ± 0.0368	-0.0084 ± 0.0348
10. internal neutrons	51.70 ± 9.00	50.98 ± 8.94
11. external neutrons	27.00 ± 8.00	27.10 ± 7.87
12. D2O β-γ	20.40 ± 9.00	19.71 ± 8.62
13. H2O+AV β-γ	9.10 ± 6.00	4.10 ± 4.35
14. PMT β-γ	16.00 ± 10.00	14.49 ± 9.43
15. ϕ_{hep}	1 ± 0	1 ± 0

4.5 Rethinking Hypothesis Testing

4.5.1 Revisiting our Null Hypothesis Test

We now reconsider Model 2a, which we previously studied in Section 4.2. In that section we did not allow the neutrino data to provide any additional information about the systematic parameters. We now lift that constraint and see that we get a marked improvement in the rejection of the null hypothesis (Model 1).

For a later comparison, we describe Model 2a in terms of the two parameters ϕ_{tot} and P_{ee}, the latter being the survival probability (assumed for Model 2a to be energy and zenith angle independent). We use the same methods as those described in Section 4.4, except that P_{ee} is now a single free parameter, neither dependent on $\Delta m^2, \tan^2 \theta$, nor on energy or zenith angle. We then extract the flux ϕ_{tot} for each value of P_{ee}, producing the blue curve shown in Fig. 4.6. The minima of $\mathcal{L}$ with respect to P_{ee} is compared to the null hypothesis $P_{ee} = 1$. The *likelihood ratio test* [55] tells us that the test statistic $\Delta \mathcal{L} = \mathcal{L}(P_{ee} = 1) - \mathcal{L}(best\ fit)$ provides a measure of how preferred the more general model is over the null hypothesis. We see that the difference between the best fit for Model 2a and the model at $P_{ee} = 1$ is $\Delta \mathcal{L} = 54.313$. For a comparison of two models, where one has an additional degree of freedom over the other (in this case P_{ee}), this is equivalent to a significance of 7.37σ.

Table 4.6: Three null hypothesis tests. The significance tells us to what degree we reject the null hypothesis in favor of the alternate hypothesis.

null hypothesis	alternate hypothesis	$\Delta \mathcal{L} =$ $\mathcal{L}_{min}(null) - \mathcal{L}_{min}(alt)$	additional d.o.f.'s	significance
Model 1	Model 2a	54.313	1	7.37σ
Model 1	Model 3	56.414	2	7.21σ
Model 2a	Model 3	2.102	1	1.45σ
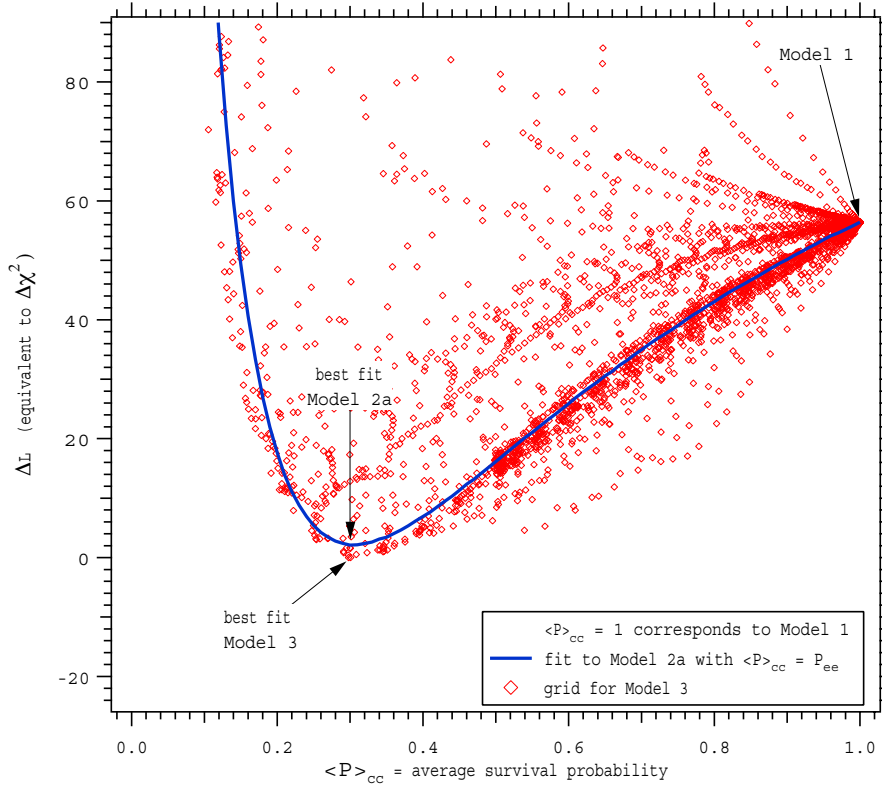
Figure 4.6: Comparison of three models fitted to the same data set. There are other parameters allowed to float in this fit but not shown. For model 3, the test is done over a grid in $\Delta m^2, \tan^2 \theta$, and so appears as a scatter plot. The best fit of model 3 is used as the reference point for calculating $\delta \mathcal{L}$.

We note the improved rejection of hypothesis 1, compared to the simple treatment of Section 4.2. There are two significant changes between Section 4.2 (where we calculated 5.3σ) and the new analysis (7.4σ).

• We have allowed the neutrino data to further constrain the possible values of the systematics.

• We used the likelihood ratio test, which is symmetric with respect to the two hypotheses and makes no assumptions about how the additional parameter $\phi_{\mu\tau}$ is distributed. In Section 4.2, $\phi_{\mu\tau}$ was assumed Gaussian distributed.

4.5.2   Some New Hypothesis Tests

We shall now consider some additional hypothesis tests. The full MSW model has two additional degrees of freedom over the null hypothesis (Model 1). We can compare the fit to these models, finding a difference $\Delta\mathcal{L} = 56.414$. However, because there are two additional degrees of freedom, the rejection of the null hypothesis is made with a significance of only 7.21σ (see appendix A.5). We see that the linear flavor change model is slightly more powerful in rejecting the null hypothesis.

We now switch to a new null hypothesis test, comparing Models 3 and 2a. Model 2a has two physics parameters (ϕ_{tot} and P_{ee}) and Model 3 has three (ϕ_{tot}, Δm^2, $\tan^2\theta$). We create a correspondence between the models by changing the basis for Model 3 $\{\Delta m^2,\ \tan^2\theta\} \to \{< P >_{cc}, \zeta\}$. Here $< P >_{cc}$ is the average value of the survival probability for the CC reaction[6], defined in Fig. 1.6. For Model 2a, $< P >_{cc}$ and P_{ee} are identical. The second parameter ζ is redundant when comparing the models and there are a number of ways to construct it so that Model 3 reduces to Model 2a as $\zeta \to 0$. Figure 4.6 shows the comparison of the two models. Because Model 3 is defined on a grid, it is shown as a scatter plot. For Model 2a, P_{ee} is a non-linear parameter, hence the non-quadratic shape of $\delta\mathcal{L}$. A symmetric figure is obtained if we plot against *e.g.* $\phi_{\mu\tau} = \phi_{tot}(1 - P_{ee})$, although the conclusions are identical. We note that the two models converge as $P_{ee} \to 1$, where there is a high density of points for Model 3. This is because the lower left quadrant of the MSW plane describes only very weak oscillation. In Table 4.6, we see that Model 3 is preferred over Model 2a at just 1.45σ. This is telling us that there is a slight preference for a model which, in addition to flavor change, allows for distortions in the day and night spectra.

---

[6]Actually, there are a number of choices we could have made for the correspondence between the models. The above may not be the most ideal choice but is expected to be close to optimal.
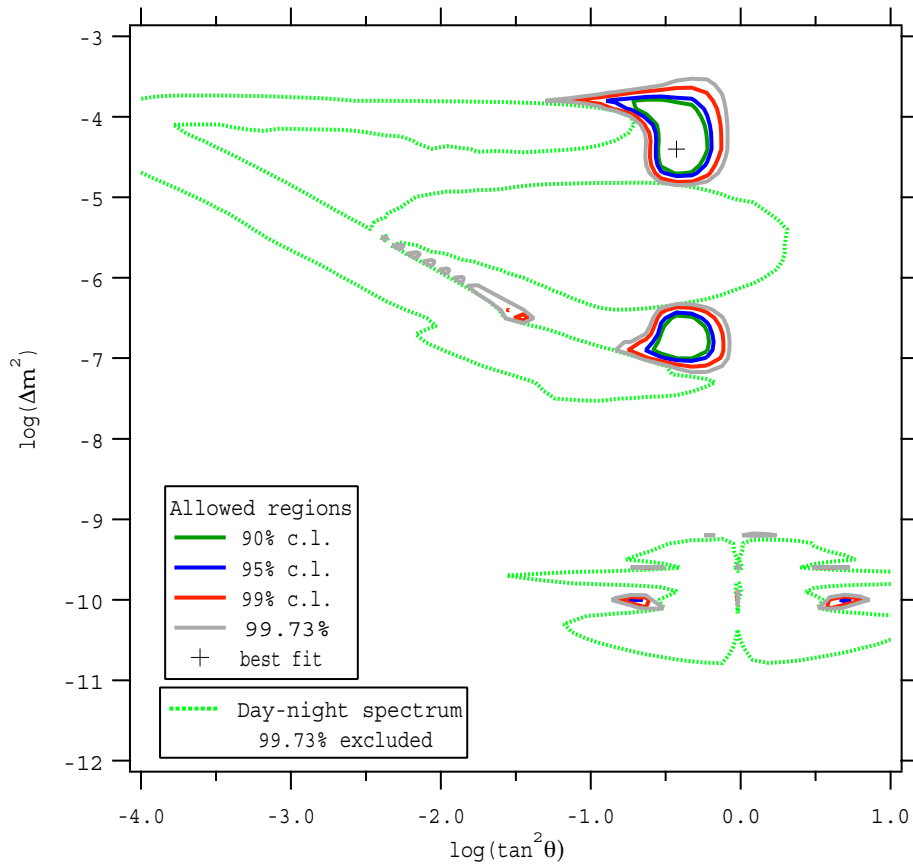
Figure 4.7: 99.73% excluded region from SNO day-night and spectral shape. This region is independent of information regarding the average survival probability.

4.6 Exclusion Region from Day-Night and Spectral Shape

We saw in the last section that the addition of day-night asymmetry and spectral distortions, as described by two neutrino MSW oscillations, is only weakly favored over a simple flavor change model. However, we know that there are large regions of the MSW plane which predict significant spectral distortions and day-night asymmetry (see Figures 1.7 and 4.3). This means that the day-night and spectral shape, independent of the flavor change component of the model, must be strongly excluding these regions.

For each $\Delta m^2, \tan^2 \theta$, we ask if Model 3 is a much worse fit than Model 2a. To do this we calculate $< P >_{cc}$ for Model 3 and compare this to Model 2a, evaluated at $P_{ee} = < P >_{cc}$. Both ϕ_{tot} and P_{ee} are free parameters in the comparison, so we have increased the number of degrees of freedom by one in going from Model 2a to 3. The 99.73% exclusion region, due to day-night asymmetry and spectral shape information, therefore corresponds to $\delta \mathcal{L} > (3\sigma)^2 = 9$. This excluded region is shown as a dashed green line in Figure 4.7, where we again show the allowed regions for comparison. The 99.73% allowed region is *not* the complement of our excluded region because the former includes information about the average survival probability P_{ee} (equivalently the ratio ϕ_e/ϕ_{tot}). The exclusion region discussed here is independent of the average survival probability.

4.7 Combining With Other Experimental Data

We wish to further constrain the MSW contours by adding data from other experiments. To do this, we add two terms terms to the likelihood function.

$$\mathcal{L}_{total} = \mathcal{L}_{SNO} + \chi^2_{other\ exps.} + \chi^2_{SSM} \qquad (4.28)$$

The other experiments typically have bins with sufficient statistics, so that we can use a χ^2 measure for them. We also introduce a term χ^2_{SSM} which constrains the pp,

pep, and ^{7}Be fluxes (but not the ^{8}B flux) using the SSM. These fluxes have a much more robust prediction from the SSM.

Prior to the analysis described in Section 4.4, the SNO collaboration pursued a much simpler approach. The simpler analysis performed a χ^2 fit to the day and night energy distributions. This allows one to circumvent the need (and advantages) of having the neutrino data to constrain systematic parameters. It is seen in Appendix A.6 that the energy-only analysis produces very similar contours to Fig. 4.5, although slightly more conservative. Also in Appendix A.6, we compare both analyses to the published SNO contours of [53]. It is argued that the published analysis includes a crude approximation that makes it unnecessarily conservative.

In Fig. 4.9, we have combined data from other experiments with the (unpublished) energy-only SNO analysis. This involves a simultaneous χ^2 fit to the SNO day and night energy histograms, the SK day and night energy histograms, the measured event rate for the Gallium and Chlorine experiments, and the predicted pp, pep and ^{7}Be fluxes. Only a single region survives, as seen in Fig. 4.9. For interest, we have replaced the grid with the contours of constant $<P>_{cc}$ and A_e.

Note: The contours presented here are considerably smaller than those of [1]. The differences between the two analyses are discussed in Appendix A.7.
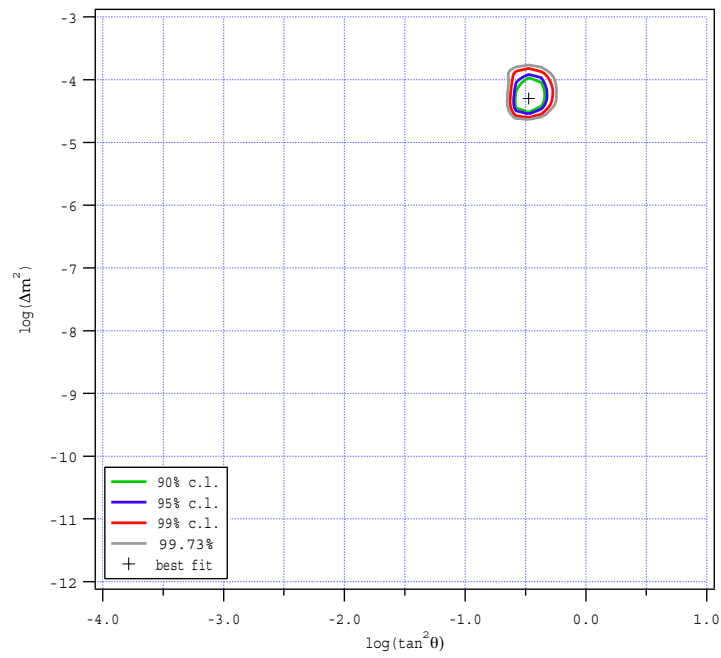
Figure 4.8: Result of a combined fit of SNO day and night spectra, SK day and night spectra, and the event rates of the Gallium and Chlorine experiments.
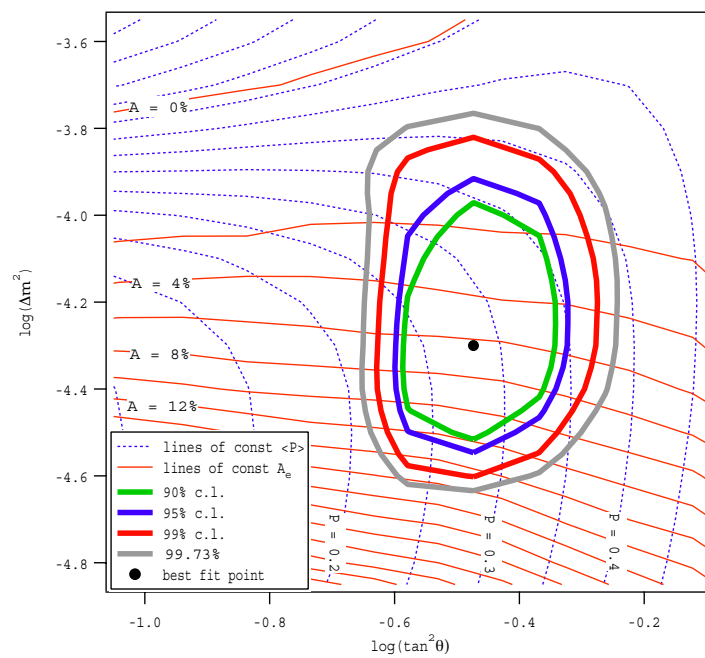
Figure 4.9: A closer look at the combined analysis, overlaid with lines of constant A_e and $< P >_{cc}$.

Chapter 5

FUTURE WORK

5.1 Refinement of MSW Analysis

5.1.1 Theoretical Systematics

As pointed out in Section 4.4.1, there are some systematics neglected in our MSW analysis.

- *Uncertainty in the ^8B neutrino spectrum*

The neutrino spectrum used in our analysis was obtained from a fit to experimental data and reported in [44]. The best-fit shape for this spectrum and its 1σ errors $(\lambda_o(E_\nu) \pm \delta\lambda(E_\nu))$ are available from [56]. A simple way to include the uncertainty in the spectrum is to assume that there is a single dominant systematic α. In this case, one can write the spectrum as

$$\lambda(E_\nu) = \lambda_o(E_\nu) + \alpha \times \delta\lambda(E_\nu) \tag{5.1}$$

This approach has the uncertainty completely correlated from bin to bin and some investigation is needed to determine if this is appropriate.

A second approach would have us compare the spectra of different authors (*e.g.* [57]), linearly interpolating between the two models with a parameter α. However, this approach would tend to unnecessarily inflate this systematic. The Ortiz spectrum of [44] is derived from a more refined experimental technique, so provides the best estimate of the spectral uncertainty.

- *Uncertainty in the SNO cross sections*

We also neglected the uncertainty in the NC and CC cross sections. Fortunately, as

described in [45], these can both be parametrized by a single linear parameter L_{1A}. One can even use the SNO data to provide additional constraint on this free parameter of Effective Field Theory, although it is expected that very little information will be gained [58].

- *Uncertainty in the Earth Density Profile*

This uncertainty has not been included and, in principle, one could do so with something similar to Eqn. 5.1. However, with the day-night uncertainty being statistically limited, this is unlikely to be an important systematic.

Refer to Appendix A.7 for further discussion on how these systematics might be affecting the MSW contours. There we examine the MSW contours of other authors and find some significant differences from the analysis of Section 4.7.

5.1.2 Explicit Correlation Between Systematics

For all analyses, we assumed that the systematics were explicitly uncorrelated, taking the error matrix $\boldsymbol{\sigma}^2$ to be diagonal[1]. This turns out to be a very good approximation for instrumental parameters, which are each determined by separate calibration techniques. However, for background amplitudes, there are some significant correlations that we ignored.

The most significant explicit correlation is between the internal neutrons and Cherenkov backgrounds, since these were related by a scaling parameter. A crude estimate suggests that this correlation could be as large as +0.50. The second largest correlation is thought to arise intrinsically from the radial decomposition of external backgrounds, between the AV and H_2O sources. However, we have summed these, so the correlation is no longer important (see Section 3.4 for more details). Fortunately, the backgrounds are small and the assumption of no correlation probably does not

---

[1]We later used neutrino information to further constrain these parameters and this process *induced* correlations between the systematics.

radically alter the final analysis.

5.1.3 Finer Binned Zenith Angle Information

Our division of data into day and night is perfectly correct, but does not use all of the available information. There can be some additional dependence of the ν_e rate on $\cos\theta_z$, the cosine of the solar zenith angle. For the LMA region, this dependence is approximately linear with the path length through the Earth ($L \approx -2R\cos\theta_z$ for $\cos\theta_z < 0$).

One can access this additional information by using more than two zenith angle bins. Alternatively, since there is essentially no uncertainty in our measurement of $\cos\theta_z$, we could leave the distribution *unbinned* as shown in Eqn. 3.26.

5.2 Future Phases of the SNO Experiment.

This thesis has presented an analysis of the first phase of SNO, the *pure D_2O phase.* The *salt phase* is currently underway and the *NCD phase* will follow soon.

5.2.1 The Salt Phase

During the salt phase, we have added 2 tonnes of NaCl to the D_2O. This enhances the capture of neutrons *via*

$$n + {}^{35}Cl \rightarrow {}^{36}Cl + \Sigma\gamma + e^- \qquad E_{\Sigma\gamma} = 8.6 MeV \qquad (5.2)$$

There is now a cascade of γ's, with total energy 8.6 MeV, giving greater light output for each neutron capture. In addition, the neutron capture efficiency is increased to $\approx 86\%$. Finally, the multiple γ's yield a more isotropic distribution of light, allowing for a stronger separation of neutron capture events from single electron events (CC and ES). To make use of this, one adds an isotropy parameter (*e.g.* Θ_{IJ}) to the set of measurable quantities. Some care must be taken, because Θ_{IJ} may depend strongly on other parameters, such as the energy.

5.2.2 The NCD Phase

The Neutral Current Detectors (NCDs), discussed in Appendix B.1, are an array of proportional counters to be deployed into the heavy water volume. They are constructed from 5cm-diameter thin-walled ultra-pure nickel and filled with a mix of ^{3}He and CF$_4$. An anode of Cu wire runs down the center, held at 1825 V. These counters will detect neutrons *via*

$$n + {}^3He \rightarrow p + {}^3H^+ + 764 keV \tag{5.3}$$

The proton and triton ionize the gas, with the ionized electrons cascading at the anode. This produces a signal *independent* of the PMT array. The additional information from the NCDs allows one to break the correlations shown in Figs. 4.2 and 4.3. A simulation of how this occurs is shown in Fig. 5.1.

The total length of NCDs that can make up the array is $L_{total} = 776$ m, although we wish to consider the possibility of deploying only a fraction of this ($L < L_{total}$). We assume that the neutron capture efficiency on ^{3}He increases linearly with L. Monte Carlo simulations suggest that the efficiency is 47% for $L = L_{total}$. Cuts on the NCD signal, designed to remove ionization events from α's, will cut $\approx 50\%$ of the captured neutrons. We also assume that the light loss due to absorption of photons by nickel increases linearly with L.

We use the SNOMAN Monte Carlo to simulate both a fully deployed array ($L = L_{total}$) and a pure D$_2$O configuration ($L = 0$). The simulation includes a model for PMT loss during the future running of SNO. For simplicity, we consider only the number of hit PMTs (Nhit), generating a distribution for each configuration. Using linear interpolation, we create a model for the Nhit distribution as a function of L. Backgrounds are taken to be the same as the D$_2$O phase presented in Chapters 2 to 4. The NCDs will introduce additional U and Th, with the number of decays increasing linearly with L. We assume that this contributes an additional $\approx 4.5\%$ uncertainty to the total NCD background. No systematics are considered for this analysis.

With a 1-dimensional distribution over Nhit, we are able to make a χ^2 fit, extracting the two parameters ϕ_e and ϕ_{tot}, as well as the amplitude of the various backgrounds. Additional constraints are added to χ^2, accounting for the calibration measurements of the backgrounds. A final term is added, corresponding to the NCD measurement, constraining the total number of neutrons. The extracted physics parameters are shown in Figs. 5.1 and 5.2. We see that the uncertainties on ϕ_e and ϕ_{tot} and the magnitude of the correlation decrease by adding NCDs. For a simulation of 306 days of data, the optimal configuration for the measurement of ϕ_{tot} is one where $L \approx 0.7$. Other considerations, such as the sensitivity to day-night and spectral distortions, will be studied before settling on a final NCD configuration.
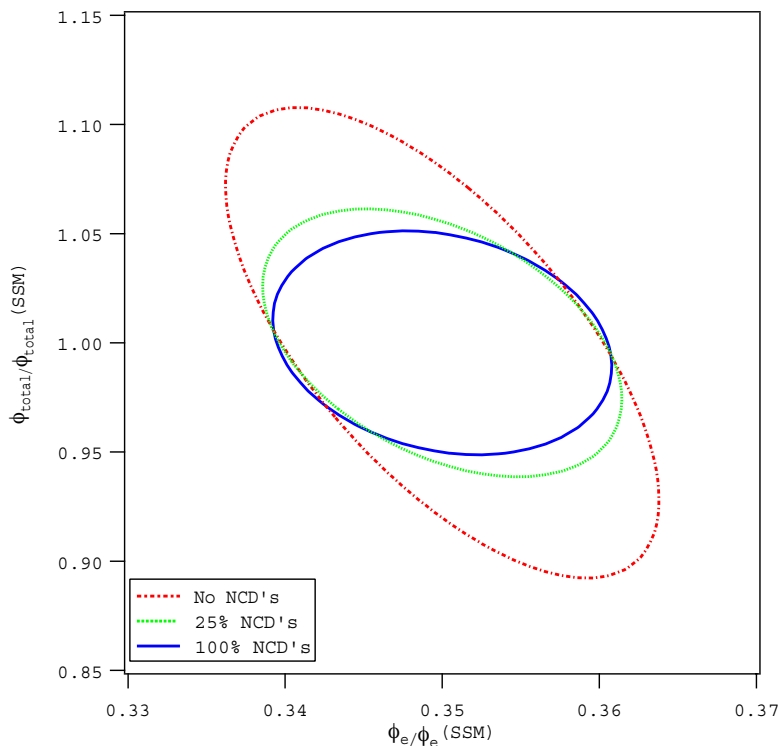
Figure 5.1: $\Delta\chi^2 = 1$ ellipses for ϕ_e and ϕ_{tot}, with zero, 25%, and 100% of the NCD array deployed. Simulation is for 306 days of livetime. This is a variant of a figure created by Jeff Manor.
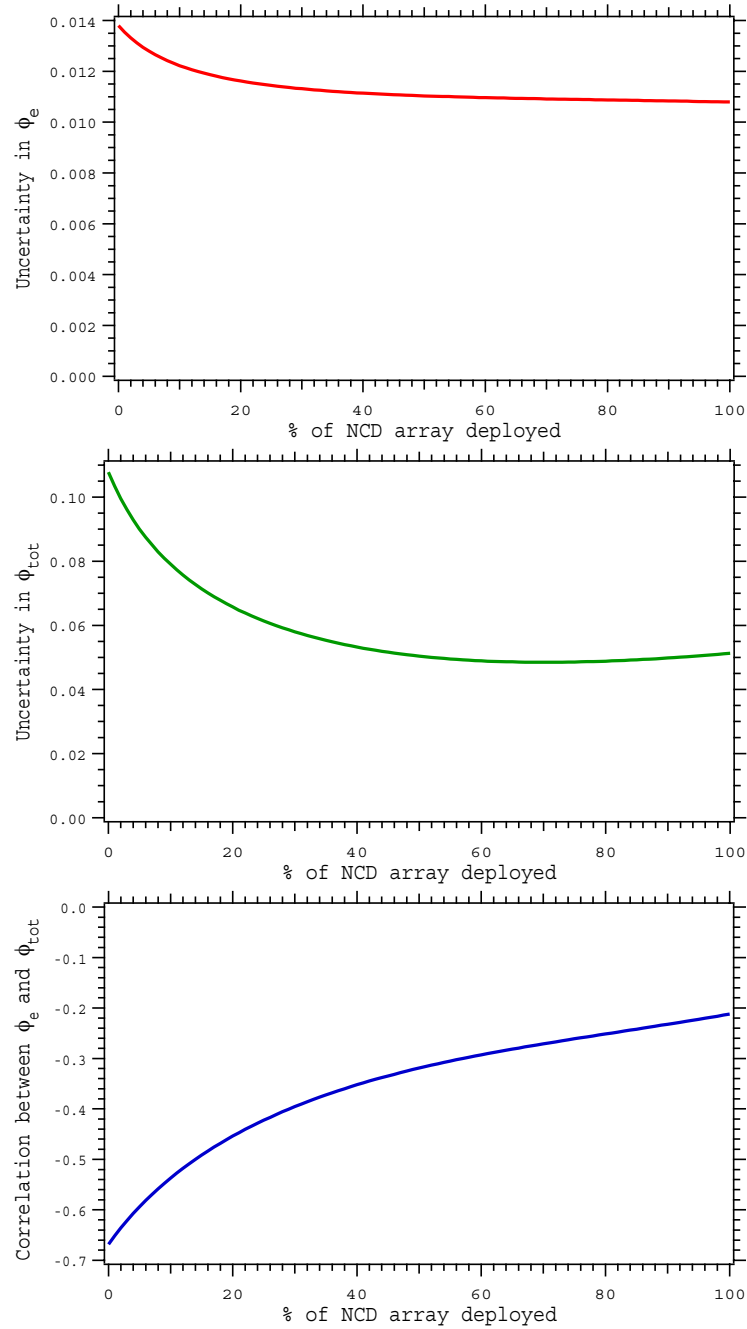
Figure 5.2: Uncertainty for ϕ_e, ϕ_{tot}, and their correlation, shown as a function of the percentage of the NCD array deployed.

5.3   *Future Neutrino Experiments*

Borexino [59]

Borexino is a real time experiment, located at the *Laboratori Nazionali del Gran Sasso*, Italy. It is designed to detect the elastic scattering of electrons by the 863 keV ^{7}Be neutrino line. This is achieved by viewing 300 tonnes of liquid scintillator with 2200 photomultiplier tubes. This will provide a critical data point. As discussed in Section 1.2.2, one can constrain the three fluxes ϕ_{pp+pep}, ϕ_{7Be}, and ϕ_{8B} using the measurements from Ga, Cl and water Cherenkov detectors. Unfortunately, if one uses these data to constrain the flux of each reaction in a completely model independent way, there is limited information for studying MSW parameters. That is why, in Section 4.7, we chose to combine the experimental data with information the SSM regarding the pp, pep and ^{7}Be fluxes. By adding the information from Borexino, we may be able to carry out a completely model independent MSW analysis. This may provide the first model-independent evidence that the suppression of ν_e is not uniform across all energies.

KamLAND [60]

The Kamioka Liquid-scintillator Anti-Neutrino Detector (KamLAND) is not strictly a solar neutrino experiment. However, it is worth mentioning here because it is sensitive to the same regions of MSW space as solar neutrinos experiments. It is located in the Kamioka mine in Japan, with approximately 2000 PMTs viewing a liquid scintillator core. Reactor anti-neutrinos are detected over baselines of 150 - 200 km. This length scale makes KamLAND sensitive to *vacuum oscillations*, with similar values of $\Delta m^2, \tan^2 \theta$ to those that produce *matter enhanced oscillation* for solar neutrino experiments. If KamLAND confirms the allowed region in parameter space, this solution will have been identified with two completely independent sources. There is no known mechanism that predicts flavor change for both solar neutrino experiments and KamLAND, other than neutrino oscillation.

BIBLIOGRAPHY

[1] J. N. Bahcall, M. C. Gonzalez-Garcia, C. Pena-Garay. Before and After: How has the SNO Neutral Current Measurement Changed Things? *JHEP07, 054*, 2002.

[2] J. N. Bahcall, M. H. Pinsonneault, and S. Basu. Solar Models: Current Epoch and Time Dependences, Neutrinos, and Helioseismological Properties. *Ap.J., 555:990-1012*, 2000.

[3] W. Pauli. Letter to Tubingen Conference. *December 4*, 1933.

[4] F. Reines, and C. L. Cowan Jr. Detection of the Free Neutrino. *Phys. Rev. Lett.* **92***: 330*, 1953.

[5] G. Danby, *et al.* Observation of High-Energy Neutrino Reactions and the Existence of Two Kinds of Neutrinos. *Phys.Rev.Lett.9:36-44*, 1962.

[6] The DONUT Collaboration. The Observation of Tau Neutrino Interactions. *Phys. Lett. B504, 218-224*, 2001.

[7] G. Steigman, D. N. Schramm, and J. Gunn. *Phys. Lett. B66, 202*, 1977.

[8] R. H. Cyburt, B. D. Fields, K. A. Olive. Primordial Nucleosynthesis with CMB Inputs. *Astropart. Phys. 17, 87-100*, 2002.

[9] The LEP Collaborations. Results from LEP Concerning the Width of the Z from L3, ALEPH, OPAL and DELPHI. *Physics Letters B 509,519,530,539*, 1989.

[10] T. D. Lee and C. N. Yang. Parity Nonconservation and a Two-Component Theory of the Neutrino. *Phys. Rev.* **105***(5): 1671*, 1957.

[11] H. A. Bethe. Energy Production in Stars. *Phys. Rev., 55, 434.*, 1939.

[12] J. N. Bahcall. *Neutrino Astrophysics*. Cambridge University Press, 1989.

[13] A. S. Brun, S. Turck-Chieze, and J. P. Zahn. *Ap.J., 555*, 2001.

[14] J. N. Bachall. http://www.sns.ias.edu/~ jnb/.

[15] R. Davis Jr., *et al. Phys. Rev. Lett.,* **20***, 1205 & 1209*, 1968.

[16] B. T. Cleveland, *et al.* Measurement of the Solar Electron Neutrino Flux with the Homestake Chlorine Detector. *Astrophysical Journal v.496, p.505*, 1998.

[17] J. N. Abdurashitov, *et al.* Solar Neutrino Flux Measurements by the Soviet-American Gallium Experiment (SAGE) for Half the 22-Year Solar Cycle. *JETP, 95, No.2:181-193*, 1999.

[18] W. Hampel, *et al. Phys. Lett. B, 447. 127*, 1999.

[19] M. Altmann, *et al.* GNO Solar Neutrino Observatory: Results for GNO I. *Phys. Lett. B 490, 16*, 2000.

[20] S. Fukuda, *et al.* Solar ^{8}B and *hep* Neutrino Measurements from 1258 Days of Super-Kamiokande Data. *Phys. Rev. Lett. 86:5651-5655*, 2001.

[21] S. Fukuda, *et al.* Determination of Solar Neutrino Oscillation Parameters Using 1496 Days of Super-Kamiokande I Data. *Phys. Lett. B539:179-187*, 2002.

[22] R.G.H. Robertson K. M. Heeger. Probability of a Solution to the Solar Neutrino Problem Within the Minimal Standard Model. *Phys. Rev. Lett. 77:3720-3723*, 1996.

[23] N. Hata and P. Langacker. Model Independent Determination of the Solar Neutrino Spectrum with and without MSW. *Phys. Rev. D52, 420*, 1995.

[24] N. Cooper, editor. *Celebrating the Neutrino.* Los Alamos National Laboratory, 1997.

[25] C. Giunti. Neutrino Wave Packets in Quantum Field Theory. *hep-ph/0205014*, 2002.

[26] Y. Fukuda, *et al. Phys. Rev. Lett.* **81** *1562*, 1998.

[27] A. de Gouvea, A. Friedland, H. Murayama. The Darkside of the Solar Neutrino Parameter Space. *Phys. Lett. B490, 125-130*, 2000.

[28] S. M. Bilenky et al. Constraints on $|U_{e3}|^2$ From a Three-Neutrino Oscillation Analysis of the CHOOZ Data. *Phys. Lett. B***466** *415*, 1999.

[29] M. Apollonino et al. *Phys. Lett. B***466** *415*, 1999.

[30] S. P. Mikheyev and A. Yu. Smirnov. *Sov. J. nucl. Phys.* **42***, 913.*, 1986.

[31] L. Wolfenstein. *Phys. Rev. D,* **17***, 2369 and* **20***, 2634., 1978*, 1979.

[32] This was pointed out to me in a talk given by Lincoln Wolfenstein.

[33] A. M. Dziewonski and D. L. Anderson. The Prelinary Reference Earth Model. *Earth Planet. Inter., 25, 297-356*, 1981.

[34] C-W. Chiang, L. Wolfenstein. The Sign of the Day Night Asymmetry for Solar Neutrinos. *Phys. Rev. D 63:057303*, 2000.

[35] C. Athanassopoulos, *et al. Phys. Rev. Lett.* **81** *1774*, 1998.

[36] C. Giunti, *et al.* Four Neutrino Oscillation Solutions of the Solar Neutrino Problem. *Nucl. Instrum. Meth. A 472: 364-370*, 2000.

[37] R. L. Boger, et al. The Sudbury Neutrino Observatory. *Nuc. Inst. Meth.*, 1999.

[38] Neil K. McCauley. *Producing a Background Free Data Set for the Measurment of the Charge Current Flux and Day-Night Asymmetry at the Sudbury Neutrino Observatory.* PhD thesis, Oxford University, 2001.

[39] Mark S. Neubauer. *Evidence for Electron Neutrino Flavor Change through Measurement of the ^8B Solar Neutrino Flux at the Sudbury Neutrino Observatory.* PhD thesis, University of Pennsylvania, 2001.

[40] H. Goldstein. *Classical Mechanics.* Addison-Wesley, 1980.

[41] D. R. Lide, editor. *CRC Handbook of Chemistry and Physics.* CRC Press, 1995.

[42] Electron Gamma Shower (EGS) Code. www.slac.stanford.edu/egs/.

[43] MCNP-A General Monte Carlo N-Particle Transport Code. www-xdiv.lanl.gov/x5/mcnp/.

[44] C. E. Ortiz, *et al.* Shape of the ^{8}B Alpha and Neutrino Spectra. *Phys.Rev.Lett.85:2909-2912*, 2000.

[45] M. Butler, J. Chen, and X. Kong. *Phys. Rev. C 63, 035501*, 2001.

[46] Mark G. Boulay. *Direct Evidence for Weak Flavor Mixing with the Sudbury Neutrino Observatory*. PhD thesis, Queen's University, 2001.

[47] Andre Hamer. *Energy Calibration of SNO for Measurements of the Charged-Current Neutrino Reaction*. PhD thesis, Queen's University, 1999.

[48] M. Dragowski and A. Hime. Neutron Response and Efficiency for the Pure D_2O Phase in SNO. *SNO internal document*, 2002.

[49] A. Poon, *et al.* The Low Energy Backgrounds in the Pure D_2O Phase of the SNO Experiment. *SNO internal document*, 2002.

[50] M. Smith, *et al.* The Day-Night Unified Document. *SNO internal document*, 2002.

[51] These particular models were suggested by Scott Oser.

[52] Q. R. Ahmad, et al. Direct Evidence for Neutrino Flavor Transformation from Neutral Current Interactions in the Sudbury Neutrino Observatory. *Phys. Rev. Lett. 89: 011301*, 2002.

[53] Q. R. Ahmad, et al. Measurement of Day and Night Neutrino Energy Spectra at Sno and Constraints on Neutrino Mixing Parameters. *Phys. Rev. Lett. 89: 011302*, 2002.

[54] G.L. Fogli, *et al.* Getting the Most from the Statistical Analysis of Solar Neutrino Oscillations. *hep-ph/0206162*, 2002.

[55] W. T. Eadie, *et al. Statistical Methods in Experimental Physics*. American Elsevier Pub. Co., 1971.

[56] C. Ortiz, *et al.* www.nd.edu/ nsl/BeyondSM/boron8/tables/spectrum.nu.

[57] J. N. Bahcall, *et al. Phys. Rev.C 54, 411*, 1996.

[58] Karsten Heeger. Private Communication.

[59] Borexino Collaboration. www.almime.mi.infn.it/.

[60] The KamLand Collaboration. www.awa.tohoku.ac.jp/html/kamland/.

[61] Q. R. Ahmad, et al. Measurement of the Rate of $\nu_e + d \rightarrow p + p + e^-$ Interactions Produced By ^{8}B Solar Neutrinos at the Sudbury Neutrino Observatory. *Phys. Rev. Lett. 87: 071301*, 2001.

Appendix A

MATHEMATICAL FORMALISM

A.1 Linear Expansion in Systematics

The number density of events $\mu(X|\eta, \alpha)$, distributed over measurable quantities X, also depends continuously on a vector of physics parameters $\boldsymbol{\eta}$ and a vector of systematics $\boldsymbol{\alpha}$. To a very good approximation, because $\boldsymbol{\alpha}$ is small, we can expand the model as a linear function of the systematics. This provides a continuous parametrization with respect to α.

$$\mu(X|\eta, \alpha) = \mu_o \times \left[1 + \boldsymbol{\beta}^T(\boldsymbol{\alpha} - \boldsymbol{\alpha_o})\right] \tag{A.1}$$

where $\mu_o(X|\eta)$ is independent of α and

$$\boldsymbol{\beta}(X|\eta) = \frac{1}{\mu_o} \left.\frac{\partial \mu}{\partial \boldsymbol{\alpha}^T}\right|_{\boldsymbol{\alpha}=\boldsymbol{\alpha_o}} \tag{A.2}$$

We make measurements of the systematics using the calibration data, with the best fit values referred to as $\boldsymbol{\alpha}_{cal}$. It should be noted that $\boldsymbol{\alpha_o}$ is not necessarily set to $\boldsymbol{\alpha}_{cal}$. We can choose to expand around any value we like, provided the linear approximation is still good. Broadly speaking, there are two kinds of systematics, *instrumental parameters* such as energy scale, position reconstruction, etc., and *backgrounds amplitudes*. These two kinds are treated differently here. For instrumental parameters, the obvious choice is $\alpha_o = \alpha_{cal}$, so that μ_o, the model we expand around, includes our best estimate of the detector response. However, for background amplitudes, we might choose to set $\alpha_o = \alpha_{cal}$ or $\alpha_o = 0$. In the latter case, μ_o describes a detector with zero backgrounds. We will find this choice useful for creating MSW contours (see Appendix A.4).

A.1.1 Background Amplitudes

The expected number of events B, for a particular background source, is measured to be

$$B = B_{cal} \pm \sigma(B) \tag{A.3}$$

The expansion coefficient we will use is $\alpha = B$. However, the addition of this background to the model is made by expanding around $B = 0$, not B_{cal}.

$$\mu(X|\eta, B) = \mu_o + B \times \rho_B(X)$$
$$= \mu_o \times (1 + \frac{\rho_B}{\mu_o} B) \tag{A.4}$$

where $\rho_B(X)$ is the multi-dimension PDF for the background. We see that the first order derivative β is defined as

$$\beta(X|\eta) = \frac{\rho_B(X)}{\mu_o(X|\eta)} \tag{A.5}$$

It is interesting to note that the treatment of a background amplitude in this way is *exact*. Because any background adds linearly, there are no higher order terms.

We can also treat the contribution from hep neutrinos perturbatively, with only a slight change in formalism.

$$\beta(X|\eta) = \frac{\mu_{hep}(X|\eta)}{\mu_o(X|\eta)} \tag{A.6}$$

The expansion coefficient in now $\alpha = \phi_{hep}$, the flux of hep neutrinos relative to the SSM hep flux.

In addition to an uncertainty in the background amplitude, there can also be an uncertainty in the *shape* of the PDF ρ_B. This is dealt with in Section A.1.2.

A.1.2 Instrumental Parameters

For instrumental parameters we must calculate the derivatives of Eqn. A.2. In this case, we construct β out of individual contributions from each reaction

$$\beta = \frac{S^{cc}\rho^{cc}\beta^{cc} + S^{es}\rho^{es}\beta^{es} + S^{nc}\rho^{nc}\beta^{nc}}{S^{cc}\rho^{cc} + S^{es}\rho^{es} + S^{nc}\rho^{nc}} \tag{A.7}$$

where $\rho^{cc}(X|\eta)$ is the PDF for the CC reaction and S^{cc} is the expected number of events. The individual derivatives such as β^{cc} are defined by Eqn. A.2, but with all other contributions to the model (except CC) turned off. These individual β-functions are largely independent of the physics parameters η. We can therefore derive them using undistorted SSM distributions. On the other hand, the weighting factors $S^{cc}\rho^{cc}$, *etc.*, have a strong effect on the overall shape of β and should not be considered independent of η. Since the α are small, we can replace the derivatives β^{cc}, *etc.*, with discrete approximations, derived from Monte Carlo simulations.

In this formulation, the shape of the background distributions are assumed to be unperturbed by the variation of instrumental parameters. This is not strictly true, although such variations are 2nd order in α (a cross term between two different perturbations) and are therefore neglected.

A.2 Solving for a Linear Physics Model (Models 2a, b, c)

In this Appendix we consider models which are linear in the physics parameters, *e.g.* ϕ_e and $\phi_{\mu\tau}$. We will show how to extract these linear physics parameters from the likelihood function and determine an error matrix. The approach outlined here does *not* use all of the available information. The neutrino data set, in addition to the calibration data, contains information regarding the systematics. However, we will not use this additional handle on systematics here, reserving neutrino data to only give us information about physics parameters. We pursue the simpler approach first because it was the approach of SNO publications [52] and [53].

A.2.1 Extracting physics parameters

For a linear physics model, we have a vector of flux amplitudes, *e.g.* $\boldsymbol{\eta} = \{\phi_{eD}, \phi_{eN}, \phi_{totD}, \phi_{totN}\}$ for Model 2c. In the approach taken here, we define the best model with $\boldsymbol{\alpha} = \boldsymbol{\alpha}_{cal}$, for both instrumental parameters and background am-

plitudes. This model is then used to perform the flux extraction. Although the full log-likelihood function depends on many more parameters, we have now created the simpler 4 parameter function $\mathcal{L}_o = \mathcal{L}(\eta, \alpha = \alpha_{cal})$. We then solve the set of 4 (non-linear) equations[1] given by

$$\frac{\partial \mathcal{L}_o}{\partial \boldsymbol{\eta}^T} = 0 \tag{A.8}$$

A.2.2 Error matrix determination

Collectively, let us refer to the full set of parameters as $\zeta = \{\eta, \alpha\}$. The combined statistical + systematic error matrix is given by first calculating the error matrix for the full set of parameters

$$[\sigma^2(\zeta)] = \left[\frac{\partial^2 \mathcal{L}}{\partial \zeta \partial \zeta^T}\right]^{-1} \tag{A.9}$$

The 4×4 submatrix, defined by $\boldsymbol{\eta} = \{\phi_{eD}, \phi_{eN}, \phi_{totD}, \phi_{totN}\}$, is the *reduced* error matrix we seek for the physics parameters.

In this example, we can make a fast determination of this reduced error matrix, without the need to invert a large $(4 + n) \times (4 + n)$ system. To do this, we break the matrix into statistical and systematic parts. The statistical part is determined by

$$[\sigma_\eta^2]_{stat} = \left[\frac{\partial^2 \mathcal{L}_o}{\partial \boldsymbol{\eta} \partial \boldsymbol{\eta}^T}\right]^{-1} \tag{A.10}$$

We now determine the systematic part. For each systematic parameter α_k, we perturb the model by an amount equal to $\pm\sigma(\alpha_k)$, while leaving all other systematics fixed to their nominal values. This allows us to re-extract the vector of fluxes $\boldsymbol{\eta}$ and compare them to $\boldsymbol{\eta}_o$, the extraction of section A.2.1. We then calculate the perturbation $\delta_k \boldsymbol{\eta} = \boldsymbol{\eta} - \boldsymbol{\eta}_o$, where k labels the perturbation with respect to the kth systematic.

---

[1]The more complicated approach is to solve the full likelihood function given by $\mathcal{L} = \mathcal{L}(\eta, \alpha)$. This approach allows neutrino data to add further constraint to the size of the systematics. For further discussion, see Appendix A.4.

This allows us to define a systematic component to the error matrix.

$$\boldsymbol{\sigma}_\eta^2 = (\boldsymbol{\sigma}_\eta^2)_{stat} + \sum_{jk} \delta_j \boldsymbol{\eta} \otimes \delta_k \boldsymbol{\eta}^T \frac{(\boldsymbol{\sigma}_\alpha^2)_{jk}}{\sigma(\alpha_j)\sigma(\alpha_k)} \tag{A.11}$$

In the case where the separate calibrations are independent, $\boldsymbol{\sigma}_\alpha^2$ is diagonal and we get

$$\boldsymbol{\sigma}_\eta^2 = (\boldsymbol{\sigma}_\eta^2)_{stat} + \sum_{k} \delta_k \boldsymbol{\eta} \otimes \delta_k \boldsymbol{\eta}^T \tag{A.12}$$

One can make some additional approximations when determining the size of the systematic perturbations $\delta\boldsymbol{\eta}$. For example, an error in energy scale requires that we perturb the modelled energy measure T_{eff} by an amount $\pm 1.21\%$ and re-extract the physics parameters to give $\delta\boldsymbol{\eta}$. Alternatively, one could perturb the value of T_{eff} assigned to each event and re-extract the physics parameters. The results will be slightly different, although close enough for the purposes of studying systematics.[2]

A.3   Combining the SNO and SK Day-Night Results

The SK experiment has measured the day-night asymmetry in the ES reaction [20]. Assuming that there is no NC asymmetry, their measurement is diluted by the NC component of the ES reaction. One can use the SNO data to remove this dilution. One begins with the set of 3 measurements

$$\boldsymbol{\eta} = \begin{pmatrix} \phi_{total}^{SNO} \\ \\ \phi_{ES,D}^{SK} \\ \\ \phi_{ES,N}^{SK} \end{pmatrix}$$

---

[2]This approximation is akin to the standard replacement $\sigma_i^2 \approx n_i$ in $\chi^2 = \sum_i \frac{(n_i - y_i)^2}{\sigma_i^2}$

and changes variables to

$$\boldsymbol{\eta}' = \begin{pmatrix} \phi_{total}^{SNO} \\ \\ \phi_{e,D}^{SK} \\ \\ \phi_{e,N}^{SK} \end{pmatrix}$$

The variable change can be expressed as $\boldsymbol{\eta} = \boldsymbol{V}^{-1}\,\boldsymbol{\eta}'$, where $\boldsymbol{V}$ is the 3×3 matrix

$$\boldsymbol{V}^{-1} = \begin{pmatrix} 1 & 0 & 0 \\ \epsilon & 1-\epsilon & 0 \\ \epsilon & 0 & 1-\epsilon \end{pmatrix} \quad or \quad \boldsymbol{V} = \begin{pmatrix} 1 & 0 & 0 \\ -\frac{\epsilon}{1-\epsilon} & \frac{1}{1-\epsilon} & 0 \\ -\frac{\epsilon}{1-\epsilon} & 0 & \frac{1}{1-\epsilon} \end{pmatrix}$$

and $\epsilon = 0.1559$. We solve to get

$$\phi_{e,D}^{SK} = \frac{\phi_{ES,D}^{SK} - \epsilon\,\phi_{total}^{SNO}}{1-\epsilon}$$

$$\phi_{e,N}^{SK} = \frac{\phi_{ES,N}^{SK} - \epsilon\,\phi_{total}^{SNO}}{1-\epsilon}$$

If $\boldsymbol{\sigma}^2$ is the 3×3 error matrix for ϕ, we can also transform it

$$(\boldsymbol{\sigma}^2)' = \boldsymbol{V}\,\boldsymbol{\sigma}^2\,\boldsymbol{V}^T$$

$$= \begin{pmatrix} \sigma_{tot}^2 & -\frac{\epsilon}{1-\epsilon}\sigma_{tot}^2 & -\frac{\epsilon}{1-\epsilon}\sigma_{tot}^2 \\ -\frac{\epsilon}{1-\epsilon}\sigma_{tot}^2 & \frac{\epsilon^2}{(1-\epsilon)^2}\sigma_{tot}^2 + \frac{1}{(1-\epsilon)^2}\sigma_D^2 & \frac{\epsilon^2}{(1-\epsilon)^2}\sigma_{tot}^2 + \frac{1}{(1-\epsilon)^2}\sigma_{DN}^2 \\ -\frac{\epsilon}{1-\epsilon}\sigma_{tot}^2 & \frac{\epsilon^2}{(1-\epsilon)^2}\sigma_{tot}^2 + \frac{1}{(1-\epsilon)^2}\sigma_{DN}^2 & \frac{\epsilon^2}{(1-\epsilon)^2}\sigma_{tot}^2 + \frac{1}{(1-\epsilon)^2}\sigma_N^2 \end{pmatrix}$$

where $\begin{pmatrix} \sigma_D^2 & \sigma_{DN}^2 \\ \sigma_{DN}^2 & \sigma_N^2 \end{pmatrix}$ is the SK error matrix.

We now form the SK electron neutrino asymmetry and find:

$$A_e^{SK} = A_{ES}^{SK}\left(1 - \frac{2\epsilon\,\phi_{total}^{SNO}}{\phi_{ES,D}^{SK} + \phi_{ES,N}^{SK}}\right)^{-1}$$

By simple propagation of errors, we can calculate the uncertainty $\sigma(A_e^{SK})$. Doing so, we find that the σ_{tot} terms cancel in this calculation. One can see why this happens by looking at the above error matrix. For the SK sub-matrix, the σ_{tot} contribution is completely correlated from day to night.

Although σ_{tot} does not contribute to the uncertainty, there is still a correlation between SK and the SNO total flux $\rho(\phi_{total}^{SNO}, A_e^{SK})$, but we shall not calculate it here.

A.4 Solving for the MSW Model

In Appendix A.1, we argued that one could make a linear expansion of the model with respect to the systematics α. In terms of the number density of events, we have

$$\mu(X|\eta, \alpha) = \mu_o \times \left[1 + \boldsymbol{\beta}^T(\boldsymbol{\alpha} - \boldsymbol{\alpha_o})\right] \tag{A.13}$$

where $X = \{T_{eff}, R_{fit}^3, \cos\theta_\odot\}$ represents the measurable quantities, $\boldsymbol{\eta}$ are the physics parameters and $\boldsymbol{\alpha}$ are the systematics. μ_o is represents the model with backgrounds set to zero and instrumental parameters set to their nominal values, determined by calibrations. In fact, there is no reason why we can't redefine te instrumental parameters, so that $\alpha_o = 0$ corresponds to the nominal values of the instrumental parameters. For simplicity, we shall henceforth define the notation so that $\boldsymbol{\alpha_o} = 0$ for the zero background, nominal instrumental parameter model.

For the MSW model, the physics parameters are $\eta[0] = \phi_{tot}$, $\eta[1] = \tan^2\theta$, $\eta[2] = \Delta m^2$. Since $\mu_o(X|\eta)$ describes only the ^{8}B neutrinos, we can write it as

$$\mu_o = \phi_{tot}\ y_o(X|\Delta m^2, \tan^2\theta) \tag{A.14}$$

Recall that ϕ_{tot} is the flux relative to the SSM flux, so that y_o is the number density of events for the case that the solar flux of ^{8}B neutrinos is exactly $5.05 \times 10^6 cm^{-2}s^{-1}$. We also define the total expected number of events for the case that $\phi_{tot} = 1$, no

backgrounds and instrumental parameters set to their nominal values.

$$S_o \equiv \sum_X y_o(X|\Delta m^2, \tan^2 \theta) \tag{A.15}$$

To minimize the log-likelihood function, we write $\phi_{tot} = \phi_o + \Delta\phi$ Our model becomes

$$\mu = \phi_o \times y_o \left(1 + \frac{\Delta\phi}{\phi} + \boldsymbol{\beta}^T \boldsymbol{\alpha}\right) \tag{A.16}$$

where, in the spirit of linearization, we recognize that the cross terms $\frac{\Delta\phi}{\phi} \times \boldsymbol{\alpha}$ are insignificant and are hence neglected. This suggests that we redefine the vectors $\boldsymbol{\alpha}$ and $\boldsymbol{\beta}$ to have zeroth components

$$\alpha[0] = \frac{\Delta\phi}{\phi} \qquad \beta[0] = 1 \tag{A.17}$$

Doing this, Equation A.16 returns to the form

$$\mu = \phi_o \, y_o (1 + \boldsymbol{\beta}^T \boldsymbol{\alpha}) \tag{A.18}$$

and, to within a constant, Equation 4.8 becomes

$$\mathcal{L} = 2\phi_o \, S_o - 2N \, ln\phi_o - 2\sum_m ln \, y_o(X_m)$$
$$+ 2\phi_o \sum_X y_o(X)\boldsymbol{\beta}^T(X)\boldsymbol{\alpha} - 2\sum_m ln(1 + \boldsymbol{\beta}^T(X_m)\boldsymbol{\alpha}) \tag{A.19}$$
$$+ (\boldsymbol{\alpha} - \boldsymbol{\alpha}_{cal})^T \boldsymbol{\sigma}_\alpha^{-2} (\boldsymbol{\alpha} - \boldsymbol{\alpha}_{cal})$$

where S_o, y_o, $\boldsymbol{\beta}$ all depend on $\eta[1] = \tan^2 \theta, \eta[2] = \Delta m^2$ but not on the systematics. Recall that $\alpha_{cal} \neq 0$ for background amplitudes, even though we have defined $\boldsymbol{\alpha_o} = 0$.

By construction, ϕ_o minimizes the simpler equation

$$\mathcal{L}_0 = 2\phi_o \, S_o - 2N \, ln\phi_o - 2\sum_m ln \, y_o(X_m) \tag{A.20}$$

and, with the way we have set the problem up, it turns out that ϕ_o has an analytic solution.

$$\phi_o = \frac{N}{S_o(\Delta m^2, \tan^2 \theta)} \tag{A.21}$$

Where N is the total number of events. By substituting this result back into Equation A.20, we can generate contours for the simplified problem of a detector with assumed zero background and no systematic error in its description. The result is shown in Fig. 4.4.

The remainder of $\mathcal{L} = \mathcal{L}_0 + \mathcal{L}'$ is then expanded to 2nd order[3] in α about $\mathcal{L}_0$. To within a constant, we find that

$$\mathcal{L}' = 2(\boldsymbol{p} - \boldsymbol{q} - \boldsymbol{r})^T \boldsymbol{\alpha} \; + \; \boldsymbol{\alpha}^T(\boldsymbol{\sigma}^{-2} + \boldsymbol{M})\boldsymbol{\alpha} \tag{A.22}$$

where

$$\boldsymbol{M} = \sum_m \boldsymbol{\beta}(X_m) \otimes \boldsymbol{\beta}(X_m)^T$$
$$\boldsymbol{r} = \boldsymbol{\sigma}_\alpha^{-2}\boldsymbol{\alpha}_o$$
$$\boldsymbol{p} = \sum_X y_o(X)\boldsymbol{\beta}(X)$$
$$\boldsymbol{q} = \sum_m \boldsymbol{\beta}(X_m)$$

The value of $\boldsymbol{\alpha}$ that minimizes $\mathcal{L}'$ (and hence $\mathcal{L}$) is

$$\boldsymbol{\alpha}_{\min} = (\boldsymbol{\sigma}_\alpha^{-2} + \boldsymbol{M})^{-1}(\boldsymbol{r} + \boldsymbol{q} - \boldsymbol{p}) \tag{A.23}$$

by combining Equations A.20, A.21, A.22, and A.23, we have minimized $\mathcal{L}$ with respect to both the ^{8}B flux and systematic parameters. We repeat this for each point of MSW space, thus generating the MSW contours shown in Fig. 4.5.

We also note that the fitted values of α have a new error matrix

$$\overline{\boldsymbol{\sigma}}^2 = (\boldsymbol{\sigma}_\alpha^{-2} + \boldsymbol{M})^{-1} \tag{A.24}$$

Here we see that $\boldsymbol{M}^{-1}$ carries the information about systematics from the neutrino data while, as before, $\boldsymbol{\sigma}_\alpha^2$ is the information provided by calibrations. Table 4.5 shows what the neutrino data adds to our knowledge of systematics.

---

[3]Why expand to 2nd order, when we have already neglected cross terms in α? Actually, the cross terms behave as 3rd order, since they are always contracted with $\sum_X(y_X - n_X)$.

A.5   Some Notes About the χ^2 Distribution

For ν degrees of freedom, the standard χ^2 probability distribution is given by

$$\rho(\chi^2; \nu) = \frac{(\chi^2)^{(\nu-2)/2} e^{-\chi^2/2}}{2^{\nu/2} \Gamma(\nu/2)}$$

In general, we want the integral of this

$$\alpha_c = P(\chi^2 > \chi_c^2) = \int_{\chi_c^2}^{\infty} d\chi^2 \rho(\chi^2; \nu)$$

There are two special cases that we will consider here. For $\nu = 2$ degrees of freedom

$$\alpha_c = \int_{\chi_c^2}^{\infty} d\chi^2 \frac{e^{-\chi^2/2}}{2}$$

$$= e^{-\chi_c^2/2}$$

$$\text{(A.25)}$$

In the case of 1 degree of freedom we have

$$\alpha_c = \int_{\chi_c^2}^{\infty} d\chi^2 \frac{e^{-\chi^2/2}}{\sqrt{2\pi\chi^2}}$$

which can not be integrated analytically. Even a numerical integration can be tricky because of the divergence of the integrand as $\chi^2 \to 0$. However we can easily circumvent these problems by changing variables to the significance $\zeta = \sqrt{\chi^2}$. Doing this we get

$$\alpha_c = P(|\zeta| > \zeta_c) = 2 \int_{\zeta_c}^{\infty} d\zeta \frac{e^{-\zeta^2/2}}{\sqrt{2\pi}}$$

$$= 1 - erf(\frac{\zeta_c}{\sqrt{2}})$$

$$\text{(A.26)}$$

where we have multiplied by 2 in the second line, to account for the fact that we test for $|\zeta| > \zeta_c$ (This is for a *two sided* test).

The application of these ideas comes when we make a hypothesis test with two degrees of freedom distinguishing the null hypothesis and the alternate hypothesis ($\nu = 2$). In this case, the $\Delta\chi^2$ between the new model and the null hypothesis should be distributed by Equation A.25. One determines the size of α_c for this hypothesis test and then solves Equation A.26 to find the *equivalent* significance of the data.

A.6 Comparing the Current MSW Analysis to Previous SNO Analyses

Prior to the analysis described in Section 4.4, the SNO collaboration pursued a much simpler approach. The simpler analysis used only the day and night energy distributions and, because there was sufficient statistics in each bin, the log-likelihood formulation simplified to a χ^2 formulation. Being a χ^2 analysis, one could create a systematic error matrix for the energy histogram, thus circumventing the need (and advantages) of allowing the neutrino data to constrain systematic parameters.

There was also another notable difference. Let us revisit Equation A.7 for instrumental parameters.

$$\beta = \frac{S^{cc}\rho^{cc}\beta^{cc} + S^{es}\rho^{es}\beta^{es} + S^{nc}\rho^{nc}\beta^{nc}}{S^{cc}\rho^{cc} + S^{es}\rho^{es} + S^{nc}\rho^{nc}}$$

The individual functions β^{cc}, β^{es} are largely independent of physics parameters and, in all analyses, were calculated by perturbing the SSM distribution (β^{nc} is always independent of physics parameters, provided the model describes only active neutrinos). The overall β-function, however, can depend strongly on $\Delta m^2, \tan^2\theta$ through the weightings $S^{cc}\rho^{cc}$, *etc.* When performing the initial SNO MSW analysis, we did not have a full implementation of Equation A.7 and instead used two alternate approximations.

- **Approximation A** Replace $S^{cc}\rho^{cc}(X|\eta)$ with its SSM distribution $S^{cc}_{ssm}\rho^{cc}(X|ssm)$. Similarly for the ES reaction.

- **Approximation B** Replace $S^{cc}\rho^{cc}(X|\eta)$ with the SSM distribution, weighted by the results of the flux extraction *e.g.* $\phi_e \times S^{cc}_{ssm}\rho^{cc}(X|ssm)$.

It should be obvious that Approx. A is actually nowhere near approximate. It assigns the incorrect relative weighting to the various reactions. Approximation B is certainly much closer to the truth. However, Approx. A was viewed as more conservative with

Table A.1: Differences between the analysis of this thesis and previous energy-only analyses. The treatment of β-functions in the current analysis is considered to be the most correct.

analysis	information used	statistical measure	weighting used to combine β-functions	reference
Approx. A	energy-only	χ^2	$1 \times S^{cc}_{ssm}\rho^{cc}(X\|SSM)$, *etc.*	published in [53]
Approx. B	energy-only	χ^2	$\phi_{cc} \times S^{cc}_{ssm}\rho^{cc}(X\|SSM)$	not published
This Thesis	$T, R^3, \cos\theta_{\odot}$	log-like	$S^{cc}\rho^{cc}(X\|\Delta m^2, \tan^2\theta, ...)$	section 4.4

regards to the acceptance of the LOW solution and was therefore included in our publication [53]. The differences between the various analyses are shown in Table A.1. The current analysis, presented in this thesis, does not approximate the weighting factors of Equation A.7.

Figure A.1 shows the two previous analyses, using Approx. A and B. We see that Approx. B agrees relatively well with the current analysis C. Approx. A disagrees considerably, although typically in a more conservative way. We have learned from this that the additional information from R^3, $\cos\theta_{\odot}$ is providing very little additional discriminating power. On the other hand, an improved treatment of systematics makes a significant improvement.
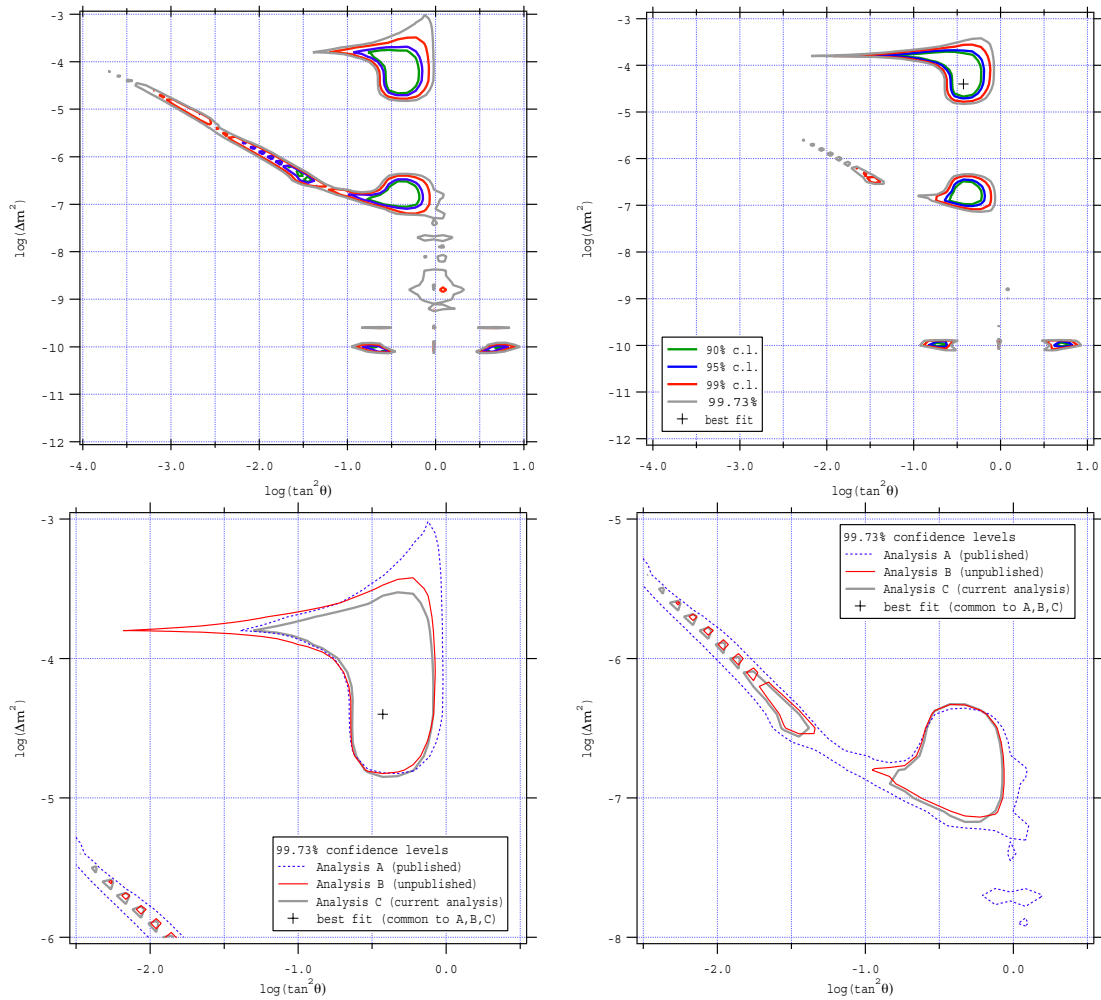
Figure A.1: Comparing the current MSW analysis to the published SNO analysis, using Approx. A (top left), and the unpublished analysis, using Approx. B (top right). Analyses with Approx. A & B use only energy information and χ^2. The three analyses are compared at the 99.97% c.l. in the bottom two plots.

A.7 Comparison to Other Published MSW Analyses

Since the publication of our results, a number of authors have incorporated SNO data into their global analysis of solar neutrino experiments. For simplicity, we will compare the analysis of Section 4.7 to just one other published analysis, that of Bahcall *et al.* [1]. They consider a number of analysis approaches, although we will only compare to one that treats SNO data in the same way that we have treated it in Section 4.7, making a χ^2 fit to SNO's day and night energy histograms while floating the ^{8}B flux. The result of their global fit is seen in Fig. A.2.
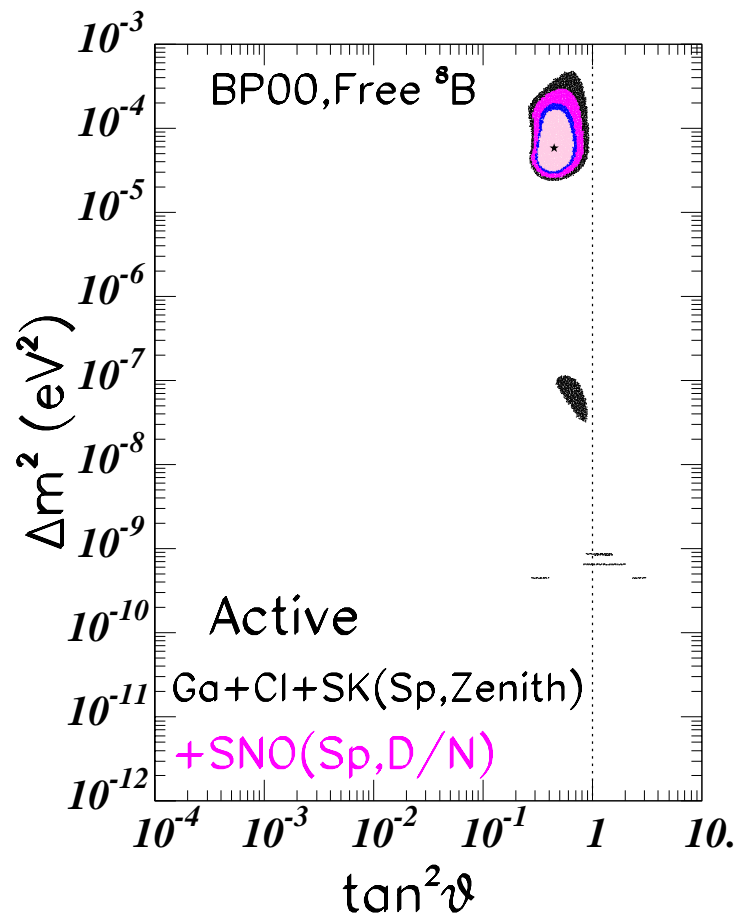
Figure A.2: A global fit to all solar neutrino data made by authors Bahcall *et al.* [1].

With regard to the *number* of distinct allowed regions, there is very good agreement between the our analysis of Fig. 4.5 and that of Fig. A.2. The only difference is some marginally allowed regions (99.73 % c.l.) around $\Delta m^2 \approx 10^{-9} - 10^{-7}$. A more serious disagreement is with the *size* of the allowed Large Mixing Angle (LMA) region at $\Delta m^2 \approx 10^{-5} - 10^{-4}$. The SNO analysis presents a much more constrained allowed region, around half the size of Fig. A.2. This difference has not yet been resolved, although a number of possibilities are being considered.
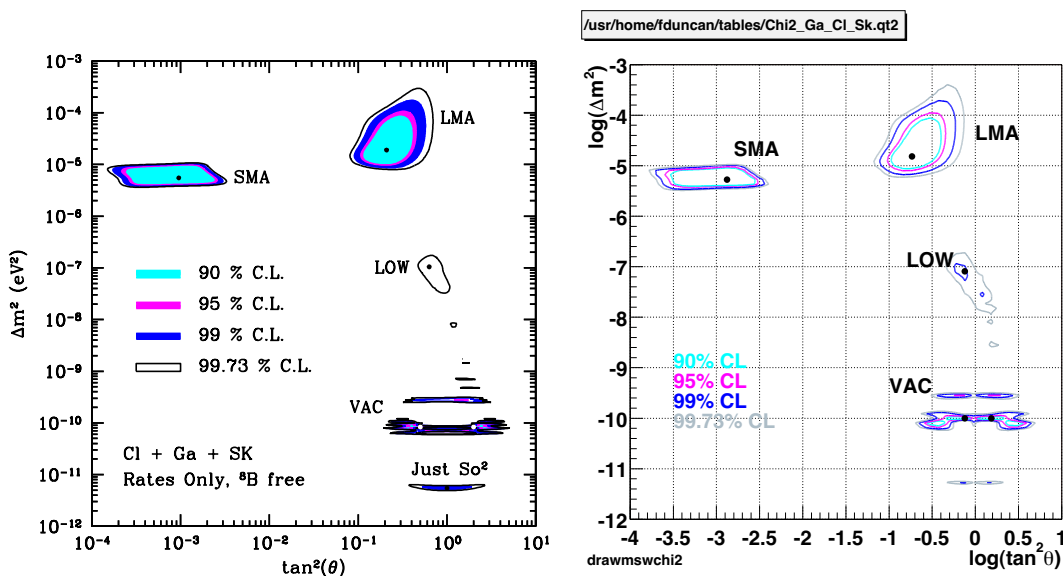
Figure A.3: A global fit to solar neutrino data, prior to the addition of SNO data. The left hand panel is taken from [14]. The right hand panel is created by SNO analysis tools and was provided by Fraser Duncan and Mark Chen.

Fig. A.3 shows us that both analyses treat the Gallium, Chlorine and H_2O experiments in an almost identical way. Therefore, the differences in the final allowed regions must be introduced by the addition of SNO data.

One possibility is that the our analysis is in error because it has neglected some important theoretical systematics (see Section 5.2). For example, the uncertainty in the NC and CC cross sections were neglected. However, these two uncertainties

are small and are correlated, largely cancelling in the measurement of the survival probability P_{ee}. They are suspected to play a small yet significant contribution to the uncertainty in ϕ_{tot}, but not in the MSW contours. In addition, the error in the CC spectral shape is neglected. This again is small and has a similar effect to the much larger energy scale uncertainty. Although we suspect these uncertainties to play only a minor role, one can not be completely sure until we have incorporated them into the set of SNO systematics. Work is underway to do this.

An interesting note is that the LMA region of Fig. A.3 does not come particularly close to the *dark side* ($ln \tan^2 \theta > 0$). In Fig. 1.6, we saw that $P_{ee} \approx 0.5$ at $ln \tan^2 \theta = 0$. However, SNO data provides a clear experimental measurement that P_{ee} is significantly less than 0.5. It is therefore surprising that the addition of SNO data could lead to $ln \tan^2 \theta = 0$ being *less* strongly rejected, as shown in Fig. A.2. Understanding this feature might help understand the differences between the two analyses.

Appendix B

NEUTRAL CURRENT DETECTORS

B.1 Description

The Neutral Current Detectors (NCDs) are an array of proportional counters to be deployed into the SNO heavy water volume, as shown in Fig. B.1. Each NCD is made from a thin walled tube of Chemically Vapor Deposited (CVD) Nickel, is 5 cm in diameter and varies from 200 cm to 300 cm in length. The CVD process assures high radiopurity for the bulk of the material that makes up the NCD. Each detector is filled with a mix of 85% ^{3}He and 15% CF_4, with the gas being contained by CVD Nickel endcaps, and has a Cu wire anode running down the center. A group of NCDs are welded together into an electrically continuous *string*, as shown in Fig. B.2.

NCDs detect thermal neutrons via the interaction

$$n +^3 He \rightarrow p +^3 H^+ \tag{B.1}$$

The proton and triton carry away a combined energy of 764 keV, which is deposited into the gas as ionization. The ionized electrons drift towards the Cu wire (held at +1825 V). As they approach the region immediately surrounding the wire, the high electric field causes an avalanche of secondary electrons, with these collecting at the wire to provide the NCD signal. The signal is read out *via* a 91-ohm coaxial cable at the top end of a string, with the cable also providing the high voltage. A delay line at the bottom end of the string lengthens it electronically. This increases the separation between the primary and reflected signals and allows for position discrimination along the active length of the string.

Events in the NCD gas with energy above $\approx 100 keV$ are digitized.
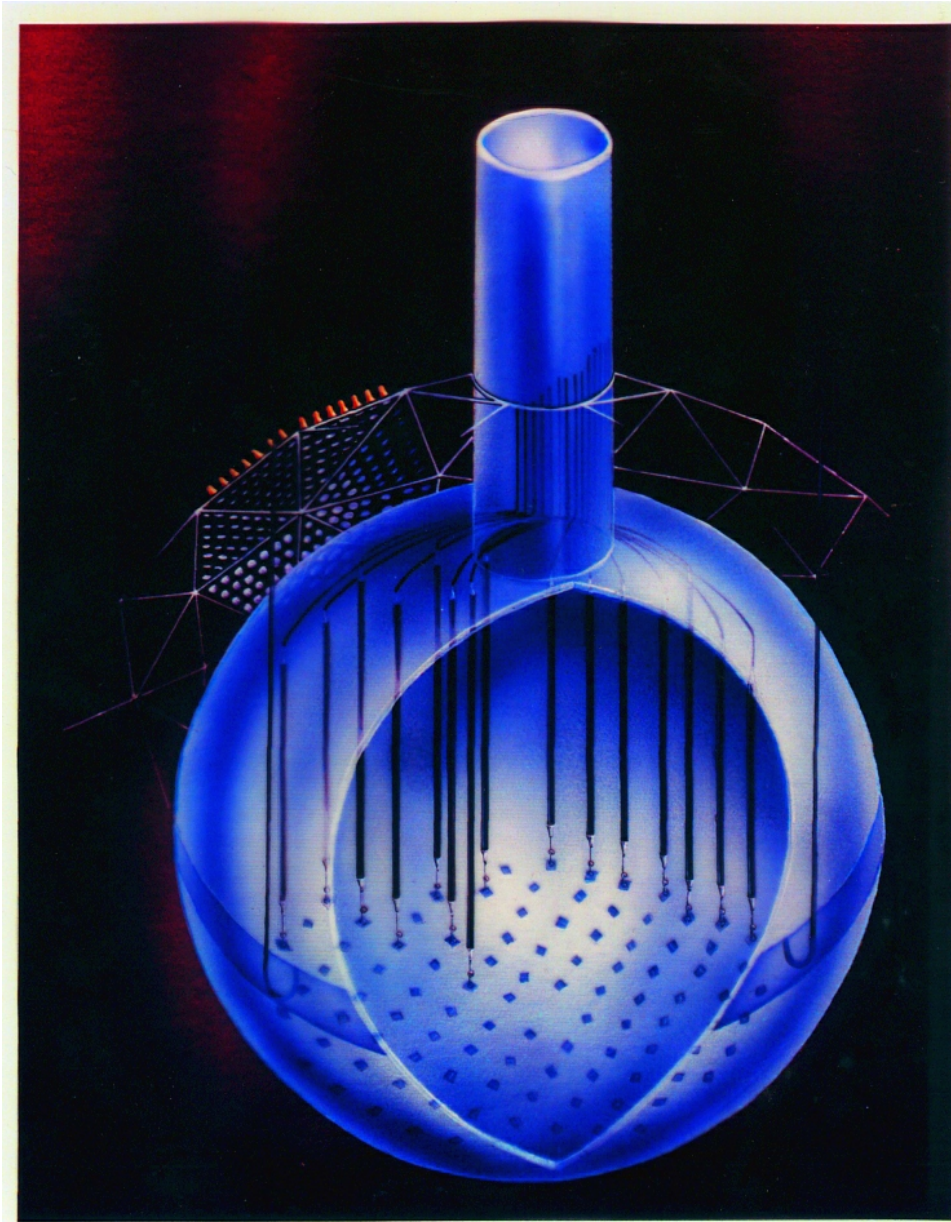
Figure B.1: The NCD array partially deployed into the SNO D_2O.
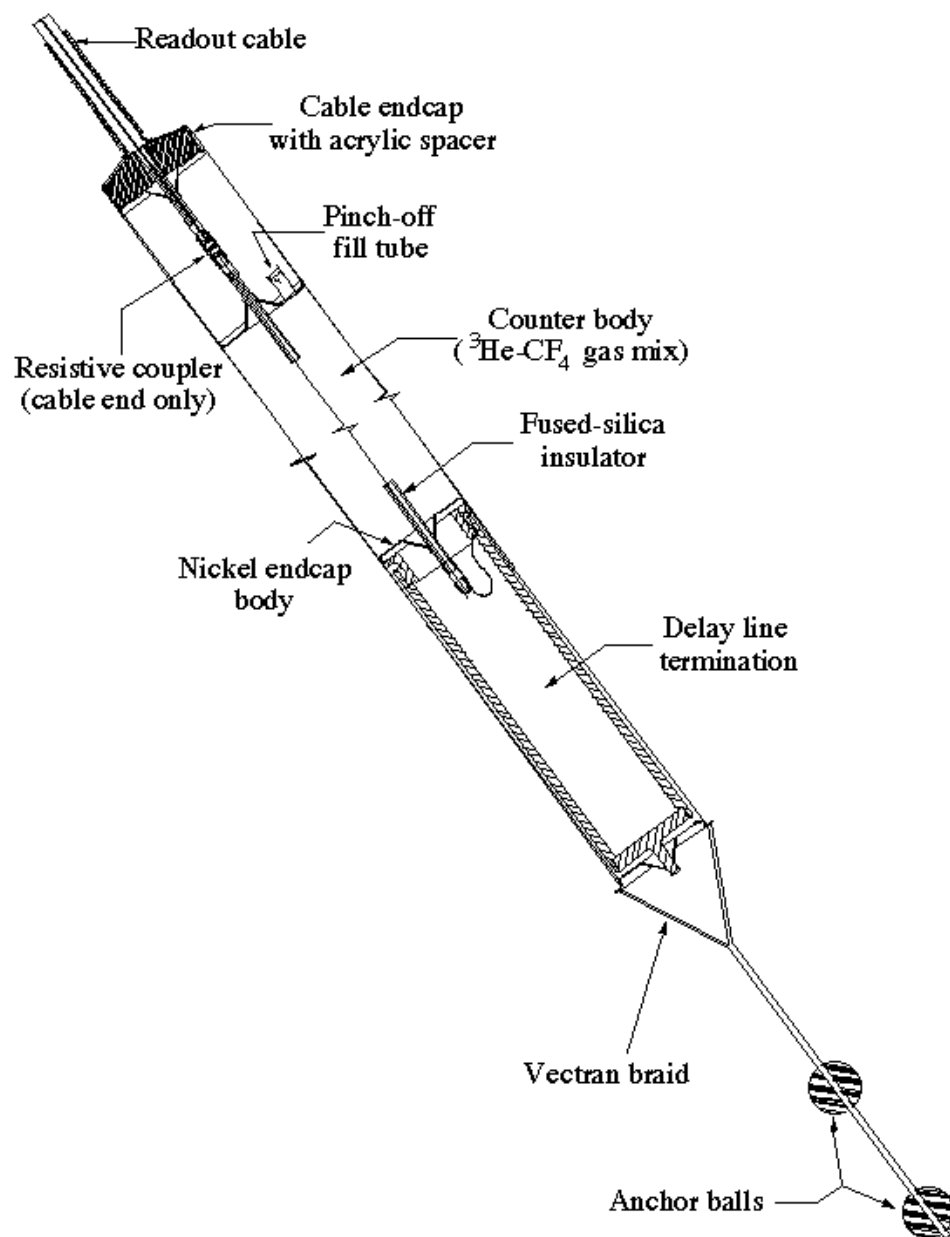
Figure B.2: Cross section of an NCD string.

B.2   Construction

Radioactive contaminants of the NCD materials can produce background events in a number of ways.

- β-γ decays of U and Th in the nickel can produce Cherenkov light that triggers the SNO PMT array.

- These chains both produce a γ with sufficient energy to photodisintegrate deuterium, generating a neutron background identical to the NC reaction. These neutrons produce a measurable signal by capturing either on ^{3}He or on D_2O. In addition, cosmic ray activation of nickel can produce ^{56}Co, which also produces a γ with sufficient energy to photodisintegrate deuterium.

- α decays of U and Th in the bulk nickel can ionize the ^{3}He gas. If the majority of the α energy is deposited in the the Ni, rather than the gas, the measured energy can be similar to that of a neutron capture on ^{3}He (764 keV).

- Surface contamination by ^{210}Po produces 5.3 MeV α's. Depending on the orientation of the ionization track, just a fraction of the energy can be deposited into the gas.

- Tritium in the ^{3}He gas produces β's with an endpoint of 18.6 keV. If there is a sufficient pileup of tritium decays, they can trigger the NCD electronics and perhaps mimic a neutron capture event.

We went to great lengths to achieve radioactive purity. The construction materials were radioassayed to ensure their low contamination levels. In addition, the NCDs were built under class 1000 cleanroom conditions, to avoid the accumulation of dust. The detectors have been stored underground for many half lives of ^{56}Co (78 days), thus mitigating this particular source. A purification system was used to remove tritium from the ^{3}He gas. A number of hurdles had to be overcome to achieve this goal, and some of these are presented here.

B.2.1   Aluminum Contamination

The CVD process deposits nickel from a carbonyl vapor onto a 2-inch diameter anodized aluminum mandrel. When the desired thickness is reached, the nickel is separated by differential contraction by cooling. Due to imperfections in the mandrel, some aluminum oxide may adhere to the inner nickel surface. Aluminum is known to contain thorium at the 1-10 ppm level. Since we require the nickel to be < 10 ppt Th, aluminum becomes a concern at the 1-10 ppm level.

Scanning Electron Microscopy (SEM) reveals the shape and chemical makeup of the nickel surface. A particularly bad area is shown in the left hand side of Fig. B.3. A beam of 20 keV electrons, 60 Angstroms wide, scans across the sample, imaging the surface. Flat flakes of aluminum oxide appear dark and the rough nickel appear as various shades of gray. Elemental abundances are determined from the scattered x rays, averaged over a depth of approximately 2 μm.

Etching of the tubes in a 10 minute bath of 4M nitric + 0.2M HF acid cleans up the surface considerably, as shown in the right hand side of Fig. B.3. An SEM scan detects no aluminum to within a sensitivity of approximately 0.5%.

Seeking a higher sensitivity for aluminum, the problem was pursued using Inductively Coupled Plasma Mass Spectroscopy (ICPMS). ICPMS works by vaporizing a fluid sample and drawing it into a plasma torch. After the sample is ionized, it is accelerated and electrostatically steered, so as to identify the various mass components. Nickel segments were etched in 4M nitric, 0.2M HF acid baths and the left over solution was analyzed. The Al concentration of the bath was measured using ICPMS, while the Ni content was determined by weighing the segments before and after, also allowing one to calculate how deeply the nickel was etched. Backgrounds were determined by subjecting blank samples of nitric + HF acid to the same reduction and analysis.
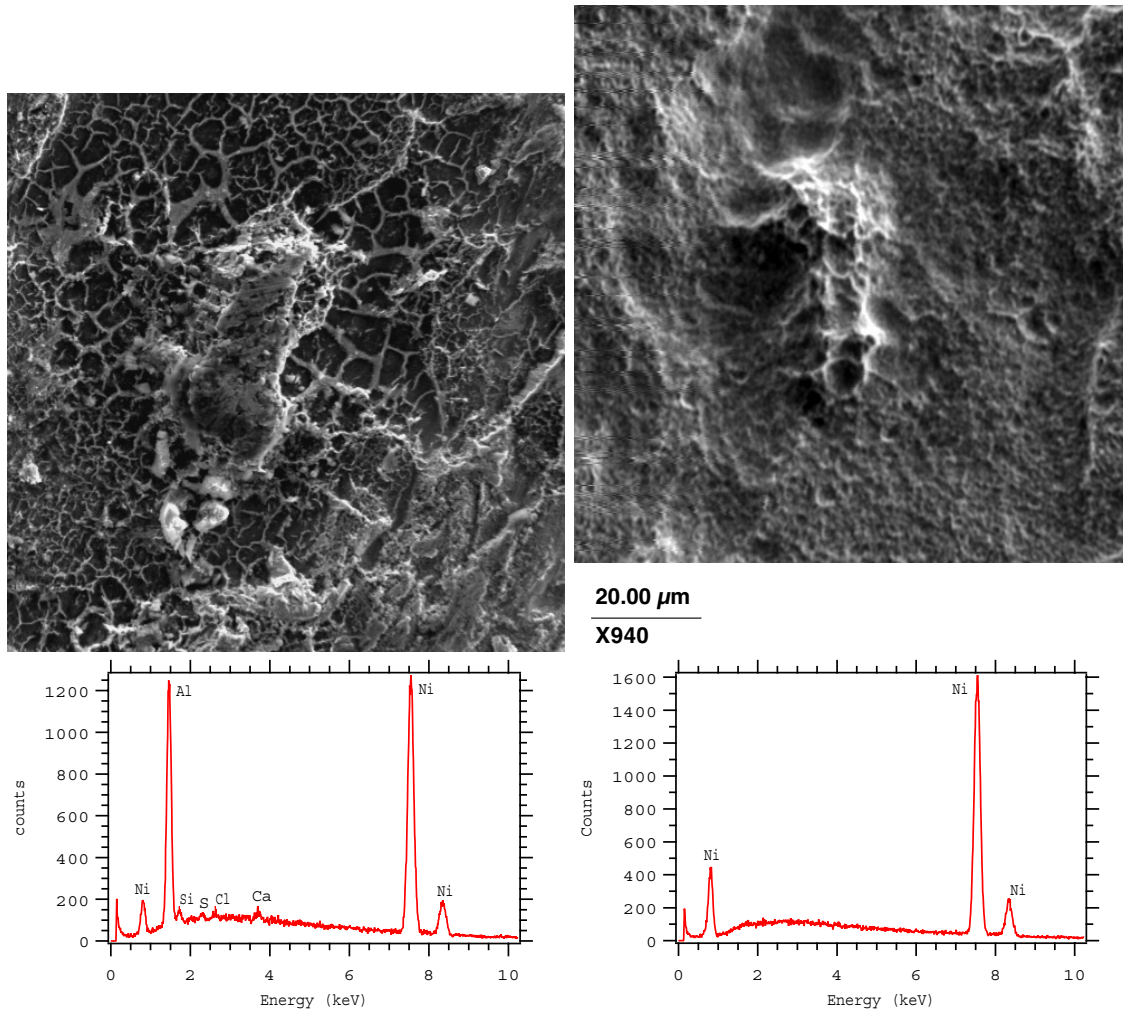
Figure B.3: A region of a nickel tube before and after acid etching, as viewed with a scanning electron microscope.

These results are also shown in Fig. B.4. If one does a linear extrapolation of the last four data points, one finds an x-intercept of $10.6 \pm 2.2 \mu m$. This result should be taken somewhat loosely, as we have made no argument for a linear fit and the data points do not represent the aluminum contamination at particular depths but rather the integrated contamination over a given depth range. However, this result still proves useful in defining the depth required for mitigating aluminum. Prior to this study, tubes were being etched for only 10 minutes, removing approximately $2\mu m$ of nickel from each side. As a consequence of this work it was decided that significantly more nickel needed to be removed from the inner surface of the tube. A procedure was implemented for electropolishing the inner surface to a depth of approximately $20\mu m$ (see section B.2.2). This is followed by an etch which removes an additional $2\mu m$ from each side, thus removing a total of approximately $22\mu m$ of material from the inner surface. Even if this linear fit is incorrect, one can still argue that the total aluminum contamination is less than 1 ppm. As the SEM photographs showed, the contamination is in the form of aluminum oxide flakes. The sections of nickel tube used in this study were deposited onto a mandrel that had a $25\mu m$ anodized layer and so one expects the contamination to go no deeper than this. The last data point is 31 ± 5 ppm (at 9 μm). Tubes are typically 0.015 - 0.020 inches thick. In a worst case scenario, if this contamination extended uniformly all the way to $25\mu m$ and we remove $22\mu m$ from electropolishing and etching, one would get an aluminum contamination of 0.2 - 0.3 ppm, averaged over the entire nickel. This is an extreme upper limit. However, many NCD tubes were laid down on a mandrel with $38\mu m$ of anodizing. Scaling to this case, the linear fit to the tail of this profile would extend the contamination to around $16 \pm 3\mu m$. The worst case scenario argument would give an upper limit of 0.9 - 1.5 ppm, averaged over the entire nickel.
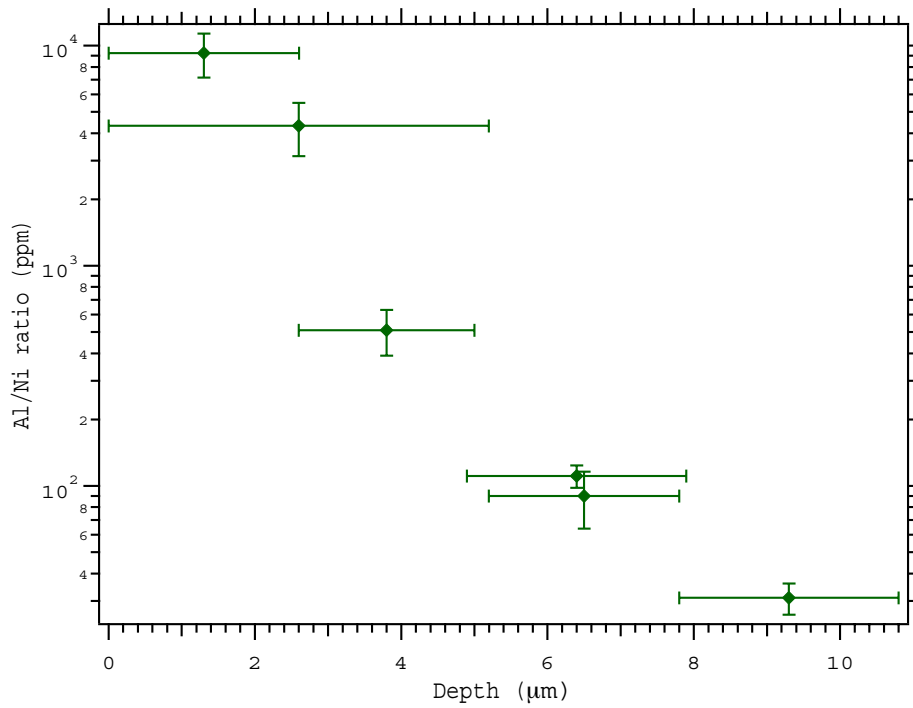
Figure B.4: Al/Ni ratio as a function of depth in an NCD tube, as determined by ICPMS. The vertical error bars are the uncertainties in the Al/Ni ratio. The horizontal bars are not errors but rather represent the range over which the sample was etched.

B.2.2 ^{210}Po Contamination

To avoid cosmic activation of the NCD nickel into ^{56}Co, the NCD tubes were stored prior to construction in a man-made cave near the town of Index, WA. This turned out to be a grave error because the granite walls of the cave emanated high levels of airborne ^{222}Rn. Its daughter product ^{210}Po (138 day half life) easily plates out on Ni surfaces. This subsequently decays via α-emission into the stable ^{206}Pb. The Po contamination led to extremely high α rates in the NCD gas. To remove this plated Po, a serious R&D effort was undertaken, leading to the construction and implementation of an electropolishing procedure. Purely chemical etches were unsuccessful because Ni displaces Po in solution and the Po remains on the surface.
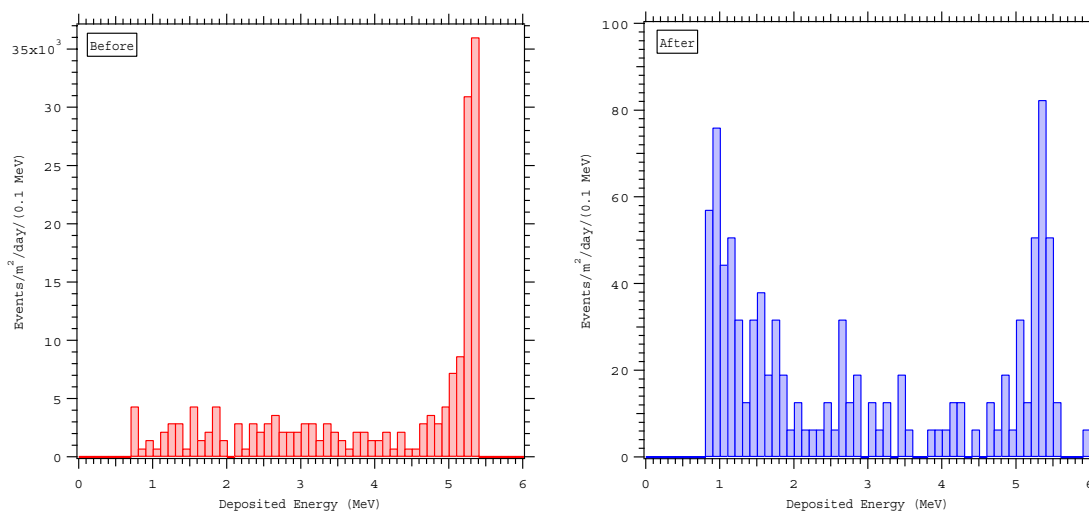
Figure B.5: Spectra of deposited energy in the NCD gas, before and after Po removal. The peak at 5.3 MeV corresponds to the α from the decay of ^{210}Po. The low energy tail is due to α events which do not deposit all of their energy and due to cosmic rays. The α tail is more prominent for the high rate data, shown in the left hand panel. The cosmic rays are more prominent for the much longer duration data on the right, where one should note the different vertical scale.

To optimize this procedure, a test bench was set up, where a temporary anode could be sealed inside a nickel tube. P-10 gas was flowed down the length of the tube, providing for α ionization. Calibration of the set up was made with the gamma emission of ^{241}Am. Figure B.5 shows the ionization spectra, both before and after electropolishing, of a typical tube that was stored at Index. Figure B.6 shows how a series of etches and polishes reduces the Po levels in a particular tube.
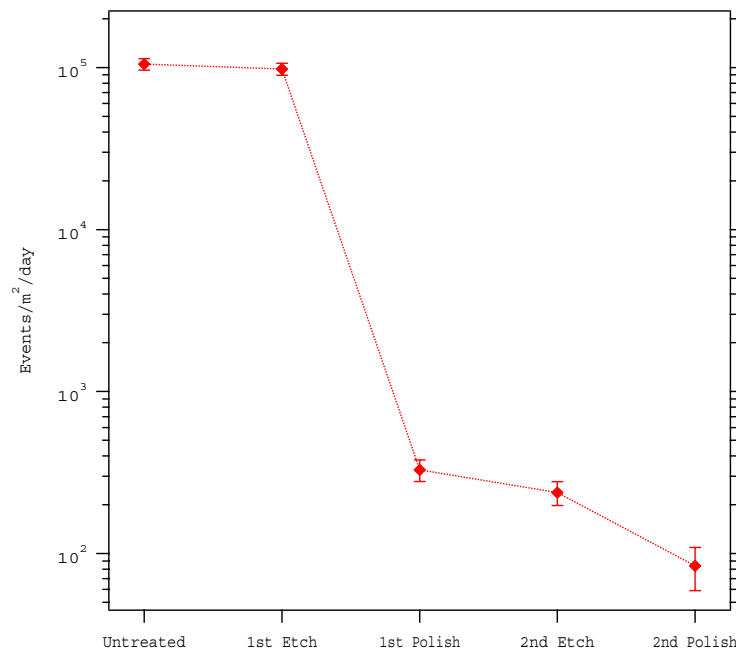
Figure B.6: Po levels as a function of etching and electropolishing. Note that etching leads to almost no reduction of the Po contamination, while electropolishing leads to a significant reduction. The Po *peak* is defined as ranging from 0.7 to 3.7 × 5.8 MeV.

B.2.3 ^3H contamination

The ^{3}He used to fill NCDs was recovered from the decay of 1950's tritium. An extensive effort was undertaken to remove residual tritium, typically in the form of HTO and T_2O. This included using a SAES Getter and various LN2 cold traps. The quantity of residual tritium is measured after raising the voltage of the NCDs to 2225 V, thus raising their gain and pulling the tritium β-spectrum out of the noise. The result of these tritium measurements are shown for 222 of the NCDs in Fig. B.7. Most NCDs were constructed with less than the specified 2.7 nCi/l. This specification was designed to keep the rate of tritium pileup to a manageable level. In a 10 m string, 2.7 nCi/l corresponds to 5000 Hz of β decay. At this rate, we expect a pileup of more than 5 β events (in the 4 μs NCD trigger widow) to occur less than once a year. Only for $n > 5$ can the β pileup lead to digitized events with energy above 100 keV.
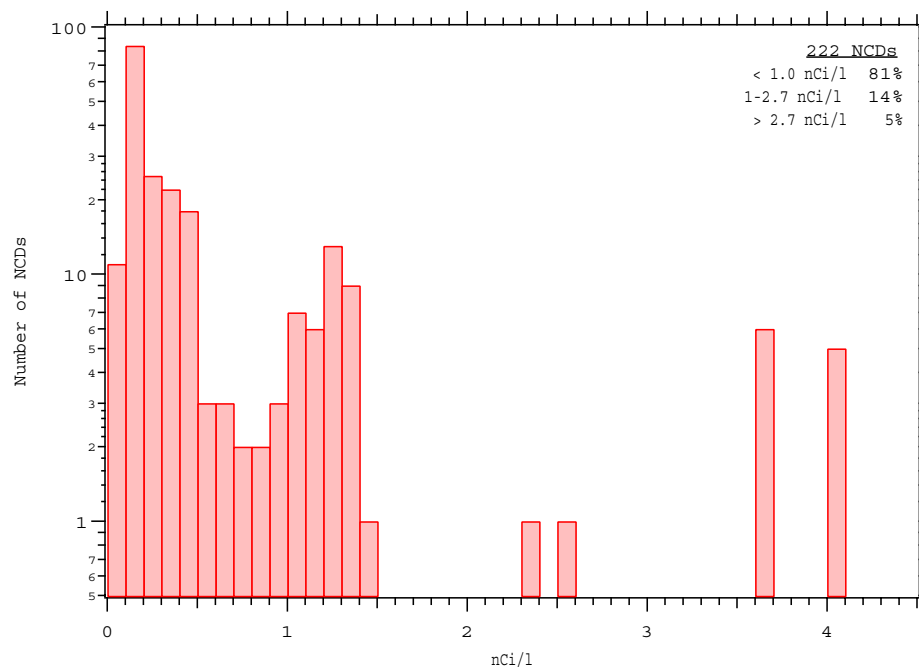
Figure B.7: Distribution of tritium contamination for 222 of the NCDs.

Appendix C

SNO PUBLICATIONS

Measurement of charged current interactions produced by ^{8}B solar neutrinos at the Sudbury Neutrino Observatory

Q.R. Ahmad[15], R.C. Allen[11], T.C. Andersen[12], J.D. Anglin[7], G. Bühler[11], J.C. Barton[13‡], E.W. Beier[14],
M. Bercovitch[7], J. Bigu[4], S. Biller[13], R.A. Black[13], I. Blevis[6,13], R.J. Boardman[13], J. Boger[1], E. Bonvin[9],
M.G. Boulay[9], M.G. Bowler[13], T.J. Bowles[6], S.J. Brice[6,13], M.C. Browne[15], T.V. Bullard[15], T.H. Burritt[15,6],
K. Cameron[12], J. Cameron[13], Y.D. Chan[5], M. Chen[9], H.H. Chen[11*], X. Chen[5,13], M.C. Chon[12], B.T. Cleveland[13],
E.T.H. Clifford[9,3], J.H.M. Cowan[4], D.F. Cowen[14], G.A. Cox[15], Y. Dai[9], X. Dai[13], F. Dalnoki-Veress[2],
W.F. Davidson[7], P.J. Doe[15,11,6], G. Doucas[13], M.R. Dragowsky[6,5], C.A. Duba[15], F.A. Duncan[9], J. Dunmore[13],
E.D. Earle[9,3], S.R. Elliott[15,6], H.C. Evans[9], G.T. Ewan[9], J. Farine[2], H. Fergani[13], A.P. Ferraris[13], R.J. Ford[9],
M.M. Fowler[6], K. Frame[13], E.D. Frank[14], W. Frati[14], J.V. Germani[15,6], S. Gil[10], A. Goldschmidt[6], D.R. Grant[2],
R.L. Hahn[1], A.L. Hallin[9], E.D. Hallman[4], A. Hamer[6,9], A.A. Hamian[15], R.U. Haq[4], C.K. Hargrove[2], P.J. Harvey[9],
R. Hazama[15], R. Heaton[9], K.M. Heeger[15], W.J. Heintzelman[14], J. Heise[10], R.L. Helmer[10†], J.D. Hepburn[9,3],
H. Heron[13], J. Hewett[4], A. Hime[6], M. Howe[15], J.G. Hykawy[4], M.C.P. Isaac[5], P. Jagam[12], N.A. Jelley[13], C. Jillings[9],
G. Jonkmans[4,3], J. Karn[12], P.T. Keener[14], K. Kirch[6], J.R. Klein[14], A.B. Knox[13], R.J. Komar[10,9], R. Kouzes[8],
T. Kutter[10], C.C.M. Kyba[14], J. Law[12], I.T. Lawson[12], M. Lay[13], H.W. Lee[9], K.T. Lesko[5], J.R. Leslie[9], I. Levine[2],
W. Locke[13], M.M. Lowry[8], S. Luoma[4], J. Lyon[13], S. Majerus[13], H.B. Mak[9], A.D. Marino[5], N. McCauley[13],
A.B. McDonald[9,8], D.S. McDonald[14], K. McFarlane[2], G. McGregor[13], W. McLatchie[9], R. Meijer Drees[15], H. Mes[2],
C. Mifflin[2], G.G. Miller[6], G. Milton[3], B.A. Moffat[9], M. Moorhead[13], C.W. Nally[10], M.S. Neubauer[14],
F.M. Newcomer[14], H.S. Ng[10], A.J. Noble[2†], E.B. Norman[5], V.M. Novikov[2], M. O'Neill[2], C.E. Okada[5],
R.W. Ollerhead[12], M. Omori[13], J.L. Orrell[15], S.M. Oser[14], A.W.P. Poon[5,6,10,15], T.J. Radcliffe[9], A. Roberge[4],
B.C. Robertson[9], R.G.H. Robertson[15,6], J.K. Rowley[1], V.L. Rusu[14], E. Saettler[4], K.K. Schaffer[15], A. Schuelke[5],
M.H. Schwendener[4], H. Seifert[4,6,15], M. Shatkay[2], J.J. Simpson[12], D. Sinclair[2], P. Skensved[9], A.R. Smith[5],
M.W.E. Smith[15], N. Starinsky[2], T.D. Steiger[15], R.G. Stokstad[5], R.S. Storey[7*], B. Sur[3,9], R. Tafirout[4], N. Tagg[12],
N.W. Tanner[13], R.K. Taplin[13], M. Thorman[13], P. Thornewell[6,13,15] P.T. Trent[13‡], Y.I. Tserkovnyak[10], R. Van
Berg[14], R.G. Van de Water[14,6], C.J. Virtue[4], C.E. Waltham[10], J.-X. Wang[12], D.L. Wark[13,6§], N. West[13],
J.B. Wilhelmy[6], J.F. Wilkerson[15,6], J. Wilson[13], P. Wittich[14], J.M. Wouters[6], M. Yeh[1]

(The SNO Collaboration)

[1] Chemistry Department, Brookhaven National Laboratory, Upton, NY 11973-5000
[2] Carleton University, Ottawa, Ontario K1S 5B6 Canada
[3] Chalk River Laboratories, AECL Research, Chalk River, Ontario K0J 1J0 Canada
[4] Department of Physics and Astronomy, Laurentian University, Sudbury, Ontario P3E 2C6 Canada
[5] Institute of Nuclear and Particle Astrophysics and Nuclear Science Division, Lawrence Berkeley National Laboratory,
Berkeley, CA 94720
[6] Los Alamos National Laboratory, Los Alamos, NM 87545
[7] National Research Council of Canada, Ottawa, Ontario K1A 0R6 Canada
[8] Department of Physics, Princeton University, Princeton, NJ 08544
[9] Department of Physics, Queen's University, Kingston, Ontario K7L 3N6 Canada
[10] Department of Physics and Astronomy, University of British Columbia, Vancouver, BC V6T 1Z1 Canada
[11] Department of Physics, University of California, Irvine, CA 92717
[12] Physics Department, University of Guelph, Guelph, Ontario N1G 2W1 Canada
[13] Nuclear and Astrophysics Laboratory, University of Oxford, Keble Road, Oxford, OX1 3RH, UK
[14] Department of Physics and Astronomy, University of Pennsylvania, Philadelphia, PA 19104-6396,
[15] Center for Experimental Nuclear Physics and Astrophysics, and Department of Physics, University of Washington, Seattle,
WA 98195
(18 June 2001)

Solar neutrinos from the decay of ^{8}B have been detected at the Sudbury Neutrino Observatory (SNO) via the charged current (CC) reaction on deuterium and by the elastic scattering (ES) of electrons. The CC reaction is sensitive exclusively to ν_e's, while the ES reaction also has a small sensitivity to ν_μ's and ν_τ's. The flux of ν_e's from ^{8}B decay measured by the CC reaction rate is $\phi^{CC}(\nu_e) = 1.75 \pm 0.07$ (stat.)$^{+0.12}_{-0.11}$ (sys.) ± 0.05 (theor.) $\times 10^6$ cm^{-2}s^{-1}. Assuming no flavor tranformation, the flux inferred from the ES reaction rate is $\phi^{ES}(\nu_x) = 2.39 \pm 0.34$ (stat.)$^{+0.16}_{-0.14}$ (sys.)$\times 10^6$ cm^{-2}s^{-1}. Comparison of $\phi^{CC}(\nu_e)$ to the Super-Kamiokande Collaboration's precision value of $\phi^{ES}(\nu_x)$ yields a 3.3σ difference, providing evidence that there is a non-electron flavor active neutrino component in the solar flux. The total flux of active ^{8}B neutrinos is thus determined to be $5.44 \pm 0.99 \times 10^6$ cm^{-2}s^{-1}, in close agreement with the predictions of solar models.

1

160

Solar neutrino experiments over the past 30 years [1–6] have measured fewer neutrinos than are predicted by models of the Sun [7,9]. One explanation for the deficit is the transformation of the Sun's electron-type neutrinos into other active flavors. The Sudbury Neutrino Observatory (SNO) measures the ^{8}B solar neutrinos through the reactions:
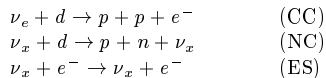
$$\nu_e + d \rightarrow p + p + e^- \qquad \text{(CC)}$$
$$\nu_x + d \rightarrow p + n + \nu_x \qquad \text{(NC)}$$
$$\nu_x + e^- \rightarrow \nu_x + e^- \qquad \text{(ES)}$$

The charged current reaction (CC) is sensitive exclusively to electron-type neutrinos, while the neutral current (NC) is sensitive to all active neutrino flavors ($x = e, \mu, \tau$). The elastic scattering (ES) reaction is sensitive to all flavors as well, but with reduced sensitivity to ν_μ and ν_τ. By itself, the ES reaction cannot provide a measure of the total ^{8}B flux or its flavor content. Comparison of the ^{8}B flux deduced from the ES reaction assuming no neutrino oscillations ($\phi^{\text{ES}}(\nu_x)$), to that measured by the CC reaction ($\phi^{\text{CC}}(\nu_e)$) can provide clear evidence of flavor transformation without reference to solar model flux calculations. If neutrinos from the Sun change into other active flavors, then $\phi^{\text{CC}}(\nu_e) < \phi^{\text{ES}}(\nu_x)$.

This Letter presents the first results from SNO on the ES and CC reactions. SNO's measurement of $\phi^{\text{ES}}(\nu_x)$ is consistent with previous measurements described in Ref [5]. The measurement of $\phi^{\text{CC}}(\nu_e)$, however, is significantly smaller than the measurements by [5] and is inconsistent with the null hypothesis that all observed solar neutrinos are ν_e. A measurement using the NC reaction, which has equal sensitivity to all neutrino flavors, will be reported in a future publication.

SNO [12] is an imaging water Čerenkov detector located at a depth of 6010 m of water equivalent in the INCO, Ltd. Creighton mine near Sudbury, Ontario. It features 1000 metric tons of ultra-pure D$_2$O contained in a 12 m diameter spherical acrylic vessel. This sphere is surrounded by a shield of ultra-pure H$_2$O contained in a 34 m high barrel-shaped cavity of maximum diameter 22 m. A stainless steel structure 17.8 m in diameter supports 9456 20-cm photomultiplier tubes (PMTs) with light concentrators. Approximately 55% of the light produced within 7 m of the center of the detector will strike a PMT.

The data reported here were recorded between Nov. 2, 1999 and Jan. 15, 2001 and correspond to a live time of 240.95 days. Events are defined by a multiplicity trigger of 18 or more PMTs exceeding a threshold of ~ 0.25 photo-electrons within a time window of 93 ns. The trigger reaches 100% efficiency at 23 PMTs. The total instantaneous trigger rate is 15-18 Hz, of which 6-8 Hz is the data trigger. For every event trigger, the time and charge responses of each participating PMT are recorded.

The data were partitioned into two sets, with approximately 70% used to establish the data analysis proce-

TABLE I. Data reduction steps.

Analysis step	Number of events
Total event triggers	355 320 964
Neutrino data triggers	143 756 178
$N_{\text{hit}} \geq 30$	6 372 899
Instrumental background cuts	1 842 491
Muon followers	1 809 979
High level cuts[a]	923 717
Fiducial volume cut	17 884
Threshold cut	1 169
Total events	1 169

[a]Reconstruction figures of merit, prompt light, and $\langle \theta_{ij} \rangle$.

dures and 30% reserved for a blind test of statistical bias in the analysis. The analysis procedures were frozen before the blind data set was analyzed, and no statistically significant differences in the data sets were found. We present here the analysis of the combined data sets.

Calibration of the PMT time and charge pedestals, slopes, offsets, charge vs. time dependencies, and second order rate dependencies are performed using electronic pulsers and pulsed light sources. Optical calibration is obtained using a diffuse source of pulsed laser light at 337, 365, 386, 420, 500 and 620 nm. The absolute energy scale and uncertainties are established with a triggered ^{16}N source (predominantly 6.13-MeV γ's) deployed over two planar grids within the D$_2$O and a linear grid in the H$_2$O. The resulting Monte Carlo predictions of detector response are tested using a ^{252}Cf neutron source, which provides an extended distribution of 6.25-MeV γ rays from neutron capture, and a ^{3}H$(p,\gamma)^4$He [13] source providing 19.8-MeV γ rays. The volume-weighted mean response is approximately nine PMT hits per MeV of electron energy.

Table I details the steps in data reduction. The first of these is the elimination of instrumental backgrounds. Electrical pickup may produce false PMT hits, while electrical discharges in the PMTs or insulating detector materials produce light. These backgrounds have characteristics very different from Čerenkov light, and are eliminated using cuts based only on the PMT positions, the PMT time and charge data, event-to-event time correlations, and veto PMTs. This step in the data reduction is verified by comparing results from two independent background rejection analyses.

For events passing the first stage, the calibrated times and positions of the hit PMTs are used to reconstruct the vertex position and the direction of the particle. The reconstruction accuracy and resolution are measured using Compton electrons from the ^{16}N source, and the energy and source variation of reconstruction are checked with a ^{8}Li β source. Angular resolution is measured using Compton electrons produced more than 150 cm from the ^{16}N source. At these energies, the vertex resolution is 16 cm and the angular resolution is 26.7 degrees.

An effective kinetic energy, T_{eff}, is assigned to each event passing the reconstruction stage. T_{eff} is calculated using prompt (unscattered) Čerenkov photons and the position and direction of the event. The derived energy response of the detector can be characterized by a Gaussian:

$$R(E_{\text{eff}}, E_e) = \frac{1}{\sqrt{2\pi}\sigma_E(E_e)} \exp[-\frac{1}{2}(\frac{E_{\text{eff}} - E_e}{\sigma_E(E_e)})^2]$$

where E_e is the total electron energy, $E_{\text{eff}} = T_{\text{eff}} + m_e$, and $\sigma_E(E_e) = (-0.4620 + 0.5470\sqrt{E_e} + 0.008722E_e)$ MeV is the energy resolution. The uncertainty on the energy scale is found to be $\pm 1.4\%$. For validation, a second energy estimator counts all PMTs hit in each event, N_{hit}, without position and direction corrections.

Further instrumental background rejection is obtained using reconstruction figures of merit, PMT time residuals, and the average angle between hit PMTs ($\langle \theta_{ij} \rangle$), measured from the reconstructed vertex. These cuts test the hypothesis that each event has the characteristics of single electron Čerenkov light. The effects of these and the rest of the instrumental background removal cuts on neutrino signals are quantified using the ^{8}Li and ^{16}N sources deployed throughout the detector. The volume-weighted neutrino signal loss is measured to be $1.4^{+0.7}_{-0.6}\%$ and the residual instrumental contamination for the data set within the D_2O is $< 0.2\%$. Lastly, cosmic ray induced neutrons and spallation products are removed based upon their time coincidence with the parent muon.

Figure 1 shows the radial distribution of all remaining events above a threshold of $T_{\text{eff}} \geq 6.75$ MeV. The distribution is expressed as a function of the volume-weighted radial variable $(R/R_{\text{AV}})^3$, where $R_{\text{AV}} = 6.00$ m is the radius of the acrylic vessel. Above this energy threshold, there are contributions from CC events in the D_2O, ES events in the D_2O and H_2O, a residual tail of neutron capture events, and high energy γ rays from radioactivity in the outer detector. The data show a clear signal within the D_2O volume. For $(R/R_{\text{AV}})^3 > 1.0$ the distribution rises into the H_2O region until it is cut off by the acceptance of the PMT light collectors at $R \sim 7.0$ m. A fiducial volume cut is applied at $R = 5.50$ m to reduce backgrounds from regions exterior to the D_2O, and to minimize systematic uncertainties associated with optics and reconstruction near the acrylic vessel.

Possible backgrounds from radioactivity in the D_2O and H_2O are measured by regular low level radio-assays of U and Th decay chain products in these regions. The Čerenkov light character of D_2O and H_2O radioactivity backgrounds is used *in situ* to monitor backgrounds between radio-assays. Low energy radioactivity backgrounds are removed by the high threshold imposed, as are most neutron capture events. Monte Carlo calculations predict that the H_2O shield effectively reduces contributions of low energy (< 4 MeV) γ rays from the PMT
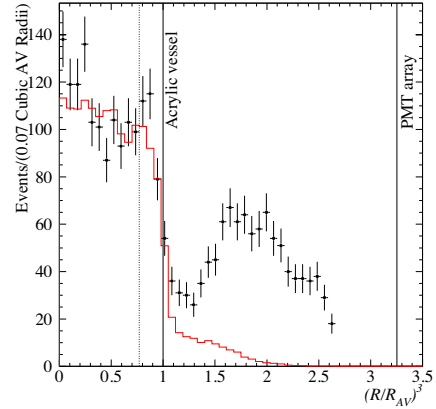

FIG. 1. Distribution of event candidates with $T_{\text{eff}} \geq 6.75$ MeV as a function of the volume weighted radial variable $(R/R_{AV})^3$. The Monte Carlo simulation of the signals, weighted by the results from the signal extraction, is shown as a histogram. The dotted line indicates the fiducial volume cut used in this analysis.

array, and these predictions are verified by deploying an encapsulated Th source in the vicinity of the PMT support sphere. High energy γ rays from the cavity are also attenuated by the H_2O shield. A limit on their leakage into the fiducial volume is estimated by deploying the ^{16}N source near the edge of the detector's active volume. The total contribution from all radioactivity in the detector is found to be $<0.2\%$ for low energy backgrounds and $<0.8\%$ for high energy backgrounds.

The final data set contains 1169 events after the fiducial volume and kinetic energy threshold cuts. Figure 2 (a) displays the distribution of $\cos\theta_\odot$, the angle between the reconstructed direction of the event and the instantaneous direction from the Sun to the Earth. The forward peak in this distribution arises from the kinematics of the ES reaction, while CC electrons are expected to have a distribution which is $(1 - 0.345\cos\theta_\odot)$, before accounting for detector response.

The data are resolved into contributions from CC, ES, and neutron events above threshold using probability density functions (pdfs) in T_{eff}, $\cos\theta_\odot$, and $(R/R_{\text{AV}})^3$, generated from Monte Carlo simulations assuming no flavor transformation and the shape of the standard ^{8}B spectrum [11] (*hep* neutrinos are not included in the fit). The extended maximum likelihood method used in the signal extraction yields 975.4±39.7 CC events, 106.1±15.2 ES events, and 87.5±24.7 neutron events for the fiducial volume and the threshold chosen, where the uncertainties given are statistical only. The dominant
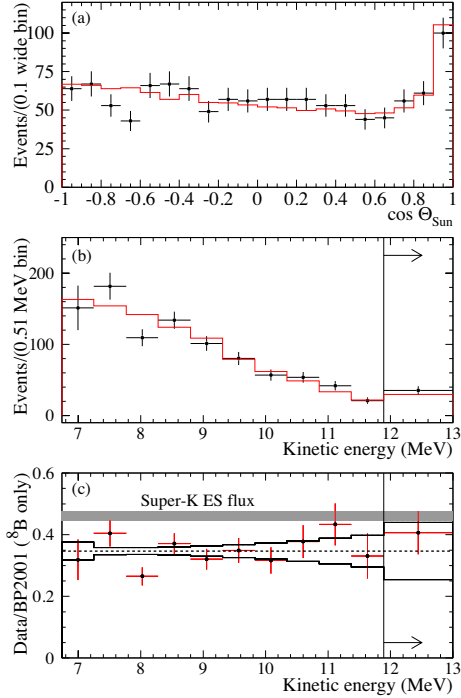
FIG. 2. Distributions of (a) $\cos\theta_\odot$, and (b) Extracted kinetic energy spectrum for CC events with $R \leq 5.50$ m and $T_{\text{eff}} \geq 6.75$ MeV. The Monte Carlo simulations for an undistorted ^{8}B spectrum are shown as histograms. The ratio of the data to the expected kinetic energy distribution with correlated systematic errors is shown in (c).

sources of systematic uncertainty in this signal extraction are the energy scale uncertainty and reconstruction accuracy, as shown in Table II. The CC and ES signal decomposition gives consistent results when used with the N_{hit} energy estimator, as well as with different choices of the analysis threshold and the fiducial volume up to 6.20 m with backgrounds characterized by pdfs.

The CC spectrum can be extracted from the data by removing the constraint on the shape of the CC pdf and repeating the signal extraction. Figure 2 (b) shows the kinetic energy spectrum with statistical error bars with the predicted standard ^{8}B spectrum [7] superimposed. The ratio of the data to the prediction is shown in Figure 2 (c). The bands represent the 1σ uncertainties derived from the most significant energy-dependent systematic errors. There is no evidence for a deviation of the spectral shape from the predicted shape under the non-oscillation

TABLE II. Systematic error on fluxes.

Error source	CC error (percent)	ES error (per cent)
Energy scale	-5.2, +6.1	-3.5 ,+5.4
Energy resolution	±0.5	±0.3
Energy scale non-linearity	±0.5	±0.4
Vertex accuracy	±3.1	±3.3
Vertex resolution	±0.7	±0.4
Angular resolution	±0.5	±2.2
High energy γ's	-0.8, +0.0	-1.9, +0.0
Low energy background	-0.2, +0.0	-0.2, +0.0
Instrumental background	-0.2, +0.0	-0.6, +0.0
Trigger efficiency	0.0	0.0
Live time	±0.1	±0.1
Cut acceptance	-0.6, +0.7	-0.6, +0.7
Earth orbit eccentricity	±0.2	±0.2
^{17}O, ^{18}O	0.0	0.0
Experimental uncertainty	-6.2, +7.0	-5.7, +6.8
Cross section	3.0	0.5
Solar Model	-16, +20	-16, +20

hypothesis.

Using the integrated rates above the kinetic energy threshold $T_{\text{eff}} = 6.75$ MeV, the measured ^{8}B neutrino fluxes assuming no oscillations are:

$$\phi_{\text{SNO}}^{\text{CC}}(\nu_e) = 1.75 \pm 0.07 \text{ (stat.)}_{-0.11}^{+0.12} \text{ (sys.)} \pm 0.05 \text{ (theor.)}$$
$$\times 10^6 \text{ cm}^{-2}\text{s}^{-1}$$

$$\phi_{\text{SNO}}^{\text{ES}}(\nu_x) = 2.39 \pm 0.34\text{(stat.)}_{-0.14}^{+0.16} \text{ (sys.)} \times 10^6 \text{ cm}^{-2}\text{s}^{-1}$$

where the theoretical uncertainty is the CC cross section uncertainty [10]. Radiative corrections have not been applied to the CC cross section, but they are expected to decrease the measured $\phi^{\text{CC}}(\nu_e)$ flux [14] by up to a few percent. The difference between the ^{8}B flux deduced from the ES rate and that deduced from the CC rate in SNO is $0.64 \pm 0.40 \times 10^6$ cm^{-2}s^{-1}, or 1.6σ. SNO's ES rate measurement is consistent with the precision measurement by the Super-Kamiokande Collaboration of the ^{8}B flux using the same ES reaction [5]:

$$\phi_{\text{SK}}^{\text{ES}}(\nu_x) = 2.32 \pm 0.03 \text{ (stat.)}_{-0.07}^{+0.08} \text{ (sys.)} \times 10^6 \text{ cm}^{-2}\text{s}^{-1}.$$

The difference between the flux $\phi^{\text{ES}}(\nu_x)$ measured by Super-Kamiokande via the ES reaction and the $\phi^{CC}(\nu_e)$ flux measured by SNO via the CC reaction is $0.57 \pm 0.17 \times 10^6$ cm^{-2}s^{-1}, or 3.3σ [8]. The probability that the SNO measurement is not a downward fluctuation from the Super-Kamiokande measurement is 99.96%. For reference, the ratio of the SNO CC ^{8}B flux to that of the BP2001 solar model [7] is 0.347 ± 0.029, where all uncertainties are added in quadrature.

If oscillation with maximal mixing to a sterile neutrino is occurring, the SNO CC-derived ^{8}B flux above a threshold of 6.75 MeV will be consistent with the integrated Super-Kamiokande ES-derived ^{8}B flux above a

threshold of 8.5 MeV [20]. Correcting for the ES threshold [5] this derived flux difference is $0.53 \pm 0.17 \times 10^6$ cm^{-2}s^{-1}, or 3.1σ. The probability that this difference is not a downward fluctuation is 99.87%. These data are therefore evidence of a non-electron active flavor component in the solar neutrino flux. These data are also inconsistent with the "Just-So^2" parameters for neutrino oscillation [15].

Figure 3 displays the inferred flux of non-electron flavor active neutrinos $(\phi(\nu_{\mu\tau}))$ against the flux of electron neutrinos. The two data bands represent the one standard deviation measurements of the SNO CC rate and the Super-Kamiokande ES rate. The error ellipses represent the 68%, 95%, and 99% joint probability contours for $\phi(\nu_e)$ and $(\phi(\nu_{\mu\tau}))$. The best fit to $\phi(\nu_{\mu\tau})$ is:

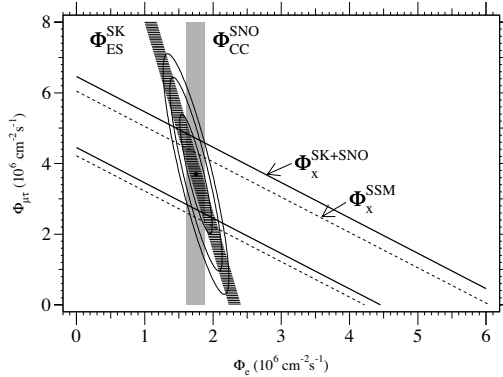$$\phi(\nu_{\mu\tau}) = 3.69 \pm 1.13 \times 10^6 \text{ cm}^{-2}\text{s}^{-1}.$$

FIG. 3. Flux of ^{8}B solar neutrinos which are μ or τ flavor vs. the flux of electron neutrinos as deduced from the SNO and Super-Kamiokande data. The diagonal bands show the total ^{8}B flux $\phi(\nu_x)$ as predicted by BP2001 (dashed lines) and that derived from the SNO and Super-Kamiokande measurements (solid lines). The intercepts of these bands with the axes represent the $\pm 1\sigma$ errors.

The total flux of active ^{8}B neutrinos is determined to be:

$$\phi(\nu_x) = 5.44 \pm 0.99 \times 10^6 \text{ cm}^{-2}\text{s}^{-1}.$$

This result is displayed as a diagonal band in Fig. 3, and is in excellent agreement with predictions of standard solar models [7,9].

The evidence for electron neutrino flavor change implies a mass squared difference between ν_e and ν_μ or ν_τ

that is less than 10^{-3} eV^2 as shown by previous analyses [16,15]. This result can also be combined with present limits on electron neutrino mass [17] of less than 2.8 eV and $\Delta m^2_{\mu\tau}$ (assuming neutrino oscillations [19]), to limit the sum of the masses of ν_e, ν_μ, and ν_τ to be between 0.05 and 8.4 eV. This corresponds to a constraint of $0.001 < \Omega_\nu < 0.18$ for the neutrino mass contribution to the critical density of the Universe [18].

In summary, the results presented here are the first direct indication of a non-electron flavor component in the solar neutrino flux, and enable the first determination of the total flux of ^{8}B neutrinos generated by the Sun.

* Deceased.
† Permanent address: TRIUMF, 4004 Wesbrook Mall, Vancouver, BC V6T 2A3, Canada.
‡ Permanent address: Birkbeck College, University of London, Malet Road, London WC1E 7HX, UK.
§ Permanent address: Rutherford Appleton Laboratory, Chilton, Didcot, Oxon, OX11 0QX, and University of Sussex, Physics and Astronomy Department, Brighton BN1 9QH, UK.
[1] B.T. Cleveland et al., Astrophys. J. **496**, 505 (1998).
[2] K.S. Hirata et al., Phys. Rev. Lett. **65**, 1297 (1990); K.S. Hirata et al., Phys. Rev. D **44**, 2241 (1991); Y. Fukuda et al., Phys. Rev. Lett. **77**, 1683 (1996).
[3] J.N. Abdurashitov et al., Phys. Rev. C **60**, 055801, (1999).
[4] W. Hampel et al., Phys. Lett. B **447**, 127 (1999).
[5] S. Fukuda et al., Phys. Rev. Lett. **86**, 5651 (2001).
[6] W. Altmann et al., Phys. Lett. B **490**, 16 (2000).
[7] J.N. Bahcall, M. H. Pinsonneault, and S. Basu, astro-ph/0010346 v2. The reference ^{8}B neutrino flux is 5.05×10^6 cm^{-2}s^{-1}.
[8] Given the limit set for the hep flux by Ref. [5], the effects of the hep contribution may increase this difference by a few percent.
[9] A.S. Brun, S. Turck-Chièze, and J.P. Zahn, Astrophys. J. **525**, 1032 (1999).

[10] S. Nakamura, T. Sato, V. Gudkov, and K. Kubodera, Phys. Rev. C **63**, 034617 (2001); M. Butler, J.-W. Chen, and X. Kong, Phys. Rev. C **63**, 035501 (2001); G. 't Hooft, Phys. Lett. **37B** 195 (1971). The Butler *et al.* cross section with $L_{I,A} = 5.6$ fm^3 is used.

[11] J.N. Bahcall *et al.*, Phys. Rev. C **54**, 411 (1996); C.E. Ortiz *et al.*, Phys. Rev. Lett. **85**, 2909 (2000).

[12] The SNO Collaboration, Nucl. Instr. and Meth. **A449**, 172 (2000).

[13] A.W.P. Poon *et al.*, Nucl. Instr. and Meth. **A452**, 115, (2000).

[14] I. Towner, J. Beacom, and S. Parke, private communication; I. Towner, Phys. Rev. C **58** 1288 (1998), J. Beacom, and S. Parke, hep-ph/0106128; J.N. Bahcall, M. Kamionkowski, and A. Sirlin, Phys. Rev. D **51** 6146 (1995).

[15] J.N. Bahcall, P.I. Krastev, and A.Yu. Smirnov, JHEP **05**, 015 (2001).

[16] M. Apollonio *et al.*, Phys. Lett. B **466**, 415 (1999).

[17] J. Bonn *et al.* Nucl. Phys. Proc. B Suppl. **91**, 273 (2001).

[18] Allen's Astrophysical Quantities, 4th ed., ed. Arthur Cox, (New York:Springer-Verlag), 2000. European Physical Journal **C15**, 1 (2000)

[19] T. Toshito *et al.* hep-ex/0105023

[20] G. L. Fogli, E. Lisi, A. Palazzo, and F.L. Villante Phys. Rev. D **63**, 113016 (2001); F.L. Villante, G. Fiorintini and E. Lisi Phys. Rev. D **59** 013006 (1999).

Direct Evidence for Neutrino Flavor Transformation from Neutral-Current Interactions in the Sudbury Neutrino Observatory

Q.R. Ahmad,[17] R.C. Allen,[4] T.C. Andersen,[6] J.D. Anglin,[10] J.C. Barton,[11,*] E.W. Beier,[12] M. Bercovitch,[10]
J. Bigu,[7] S.D. Biller,[11] R.A. Black,[11] I. Blevis,[5] R.J. Boardman,[11] J. Boger,[3] E. Bonvin,[14] M.G. Boulay,[9,14]
M.G. Bowler,[11] T.J. Bowles,[9] S.J. Brice,[9,11] M.C. Browne,[17,9] T.V. Bullard,[17] G. Bühler,[4] J. Cameron,[11]
Y.D. Chan,[8] H.H. Chen,[4,†] M. Chen,[14] X. Chen,[8,11] B.T. Cleveland,[11] E.T.H. Clifford,[14] J.H.M. Cowan,[7]
D.F. Cowen,[12] G.A. Cox,[17] X. Dai,[11] F. Dalnoki-Veress,[5] W.F. Davidson,[10] P.J. Doe,[17,9,4] G. Doucas,[11]
M.R. Dragowsky,[9,8] C.A. Duba,[17] F.A. Duncan,[14] M. Dunford,[12] J.A. Dunmore,[11] E.D. Earle,[14,1] S.R. Elliott,[17,9]
H.C. Evans,[14] G.T. Ewan,[14] J. Farine,[7,5] H. Fergani,[11] A.P. Ferraris,[11] R.J. Ford,[14] J.A. Formaggio,[17]
M.M. Fowler,[9] K. Frame,[11] E.D. Frank,[12] W. Frati,[12] N. Gagnon,[11,9,8,17] J.V. Germani,[17] S. Gil,[2] K. Graham,[14]
D.R. Grant,[5] R.L. Hahn,[3] A.L. Hallin,[14] E.D. Hallman,[7] A.S. Hamer,[9,14] A.A. Hamian,[17] W.B. Handler,[14]
R.U. Haq,[7] C.K. Hargrove,[5] P.J. Harvey,[14] R. Hazama,[17] K.M. Heeger,[17] W.J. Heintzelman,[12] J. Heise,[2,9]
R.L. Helmer,[16,2] J.D. Hepburn,[14] H. Heron,[11] J. Hewett,[7] A. Hime,[9] J.G. Hykawy,[7] M.C.P. Isaac,[8]
P. Jagam,[6] N.A. Jelley,[11] C. Jillings,[14] G. Jonkmans,[7,1] K. Kazkaz,[17] P.T. Keener,[12] J.R. Klein,[12]
A.B. Knox,[11] R.J. Komar,[2] R. Kouzes,[13] T. Kutter,[2] C.C.M. Kyba,[12] J. Law,[6] I.T. Lawson,[6] M. Lay,[11]
H.W. Lee,[14] K.T. Lesko,[8] J.R. Leslie,[14] I. Levine,[5] W. Locke,[11] S. Luoma,[7] J. Lyon,[11] S. Majerus,[11] H.B. Mak,[14]
J. Maneira,[14] J. Manor,[17] A.D. Marino,[8] N. McCauley,[12,11] D.S. McDonald,[12] A.B. McDonald,[14,13] K. McFarlane,[5]
G. McGregor,[11] R. Meijer Drees,[17] C. Mifflin,[5] G.G. Miller,[9] G. Milton,[1] B.A. Moffat,[14] M. Moorhead,[11]
C.W. Nally,[2] M.S. Neubauer,[12] F.M. Newcomer,[12] H.S. Ng,[2] A.J. Noble,[16,5] E.B. Norman,[8] V.M. Novikov,[5]
M. O'Neill,[5] C.E. Okada,[8] R.W. Ollerhead,[6] M. Omori,[11] J.L. Orrell,[17] S.M. Oser,[12] A.W.P. Poon,[8,17,2,9]
T.J. Radcliffe,[14] A. Roberge,[7] B.C. Robertson,[14] R.G.H. Robertson,[17,9] S.S.E. Rosendahl,[8] J.K. Rowley,[3]
V.L. Rusu,[12] E. Saettler,[7] K.K. Schaffer,[17] M.H. Schwendener,[7] A. Schülke,[8] H. Seifert,[7,17,9] M. Shatkay,[5]
J.J. Simpson,[6] C.J. Sims,[11] D. Sinclair,[5] P. Skensved,[14] A.R. Smith,[8] M.W.E. Smith,[17] T. Spreitzer,[12]
N. Starinsky,[5] T.D. Steiger,[17] R.G. Stokstad,[8] L.C. Stonehill,[17] R.S. Storey,[10,†] B. Sur,[1,14] R. Tafirout,[7]
N. Tagg,[6,11] N.W. Tanner,[11] R.K. Taplin,[11] M. Thorman,[11] P.M. Thornewell,[11] P.T. Trent,[11] Y.I. Tserkovnyak,[2]
R. Van Berg,[12] R.G. Van de Water,[9,12] C.J. Virtue,[7] C.E. Waltham,[2] J.-X. Wang,[6] D.L. Wark,[15,11,9]
N. West,[11] J.B. Wilhelmy,[9] J.F. Wilkerson,[17,9] J.R. Wilson,[11] P. Wittich,[12] J.M. Wouters,[9] and M. Yeh[3]

(SNO Collaboration)

[1] Atomic Energy of Canada, Limited, Chalk River Laboratories, Chalk River, ON K0J 1J0, Canada
[2] Department of Physics and Astronomy, University of British Columbia, Vancouver, BC V6T 1Z1 Canada
[3] Chemistry Department, Brookhaven National Laboratory, Upton, NY 11973-5000
[4] Department of Physics, University of California, Irvine, CA 92717
[5] Carleton University, Ottawa, Ontario K1S 5B6 Canada
[6] Physics Department, University of Guelph, Guelph, Ontario N1G 2W1 Canada
[7] Department of Physics and Astronomy, Laurentian University, Sudbury, Ontario P3E 2C6 Canada
[8] Institute for Nuclear and Particle Astrophysics and Nuclear Science
Division, Lawrence Berkeley National Laboratory, Berkeley, CA 94720
[9] Los Alamos National Laboratory, Los Alamos, NM 87545
[10] National Research Council of Canada, Ottawa, ON K1A 0R6, Canada
[11] Department of Physics, University of Oxford, Denys Wilkinson Building, Keble Road, Oxford, OX1 3RH, UK
[12] Department of Physics and Astronomy, University of Pennsylvania, Philadelphia, PA 19104-6396
[13] Department of Physics, Princeton University, Princeton, NJ 08544
[14] Department of Physics, Queen's University, Kingston, Ontario K7L 3N6 Canada
[15] Rutherford Appleton Laboratory, Chilton, Didcot, Oxon, OX11 0QX, and
University of Sussex, Physics and Astronomy Department, Brighton BN1 9QH, UK
[16] TRIUMF, 4004 Wesbrook Mall, Vancouver, BC V6T 2A3, Canada
[17] Center for Experimental Nuclear Physics and Astrophysics, and
Department of Physics, University of Washington, Seattle, WA 98195
(Dated: 19 April 2002)

Observations of neutral-current ν interactions on deuterium in the Sudbury Neutrino Observatory are reported. Using the neutral current, elastic scattering, and charged current reactions and assuming the standard ^{8}B shape, the ν_e component of the ^{8}B solar flux is $\phi_e = 1.76^{+0.05}_{-0.05}(\text{stat.})^{+0.09}_{-0.09}$ (syst.) $\times 10^6$ cm^{-2}s^{-1} for a kinetic energy threshold of 5 MeV. The non-ν_e component is $\phi_{\mu\tau} = 3.41^{+0.45}_{-0.45}(\text{stat.})^{+0.48}_{-0.45}$ (syst.) $\times 10^6$ cm^{-2}s^{-1}, 5.3σ greater than zero, providing

166

strong evidence for solar ν_e flavor transformation. The total flux measured with the NC reaction is
$\phi_{\rm NC} = 5.09^{+0.44}_{-0.43}(\text{stat.})^{+0.46}_{-0.43}$ (syst.) $\times 10^6$ cm^{-2}s^{-1}, consistent with solar models.

PACS numbers: 26.65.+t, 14.60.Pq, 13.15.+g, 95.85.Ry

The Sudbury Neutrino Observatory (SNO) detects ^{8}B solar neutrinos through the reactions:
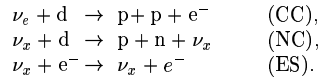
$$\nu_e + {\rm d} \rightarrow {\rm p} + {\rm p} + {\rm e}^- \quad (\text{CC}),$$
$$\nu_x + {\rm d} \rightarrow {\rm p} + {\rm n} + \nu_x \quad (\text{NC}),$$
$$\nu_x + {\rm e}^- \rightarrow \nu_x + {\rm e}^- \quad (\text{ES}).$$

The charged current reaction (CC) is sensitive exclusively to electron-type neutrinos, while the neutral current reaction (NC) is equally sensitive to all active neutrino flavors ($x = e, \mu, \tau$). The elastic scattering reaction (ES) is sensitive to all flavors as well, but with reduced sensitivity to ν_μ and ν_τ. Sensitivity to these three reactions allows SNO to determine the electron and non-electron active neutrino components of the solar flux [1]. The CC and ES reaction results have recently been presented [2]. This Letter presents the first NC results and updated CC and ES results from SNO.

SNO [3] is a water Cherenkov detector located at a depth of 6010 m of water equivalent in the INCO, Ltd. Creighton mine near Sudbury, Ontario, Canada. The detector uses ultra-pure heavy water contained in a transparent acrylic spherical shell 12 m in diameter to detect solar neutrinos. Cherenkov photons generated in the heavy water are detected by 9456 photomultiplier tubes (PMTs) mounted on a stainless steel geodesic sphere 17.8 m in diameter. The geodesic sphere is immersed in ultra-pure light water to provide shielding from radioactivity in both the PMT array and the cavity rock.

The data reported here were recorded between Nov. 2, 1999 and May 28, 2001 and represent a total of 306.4 live days, spanning the entire first phase of the experiment, in which only D$_2$O was present in the sensitive volume. The analysis procedure was similar to that described in [2]. PMT times and hit patterns were used to reconstruct event vertices and directions and to assign to each event a most probable kinetic energy, $T_{\rm eff}$. The total flux of active ^{8}B solar neutrinos with energies greater than 2.2 MeV (the NC reaction threshold) was measured with the NC signal (Cherenkov photons resulting from the 6.25 MeV γ ray from neutron capture on deuterium.) The analysis threshold was $T_{\rm eff} \geq 5$ MeV, providing sensitivity to neutrons from the NC reaction. Above this energy threshold, there were contributions from CC events in the D$_2$O, ES events in the D$_2$O and H$_2$O, capture of neutrons (both from the NC reaction and backgrounds), and low energy Cherenkov background events.

A fiducial volume was defined to only accept events which had reconstructed vertices within 550 cm from the detector center to reduce external backgrounds and systematic uncertainties associated with optics and event reconstruction near the acrylic vessel. The neutron response and systematic uncertainty was calibrated with a ^{252}Cf source. The deduced efficiency for neutron captures on deuterium is $29.9 \pm 1.1\%$ for a uniform source of neutrons in the D$_2$O. The neutron detection efficiency within the fiducial volume and above the energy threshold is 14.4%. The energy calibration was updated from [2] with the ^{16}N calibration source [4] data and Monte Carlo calculations. The energy response for electrons, updated for the lower analysis threshold, was characterized as a Gaussian function with resolution $\sigma_T = -0.0684 + 0.331\sqrt{T_e} + 0.0425T_e$, where T_e is the true electron kinetic energy in MeV. The energy scale uncertainty is 1.2%.

The primary backgrounds to the NC signal are due to low levels of uranium and thorium decay chain daughters (^{214}Bi and ^{208}Tl) in the detector materials. These activities generate free neutrons in the D$_2$O, from deuteron photodisintegration (pd), and low energy Cherenkov events. Ex-situ assays and in-situ analysis of the low energy ($4 - 4.5$ MeV) Cherenkov signal region provide independent uranium and thorium photodisintegration background measurements.

Two ex situ assay techniques were employed to determine average levels of uranium and thorium in water. Radium ions were directly extracted from the water onto either MnO$_x$ or hydrous Ti oxide (HTiO) ion exchange media. Radon daughters in the U and Th chains were subsequently released, identified by α spectroscopy, or the radium was concentrated and the number of decay daughter β-α coincidences determined. Typical assays circulated approximately 400 tonnes of water through the extraction media. These techniques provide isotopic identification of the decay daughters and contamination levels in the assayed water volumes, presented in Fig. 1 (a). Secular equilibrium in the U decay chain was broken by the ingress of long-lived (3.8 day half-life) ^{222}Rn in the experiment. Measurements of this background were made by periodically extracting and cryogenically concentrating ^{222}Rn from water degassers. Radon from several tonne assays was subsequently counted in ZnS(Ag) scintillation cells [5]. The Radon results are presented (as mass fractions in g(U)/g(D$_2$O)) in Fig. 1(b).

Independent measurements of U and Th decay chains were made by analyzing Cherenkov light produced by the radioactive decays. The β and β-γ decays from the U and Th chains dominate the low energy monitoring window. Events in this window monitor γ rays that produce photodisintegration in these chains (E$_\gamma > 2.2$ MeV). Cherenkov events fitted within 450 cm from the detector center and extracted from the neutrino data set provide

a time-integrated measure of these backgrounds over the same time period and within the fiducial volume of the neutrino analysis. Statistical separation of *in situ* Tl and Bi events was obtained by analyzing the Cherenkov signal isotropy. Tl decays always result in a β and a 2.614 MeV γ, while in this energy window Bi decays are dominated by decays with only a β, and produce, on average, more anisotropic hit patterns.

Results from the *ex situ* and *in situ* methods are consistent with each other as shown on the right hand side of Figs. 1(a) and 1(b). For the ^{232}Th chain, the weighted mean (including additional sampling systematic uncertainty) of the two determinations was used for the analysis. The ^{238}U chain activity is dominated by Rn ingress which is highly time dependent. Therefore the *in-situ* determination was used for this activity as it provides the appropriate time weighting. The average rate of background neutron production from activities in the D_2O region is 1.0 ± 0.2 neutrons per day, leading to 44^{+8}_{-9} detected background events. The production rate from external activities is $1.3^{+0.4}_{-0.5}$ neutrons per day, which leads to 27 ± 8 background events since the neutron capture efficiency is reduced for neutrons born near the heavy water boundary. The total photodisintegration background corresponds to approximately 12% of the number of NC neutrons predicted by the standard solar model from ^{8}B neutrinos.

Low energy backgrounds from Cherenkov events in the signal region were evaluated by using acrylic encapsulated sources of U and Th deployed throughout the detector volume and by Monte Carlo calculations. Probability density functions (pdfs) in reconstructed vertex radius derived from U and Th calibration data were used to determine the number of background Cherenkov events from external regions which either entered or misreconstructed into the fiducial volume. Cherenkov event backgrounds from activities in the D_2O were evaluated with Monte Carlo calculations.

Table I shows the number of photodisintegration and Cherenkov background events (including systematic uncertainties) due to activity in the D_2O (internal region), acrylic vessel (AV), H_2O (external region), and PMT array. Other sources of free neutrons in the D_2O region are cosmic ray events and atmospheric neutrinos. To reduce these backgrounds, an additional neutron background cut imposed a 250-ms deadtime (in software) following every event in which the total number of PMTs which registered a hit was greater than 60. The number of remaining NC atmospheric neutrino events and background events generated by sub-Cherenkov threshold muons is estimated to be small, as shown in Table I.

The data recorded during the pure D_2O detector phase are shown in Figure 2. These data have been analyzed using the same data reduction described in [2], with the addition of the new neutron background cut, yielding
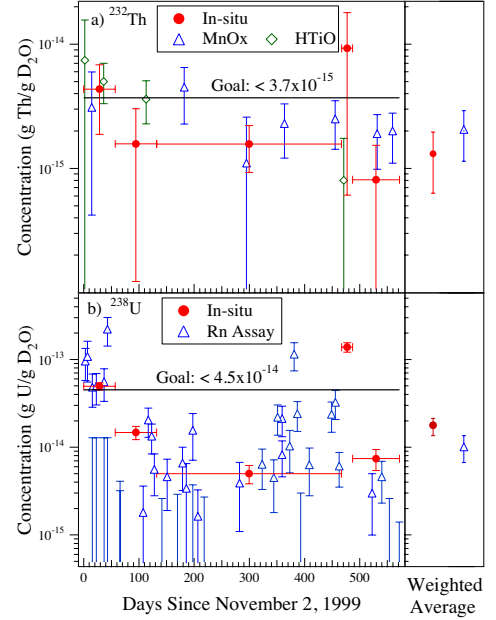

FIG. 1: Thorium (a) and uranium (b) backgrounds (equivalent equilibrium concentrations) in the D_2O deduced by *in situ* and *ex situ* techniques. The MnO_x and HTiO radiochemical assay results, the Rn assay results, and the *in situ* Cherenkov signal determination of the backgrounds are presented for the period of this analysis on the left-hand side of frames (a) and (b). The right-hand side shows time-integrated averages including an additional sampling systematic uncertainty for the *ex situ* measurement.

TABLE I: Neutron and Cherenkov background events.

Source	Events
D_2O photodisintegration	44^{+8}_{-9}
H_2O + AV photodisintegration	27^{+8}_{-8}
Atmospheric ν's and sub-Cherenkov threshold μ's	4 ± 1
Fission	$\ll 1$
^{2}H(α, α)pn	2 ± 0.4
^{17}O$(\alpha,$n$)$	$\ll 1$
Terrestrial and reactor $\bar{\nu}$'s	1^{+3}_{-1}
External neutrons	$\ll 1$
Total neutron background	78 ± 12
D_2O Cherenkov	20^{+13}_{-6}
H_2O Cherenkov	3^{+4}_{-3}
AV Cherenkov	6^{+3}_{-6}
PMT Cherenkov	16^{+11}_{-8}
Total Cherenkov background	45^{+18}_{-12}

TABLE II: Systematic uncertainties on fluxes. The experimental uncertainty for ES (not shown) is -4.8,+5.0 percent. † denotes CC vs NC anti-correlation.

Source	CC Uncert. (percent)	NC Uncert. (percent)	$\phi_{\mu\tau}$ Uncert. (percent)
Energy scale †	-4.2,+4.3	-6.2,+6.1	-10.4,+10.3
Energy resolution †	-0.9,+0.0	-0.0,+4.4	-0.0,+6.8
Energy non-linearity †	±0.1	±0.4	±0.6
Vertex resolution †	±0.0	±0.1	±0.2
Vertex accuracy	-2.8,+2.9	±1.8	±1.4
Angular resolution	-0.2,+0.2	-0.3,+0.3	-0.3,+0.3
Internal source pd †	±0.0	-1.5,+1.6	-2.0,+2.2
External source pd	±0.1	-1.0,+1.0	±1.4
D_2O Cherenkov †	-0.1,+0.2	-2.6,+1.2	-3.7,+1.7
H_2O Cherenkov	±0.0	-0.2,+0.4	-0.2,+0.6
AV Cherenkov	±0.0	-0.2,+0.2	-0.3,+0.3
PMT Cherenkov †	±0.1	-2.1,+1.6	-3.0,+2.2
Neutron capture	±0.0	-4.0,+3.6	-5.8,+5.2
Cut acceptance	-0.2,+0.4	-0.2,+0.4	-0.2,+0.4
Experimental uncertainty	-5.2,+5.2	-8.5,+9.1	-13.2,+14.1
Cross section [7]	±1.8	±1.3	±1.4

2928 events in the energy region selected for analysis, 5 to 20 MeV. Fig. 2(a) shows the distribution of selected events in the cosine of the angle between the Cherenkov event direction and the direction from the sun ($\cos\theta_\odot$) for the analysis threshold of $T_{\rm eff} \geq 5$ MeV and fiducial volume selection of $R \leq 550$ cm, where R is the reconstructed event radius. Fig. 2(b) shows the distribution of events in the volume-weighted radial variable $(R/R_{\rm AV})^3$, where $R_{\rm AV} = 600$ cm is the radius of the acrylic vessel. Figure 2(c) shows the kinetic energy spectrum of the selected events.

In order to test the null hypothesis, the assumption that there are only electron neutrinos in the solar neutrino flux, the data are resolved into contributions from CC, ES, and NC events above threshold using pdfs in $T_{\rm eff}$, $\cos\theta_\odot$, and $(R/R_{\rm AV})^3$, derived from Monte Carlo calculations generated assuming no flavor transformation and the standard ^{8}B spectral shape [6]. Background event pdfs are included in the analysis with fixed amplitudes determined by the background calibration. The extended maximum likelihood method used in the signal decomposition yields $1967.7^{+61.9}_{-60.9}$ CC events, $263.6^{+26.4}_{-25.6}$ ES events, and $576.5^{+49.5}_{-48.9}$ NC events [12], where only statistical uncertainties are given. Systematic uncertainties on fluxes derived by repeating the signal decomposition with perturbed pdfs (constrained by calibration data) are shown in Table II.

Normalized to the integrated rates above the kinetic energy threshold of $T_{\rm eff} \geq 5$ MeV, the flux of ^{8}B neutrinos measured with each reaction in SNO, assuming the standard spectrum shape [6] is (all fluxes are presented in units of 10^6 cm^{-2}s^{-1}):

$$\phi^{\rm SNO}_{\rm CC} = 1.76^{+0.06}_{-0.05}({\rm stat.})^{+0.09}_{-0.09}({\rm syst.})$$

$$\phi^{\rm SNO}_{\rm ES} = 2.39^{+0.24}_{-0.23}({\rm stat.})^{+0.12}_{-0.12}({\rm syst.})$$

$$\phi^{\rm SNO}_{\rm NC} = 5.09^{+0.44}_{-0.43}({\rm stat.})^{+0.46}_{-0.43}({\rm syst.}).$$

Electron neutrino cross sections are used to calculate all
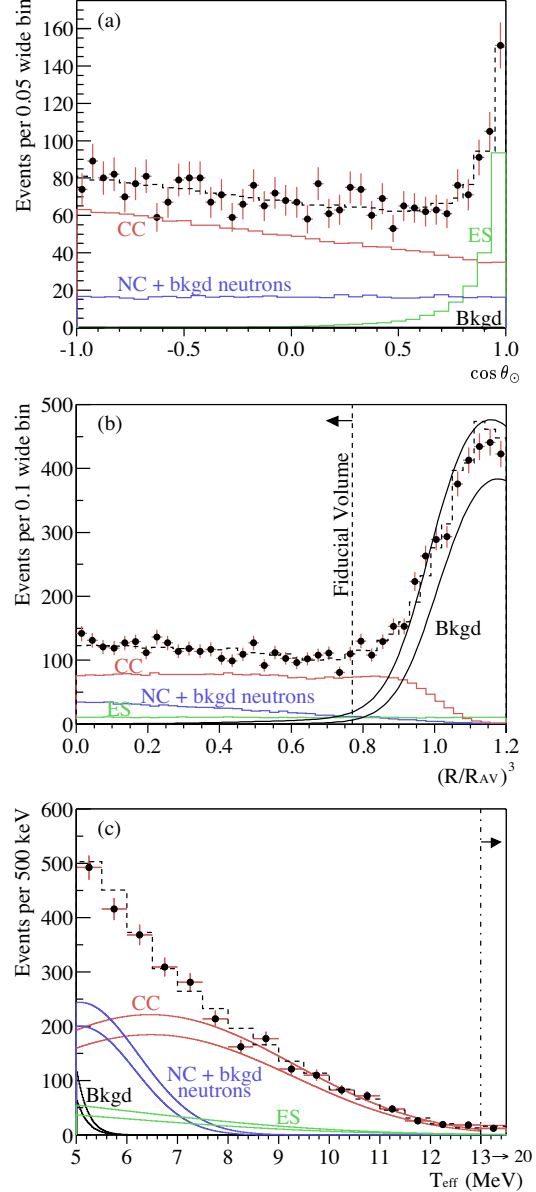
FIG. 2: (a) Distribution of $\cos\theta_\odot$ for $R \leq 550$ cm. (b) Distribution of the volume weighted radial variable $(R/R_{\rm AV})^3$. (c) Kinetic energy for $R \leq 550$ cm. Also shown are the Monte Carlo predictions for CC, ES and NC + bkgd neutron events scaled to the fit results, and the calculated spectrum of Cherenkov background (Bkgd) events. The dashed lines represent the summed components, and the bands show $\pm 1\sigma$ uncertainties. All distributions are for events with $T_{\rm eff} \geq 5$ MeV.

fluxes. The CC and ES results reported here are consistent with the earlier SNO results [2] for $T_{\rm eff} \geq 6.75$ MeV. The excess of the NC flux over the CC and ES fluxes implies neutrino flavor transformations.

A simple change of variables resolves the data directly into electron (ϕ_e) and non-electron ($\phi_{\mu\tau}$) components [13],

$$\phi_e = 1.76^{+0.05}_{-0.05}(\text{stat.})^{+0.09}_{-0.09}\ (\text{syst.})$$
$$\phi_{\mu\tau} = 3.41^{+0.45}_{-0.45}(\text{stat.})^{+0.48}_{-0.45}\ (\text{syst.})$$

assuming the standard ^{8}B shape. Combining the statistical and systematic uncertainties in quadrature, $\phi_{\mu\tau}$ is $3.41^{+0.66}_{-0.64}$, which is 5.3σ above zero, providing strong evidence for flavor transformation consistent with neutrino oscillations [8, 9]. Adding the Super-Kamiokande ES measurement of the ^{8}B flux [10] $\phi_{\rm ES}^{\rm SK} = 2.32 \pm 0.03(\text{stat.})^{+0.08}_{-0.07}$ (syst.) as an additional constraint, we find $\phi_{\mu\tau} = 3.45^{+0.65}_{-0.62}$, which is 5.5σ above zero. Figure 3 shows the flux of non-electron flavor active neutrinos vs the flux of electron neutrinos deduced from the SNO data. The three bands represent the one standard deviation measurements of the CC, ES, and NC rates. The error ellipses represent the 68%, 95%, and 99% joint probability contours for ϕ_e and $\phi_{\mu\tau}$.

Removing the constraint that the solar neutrino energy spectrum is undistorted, the signal decomposition is repeated using only the $\cos\theta_\odot$ and $(R/R_{\rm AV})^3$ information. The total flux of active ^{8}B neutrinos measured with the NC reaction is

$$\phi_{\rm NC}^{\rm SNO} = 6.42^{+1.57}_{-1.57}(\text{stat.})^{+0.55}_{-0.58}\ (\text{syst.})$$

which is in agreement with the shape constrained value above and with the standard solar model prediction [11] for ^{8}B, $\phi_{\rm SSM} = 5.05^{+1.01}_{-0.81}$.

In summary, the results presented here are the first direct measurement of the total flux of active ^{8}B neutrinos arriving from the sun and provide strong evidence for neutrino flavor transformation. The CC and ES reaction rates are consistent with the earlier results [2] and with the NC reaction rate under the hypothesis of flavor transformation. The total flux of ^{8}B neutrinos measured with the NC reaction is in agreement with the SSM prediction.

* Permanent Address: Birkbeck College, University of London, Malet Road, London WC1E 7HX, UK
† Deceased

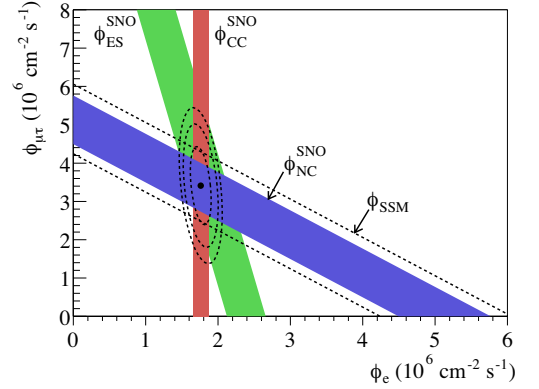[1] H. Chen, Phys. Rev. Lett. **55**, 1534 (1985).

FIG. 3: Flux of ^{8}B solar neutrinos which are μ or τ flavor vs flux of electron neutrinos deduced from the three neutrino reactions in SNO. The diagonal bands show the total ^{8}B flux as predicted by the SSM [11] (dashed lines) and that measured with the NC reaction in SNO (solid band). The intercepts of these bands with the axes represent the $\pm 1\sigma$ errors. The bands intersect at the fit values for ϕ_e and $\phi_{\mu\tau}$, indicating that the combined flux results are consistent with neutrino flavor transformation assuming no distortion in the ^{8}B neutrino energy spectrum.

[2] Q.R. Ahmad *et al.*, Phys. Rev. Lett. **87**, 071301 (2001).
[3] The SNO collaboration, Nucl. Instr. and Meth. **A449**, 172 (2000).
[4] M. R. Dragowsky *et al.*, Nucl. Instr. and Meth. **A481**, 284 (2002).
[5] M.-Q. Liu, H.W. Lee, and A.B. McDonald, Nucl. Inst. Meth. **A329**, 291 (1993).
[6] C. E. Ortiz *et al.*, Phys. Rev. Lett. **85**, 2909 (2000).
[7] Cross section uncertainty includes g_A uncertainty (0.6%), difference between NSGK (S. Nakamura, T. Sato, V. Gudkov and K. Kubodera, Phys. Rev. **C63** (2001) 034617) and BCK (M. Butler, J.-W. Chen and X. Kong, Phys. Rev. **C63** (2001) 035501) in SNO's calculations (0.6%), radiative correction uncertainties (0.3% for CC, 0.1% for NC, A. Kurylov, M. J. Ramsey-Musolf and P. Vogel, Phys. Rev. **C65** (2002) 055501), uncertainty associated with neglect of real photons in SNO (0.7% for CC), and theoretical cross section uncertainty (1%, S. Nakamura *et al.*, arXiv:nucl-th/0201062, (to be published)).
[8] Z. Maki, N. Nakagawa, and S. Sakata, Prog. Theor. Phys. **28**, 870 (1962).
[9] V. Gribov and B. Pontecorvo, Phys. Lett. **B28**, 493 (1969).
[10] S. Fukuda *et al.*, Phys. Rev. Lett. **86**, 5651 (2001).
[11] John N. Bahcall, M.H. Pinsonneault, and Sarbani Basu, Astrophys. J. **555**, 990 (2001).
[12] We note that this rate of neutron events also leads to a lower bound on the proton lifetime for "invisible" modes (based on the free neutron that would be left in deuterium (V.I. Tretyak and Yu.G. Zdesenko, Phys. Lett. **B505**, 59 (2001)) in excess of 10^{28} years, approximately

3 orders of magnitude more restrictive than previous limits (J. Evans and R. Steinberg, Science, **197**, 989 (1977).) The possible contribution of this mechanism to the solar neutrino NC background is ignored.

[13] This change of variables allows a direct test of the null hypothesis of no flavor transformation ($\phi_{\mu\tau} = 0$) without requiring calculation of the CC, ES, and NC signal correlations.

Measurement of Day and Night Neutrino Energy Spectra at SNO and Constraints on Neutrino Mixing Parameters

Q.R. Ahmad,[17] R.C. Allen,[4] T.C. Andersen,[6] J.D. Anglin,[10] J.C. Barton,[11, *] E.W. Beier,[12] M. Bercovitch,[10]
J. Bigu,[7] S.D. Biller,[11] R.A. Black,[11] I. Blevis,[5] R.J. Boardman,[11] J. Boger,[3] E. Bonvin,[14] M.G. Boulay,[9, 14]
M.G. Bowler,[11] T.J. Bowles,[9] S.J. Brice,[9, 11] M.C. Browne,[17, 9] T.V. Bullard,[17] G. Bühler,[4] J. Cameron,[11]
Y.D. Chan,[8] H.H. Chen,[4, †] M. Chen,[14] X. Chen,[8, 11] B.T. Cleveland,[11] E.T.H. Clifford,[14] J.H.M. Cowan,[7]
D.F. Cowen,[12] G.A. Cox,[17] X. Dai,[11] F. Dalnoki-Veress,[5] W.F. Davidson,[10] P.J. Doe,[17, 9, 4] G. Doucas,[11]
M.R. Dragowsky,[9, 8] C.A. Duba,[17] F.A. Duncan,[14] M. Dunford,[12] J.A. Dunmore,[11] E.D. Earle,[14, 1] S.R. Elliott,[17, 9]
H.C. Evans,[14] G.T. Ewan,[14] J. Farine,[7, 5] H. Fergani,[11] A.P. Ferraris,[11] R.J. Ford,[14] J.A. Formaggio,[17]
M.M. Fowler,[9] K. Frame,[11] E.D. Frank,[12] W. Frati,[12] N. Gagnon,[11, 9, 8, 17] J.V. Germani,[17] S. Gil,[2] K. Graham,[14]
D.R. Grant,[5] R.L. Hahn,[3] A.L. Hallin,[14] E.D. Hallman,[7] A.S. Hamer,[9, 14] A.A. Hamian,[17] W.B. Handler,[14]
R.U. Haq,[7] C.K. Hargrove,[5] P.J. Harvey,[14] R. Hazama,[17] K.M. Heeger,[17] W.J. Heintzelman,[12] J. Heise,[2, 9]
R.L. Helmer,[16, 2] J.D. Hepburn,[14] H. Heron,[11] J. Hewett,[7] A. Hime,[9] J.G. Hykawy,[7] M.C.P. Isaac,[8]
P. Jagam,[6] N.A. Jelley,[11] C. Jillings,[14] G. Jonkmans,[7, 1] K. Kazkaz,[17] P.T. Keener,[12] J.R. Klein,[12]
A.B. Knox,[11] R.J. Komar,[2] R. Kouzes,[13] T. Kutter,[2] C.C.M. Kyba,[12] J. Law,[6] I.T. Lawson,[6] M. Lay,[11]
H.W. Lee,[14] K.T. Lesko,[8] J.R. Leslie,[14] I. Levine,[5] W. Locke,[11] S. Luoma,[7] J. Lyon,[11] S. Majerus,[11] H.B. Mak,[14]
J. Maneira,[14] J. Manor,[17] A.D. Marino,[8] N. McCauley,[12, 11] D.S. McDonald,[12] A.B. McDonald,[14, 13] K. McFarlane,[5]
G. McGregor,[11] R. Meijer Drees,[17] C. Mifflin,[5] G.G. Miller,[9] G. Milton,[1] B.A. Moffat,[14] M. Moorhead,[11]
C.W. Nally,[2] M.S. Neubauer,[12] F.M. Newcomer,[12] H.S. Ng,[2] A.J. Noble,[16, 5] E.B. Norman,[8] V.M. Novikov,[5]
M. O'Neill,[5] C.E. Okada,[8] R.W. Ollerhead,[6] M. Omori,[11] J.L. Orrell,[17] S.M. Oser,[12] A.W.P. Poon,[8, 17, 2, 9]
T.J. Radcliffe,[14] A. Roberge,[7] B.C. Robertson,[14] R.G.H. Robertson,[17, 9] S.S.E. Rosendahl,[8] J.K. Rowley,[3]
V.L. Rusu,[12] E. Saettler,[7] K.K. Schaffer,[17] M.H. Schwendener,[7] A. Schülke,[8] H. Seifert,[7, 17, 9] M. Shatkay,[5]
J.J. Simpson,[6] C.J. Sims,[11] D. Sinclair,[5] P. Skensved,[14] A.R. Smith,[8] M.W.E. Smith,[17] T. Spreitzer,[12]
N. Starinsky,[5] T.D. Steiger,[17] R.G. Stokstad,[8] L.C. Stonehill,[17] R.S. Storey,[10, †] B. Sur,[1, 14] R. Tafirout,[7]
N. Tagg,[6, 11] N.W. Tanner,[11] R.K. Taplin,[11] M. Thorman,[11] P.M. Thornewell,[11] P.T. Trent,[11] Y.I. Tserkovnyak,[2]
R. Van Berg,[12] R.G. Van de Water,[9, 12] C.J. Virtue,[7] C.E. Waltham,[2] J.-X. Wang,[6] D.L. Wark,[15, 11, 9]
N. West,[11] J.B. Wilhelmy,[9] J.F. Wilkerson,[17, 9] J.R. Wilson,[11] P. Wittich,[12] J.M. Wouters,[9] and M. Yeh[3]

(SNO Collaboration)

[1] *Atomic Energy of Canada, Limited, Chalk River Laboratories, Chalk River, ON K0J 1J0, Canada*
[2] *Department of Physics and Astronomy, University of British Columbia, Vancouver, BC V6T 1Z1 Canada*
[3] *Chemistry Department, Brookhaven National Laboratory, Upton, NY 11973-5000*
[4] *Department of Physics, University of California, Irvine, CA 92717*
[5] *Carleton University, Ottawa, Ontario K1S 5B6 Canada*
[6] *Physics Department, University of Guelph, Guelph, Ontario N1G 2W1 Canada*
[7] *Department of Physics and Astronomy, Laurentian University, Sudbury, Ontario P3E 2C6 Canada*
[8] *Institute for Nuclear and Particle Astrophysics and Nuclear Science
Division, Lawrence Berkeley National Laboratory, Berkeley, CA 94720*
[9] *Los Alamos National Laboratory, Los Alamos, NM 87545*
[10] *National Research Council of Canada, Ottawa, ON K1A 0R6, Canada*
[11] *Department of Physics, University of Oxford, Denys Wilkinson Building, Keble Road, Oxford, OX1 3RH, UK*
[12] *Department of Physics and Astronomy, University of Pennsylvania, Philadelphia, PA 19104-6396*
[13] *Department of Physics, Princeton University, Princeton, NJ 08544*
[14] *Department of Physics, Queen's University, Kingston, Ontario K7L 3N6 Canada*
[15] *Rutherford Appleton Laboratory, Chilton, Didcot, Oxon, OX11 0QX, and
University of Sussex, Physics and Astronomy Department, Brighton BN1 9QH, UK*
[16] *TRIUMF, 4004 Wesbrook Mall, Vancouver, BC V6T 2A3, Canada*
[17] *Center for Experimental Nuclear Physics and Astrophysics, and
Department of Physics, University of Washington, Seattle, WA 98195*
(Dated: April 19, 2002)

The Sudbury Neutrino Observatory (SNO) has measured day and night solar neutrino energy spectra and rates. For charged current events, assuming an undistorted ^{8}B spectrum, the night minus day rate is $14.0\% \pm 6.3\%^{+1.5}_{-1.4}\%$ of the average rate. If the total flux of active neutrinos is additionally constrained to have no asymmetry, the ν_e asymmetry is found to be $7.0\% \pm 4.9\%^{+1.3}_{-1.2}\%$. A global solar neutrino analysis in terms of matter-enhanced oscillations of two active flavors strongly favors the Large Mixing Angle (LMA) solution.

The Sudbury Neutrino Observatory (SNO) has provided strong evidence that neutrinos change flavor as they propagate from the core of the Sun [1, 2], independently of solar model flux predictions. This flavor conversion can be explained by neutrino oscillation models based on flavor mixing. For some values of the mixing parameters, spectral distortions and a measurable dependence on solar zenith angle are expected [3–5]. The latter might be caused by interaction with the matter of the Earth (the MSW effect) and would depend not only on oscillation parameters and neutrino energy, but also on the path length and e^- density through the Earth. This Letter presents SNO's first measurements of day and night neutrino energy spectra, and constraints on allowed neutrino mixing parameters.

The data reported here were recorded between November 2, 1999 and May 28, 2001 UTC. The total livetimes for day and night are 128.5 and 177.9 days, respectively. The time-averaged inverse-square distance to the Sun $\langle(\frac{1AU}{R})^2\rangle$ was 1.0002 (day) and 1.0117 (night). During the development of this analysis, the data were partitioned into two sets of approximately equal livetime (split at July 1, 2000), each having substantial day and night components. Analysis procedures were refined during the analysis of Set 1 and fixed before Set 2 was analysed. The latter thus served as an unbiased test. Unless otherwise stated, the analysis presented in this paper is for the combined data set.

The data reduction in [1] was used here. For each event, the number, pattern, and timing of the hit photomultiplier tubes (PMTs) were used to reconstruct effective recoil electron kinetic energy T_{eff}, radial position R, and scattering angle $\theta_\odot$ with respect to the Sun-Earth direction. The charged current (CC), elastic scattering (ES) and neutral current (NC) reactions each have characteristic probability density functions (pdfs) of T_{eff}, R, and $\theta_\odot$. A maximum likelihood fit of the pdfs to the data determined the flux from each of these reactions.

The measured night and day fluxes ϕ_N and ϕ_D were used to form the asymmetry ratio for each reaction: $\mathcal{A} = 2(\phi_N - \phi_D)/(\phi_N + \phi_D)$. The CC interaction is sensitive only to ν_e. The NC interaction is equally sensitive to all active neutrino flavors, so active-only neutrino models predict $\mathcal{A}_{NC} = 0$ [6]. The same models allow $\mathcal{A}_{CC} \neq 0$. The ES reaction has additional contributions from $\nu_{\mu\tau}$ leading to a reduction in its sensitivity to ν_e asymmetries.

SNO used calibration sources [7] to constrain variations in detector response [8] that can lead to day-night asymmetries. A ^{16}N source [9], which produces 6.1-MeV gamma rays, revealed a 1.3% per year drift in the energy

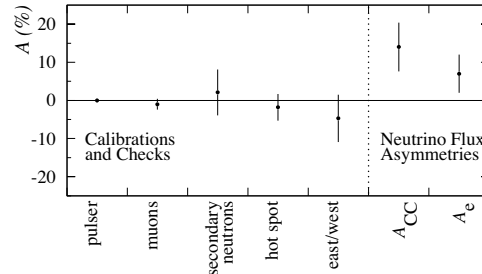*Permanent Address: Birkbeck College, University of London, Malet Road, London WC1E 7HX, UK
†Deceased

FIG. 1: Various event classes used to determine systematic differences between day and night measurements. Also shown are measured asymmetries on the CC flux, and on the electron neutrino flux derived from the CC, ES, and NC rates when the total neutrino flux is constrained to have zero asymmetry.

scale. Due to seasonal variation in day and night livetime, this drift can create an artificial asymmetry. The analysis corrected for this drift and a systematic uncertainty was assigned using worst-case drift models. Gamma rays from the ^{16}N source were also used to constrain directional dependences in SNO's response.

A set of signals that are continuously present in the detector was used to probe possible diurnal variations in detector response. The detector was triggered at 5 Hz with a pulser, verifying livetime accounting. Muons provide an almost constant signal and, through interactions with D_2O, produce secondary neutrons. After applying a cut to remove bursts with high neutron multiplicity, these muon-induced neutrons were used to limit temporal variations in detector response. A more sensitive study focused on a solitary point of high background radioactivity, or "hot spot", on the upper hemisphere of the SNO acrylic vessel, apparently introduced during construction. Its event rate was stable and sufficient to make an excellent test of diurnal variations. It also provides a sensitive test for changes in reconstruction. A limit of 3.5% on the hot spot rate asymmetry was determined, which because of its steeply falling energy spectrum constrained the day and night energy scales to be the same within 0.3%. An east/west division of the neutrino data based on the Sun's position should show no rate variations from matter effects. As expected, the CC rates for east and west data were consistent. The rate asymmetries for each test are shown in Fig. 1.

Backgrounds were subtracted separately for day and night as part of the signal extraction. The results were normalized for an Earth-Sun distance of 1 AU, yielding the results in Table I. Day and night fluxes are given separately for data Sets 1 and 2, and for the combined data. A χ^2 consistency test of the six measured fluxes

TABLE I: The results of signal extraction, assuming an undistorted ^{8}B spectrum. The systematic uncertainties (combined set) include a component that cancels in the formation of the $\mathcal{A}$. Except for the dimensionless $\mathcal{A}$, the units are 10^6 cm^{-2} s^{-1}.

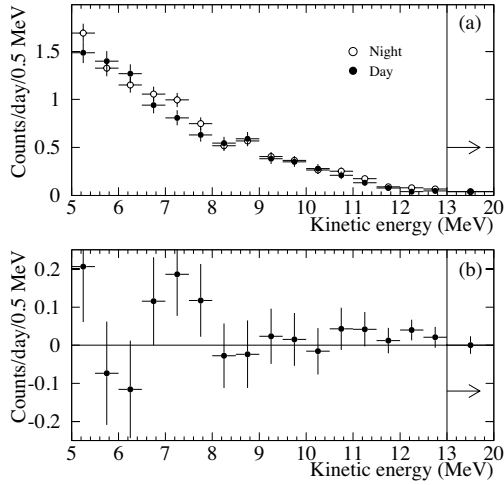| signal	Set 1		Set 2		Combined		$\mathcal{A}(\%)$
	ϕ_D	ϕ_N	ϕ_D	ϕ_N	ϕ_D	ϕ_N	
CC	1.53 ± 0.12	1.95 ± 0.10	1.69 ± 0.12	1.77 ± 0.11	$1.62 \pm 0.08 \pm 0.08$	$1.87 \pm 0.07 \pm 0.10$	$+14.0 \pm 6.3^{+1.5}_{-1.4}$
ES	2.91 ± 0.52	1.59 ± 0.38	2.35 ± 0.51	2.88 ± 0.47	$2.64 \pm 0.37 \pm 0.12$	$2.22 \pm 0.30 \pm 0.12$	$-17.4 \pm 19.5^{+2.4}_{-2.2}$
NC	7.09 ± 0.97	3.95 ± 0.75	4.56 ± 0.89	5.33 ± 0.84	$5.69 \pm 0.66 \pm 0.44$	$4.63 \pm 0.57 \pm 0.44$	$-20.4 \pm 16.9^{+2.4}_{-2.5}$

FIG. 2: (a) Energy spectra for day and night. All signals and backgrounds contribute. The final bin extends from 13.0 to 20.0 MeV. (b) Difference, *night - day*, between the spectra. The day rate was 9.23 ± 0.27 events/day, and the night rate was 9.79 ± 0.24 events/day.

FIG. 3: Joint probability contours for $\mathcal{A}_{tot}$ and $\mathcal{A}_e$. The points indicate the results when $\mathcal{A}_{tot}$ is allowed to float and when it is constrained to zero. The diagonal band indicates the 68% joint contour for the Super-K $\mathcal{A}_{ES}$ measurement.

between Sets 1 and 2 yielded a chance probability of 8%. A similar test done directly on the three asymmetry parameters gave a chance probability of 2%. No systematic has been identified, in either signal or background regions, that would suggest that the differences between Set 1 and Set 2 are other than a statistical fluctuation. For the combined analysis, $\mathcal{A}_{CC}$ is $+2.2\sigma$ from zero, while $\mathcal{A}_{ES}$ and $\mathcal{A}_{NC}$ are -0.9σ and -1.2σ from zero, respectively. Note that $\mathcal{A}_{CC}$ and $\mathcal{A}_{NC}$ are strongly statistically anti-correlated ($\rho = -0.518$), while $\mathcal{A}_{CC}$ and $\mathcal{A}_{ES}$ ($\rho = -0.161$) and $\mathcal{A}_{ES}$ and $\mathcal{A}_{NC}$ ($\rho = -0.106$) are moderatedly anti-correlated. Table II gives the systematic uncertainties on the asymmetry parameters. The day and night energy spectra for all accepted events are shown in Fig. 2.

Table III (a) shows the results for $\mathcal{A}_e$ derived from the CC day and night rate measurements, i.e., $\mathcal{A}_e = \mathcal{A}_{CC}$. The day and night flavor contents were then extracted by changing variables to $\phi_{CC} = \phi_e$, $\phi_{NC} = \phi_{tot} = \phi_e + \phi_{\mu\tau}$,
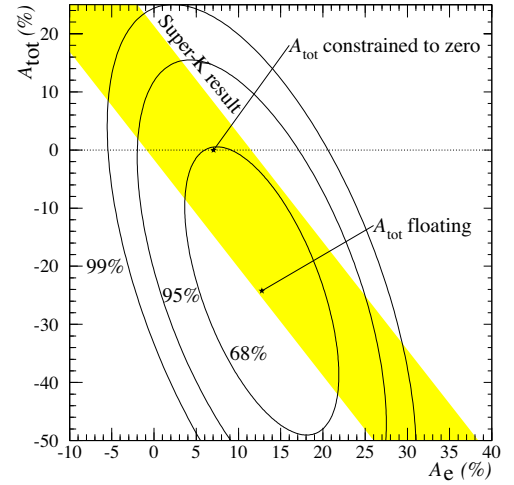
and $\phi_{ES} = \phi_e + \epsilon\phi_{\mu\tau}$, where $\epsilon \equiv 1/6.48$ is the ratio of the average ES cross sections above 5 MeV for $\nu_{\mu\tau}$ and ν_e. Table III (b) shows the asymmetries of ϕ_e and ϕ_{tot} with this additional constraint from the ES rate measurements. This analysis allowed for an asymmetry in the total flux of ^{8}B neutrinos (non-zero $\mathcal{A}_{tot}$), with the measurements of $\mathcal{A}_e$ and $\mathcal{A}_{tot}$ having a strong anti-correlation. Fig. 3 shows the $\mathcal{A}_e$ vs. $\mathcal{A}_{tot}$ joint probability contours. Forcing $\mathcal{A}_{tot} = 0$, as predicted by active-only models, yielded the result in Table III (c) of $\mathcal{A}_e = 7.0\% \pm 4.9\%$ (stat.)$^{+1.3}_{-1.2}\%$ (sys.).

The Super-Kamiokande (SK) collaboration measured $\mathcal{A}_{ES}(SK) = 3.3\% \pm 2.2\%$ (stat.)$^{+1.3}_{-1.2}\%$ (sys.) [10]. The ES measurement includes a neutral current component, which reduces the asymmetry for this reaction relative to $\mathcal{A}_e$ [11]. $\mathcal{A}_{ES}(SK)$ may be converted to an equivalent electron flavor asymmetry using the total neutrino flux measured by SNO, yielding $\mathcal{A}_e(SK)$ (Table III (d)). This value is in good agreement with SNO's direct measure-

TABLE II: Effect of systematic uncertainties on $\mathcal{A}$ (%). For presentation, uncertainties have been symmetrized and rounded.

Systematic	$\delta\mathcal{A}_{CC}$	$\delta\mathcal{A}_{ES}$	$\delta\mathcal{A}_{NC}$
Long-term energy scale drift	0.4	0.5	0.2
Diurnal energy scale variation	1.2	0.7	1.6
Directional energy scale var.	0.2	1.4	0.3
Diurnal energy resolution var.	0.1	0.1	0.3
Directional energy resolution var.	0.0	0.1	0.0
Diurnal vertex shift var.	0.5	0.6	0.7
Directional vertex shift var.	0.0	1.1	0.1
Diurnal vertex resolution var.	0.2	0.7	0.5
Directional angular recon. var.	0.0	0.1	0.1
PMT β-γ background	0.0	0.2	0.5
AV+H$_2$O β-γ bkgd.	0.0	0.6	0.2
D$_2$O β-γ, neutrons bkgd.	0.1	0.4	1.2
External neutrons bkgd.	0.0	0.2	0.4
Sacrifice	0.5	0.5	0.5
Total	1.5	2.4	2.4

TABLE III: Measurement of the ϕ_e and ϕ_{tot} asymmetry for various constraints. All analyses assume an undistorted ^{8}B spectrum.

Constraints	Asymmetry (%)
a) no additional constraint	$\mathcal{A}_{CC} = 14.0 \pm 6.3^{+1.5}_{-1.4}$ $\mathcal{A}_{NC} = -20.4 \pm 16.9^{+2.4}_{-2.5}$ (see text for correlations)
b) $\phi_{ES} = (1-\epsilon)\phi_e + \epsilon\phi_{tot}$	$\mathcal{A}_e = 12.8 \pm 6.2^{+1.5}_{-1.4}$ $\mathcal{A}_{tot} = -24.2 \pm 16.1^{+2.4}_{-2.5}$ correlation = -0.602
c) $\phi_{ES} = (1-\epsilon)\phi_e + \epsilon\phi_{tot}$ $\mathcal{A}_{tot} = 0$	$\mathcal{A}_e = 7.0 \pm 4.9^{+1.3}_{-1.2}$
d) $\phi_{ES} = (1-\epsilon)\phi_e + \epsilon\phi_{tot}$ $\mathcal{A}_{tot} = 0$ $\mathcal{A}_{ES}(SK) = 3.3\% \pm 2.2\%^{+1.3}_{-1.2}\%$	$\mathcal{A}_e(SK) = 5.3 \pm 3.7^{+2.0}_{-1.7}$ (derived from SK $\mathcal{A}_{ES}$ and SNO total ^{8}B flux)

ment of $\mathcal{A}_e$, as seen in Fig. 3.

SNO's day and night energy spectra (Fig. 2) have also been used to produce MSW exclusion plots and limits on neutrino flavor mixing parameters. MSW oscillation models between two active flavors were fit to the data. For simplicity, only the energy spectra were used in the fit, and the radial R and direction $\cos\theta_\odot$ information was omitted. This procedure preserves most of the ability to discriminate between oscillation solutions. A model was constructed for the expected number of counts in

each energy bin by combining the neutrino spectrum [12], the survival probability, and the cross sections [13] with SNO's response functions [8].

There are 3 free parameters in the fit: the total ^{8}B flux ϕ_B, the difference Δm^2 between the squared masses of the two neutrino mass eigenstates, and the mixing angle θ. The flux of higher energy neutrinos from the solar *hep* reaction was fixed at 9.3×10^3 cm^{-2} s^{-1} [14]. Contours were generated in Δm^2 and $\tan^2\theta$ for $\Delta\chi^2(c.l.) = 4.61$ (90%), 5.99 (95%), 9.21 (99%), and 11.83 (99.73%). Fig. 4(a) shows allowed mixing parameter regions using only SNO data with no additional experimental constraints or inputs from solar models. By including flux information from the Cl [15] and Ga experiments [16–20], the day and night spectra from the SK experiment [10], along with solar model predictions for the more robust pp, pep and ^{7}Be neutrino fluxes [14], the contours shown in Fig. 4(b) were produced. This global analysis strongly favors the Large Mixing Angle (LMA) region (see Table IV), and $\tan^2\theta$ values < 1. Repeating the global analysis using the total SNO energy spectrum instead of separate day and night spectra gives nearly identical results.

In summary, SNO has measured the day-night asymmetries of the CC, NC, and ES reaction rates. From these results the first direct measurements of the day-night asymmetries in the ν_e flux and the total ν flux from the Sun have been deduced. A global fit to SNO's day and night energy spectra and data from other solar neutrino experiments strongly favors the LMA solution in a 2-flavor MSW neutrino oscillation analysis.

TABLE IV: Best fit points in the MSW plane for global MSW analysis using all solar neutrino data. ϕ_B is the best-fit ^{8}B flux for each point, and has units of 10^6 cm^{-2} s^{-1}. Δm^2 has units of eV^2. $\mathcal{A}_e$ is the predicted asymmetry for each point.

Region	$\chi^2_{min}/$dof	ϕ_B	$\mathcal{A}_e(\%)$	Δm^2	$\tan^2\theta$	c.l.(%)
LMA	57.0/72	5.86	6.4	5.0×10^{-5}	0.34	—
LOW	67.7/72	4.95	5.9	1.3×10^{-7}	0.55	99.5

[1] Q. R. Ahmad *et al.*, Phys. Rev. Lett. (2002), SNO NC PRL, submitted for publication.

[2] Q. R. Ahmad *et al.*, Phys. Rev. Lett. **87**, 071301 (2001).

[3] S. P. Mikheyev and A. Y. Smirnov, in *'86 Massive Neutrinos in Astrophysics and in Particle Physics, Proceedings of the Moriond Workshop*, edited by O. Fackler and J. Tran Thanh Van (1986), vol. Editions Frontières, Gif-sur-Yvette, 1986, p. 335.

[4] A. J. Baltz and J. Weneser, Phys. Rev. D **37**, 3364 (1988).

[5] M. C. Gonzalez-Garcia, C. Peña-Garay and A. Y. Smirnov, Phys. Rev. D **63**, 113004 (2001).

[6] A non-zero value for $\mathcal{A}_{NC}$ might be evidence for sterile neutrinos.

[7] The SNO Collaboration, Nucl. Instr. and Meth. **A449**, 172 (2000).

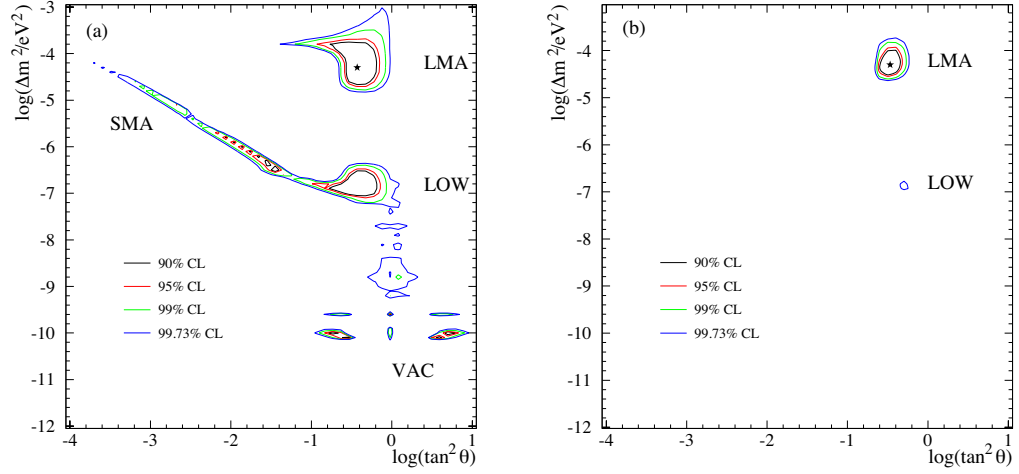[8] Details of SNO response functions are available from the

FIG. 4: Allowed regions of the MSW plane determined by a χ^2 fit to (a) SNO day and night energy spectra and (b) with additional experimental and solar model data. The star indicates the best fit. See text for details.

SNO web site: http://sno.phy.queensu.ca

[9] M. Dragowsky *et al.*, Nucl. Instr. and Meth. **A481**, 284 (2002).

[10] S. Fukuda *et al.*, Phys. Rev. Lett. **86**, 5651 (2001).

[11] J. N. Bahcall, M. C. Gonzalez-Garcia, and C. Peña-Garay (2002), hep-ph/0111150 v2.

[12] C. E. Ortiz *et al.*, Phys. Rev. Lett. **85**, 2909 (2000).

[13] S. Nakamura *et al.* (2002), nucl-th/0201062.

[14] J. N. Bahcall, H. M. Pinsonneault and S. Basu, Astrophys. J **555**, 990 (2001).

[15] B. T. Cleveland *et al.*, Astrophys. J **496**, 505 (1998).

[16] J. N. Abdurashitov *et al.*, Phys. Rev. C **60**, 055801 (1999).

[17] J. N. Abdurashitov *et al.* (2002), astro-ph/0204245

[18] M. Altmann *et al.*, Phys. Lett. B **490**, 16 (2000).

[19] W. Hampel *et al.*, Phys. Lett. B **447**, 127 (1999).

[20] C. M. Cattadori *et al.*, in *Proceedings of the TAUP 2001 Workshop*, (September 2001), Assergi, Italy.

VITA

Miles Smith was born in Melbourne, Australia. In 1992, attending Monash University, he completed a Bachelor of Science Degree with Honors in Physics. Upon graduation he was awarded the Laby Medal by the Australian Institute of Physics, recognizing the top undergraduate physics student. In 1994, at Cambridge University as a Trinity Scholar, he completed the Certificate of Advanced Study in Mathematics, focusing on Quantum Field Theory and General Relativity. After spending the following year as the Broad Scholar at Rice University, he began at the University of Washington. In 1996 he completed his Master of Science and went on to join the Center for Experimental Nuclear Physics and Astrophysics. During his early years in Washington, he was awarded the University's Karrer Prize for *a student who shows promise of a productive career in physics* (1996) and a National Interest Waiver from the United States Government for *a person of exceptional ability* (1999). For his Ph. D. research he joined an international collaboration of scientists working on the Sudbury Neutrino Observatory (SNO), located 6800 ft underground in Sudbury, Ontario. In 2002 he was awarded a Doctor of Philosophy in Physics from the University of Washington. He is currently spending a year from November 2002 - November 2003 at the South Pole, working for the University of Chicago.